Stability Analysis and Design of Grid-Interactive Power Electronic Converters

A Dissertation Presented for the

Doctor of Philosophy

Degree

The University of Tennessee, Knoxville

Le Kong

August 2022

Acknowledgment

I could not have undertaken my Ph.D. research journey without the help from the professors, staff, and colleagues at the CURENT center. My deepest gratitude goes to my advisor, Dr. Fred Wang, for his guidance along this long journey. During the past five years, his profound knowledge, insightful suggestions, and challenging questions help me a lot in my research work. He taught me effective methods in doing academic research by not only thinking about how to solve problems but also thinking deeper about why we need to do this. He not only always provides me timely support on my research work but is also willing to share his life experiences with me, which gives me a lot of help in my personal life and future career development.

I would also like to express my deepest appreciation to Dr. Leon M. Tolbert for giving me advice and encouragement on my research, providing me with a broad view of power electronics in his courses, and helping me improve the writing of this dissertation.

Special thanks to Dr. Jian Sun and Dr. Kai Sun for kindly serving as my Ph.D. committee members and giving me valuable suggestions on improving my dissertation.

I would also like to thank Mr. Yaosuo Xue from Oak Ridge National Laboratory for his generous and continuous support in my research projects. I would like to extend my sincere thanks to Dr. Min H. Kao and Mrs. Kao for their generous financial support for my Ph.D. education so that I can focus on my study without worrying about the finances.

I am also grateful to my colleagues and friends at the CURENT center, for their help in both my research project and my personal life. Especially, I want to thank Dr. Shuyao Wang, Mr. Nattapat Praisuwanna, and Mr. Liang Qiao for their help in the Actuation project and APEG project. I would also like to thank all the other colleagues for their help, companionship, and encouragement over the years.

Last, but most importantly, I am deeply indebted to my family, especially my parents, for their unconditional love and support during this process. I would also like to thank my cats for their entertainment and emotional support.

This dissertation was supported in part by the U.S. Department of Energy, Office of Electricity, Advanced Grid Modeling Program, under Contract DE-AC05-00OR22725; in part by the Engineering Research Program of the National Science Foundation and the DOE through NSF under Award EEC1041877, and in part by the CURENT.

Abstract

The increasing penetration of power electronic converters (PECs) can provide high flexibility, full controllability, sustainability, and improved efficiency for future electric power systems. However, it also introduces new challenges since the wide-frequency-band control dynamics of PECs can interact with the power system and result in different types of instability issues. To holistically address the instability issues, several research activities are conducted in this dissertation.

The modular multilevel converter (MMC), which is one of the most common PECs in high- or medium-voltage power systems, is investigated. An improved MMC dc impedance model is developed by considering both the submodule voltage and circulating current dynamics. The control parameters are then designed accordingly for system stability enhancement. Additionally, to verify the proposed impedance model, a simple-to-use dc impedance measurement unit is developed. To avoid using any extra dedicated equipment, an existing converter in the system under test is leveraged.

The grid-forming inverter (GFM), which is also one of the most popular PECs in power systems, is studied. First, two linear control methods are proposed to improve the stability of the system under small disturbances. Then, a passivity-based control (PBC) approach for GFMs based on the port-Hamiltonian (pH) framework is proposed. It consists of three loops, including the two-channel outer power loop, the virtual oscillator loop, and the inner current loop. The proposed pH-based PBC can render GFMs passive so that it will facilitate the stability design of multi-inverter systems since interconnections of passive systems remain passive. Additionally, the proposed PBC method is extended for any existing stable but non-passive power system. Under the prespecified power flow solutions, the GFMs are proved to be globally asymptotically stable so that they can be stably integrated into any other stable systems without their explicit knowledge.

In addition, the impacts of stability requirements on the system-level design under both small and large disturbances are investigated. Notional ac and dc aircraft electric power systems are selected as example case studies with the system weight being the design target. Impacts of the stability requirements on PEC-rich power system design are then analyzed and quantified.

Table of Contents

List of Tables

List of Figures

Chapter 1. Introduction

1.1 Background and Motivation

In recent decades, growing demand for the development of eco-friendly technology to achieve energy savings and reduction of carbon emissions has been seen globally. As shown in Figure 1-1, the green technology and sustainability market (e.g., green building, carbon footprint management, etc.) value was $8.3 billion in 2019 and is predicted to rise to $57.8 billion by 2030 [1].

One of the main factors driving the market advance is the increasing utilization of power-electronic converters (PECs) in electric power systems. Figure 1-2 shows some example applications of PEC in power systems [2-5], ranging from nano-scale integrated power circuits to large-scale utility power grids, such as:

- renewable energy sources (e.g., photovoltaics, wind turbines), high-voltage dc transmission lines (HVDC), or flexible ac transmission systems (FACTS) in utility power systems;
- transportation electrification systems, e.g., more electric aircraft systems, medium voltage dc (MVDC) shipboard power systems, or electric vehicles;
- heavy industries;
- home appliances, portable devices, etc.

The ongoing extensive replacement of the primary equipment with PECs can improve technical and financial efficiency which contributes to the construction of eco-friendly systems. It is also these substitutions that introduce new challenges to the planning and operation of modern electric power systems, such as system stability [6], reliability [7], security [8], etc. These challenges might be mild in small-scale and low power/voltage autonomous systems, such as the

Figure 1-1. Global green technology and sustainability market [1].

Figure 1-2. Examples of power-electronic converter-rich power systems.

notebook power systems or residential power systems, but they will become significant in large-scale and high-power/voltage systems, such as utility systems or other high/medium voltage applications. For example, as indicated by the major results of the work of the IEEE Task Force in [6], in addition to the impacts of PECs on classic power system stability issues (i.e., rotor angle stability, voltage stability, and frequency stability) [9], two new stability classes, resonance stability and converter-driven stability, are also introduced by PECs. These new types of stability issues will bring new challenges for stable and reliable operations of future power systems.

Therefore, to address the stability issues in PEC-dominated power systems, this dissertation will focus on the analysis and design of PECs to enhance system stability.

To conduct such analysis, four steps are usually followed as discussed below.

Step 1: Building system models

To capture the dynamic characteristics of systems, proper analytical models are often required. There are many modeling methods for PEC-rich power systems for different purposes [10, 11], such as the state-space averaging method, describing function method, harmonic state-space method, black-box method, etc.

Among these modeling methods, the ones that can describe the behaviors of input and output ports will have some advantages for stability analysis in power systems with multiple PECs, especially in large-scale systems. For example, the linearized input or output terminal impedance modeling method can be used for small-signal stability analysis; or the input-output stability criteria can be adopted at the interconnected terminals for system stability analysis under some large disturbances.

Step 2: Applying stability analysis approaches

With the appropriate model to describe system dynamics, mathematical tools are then applied for system stability analysis. Many analytical methods have been developed targeting different types of stability issues [12]. For example, the eigenvalue-based approach, Nyquist stability analysis approach, General Bode approach, or linearized passivity-based approach are used for system small-signal stability analysis; the Lyapunov approach or nonlinear passivity-based approach can be used for large-signal stability analysis. Based on the needs, one can select the most suitable analytical tool for stability analysis.

Step 3: Developing system stability enhancement strategies

In Step 2, the weakest part or the root cause of potential instability issues in the system can be identified. Accordingly, some stability improvement methods can be developed, such as the passive or active damping approach [13, 14], the impedance shaping approach [15], the passivity-based control approach [16], etc. With appropriate instability mitigation strategies, stability issues can then be eliminated.

Step 4: Conducting simulation/experimental validations

With the stability analysis and corresponding stability improvement approaches, commercial simulation software, such as MATLAB/Simulink, PSCAD, PSS/E, etc., or experimental setups, such as Hardware Testbed (HTB) in the CURENT center at the University of Tennessee [17, 18], can then be used to verify the methods and the findings.

Following Step 1 to Step 4 as discussed above, it is promising to solve the problems regarding the analysis and control design of PECs to enhance the stability of power systems. However, there are still some challenges in the practice of this procedure.

First, in Step 1, it is of significance to have sufficiently accurate models for the PECs so that system stability performance can be predicted correctly. For example, in terms of the impedance-based small-signal stability analysis approach, the impedance models of PECs are important. There are different types of PECs in power systems, including dc/dc converters and dc/ac converters. The dc/dc converters or the two-level dc/ac converters have been studied, and their input impedance and output impedances have been well developed [19-32]. However, no accurate dc impedance model for a multilevel modular converter (MMC) has been developed due to its multi-module structure.

In addition, the impedance model of PECs may need to be measured under some situations, e.g., when the internal control information of the PECs cannot be obtained, or when the derived small-signal impedance model needs to be verified with real measurement results. But the impedance measurement usually requires dedicated equipment, which is not easy to set up. A simple and effective way to measure the ac terminal impedance has been developed in [33]; however, no such technique has been developed for dc terminal impedance in high-power and medium- or high-voltage applications yet.

Furthermore, in Step 3, with the stability analysis results in Step 2, the root causes for system instability can be located, and the corresponding stability enhancement solution could be developed. However, there might be one situation in which the system stability cannot be analyzed since the information of the system is not always readily available. For example, when connecting PECs to an unknown power system, how to guarantee the interconnection is always stable? Or how to design PECs so that they could have plug-and-play capability? This remains a challenge for the control design of PECs to be stably integrated into an unknown system under both small disturbances and large disturbances. Another challenging issue is that when multiple converters are operated together, how to maintain the system stability in a local way?

Finally, in addition to the control approaches for the improvement of system stability, the intrinsic limitations of stability requirements on the system-level design, including hardware selections, remain unclear.

To cope with these challenges, the scope of this research can be summarized as (1) improving system-oriented modeling of PECs (specifically, dc impedance modeling of MMC in this dissertation), (2) developing a simple way to measure the dc impedance in high power applications for system stability analysis, (3) investigating the control strategies of PECs for stable integrations into any power grids, and (4) studying the impacts of stability requirements on system design.

1.2 Dissertation Organization

The chapters of this dissertation are organized as follows.

Chapter 2 introduces some preliminaries about stability analysis theorem and tools, including system stability under both small disturbances and large disturbances. The remaining part of this chapter reviews the research activities in stability analysis and design for PEC-rich power systems, including the modeling of PECs in utility power systems, the impedance measurement approach for high-power, high- or medium-voltage applications, and the existing control methods of PECs to be stably integrated into an unknown power system. Based on the review, the research challenges in these areas and the objectives of this dissertation are brought up.

Chapter 3 proposes a refined dc impedance model of MMC for system small-signal stability design, with the consideration of the dynamics of both submodule capacitor voltages and circulating currents.

Chapter 4 develops a simple and effective method for dc impedance measurement in high- or medium-voltage, high-power applications. By using an existing converter in the system, which is connected in parallel with the system under test, the dc terminal impedance of the system can be measured without the need for any dedicated equipment.

Chapter 5 investigates the existing linearized passivity-oriented control method for two-level grid-forming inverters (GFMs) and identifies the research gaps. Accordingly, an online harmonic detection-based approach is proposed to eliminate high-frequency instability issues. In addition, an angle droop compensation control approach is proposed to eliminate the virtual impedance control-induced low-frequency instability issues.

Chapter 6 proposes a nonlinear passivity-based control method for GFMs so that they can be stably connected to any passive power grid. To render the GFMs passive, a port-Hamiltonian (pH)-based control framework is proposed, which is composed of three loops including the two-channel outer power loop to generate the voltage and frequency references, the virtual oscillator loop to emulate the spontaneous synchronization of the oscillators, and the inner current loop to maintain lossless interconnection in pH systems. It is shown that the proposed control strategy can guarantee the passivity of GFMs so that it will facilitate the stable design of multi-inverter systems since interconnections of passive systems remain passive.

Chapter 7 extends the proposed passivity-based control for any stable but non-passive power systems. A Lyapunov function is constructed based on the Hamiltonian function for the proposed approach, and system stability can then be verified. It has been proven that the proposed GFM is global asymptotically stable (GAS) from any initial condition and can eventually reach the prespecified steady-state operating point. Therefore, when directly connecting the proposed GFM to other unknown stable systems, the stability of the entire system will be guaranteed.

Chapter 8 adopts a small-scale PEC-rich power system, i.e., a notional aircraft electric power system, as an example, to study the impacts of stability requirements on system design, including the small-signal stability requirements and the large-signal stability requirements.

Chapter 9 summarizes the work that has been done in this dissertation and recommends some future work.

Chapter 2. Preliminaries, Literature Review, and Research Objectives

This chapter introduces some preliminaries on system stability first. It then reviews the research activities in the corresponding area of stability analysis and control design of grid-interactive power-electronic converters. The research challenges and objectives are proposed next to identify the originality of the work.

2.1 Stability Definitions and Different Classifications

2.1.1 General Stability Definitions for Dynamic Systems

The stability of a system refers to its ability to reach and remain at the desired operating point, which mathematically means an equilibrium state of the system dynamic equations. In general, there are three types of system stability problems, including steady-state (or static) stability, small-signal stability, and large-signal stability [34, 35]. Steady-state (or static) stability is defined as the existence of equilibrium points of system dynamic equations. If there is no steady-state solution for the system dynamic equations, then the system is statically unstable. In the cases where equilibrium points exist, if the trajectories remain in the neighborhood of the equilibrium point, then this point is called a stable equilibrium point; if the trajectories diverge from the equilibrium point, then it is called an unstable equilibrium point. Small-signal stability refers to the ability of a system to maintain steady-state operating points when it is subject to small disturbances, such as incremental changes in system loads. Under small disturbances, there is no significant change in the system dynamic equations or the system working conditions. Therefore, the system can be linearized and analyzed around the operating equilibrium point. Large-signal stability is defined as the ability of a system during large disturbances, such as load transients or faults, that the system response will be able to return to an acceptable equilibrium range. Under large disturbances, the system structures or working conditions might be changed, and a transition between different equilibrium points would happen. Also, note that the studied systems in this dissertation are assumed to be steady-state (or static) stable.

2.1.2 Commonly Used Stability Definitions for PEC-Rich Power Systems

A. Classification 1 of PEC-rich power system stability

The stability issues of electric power systems can be defined based on the practical physical meanings as shown below [9]:

‘*Power system stability is the ability of an electric power system, for a given initial operating condition, to regain a state of operating equilibrium after being subjected to a physical disturbance, with most system variables bounded so that practically the entire system remains intact*.’

Power system stability can be further classified by considering (1) the physical nature of the instability phenomena, (2) the size of disturbances that cause instabilities, and (3) the devices, processes, and the time span of the instability phenomena. Accordingly, the conventional power system stability is classified as rotor angle stability, voltage stability, and frequency stability. Rotor angle stability is defined as the ability of synchronous generators in an interconnected power system to maintain synchronism under either a small disturbance or a large disturbance. Voltage stability refers to the ability of a power system to keep steady voltages at all buses under some load disturbances from a given initial operating point. Frequency stability is defined as the ability of power systems to maintain steady frequency under some system contingencies.

However, since the dynamic behaviors of PECs are different from that of conventional synchronous generators, the stability issues may exhibit different forms from classic power system stability [6]. For example, as shown by some documented incidents of the unstable operations of PEC-rich power systems, there were small-signal slow-interaction low-frequency oscillations induced between wind turbines generations and series compensated lines in the ERCOT region [36], small-signal fast-interaction high-frequency harmonic instability issues in photovoltaic farms [37, 38], or large-signal stability issues when the PEC cannot export the generated power or the PEC reaches its current limit [39, 40]. Therefore, with respect to the conventional power system stability classifications presented in [9], two new categories of stability issues are introduced: converter-driven stability and resonance stability as shown in Figure 2-1. The converter-driven stability issues are mainly caused by the wideband dynamic interactions of the control systems of PECs and the components in the power systems. The resonance stability mainly refers to the electrical resonance stability that is caused by doubly-fed induction generator (DFIG) controls, and the torsional resonance that is affected by the HVDC and FACTs. This classification is based only on intrinsic system dynamics and not on the causes that initiate the instability phenomenon. These two new types of stability classes provide a way to address the challenges and account for the emerging stability issues that are related with the increasing penetration of PECs into bulk power systems. However, these classification might cause some confusion [41]. For example, it is hard to distinguish the 'resonance stability' and 'converter-driven stability' since the resonance stability might also be affected by PECs, etc.

B. Classification 2 of PEC-rich power system stability

Another way to classify the power system stability by considering the impacts of PECs is introduced in [41]. The power system oscillation is divided into '*fundamental-frequency (f_0) component*' and '*non-fundamental-frequency component'*. To achieve stable operations of power systems, it is necessary to maintain the fundamental components and avoid the non-fundamental

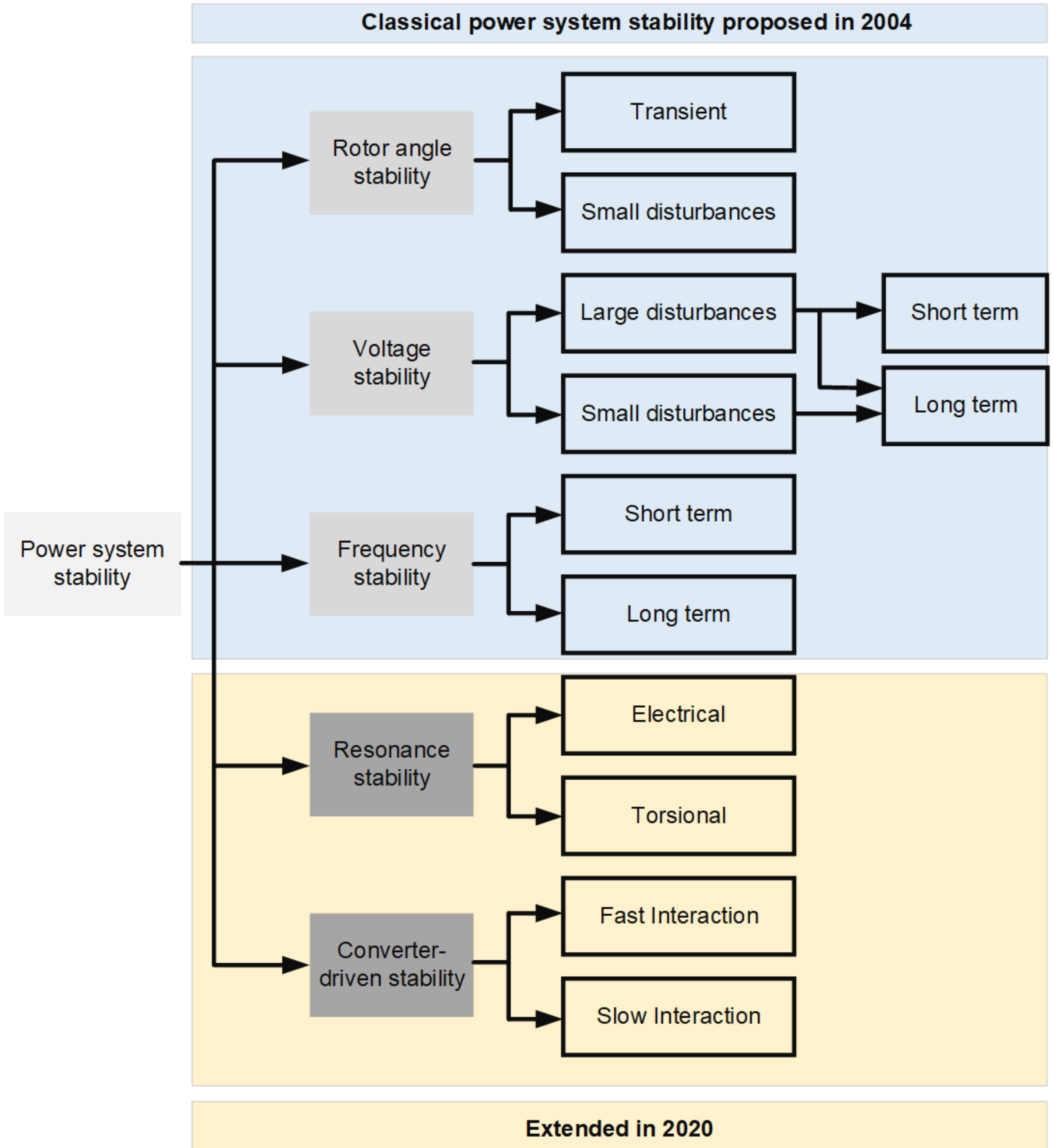

Figure 2-1. Classification of power system stability considering impacts of PECs in [6].

components. Therefore, a revised classification for power system stability is recommended as shown in Figure 2-2. The existing rotor angle stability is modified as angle/synchronous stability which adapts to both classical rotor angle stability of synchronous generators and the angle stability of PECs. Additionally, non-fundamental component stability is considered, including the sub-/super- synchronous stability (0 Hz – $2f_0$ Hz), the intermediate frequency oscillation ($2f_0$ Hz – 1 kHz), and the high-frequency oscillation (above 1 kHz). The frequency ranges for the medium- and high-frequency oscillations are arbitrary values and might be adjusted in the future. As can be seen, the classification in Figure 2-1 is mainly based on the system intrinsic dynamics, while the classification in Figure 2-2 adds one more layer and is based on the instability resonance frequency ranges in the system.

C. Other classification: harmonic stability and synchronization stability

Additionally, there are two types of power system stability issues that are widely reported in the literature: harmonic stability and synchronization stability.

Harmonic Stability

Harmonic stability is a sort of small-signal stability issue, featuring distorted waveforms with oscillation frequencies below and above the system fundamental frequency [11]. The harmonic stability problem was earlier reported in the HVDC system in 1961 [42], where the high grid impedance causes the voltage distortion and leads to the asymmetric firing angle of the Line-Commutated Converters (LCCs), which consequently induces unexpected harmonics in grid current. The harmonic component in the dc side (f_{dc}) would be coupled to the ac side and transformed into two frequency components around the system's fundamental frequency ($f_0 \pm f_{dc}$).

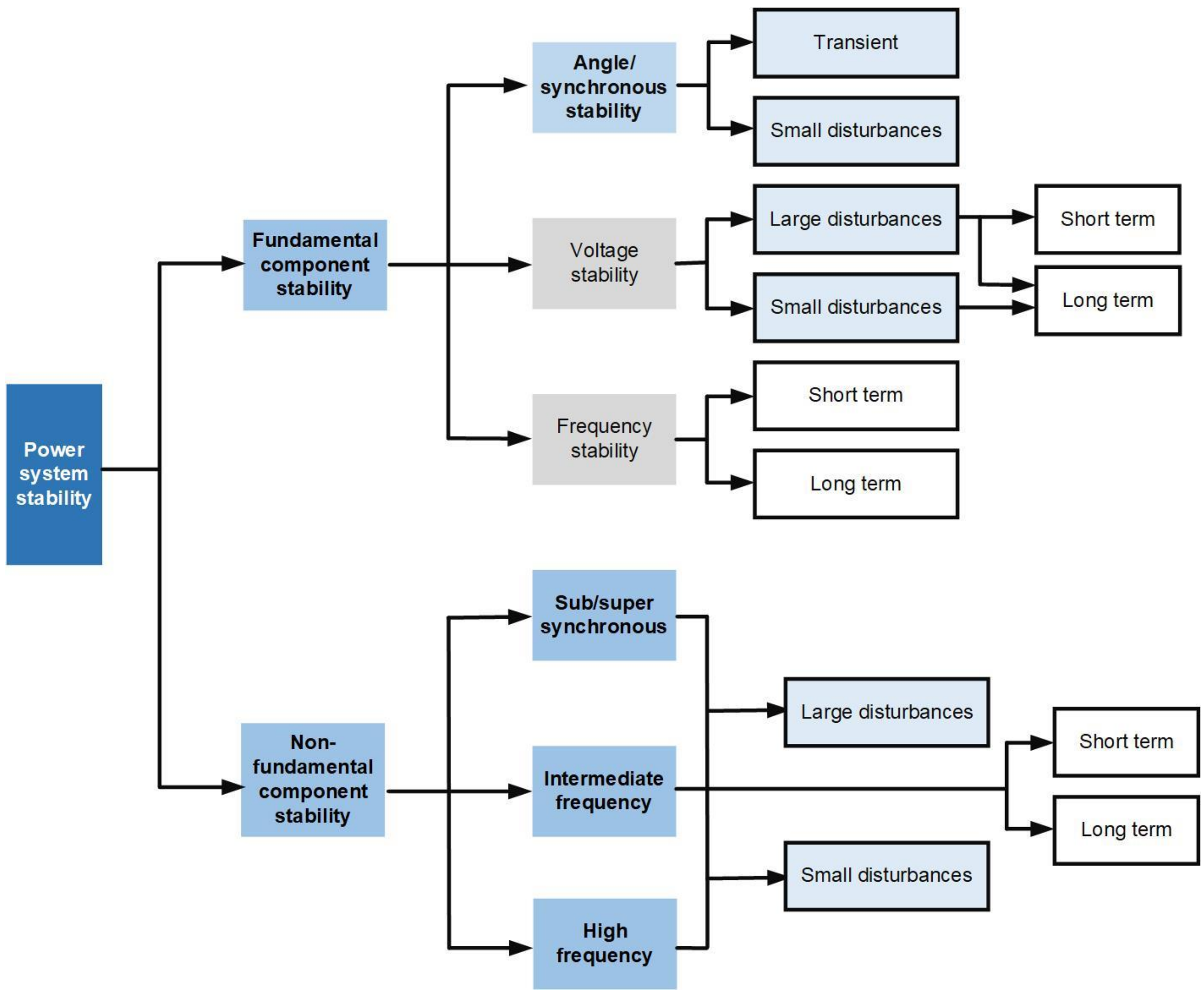

Figure 2-2. Classification of power system stability considering impacts of PECs in [41].

The harmonic instability issues can also be found in the voltage-source converter (VSC)-dominated power systems, but with different formats due to the wideband control dynamics. As shown in Figure 2-3, there are mainly four different types of harmonic instability issues based on the frequency bands: the sub-synchronous oscillation, the near-synchronous oscillations, the harmonic oscillation, and the sideband oscillations. The causes for these harmonic stability issues will be discussed in Section 2.3.3 later when considering the control dynamics of PECs in detail.

Synchronization Stability

Synchronization stability is a type of stability issue of PEC-based resources, including small-signal stability and large-signal (transient) stability [43], which is similar to the rotor angle stability of synchronous generators in legacy power systems. The small-signal synchronization stability refers to the ability of the PEC-based resources to maintain synchronism with the grid under small disturbances; while the large-signal synchronization stability refers to the ability of PEC-based resources to maintain synchronism with the grid under large disturbances. These synchronization stability issues of grid-connected PECs are mainly caused by the interactions of the converter control dynamics and the grid strength, or other slow dynamics in the system. The root causes for the synchronization instability issues will be discussed later in Section 2.3.3 and Section 2.4.2 in detail.

D. Discussions

So far, there have not been a widely accepted definition and classification for the PEC-rich power system stability issues yet. Therefore, in this dissertation, the system stability will be studied with the general definition for any dynamic system first, including small-signal stability and large-signal stability, then mapped to some of the commonly used stability definitions for power systems.

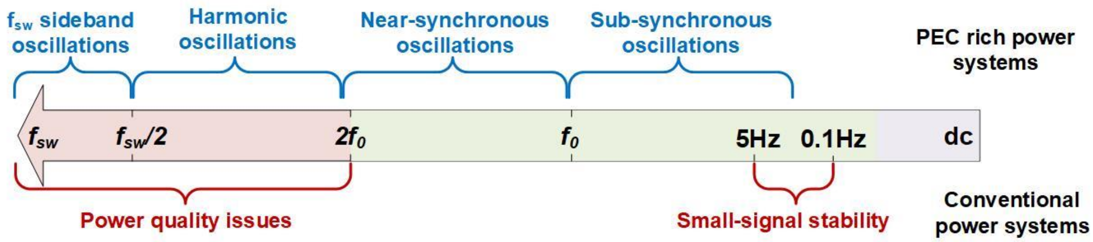

Figure 2-3. Harmonic instability issues in PEC-rich power systems [11].

2.2 Stability Analysis Approaches for PEC-Rich Power Systems

This section briefly summarizes the existing modeling and analysis approaches for small-signal stability and large-signal stability of PEC-rich power systems, to justify

(1) the selection of the impedance-based method for descriptions of PEC portal (terminal) behaviors in terms of system small-signal stability;

(2) the adoption of the port-Hamiltonian framework for descriptions of PEC portal behaviors in terms of system stability under large disturbances;

(3) the use of linear and nonlinear passivity-based criteria for the control design of PECs to have a stable connection to any existing power system under small disturbances and large disturbances, respectively.

2.2.1 Small-Signal Modeling and Stability Analysis Approaches

There are several approaches to analyze the small-signal stability of the PEC-rich power systems, which can be roughly categorized as state-space model-based approaches and impedance model-based approaches based on the modeling methods.

A. State-space model-based approach

The state-space model-based approach has been widely used for the stability analysis of conventional power systems [44] and has also been applied for the stability analysis of PEC-rich power systems. The dynamic behavior of the system can be described by a set of nonlinear ordinary differential equations (ODEs) in state space form as (2. 1), where, x is the state variable vector, y is the output variable vector, and u is the input variable vector.

$$\begin{cases}\dot{x} = f(x,u) \\ y = g(x,u)\end{cases} \tag{2. 1}$$

By linearizing these ODEs at the equilibrium operating point (x_o, y_o, and u_o) under the assumption of small disturbances (Δx, Δy, and Δu), and neglecting the terms containing second and higher-order powers of Δx and Δu, the system equation (2. 1) can then be written as (2. 2), where *A* is the state or plant matrix, *B* is the control or input matrix, *C* is the output matrix, and *D* is the feed-forward matrix. The system eigenvalues $\lambda_i = \alpha_i + j\omega_i$, right eigenvectors Φ_i, and left eigenvectors Ψ_i $(i = 1,2,\cdots,n)$ can then be obtained from the state matrix *A*.

$$\begin{cases}\Delta\dot{x} = A\Delta x + B\Delta u \\ \Delta y = C\Delta x + D\Delta u\end{cases} \tag{2. 2}$$

The eigenvalues contain the information on system dynamics, i.e., the real part of each eigenvalue indicates the system damping capability, and the imaginary part contains the information on the system oscillation frequency. System small-signal stability can then be determined as follows:

(1) The eigenvalues with only real parts indicate non-oscillatory modes. To be more specific, a negative eigenvalue means a decaying mode, and a positive eigenvalue indicates an aperiodic unstable mode.

(2) For eigenvalues with both real part and imaginary part, each conjugate pair corresponds to an oscillatory mode. If the real parts of all the eigenvalues are negative, then the system will be asymptotically stable with a damped oscillation. And if at least one of the eigenvalues has a positive real part, then the system will be unstable with amplitude-increasing oscillations.

The right and left eigenvectors can be used to determine the participation factor (PF) of system states, which is a measure of the correlation between system oscillation modes and state variables of a linear system. The larger the PF is, the more participation of the respective state is to the critical oscillation mode. Therefore, if there are instability issues in the system, the PF method can be adopted to identify the root causes of the system instabilities, and stabilization methods can then be designed accordingly.

The system stability can also be determined by another approach called the transfer-function-based approach which could be derived from the state-space model. By taking Laplace transform on (2. 2), (2. 3) can then be obtained by assuming zero initial conditions.

$$\begin{cases} sX(s) = AX(s) + BU(s) \\ Y(s) = CX(s) + DU(s) \end{cases} \tag{2. 3}$$

The transfer function matrix $T(s)$ from the input $U(s)$ to output $Y(s)$ of the system can then be derived as (2. 4). By checking the pole-zero maps of the closed-loop transfer function $T(s)$, the system stability can then be determined, that is, if all the poles are in the left half plane (LHP), then the system is stable. The relative stability of the system can also be observed from the Bode plot or the Nyquist plot of the open-loop transfer function.

$$T(s) = \frac{Y(s)}{U(s)} = C(sI - A)^{-1}B + D \tag{2. 4}$$

The eigenvalue-based state-space model-based approach or its variation (i.e., the transfer-function-based approach), can be used for stability analysis of a dynamic system, however, they both have some limitations when being applied to PEC-rich power systems. The state-space model is often used for the analysis of low-frequency dynamics (< 10 Hz, e.g., resonance issues in conventional power systems, or slow control loop dynamics in PEC-rich power systems). If faster dynamics in PEC-rich power systems (e.g., harmonic instability issues) are considered, it will result in a high-order matrix that is difficult to compute and analyze. The transfer function model-based approach is often adopted for a single converter analysis. For systems with multiple converters, it will be difficult to analyze the root cause of the potential instability issues since all the interactions among the converters are embedded in one loop transfer function model. Additionally, the model in either state-space form or transfer function form requires detailed control information and network information for the whole system analysis, which may not always be available from the vendors of converters or utility companies.

B. Impedance model-based approach

The impedance model-based approach is prevailing since it only requires the terminal information at the interconnection point, which can be obtained either through an analytical model or practical measurement of the port behaviors. For instance, a PEC-rich power system can be considered as two subsystems (*Subsystem A* and *Subsystem B*) connected as shown in Figure 2-4. The whole system transfer function G_{AB} from input to output can be derived as (2. 5), with a minor loop gain T_{MLG} defined as Z_{out_A}/Z_{in_B}. Since the transfer functions G_A and G_B are stable, the whole system stability can then be determined by only checking T_{MLG}. Note that the subsystem can be a piece of equipment such as a dc/dc converter or ac/dc converter, or a group of equipment connected that can be characterized from the terminal.

$$G_{AB} = \frac{V_{out\_B}}{V_{in\_A}} = G_A G_B \frac{Z_{in\_B}}{Z_{out\_A} + Z_{in\_B}} = G_A G_B \frac{1}{1 + T_{MLG}} \tag{2. 5}$$

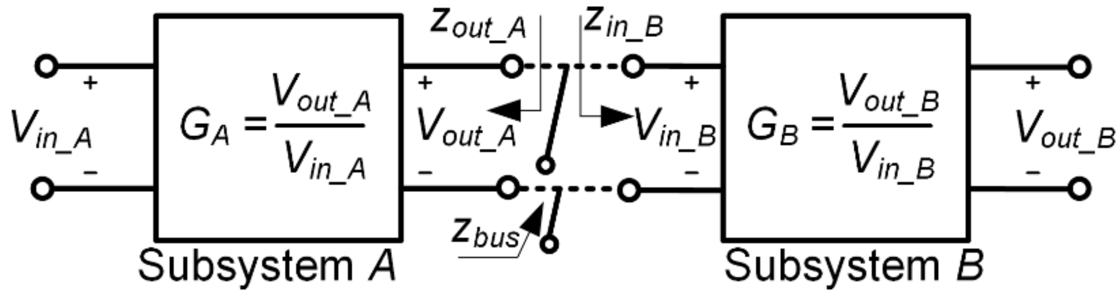

Figure 2-4. Interconnection of two stable subsystems in a PEC-rich power system [45].

In addition to the impedance ratio-based model T_{MLG}, system stability can also be analyzed through the impedance-sum model $Z_{sum} = Z_{out\_A} + Z_{in\_B}$ [46] or the equivalent impedance Z_{bus} seen from the bus port, i.e., $Z_{bus} = Z_{out\_A} // Z_{in\_B}$ [47]. Based on different forms of system impedance models, many small-signal stability analysis tools have been developed to investigate system stability, including the Middlebrook criterion, forbidden region criteria, linearized passivity-based criterion, and Nyquist stability criterion and its extensions.

1) Middlebrook Criterion and Forbidden Region

To guarantee system stability, Middlebrook first applied the minor loop gain T_{MLG} term into the design of input filters of dc-dc converters in 1976, by confining the ratio of filter output impedance and converter input impedance within the unit circle on the complex plane [48], i.e., $|T_{MLG}| << 1$ or $|Z_{out\_A}| << |Z_{in\_B}|$ for all frequencies. Later, this criterion was adopted for stability analysis in distributed power systems. The Middlebrook approach provides an intuitive way of defining the impedance specification to assure system stability, but it is too conservative. Therefore, to relax the conservativeness of the Middlebrook criterion, several forbidden region-based stability criteria were developed, such as the Gain/Phase Margin (GMPM) Criterion [45], the Opposing Argument (OA) Criterion [49], the Energy Source Analysis Consortium (ESAC) Criterion [50], the Root Exponential Stability Criterion (RESC) [51], etc. Compared with the Middlebrook criterion, of which the forbidden region is outside the solid circle as shown in Figure 2-5, the GMPM criterion can allow $|Z_{out\_A}| > |Z_{in\_B}|$ at some frequencies, i.e., the Nyquist contour of T_{MLG} can be outside the unit circle, while ensuring the desired gain margin and phase margin to not encircle (-1, j0) point. The OA criterion is an extension of the GMPM criterion for systems with multiple paralleled load converters. The forbidden region defined by the OA criterion is to the left of the vertical line that intersects of real axis at $-1/GM$, where the encirclement of the (-1, j0) point

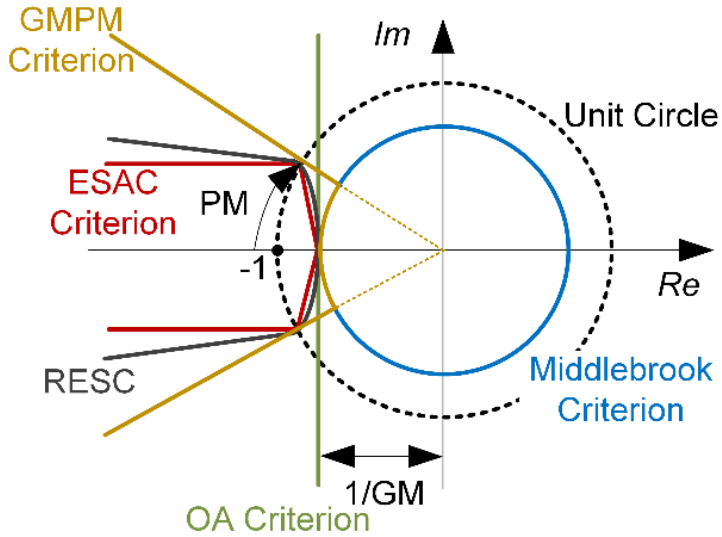

Figure 2-5. Boundaries of the stability criteria on the complex plane [52].

is avoided. The ESAC criterion can further reduce the forbidden region, which is to the left of the defined boundary, but keeps the same values of gain margin and phase margin as in the GMPM criterion. As an extension of ESAC, the RESC has a larger forbidden region that is to the left of the defined boundary, but it is more robust to the numerical variations of the load impedances. Yet, all those stability criteria are sufficient but not necessary conditions. Additionally, the forbidden-region-based stability criteria with only considering avoidance of encirclements of (-1, j0) point are based on a prerequisite, i.e., all the poles of $T_{MLG}(s)$ are in the LHP. If the open-loop right-half plane (RHP) poles exist, those stability criteria cannot work properly.

2) Linearized Passivity-based Stability Criterion (PBSC)

In addition to T_{MLG}-based stability criteria, passivity-based stability criterion (PBSC) has also been proposed for single-bus dc systems [52, 53] or grid-connected PEC design [16, 54-58]. The linearized passivity-based stability criteria are defined as follows. For a linear time-invariant multiple-input-multiple-output (MIMO) system which is represented by a rational transfer function matrix $G(s)$, it is passive if it satisfies [59]:

a) all poles of $G(s)$ are in the LHP, and

b) $\lambda_{min}[G(j\omega) + G^H(j\omega)] \geq 0 \; \forall\omega \in (-\infty, \infty)$, where, λ_{min} is the minimum eigenvalue of the impedance matrix $[G(j\omega) + G^H(j\omega)]$ across the whole frequency and G^H is the conjugate transpose of G.

In addition, for a linear time-invariant single-input-single-output (SISO) system described by a rational transfer function $Z(s)$, it is passive if it satisfies:

a) all poles of $Z(s)$ are in the LHP, and

b) $\mathcal{R}e[Z(j\omega)] \geq 0$ or $phase[Z(j\omega)] \in (-90^o, 90^o) \; \forall\omega \in (-\infty, \infty)$.

Applying the passivity-based stability concept to the example system as shown in Figure 2-4, if the bus impedance Z_{bus} satisfies the passivity conditions, then the overall system is stable. This also implies that the Nyquist contour of $Z_{bus}(j\omega)$ must lie in the RHP. The PBSC can also be applied for single-bus systems with multiple source converters and load converters, where $Z_{bus}(s)$ will be the parallel combination of the input/output impedances of all the converters in the system. In addition to treating the system as a whole through checking Z_{bus}, the system stability can also be determined from the passivity of each subsystem, that is, if the terminal impedance of each subsystem is passive, the system will also be stable when they are connected. Therefore, the PBSC approach is suitable for the PEC design for stable integration of another passive system. However, like Middlebrook Criterion and other forbidden region-based stability criteria, the PBSC can only provide a sufficient but not necessary condition.

3) *Nyquist Stability Criterion (NSC), Inverse Nyquist Stability Criterion (INSC), and Generalized Nyquist Stability Criterion (GNSC)*

A sufficient and necessary condition for the small-signal stability of PEC-rich power systems can be obtained based on the Nyquist stability criterion (NSC). For example, as indicated in (2. 5), the stability of the interconnected system in Figure 2-4 can be determined by the locations of zeros of $(1+T_{MLG}(s))$ under the assumption of stable G_A and G_B. Namely, if there are one or more RHP zeros of $(1+T_{MLG}(s))$, meaning there are one or more RHP poles in G_{AB}, then the system is unstable. The number of RHP zeros (N_Z) in $(1+T_{MLG}(s))$ equals the sum of N_P and N_{CW}, where N_p is defined as the number of RHP poles of $T_{MLG}(s)$; and N_{CW} is defined as the number of clockwise encirclements of (-1, j0) in the Nyquist contour of $T_{MLG}(j\omega)$ in polar plots. Therefore, the system is stable if $N_Z = N_P + N_{CW} = 0$; otherwise, the system is unstable.

A common and simple way to use the NSC for stability analysis of PEC-rich power system is to formulate an impedance ratio according to the types of converters in the system to avoid any open-loop RHP pole so that the system stability depends upon the Nyquist contour of $T_{MLG}(j\omega)$ only. For instance, the numerator of the impedance ratio has to be the impedance of voltage-type converters, and the denominator should be the impedance of current-type converters [60]. However, if the open-loop RHP poles in T_{MLG}(s) cannot be avoided [61], numerical calculation of the number of RHP poles will be required, and the graphical analysis of the Nyquist contour may be cumbersome as well.

An alternative way is to use the inverse Nyquist stability criterion (INSC) if there are no open-loop RHP poles in $1/T_{MLG}(s)$, and the system stability can then be determined by checking merely the Nyquist contour of $1/T_{MLG}(s)$. In addition to applying NSC to the impedance-ratio model, it can also be applied to impedance-sum models of the system by checking encirclement types of the Nyquist contour with the origin as the critical point. That is, a system with two individually stable subsystems is stable, if and only if the impedance sum of the two subsystems does not encircle the origin clockwise [46].

The NSC-based approach can also be extended to MIMO systems, e.g., multi-port MVDC distribution networks for all-electric ships [62], with the Generalized Nyquist stability criterion (GNSC). In a SISO system, the system stability is dependent on the minor loop gain term T_{MLG} as shown in Figure 2-6 (a). Similarly, in a MIMO system, a return-ratio matrix $L_{MLG}(s)$ of the system can be derived based on the Component Connection Method (CCM) in the frequency domain with converters separated from the passive connection network [63]. Then the generalized Nyquist stability criterion is applied to analyze the characteristics loci of the eigenvalues of $L_{MLG}(s)$ as shown in Figure 2-6(b).

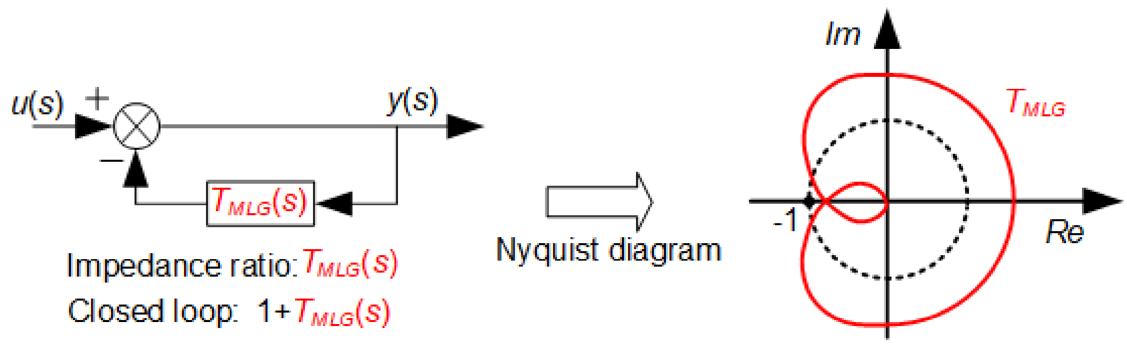

(a)

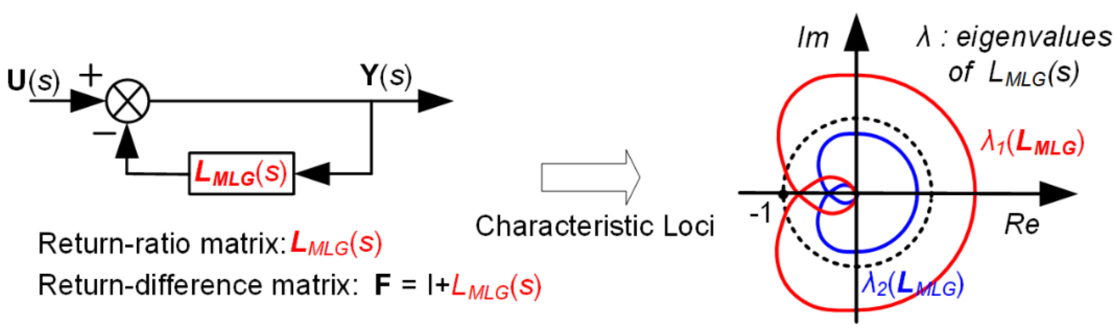

(b)

Figure 2-6. Impedance-ratio-based system stability analysis with NSC (a) for a SISO system and (b) for a MIMO system [35].

4) Generalized Bode Criterion (GBC)

In addition to Nyquist plots, the Bode diagram is also a commonly used graphical representation for the frequency response of a system. Its main advantage is that the impedance ratio term can be separated into the impedance of each subsystem so that interactions between different subsystems can be more intuitively analyzed. The commonly used Bode criteria in power electronics systems, including the classic Bode criterion, the revised Bode criterion I, and the revised Bode criterion II, are to check if there are enough gain margin and phase margin of the open-loop transfer function under certain conditions [64]. However, these criteria are based on some specific cases of the Nyquist criterion, which can only provide a sufficient condition for stability; for example, the classic Bode criterion is only suitable for a minimum phase system without RHP poles or RHP zeros, the revised Bode criterion I can be extended to systems with multiple gain margins and phase margins but with no RHP poles, and the revised Bode criterion II can be applied to systems with RHP poles but with no more than two integrators in the transfer function. Therefore, none of these Bode criteria are like the Nyquist criterion that can apply to any type of system. Hence, a generalized Bode criterion (GBC) which is equivalent to the Nyquist stability criterion for arbitrary systems is needed. The GBC can be derived from the Nyquist stability criterion with system minor loop gain and formulated on Bode diagrams with impedances of each subsystem by mapping between Nyquist and Bode plots as shown in Figure 2-7 [61, 64, 65]. The system minor loop gain is assumed as $T_1 = Z_1/Z_2$ with one magnitude crossing of Z_1 and Z_2, where Z_1 and Z_2 are the terminal impedances of each subsystem. And the goal is still to check the encirclement type of the critical point (-1, j0) of the Nyquist contour of T_1. Thus, the general rules of using Bode plots for system stability analysis can be summarized in Table 2-1, where the relationships of magnitude, phase, and phase derivatives (i.e., $(\angle Z_1)'$ or $(\angle Z_2)'$) of the impedance

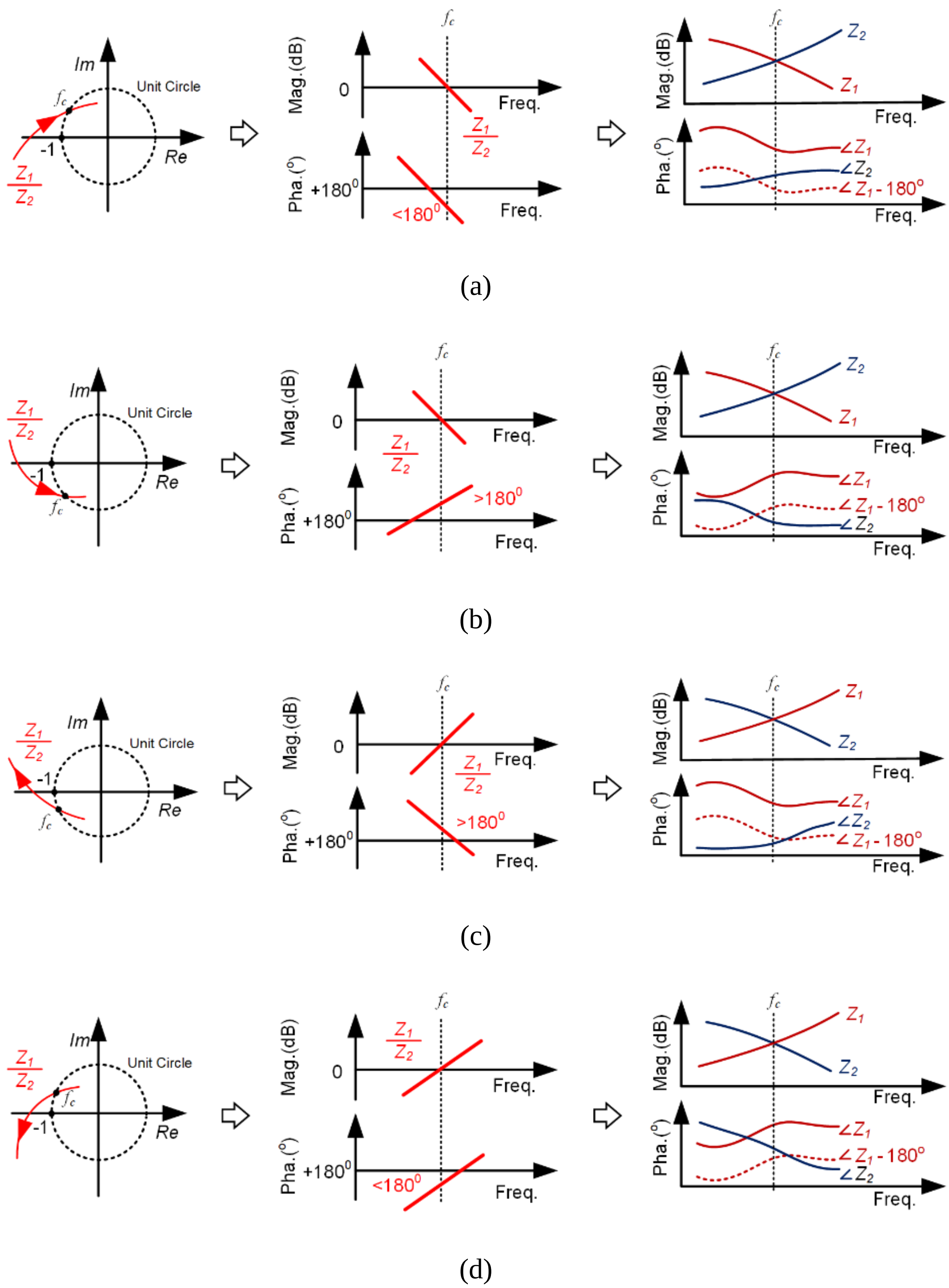

Figure 2-7. Mapping from Nyquist to Bode diagrams: (a) into the unit circle clockwise, (b) into the unit circle counterclockwise, (c) out of the unit circle clockwise, and (d) out of the unit circle counterclockwise [65].

Table 2-1. General rules of using Bode plots for system stability analysis [65].

Case	Magnitude (lower than f_c)	Phase at f_c	Encirclement type	Encirclement condition
(a)	$\lvert Z_1\rvert > \lvert Z_2\rvert$	$(\angle Z_1)' < (\angle Z_2)'$	Clockwise	$\angle Z_1 - \angle Z_2 < 180^o$
(b)	$\lvert Z_1\rvert > \lvert Z_2\rvert$	$(\angle Z_1)' > (\angle Z_2)'$	Counterclockwise	$\angle Z_1 - \angle Z_2 > 180^o$
(c)	$\lvert Z_1\rvert < \lvert Z_2\rvert$	$(\angle Z_1)' < (\angle Z_2)'$	Clockwise	$\angle Z_1 - \angle Z_2 > 180^o$
(d)	$\lvert Z_1\rvert < \lvert Z_2\rvert$	$(\angle Z_1)' > (\angle Z_2)'$	Counterclockwise	$\angle Z_1 - \angle Z_2 < 180^o$

are all needed to determine system stability. For cases with multiple crossings of the magnitude of the impedances, general rules using Bode plots to identify the encirclements of the critical point of Z_1/Z_2 consist of four steps as shown in Table 2-2 [61]. Since the Bode plots only show the response in the positive frequency region, the number of crossings at different frequencies should be doubled except at 0 Hz. If the crossing occurs at 0 Hz, it will only be counted once.

C. Discussions on the small-signal modeling and stability analysis methods

Based upon the review of existing small-signal stability studies, the modeling approach and stability analysis method in this research can be determined. First, the impedance-based modeling approach is preferred mainly due to the following advantages:

(1) The impedance model can be obtained either through analytical derivation with all the detailed information or through practical measurement with a black box.

(2) The root cause of the instability issues in the system can be identified easily by observing the interactions among different terminal impedances.

(3) With only the need for portal behaviors of each piece of equipment, it is feasible to stably integrate multiple converters into a large-scale power system.

Second, proper small-signal stability analysis approaches based on the impedance models can be selected according to the given conditions. For instance, the PBSC can be used to design the control parameters of each subsystem separately and independently, if a conservative design is allowed in the system. Also, the PBSC can be used for the passivity-based control (PBC) design of PECs so that they can be stably connected to any other passive system. The NSC or the GBC is preferred for stability analysis of a known system. It can be used to identify the root cause of an unstable phenomenon or to find the potential unstable connection in the system.

Table 2-2. Indication rules of the critical point encirclements in Bode plot [61].

Steps	Mathematical representation	Detailed Descriptions
1	$\lvert Z_1 \rvert > \lvert Z_2 \rvert$	Find all the exterior regions (ERs) outside the unit circle of the Nyquist diagram of T_1, where the numerator impedance Z_1 is larger than the denominator impedance Z_2.
2	$\angle Z_1 - \angle Z_2 = \pm 180^o$	Check whether there are crossings of the critical boundaries (CBs) and phase of Z_2 within the ERs, where the CBs are defined as the shifted phase of Z_1, i.e., $\angle Z_1 \pm 180^o$.
3	$(\angle Z_1)' < (\angle Z_2)'$ or $(\angle Z_1)' > (\angle Z_2)'$	Determine the encirclement types if there is phase crossing. At each crossover frequency, if $(\angle Z_1)' < (\angle Z_2)'$, the crossing type will be clockwise crossing; if $(\angle Z_1)' > (\angle Z_2)'$, it will be counterclockwise encirclement.
4	Counting	Calculate the number of crossings. If the crossover frequency is not 0 Hz, then the crossing number should be doubled, whereas, for a crossover frequency equal to 0 Hz, the number should be counted separately.

2.2.2 Large-Signal Modeling and Stability Analysis Approaches

Many small-signal stability analysis approaches have been developed to address the instability issues in PEC-rich power systems. However, they are only applicable to systems under small disturbances; for stability analysis under large disturbances, large-signal stability analysis methods are required. Historically, there are two types of dominant large-signal stability analysis techniques: Lyapunov techniques and input-output techniques [66].

A. Lyapunov techniques

In 1892, Aleksandr Lyapunov published his doctoral dissertation entitled '*The General Problem of the Stability of Motion'*, which introduced a way to assess the stability of a nonlinear system under given initial conditions without the need of solving the system ODEs. Since then, the Lyapunov stability theory has been found to be practical and powerful in solving control problems of nonlinear systems. The basic concept of Lyapunov techniques is to use the energy function for the stability analysis of a dynamic system, i.e., if there is an asymptotic stable equilibrium point in the system, then when the states are in the region of attraction, the energy function should be decreasing as time increases; while if the energy function is increasing as time increases, then the system is unstable. Many theorems have been developed according to the Lyapunov energy function, and one of the most important methods for engineering applications is the Lyapunov direct method.

The Lyapunov direct method, which is also called the second method of Lyapunov, can be used to determine the stability of a system. In a PEC-rich power system, such as a dc microgrid [67], the inductor currents i_L and capacitor voltages u_C are normally selected as state variables x, and then a Lyapunov function $V(x)$ can be constructed. The system is asymptotically stable if the Lyapunov function $V(x)$ satisfies:

(1) $V(x,t)$ is positive definite, and

(2) $\dot{V}(x,t)$ is negative definite, where $\dot{V}(x,t)$ is the full derivative of $V(x,t)$.

This means the energy defined by V is always dissipated, except at $x = 0$. Furthermore, if when $\|x\| \to \infty$, $V(x) \to \infty$, then the system is globally asymptotically stable.

The construction of the Lyapunov energy function is the key to system stability analysis, which is also a complicated task. Several other methods have been developed to be combined with the Lyapunov theorem to generate the candidate Lyapunov function, such as the Takagi-Sugeno fuzzy model [68, 69]. However, there might still be cases where finding the Lyapunov function of the system is even more difficult than solving the ODEs directly. In addition, when applying the Lyapunov method for system stability assessment, the assumption is that there are no external disturbances, but rather the system starts from an initial condition that is away from the desired equilibrium point. This is a good assumption for some problems, however, for interconnected systems, the more important issue should be the relationships in the sense of stability between the input terminals and output terminals in the system, rather than the stability of an equilibrium point under any given initial condition.

B. Input-output techniques

The input-output techniques specifically investigate the interconnection stability based on the input-output relationship among different systems, which was first proposed by two independent researchers: Irwin Sandberg from Bell Laboratories [70-72] and George Zames from Massachusetts Institute of Technology [73, 74]. Three ways of assessing closed-loop stability in terms of input-output relationships between the plant and the controller have been summarized [73]: the small-gain theorem, the passivity theorem, and the conic sector stability theorem. Among them, the small gain theorem and the passivity theorem have attracted much attention over the years in the research field of analysis and design for nonlinear systems. The input-output stability analysis techniques can be considered with a classical interconnected system as shown in Figure 2-8.

If the subsystems G_1 and G_2 are stable, it will result in a stable closed-loop system provided that the small gain theorem is satisfied. Specifically, suppose that G_1 and G_2 have L_q-gains $\gamma_q(G_1)$ and $\gamma_q(G_2)$, respectively, then the closed-loop system will have finite L_q-gain as long as it meets the criterion in (2. 6), where q can be defined as any positive integer up to positive infinite.

$$\gamma_q(G_1)\gamma_q(G_2) < 1 \tag{2. 6}$$

The nonlinear passivity theory has also gained much attention because of its feasibility and practicality in system modeling and control design. In general, a system is passive if there exists a storage function S: $\mathbb{R}^n \rightarrow \mathbb{R}_+$ satisfying (2. 7), where $x \in \mathbb{R}^n$ is state variable, $u, y \in \mathbb{R}^n$ are the input and output variable (or port variables), and the product $u^T y$ is the supply rate [75]. That is the stored energy in the system should never exceed the supplied energy if the system is passive.

$$S\big(x(t)\big) - S(x(0)) \leq \int_0^t u^T y dt \tag{2. 7}$$

To apply the passivity properties for system stability analysis, a storage function is required to be defined first. In order to get the storage function, it is helpful to reformulate the system ODEs into a known framework, such as the energy-based Euler-Lagrange (EL) formulation and the port-Hamiltonian (pH) formulation, or the power-based Brayton-Moser (BM) formulation [76, 77].

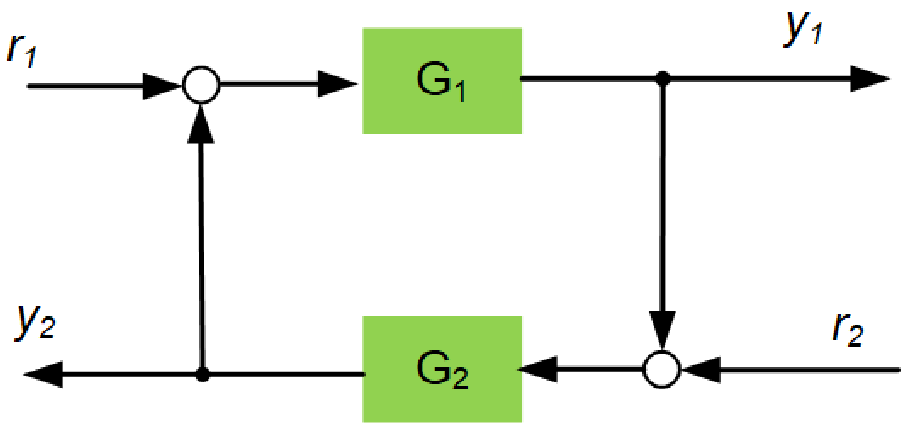

Figure 2-8. Configuration of feedback interconnected systems.

The EL formulation is a special format by the Lagrangian equation of the motion, i.e., Lagrange's equations of the second kind, as shown in (2. 8), where $q = (q_1, \cdots, q_n)^T$ are the generalized coordinates for the system with *n* degrees of freedom, $\mathcal{F}(\dot{q})$ is the Rayleigh dissipation function satisfying $\dot{q}^T \frac{\partial \mathcal{F}}{\partial \dot{q}}(\dot{q}) \geq 0$ for all $\dot{q}$, $\mathcal{M}$ is a constant matrix, u is the control vector, Q_ς is the external signal that models the effect of disturbances, and $\mathcal{L}(q, \dot{q})$ is the Lagrangian function which is defined as the difference between the kinetic energy $\mathcal{T}(q, \dot{q})$ and potential energy $\mathcal{V}(q)$ as shown in (2. 16) [78].

$$\frac{d}{dt}\left(\frac{\partial L}{\partial \dot{q}}(q, \dot{q})\right) - \frac{\partial \mathcal{L}}{\partial q}(q, \dot{q}) + \frac{\partial \mathcal{F}}{\partial \dot{q}}(\dot{q}) = \mathcal{M}u + Q_\varsigma \tag{2. 8}$$

$$\mathcal{L}(q, \dot{q}) \triangleq \mathcal{T}(q, \dot{q}) - \mathcal{V}(q) \tag{2. 9}$$

The system total energy can then be denoted by $\mathcal{H}(q, \dot{q})$, also regarded as the system storage function, as given in (2. 10).

$$\mathcal{H}(q, \dot{q}) \triangleq \mathcal{T}(q, \dot{q}) + \mathcal{V}(q) \tag{2. 10}$$

Therefore, the passivity of the EL system should satisfy (2. 11).

$$< u|\mathcal{M}^T \dot{q} >_T \geq \mathcal{H}[q(T), \dot{q}(T)] - \mathcal{H}[q(0), \dot{q}(0)] \tag{2. 11}$$

By defining the vector of generalized momenta $p = (p_1, \cdots, p_n)^T$ as (2. 12), the *n* second-order equation (2. 8) can be transformed into 2*n* first-order equations as in (2. 13), where τ is the vector of generalized force acting on the system, H is the Hamiltonian function which is the Legendre transform of $\mathcal{L}$, also equals to system total energy in (2. 10). For electrical networks, the Hamiltonian is the sum of total stored magnetic energy and electric energy.

$$p := \frac{\partial L}{\partial \dot{q}}(q, \dot{q}) \tag{2. 12}$$

$$\begin{aligned} \dot{q} &= \frac{\partial H}{\partial p}(q, p) \\ \dot{p} &= -\frac{\partial H}{\partial p}(q, p) + \tau \end{aligned} \tag{2. 13}$$

The pH framework is the special formalism of the general classical Hamiltonian equations of motion (2. 13) [75, 79]. The framework of input-state-output port-Hamiltonian structure is shown in (2. 14), where x is the state vector, u and y are the input and output, $\mathcal{J}(x)$ is the n-order interconnection matrix satisfying $\mathcal{J}(x) = -\mathcal{J}^T(x)$, $\mathcal{R}(x)$ is the damping matrix satisfying $\mathcal{R}(x) = \mathcal{R}^T(x) \geq 0$, $G(x)$ is the input matrix, and $D(x)$ is the feedthrough term. If the Hamiltonian $H(x)$ is bounded from below and satisfies (2. 15), then the system is passive.

$$\begin{aligned} \dot{x} &= \{\mathcal{J}(x) - \mathcal{R}(x)\}\nabla H(x) + G(x)u \\ y &= G^T(x)\nabla H(x) + D(x)u \end{aligned} \tag{2. 14}$$

$$H(x(t)) \leq H\big(x(0)\big) + \int_0^t u^T y dt \tag{2. 15}$$

Another well-known formulation that has been extensively applied for nonlinear resistive-inductive-capacitive (RLC) circuit modeling is the BM framework as shown in (2. 16), where L and C are the inductance and capacitance matrix, respectively; u_s is the voltage sources; i and v are the state variables denoting the currents through the inductor and the voltages across the capacitors, respectively; B is the input matrix; and $P(u, i, v)$ is the system power-related function, i.e., the mixed potential function, as shown in (2. 17) to be the storage function or a Lyapunov-like energy function, where $\Gamma(u)$ is the power circulating across the dynamic elements, $P_R(i)$ is the power dissipated in the resistors connected in series to the inductor, and $P_G(v)$ is the power dissipated in the resistors connected in parallel to the capacitors [67, 80-83]. In the BM framework, the total system energy can also be selected as the storage function, and the passivity criterion can be applied accordingly.

$$\begin{cases} -L\dfrac{di}{dt} = \dfrac{\partial P(u,i,v)}{\partial i} - Bu_s \\ \quad C\dfrac{dv}{dt} = \dfrac{\partial P(u,i,v)}{\partial v} \end{cases} \tag{2. 16}$$

$$P(u,i,v) = i^T\Gamma(u)v + P_R(i) - P_G(v) \tag{2. 17}$$

However, the BM mixed potential theorem might be incomplete in some sense [84]. First, the mixed potential function P^* should be defined as P^*: $R^n \rightarrow R$ and be of the class C^1, C^2. Second, BM theory can provide sufficient conditions for the convergence to the set which includes all the equilibrium points. However, it cannot indicate the specific equilibrium point to which the system will converge.

C. Discussions on the large-signal modeling and stability analysis method

Based on the review, the large-signal modeling and stability analysis approach, though all of them can only give sufficient conditions for system design, can be used to have closed-form analysis results.

In this dissertation, the input-output stability criterion, specifically, the passivity-based stability criterion, is selected for system large-signal stability analysis due to the following reasons. First, the Lyapunov method requires that there are no external inputs for the system, and assumes the system starts from a group of initial points that are away from the desired equilibrium. However, external disturbances or noises are constantly being applied to the system being controlled. Therefore, it is more feasible to study the relationships between the input and output of the system. Second, it is convenient to use the passivity properties since connections of any passive subsystems will lead to an entirely passive system. This feature can facilitate the design of a single device in PEC-rich power systems, that is, if all the PECs are designed to be passive when they are connected, the system stability can be guaranteed. Also, comparisons of different formats to achieve passivity-based control are summarized in Table 2-3. Based on this, the pH framework can be selected because it has simpler dynamic equations which are in first-order format, and it can be easily mapped to Lyapunov stability analysis by constructing the Lyapunov functions from the Hamiltonian functions.

In summary, in this dissertation, the pH formulation is adopted for the modeling of the PEC since only the portal behavior is required, and the PBC method is applied directly to design the converter to be passive to ensure a stable connection with other passive systems.

2.3 Review of Analysis and Control Design of PECs for System Small-Signal Stability

2.3.1 Small-Signal Impedance Model

To apply the small-signal stability analysis approaches to a PEC-rich power system, the most fundamental step is to have an accurate system model which can be obtained either through a white-box way, i.e., mathematical derivation with the knowledge of the entire system, or through a black-box way, i.e., numerical calculation with measured data.

With regard to the white-box modeling approach, all the different types of PECs need to be investigated based on the specific circuit diagrams and control blocks. There are mainly two types of typical PECs in power systems in general, including dc/dc PECs (i.e., Buck converter, Boost

Table 2-3. Large-signal stability analysis with passivity theorem in different frameworks

Frameworks	Definition	Features
EL framework	The special format of the Lagrangian equation of motion	▪ *N* second-order equations ▪ Energy-based equation ▪ A candidate for the Lyapunov function
pH framework	▪ The Hamiltonian function is the Legendre transform of the Lagrangian function ▪ The special format of the classical Hamiltonian equation of motion	▪ *2N* first-order equations ▪ Energy-based equation ▪ A candidate for the Lyapunov function
BM framework	Modeling for nonlinear RLC circuit	▪ Power-based equation ▪ The criterion is incomplete in some sense [84]

converter, Buck-Boost converter, etc.) and dc/ac PECs (i.e., two-level voltage source converter, modular multilevel converter, etc.). Therefore, in general, there will be two types of impedance models in PEC-rich power systems, that is dc impedance models and ac impedance models. The dc impedance model is obtained at the dc terminal of dc/dc PECs or dc/ac PECs, and the ac impedance model is obtained at the ac point of common connection of dc/ac PECs. So far, the dc impedance models of dc/dc converters and the dc and ac impedance models of the two-level voltage source converters (2L-VSCs) have been well developed in [19-32].

However, due to the complicated dynamics in the circuit, it is challenging to derive the impedance models of MMC. Several research efforts have been conducted to obtain the impedance models of MMC for system analysis. In [85, 86], the ac impedance model of MMC has been developed, and the ac bus stability was investigated but not the dc bus. In [87], both ac and dc impedances of MMC were derived, but it only considered the effects of circulating current control. The dc impedance model was simplified as an RLC branch without considering the effects of MMC control blocks. Another dc impedance model of MMC was developed in [88]. This model was developed for single line-to-ground fault conditions with/without circulating current control. But the submodule capacitor voltage is assumed to be constant. Reference [89] developed a dc impedance model of MMC and analyzed the stability in MVDC applications, but this model relies on the assumption of large enough submodule capacitors, which ignores the submodule voltage dynamics. In [90], an average model represented by an equivalent 2L-VSC was proposed. This model considered the effect of the submodule capacitor voltage ripple. Therefore, it can reveal some dynamic behaviors of MMCs. However, it cannot predict the effect of circulating current dynamics due to the intrinsic limits of the equivalent two-level structure. Note that details of dc impedance models in [89] and [90] will be further discussed in Chapter 3.

Although the impedance models of MMC developed so far have addressed certain issues, there are still some limitations due to the assumptions in the model-derivation process. An accurate MMC dc impedance model considering the effects of submodule capacitor voltage dynamics and circulating current suppression control has not been discussed in the literature yet.

2.3.2 Small-Signal Impedance Measurement

The impedance-based stability analysis approach is preferred since it only requires the terminal characteristics of each piece of equipment (e.g., PEC) or subsystem, which can be acquired through measurement or provided by the vendors. For an equipment vendor, the impedance models can be derived based on the internal structure of the equipment and then validated through measurement. Or for some complex systems, vendors or system integrators can obtain the impedance models through measurement. Therefore, impedance measurement of connected subsystems plays an important role in system stability analysis and design [91].

The impedance measurement setup with commercial products for impedance measurement usually requires dedicated equipment as shown in Figure 2-9, including the frequency response analyzer (FRA) and input modulators (e.g., the power amplifier (PA) or the line injector). Both FRA and PA have isolated output so that they can be directly connected to the system at any potential. However, no commercial product has been released for impedance measurement for high-power applications [92]. The challenge is mainly on how to generate and inject needed perturbation signals that should be effective and measurable under medium- or high-voltage, high-power conditions. Additionally, isolation issues also need to be considered. For the commercially available FRA and PA, the isolation voltage is usually around a few hundred volts. Therefore, if applying them to medium- or high-voltage systems, transformers with high bandwidth will be required, otherwise, the measurable frequency range will be limited.

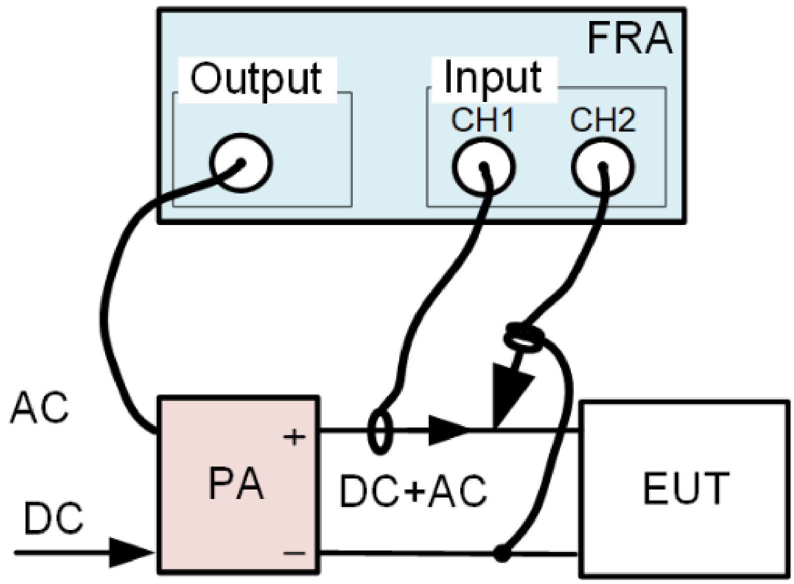

Figure 2-9. Example of dc impedance measurement setup.

Another solution is to build an impedance measurement unit (IMU) for the dc system. As shown in Figure 2-10, the IMU consists of several power electronics building block (PEBB) subsystems [92]. In each PEBB, high voltage silicon-carbide (SiC) H-bridge modules are used to reduce the number of PEBBs and achieve a high switching frequency for higher control bandwidth. The output inductor is to limit the current ripple in the current injection mode. The capacitor bank provides the energy buffer to avoid a large voltage ripple when the generated perturbations are at a very low frequency. The Si IGBT inserted on the dc source side in the internal circuit of PEBB is to protect in case of overcurrent faults. Besides, the PEBBs can also be designed to get energy from the system under test without the need for an extra dc power supply. The dc side of the PEBB is floating. And since the injected power is reactive, only losses in the PEBB are active, which is negligible compared to the power rating of the system under test. In this example, three PEBBs form an IMU, which can operate in either shunt injection mode or series injection mode. In the shunt injection mode, the PEBBs are connected in series to form an IMU which is to sustain system voltage and inject perturbation currents into the dc-link of the system under test. And the anti-series IGBTs in the path from the source converter to the load converter are always on. In the series injection mode, the PEBBs are in parallel to sustain the system current and inject voltage perturbations into the system under test. The anti-series IGBTs are initially on, and after the IMU is started, they are turned off. The capacitor in parallel with the anti-series IGBTs is to maintain the perturbation voltage. However, the PEBB-based approach also requires extra effort in building the IMU.

Without the need for extra equipment, the existing converter in the system under test can be used. The perturbation signals can be integrated into the control signal of the converter, then the converter output will contain the desired perturbation power. With different injected perturbations,

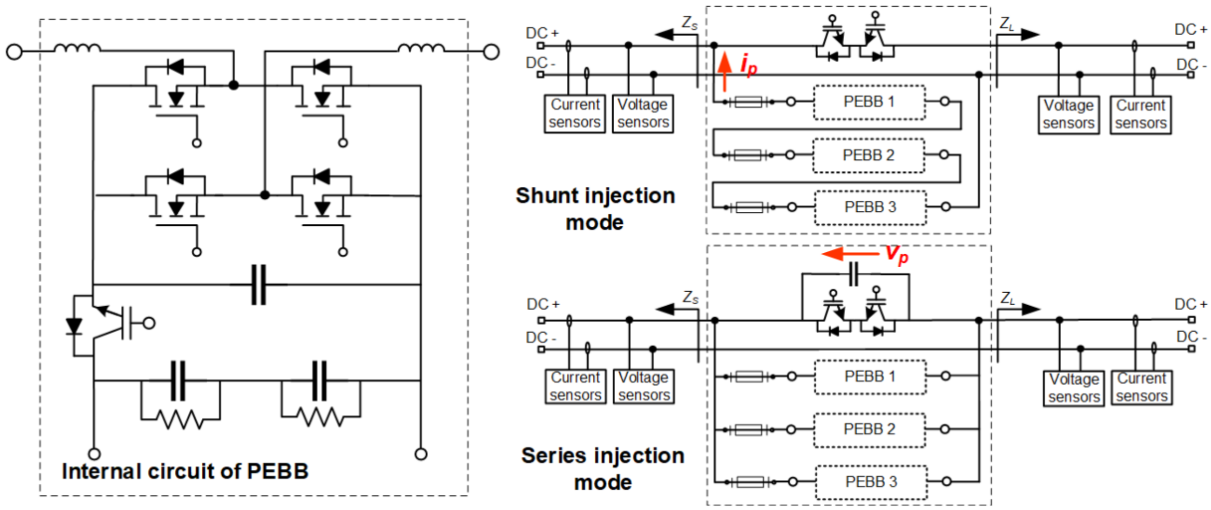

Figure 2-10. Perturbation injection circuits in MVDC systems[92].

the terminal response of the system under test can be measured to extract the impedance characteristics. A solution with such a concept has been developed in [33] for ac impedance measurement as shown in Figure 2-11, but no such method has been developed for dc impedance measurement for medium- or high- voltage, high power applications in literature yet.

2.3.3 Control Design to Enhance System Small-Signal Stability

A. Control design for known systems

The dynamics of the entire power grid are determined by the dynamics of each piece of equipment in the system. Therefore, the characteristics of each device in the system need to be investigated. In conventional power grids driven by physical laws, general models for synchronous generators (SGs) can be obtained in a quasi-static format since the transients of interest are within a narrow band (0.1 Hz to 5 Hz [93]) and the fundamental frequency fluctuations are negligible (due to the large inertia of the rotor [94]).

However, in PEC-rich power systems which are driven by converter controls, there has not been a generic model yet since PECs highly depend on manufacturers and are effective in wide control regions. Plus, the frequency variations cannot be neglected due to the low system inertia. Hence, this subsection attempts to review the most common PECs with the root cause analysis for small-signal stability issues in a wideband control range in power systems.

The PEC-interfaced generations and loads in power systems generally use voltage-sourced converters (VSCs), which can be further classified as current-type VSCs as shown in Figure 2-12 and voltage-type VSCs as shown in Figure 2-13. The current-type VSCs (also termed as grid-following inverters, GFLs) have been used in many applications, such as PVs, ESSs, and Type-4 WTGs at the generation side or fast-charging stations at the load side. The output current i_L is

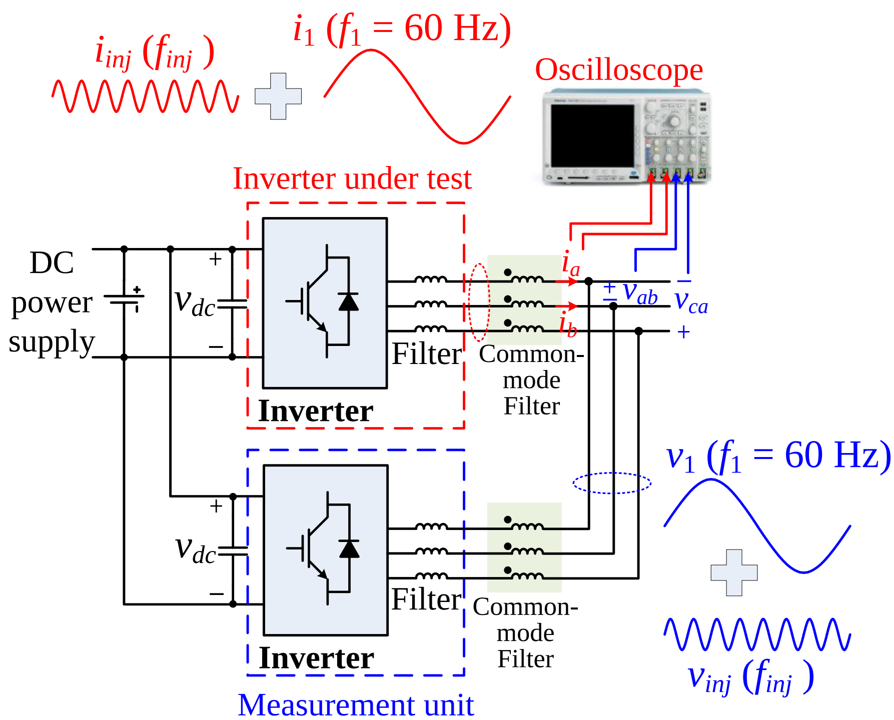

Figure 2-11. An easy-to-use setup for ac impedance measurement [33]

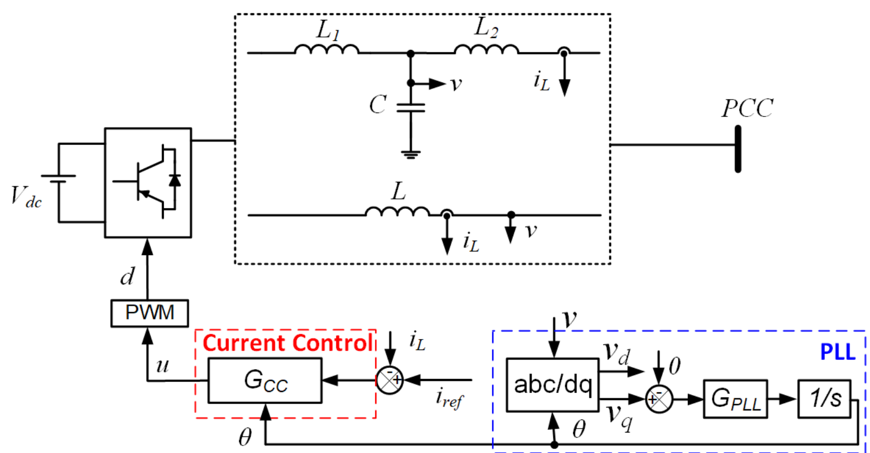

Figure 2-12. Circuit diagram of current-type VSCs [95, 96].

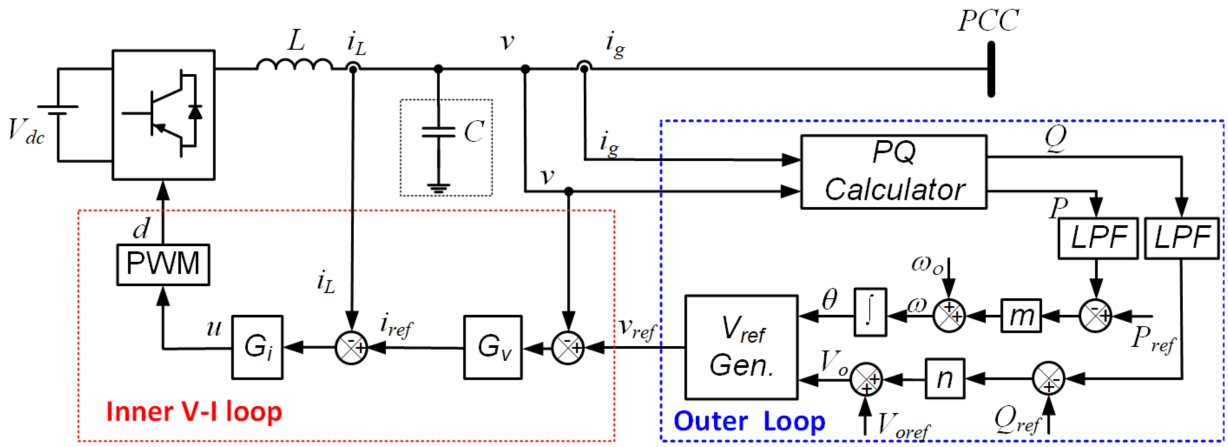

Figure 2-13. Circuit diagram of voltage-type VSCs [30, 31].

usually controlled with a proportional-integral (PI) controller in the synchronous frame or with a proportional-resonance controller in the stationary frame. Additionally, a PLL unit is used to obtain the angle θ of the converter terminal voltage in the stationary frame or of measured signals in the synchronous frame.

The voltage-type VSCs (also termed as grid-forming inverters, GFMs) are to establish system voltage and frequency autonomously [97]. A typical P-f and a Q-v droop control are adopted to realize power synchronization. The voltage control is to regulate the output voltage, and the current control is to provide damping for the LC resonance and to limit the overcurrent.

Additionally, the converter-interfaced dc transmission lines normally have a rectifier station and an inverter station with either line commutated converter (LCC) as shown in Figure 2-14, or VSC as shown in Figure 2-15.

The LCC-HVDC has been widely used in long-distance transmissions with two common LCC control loops, i.e., constant extinction angle control (CEAC) and constant dc voltage control (CDVC).

The VSC-HVDC is also a preferred transmission solution, especially in offshore wind farms with two- or three-level VSC or modular multilevel converters. The rectifier side of VSC-HVDC is normally with PLL control, active power/dc voltage control, and reactive power/ac voltage control loops [98], and the inverter side structure is like a current-type VSC.

The control-induced small-signal stability issues arising from these four kinds of converters in power systems will be discussed from the following aspects: control delay, inner/outer control, and switching actions. These causes of instability are coupled and may mix to cause problems under small disturbances.

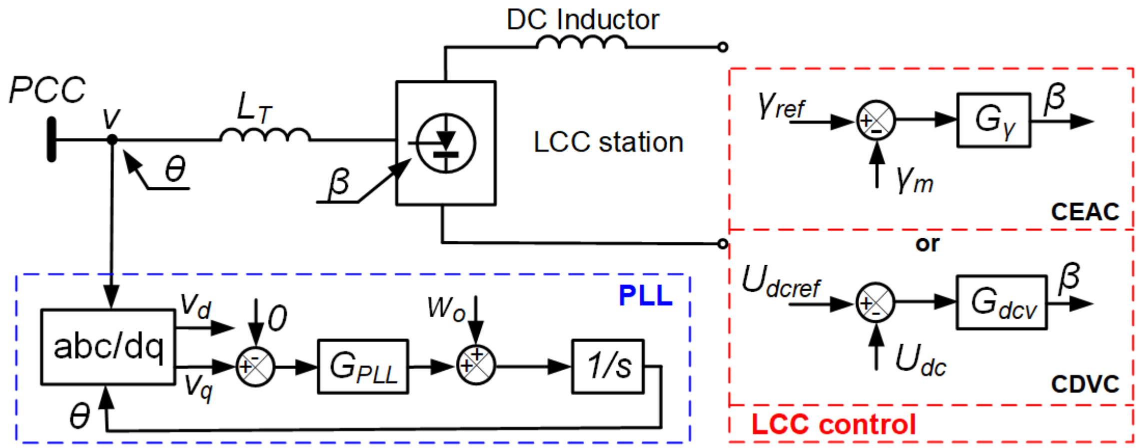

Figure 2-14. Configuration of stations in the LCC-HVDC system [99].

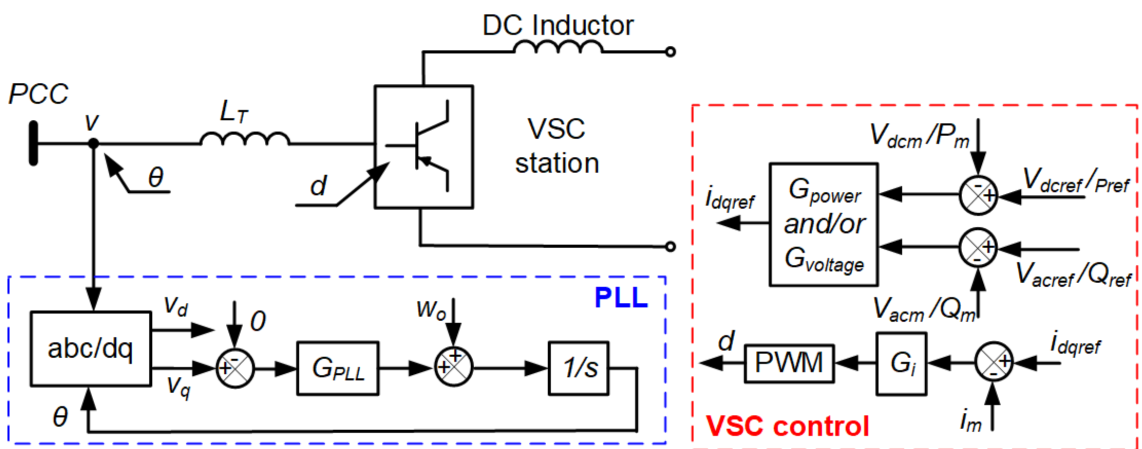

Figure 2-15. Configuration of stations in the VSC-HVDC system [98, 100].

1) Control delay

The PECs may cause current harmonics in power systems as shown in Figure 2-16 with 830 Hz harmonics in a wind farm [101]. The unstable sources can be identified with the bus participation factors (PFs) calculated from the multi-input-multi-output transfer function matrix model of the power system and eigenvalue sensitive analysis. Specifically, the converters with larger PFs would introduce harmonic resonances into the system.

The fundamental mechanism behind the phenomena can be further revealed by the passivity-based stability criterion (PBSC) by checking the output impedance $Z(s)$. If a converter impedance is non-passive at some frequencies when connecting to another passive system, instability will possibly happen within these non-passive regions (NPRs). Accordingly, the output admittance of current-type VSCs with *LCL* filters $Y_{o1}(s)$ is derived, and the converter passivity is examined to identify the root causes. The results show that there is a high frequency (HF) NPR which is caused by the interactions between *LC* resonance frequency f_r and system control delay T_d. The delay here is assumed to be k times of switching period T_{sw}, which is typically 1.5 and can be reduced to 0.5 with more advanced digital control. The conclusions are: (1) when $f_r < \frac{f_{sw}}{4k}$, the HF-NPR in GFLs with *LCL* filter is $(f_r, \frac{f_{sw}}{4k})$ as shown in Figure 2-17(a); (2) when $f_r = \frac{f_{sw}}{4k}$, there is no HF-NPR, and (3) when $f_r > \frac{f_{sw}}{4k}$, the HF-NPR will be $(\frac{f_{sw}}{4k}, f_r)$, where $f_r = \frac{1}{2\pi\sqrt{L_1 C}}$ [16, 55, 56, 58, 102]. According to the conclusions above, the instability causes for the system in [101] can be more deeply investigated, where the converter switching frequency f_{sw} is 4 kHz and the control delay is $0.5T_{sw}$. Besides, f_r is 729 Hz which is smaller than 2 kHz. Therefore, the harmonic instability issues would happen within (729 Hz, 2 kHz), which matches with the current waveforms with 830 Hz resonance.

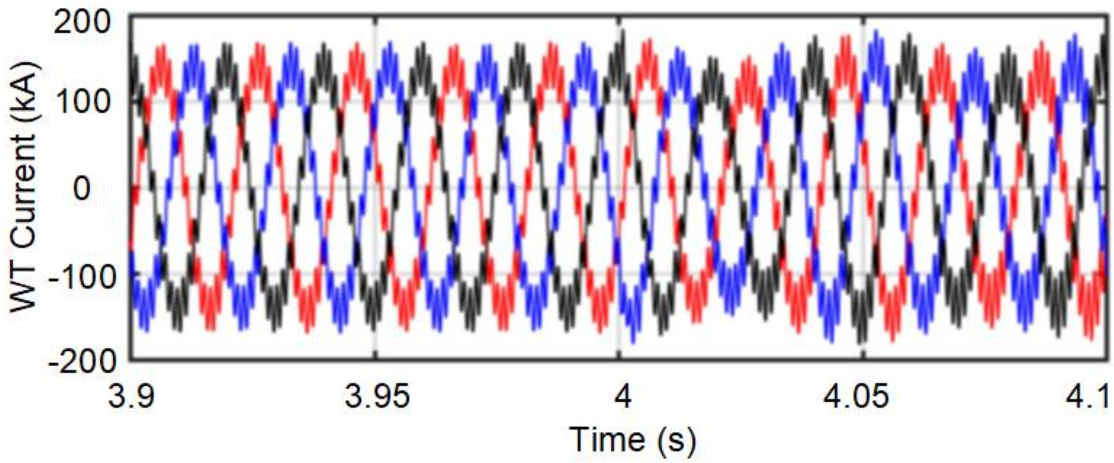

Figure 2-16. Currents of a 400 MW WTG injected into power grids [101].

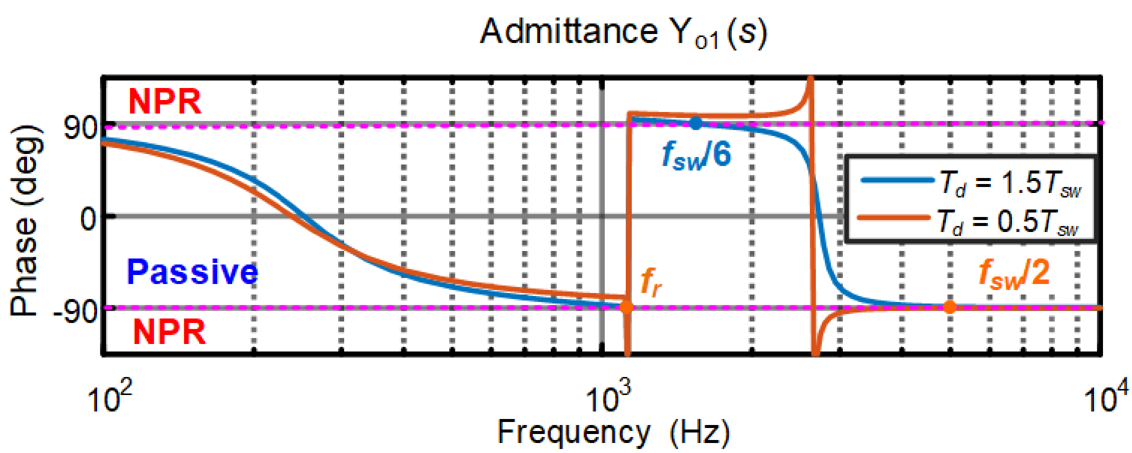

(a)

Figure 2-17. Passivity analysis of (a) *LCL*-filtered current-type VSCs (b) *L*-filtered current-type VSCs, and (c) voltage-type VSCs.

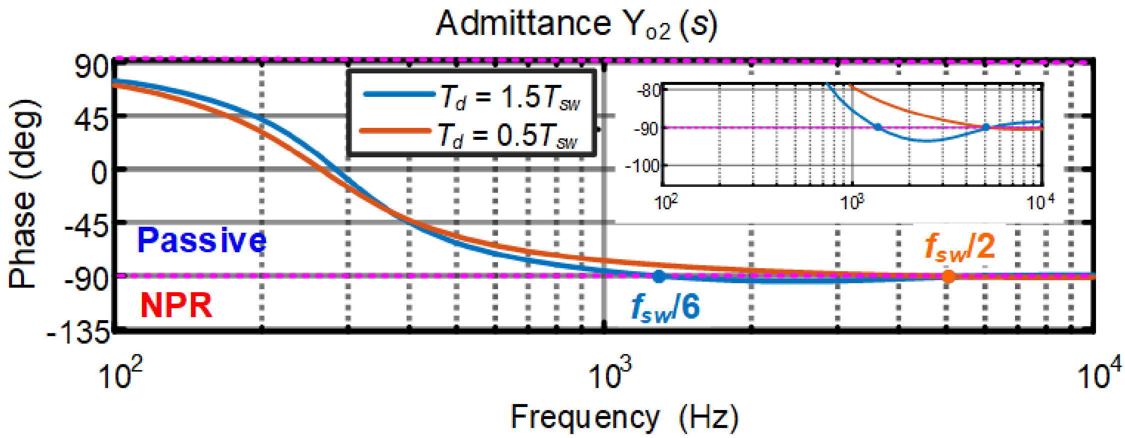

(b)

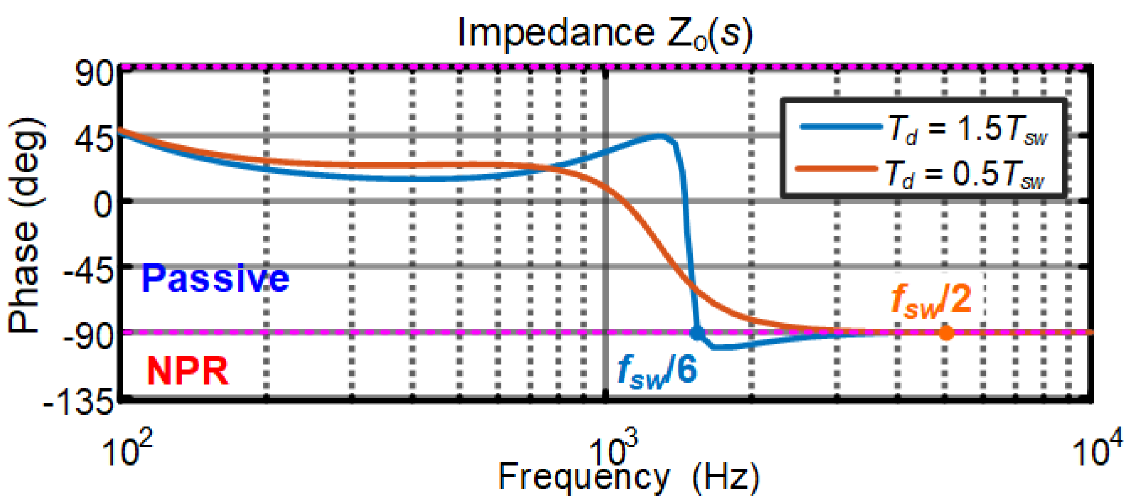

(c)

Figure 2-17. (continued).

Following the same approach, the HF-NPR of current-type VSCs with an L filter is identified to be $(\frac{f_{sw}}{4k}, \frac{3f_{sw}}{4k})$ using the output admittance $Y_{o2}(s)$ as shown in Figure 2-17 (b) [96, 103, 104]. And the HF-NPR of voltage-type VSCs is identified to be $(\frac{f_{sw}}{4k}, \frac{3f_{sw}}{4k})$ with an examination on phase angles of converter output impedance $Z_o(s)$ as shown in Figure 2-17 (c), which is analogous to the L-filtered current-type VSCs [30, 54, 105]. When the control delay is small enough, e.g., $k = 0.5$, the converter could be passive up to Nyquist frequency $0.5f_{sw}$, which means there would be no harmonic stability issues if connecting the converter to another passive grid. Plus, if the converter is implemented with silicon-carbide devices instead of silicon devices with a higher switching frequency, the converter passivity could also be guaranteed to a higher absolute value of frequency range, and system stability could be improved.

Therefore, to eliminate the control-delay-related small-signal stability issues, one direct method is to use advanced controllers to achieve small control delays. Other than that, system stability can also be enhanced by some passivity compensation methods. For example, for current-type VSCs, there are voltage feedforward control [55, 96, 102], lead-lag control [58], active damping [55, 56, 102], passivity-based robust control [16], and adaptive bandpass-filter-based compensation control [106]; for voltage-type VSCs, there are adaptive notch-filter-based compensation control [106], and voltage feedforward control with virtual impedance control block [54, 105]. Note that virtual impedance control may also affect system slow-interaction converter-driven stability. Therefore, the outer loop needs to be refined accordingly.

2) Inner Loop Control

In addition to the control delays as the root cause for system harmonic instability issues, the inner loop control bandwidth will also have some impacts since the control delays typically add negative damping into the alternating current control (ACC) loops of PECs [105, 107].

For example, in a system with multiple paralleled *LCL*-filtered current-type VSCs, the interactions among the ACC loops with larger control bandwidth will cause the interactive circulating currents to arise, because the resonance frequency tends to shift to the negative damping region caused by control delays when control bandwidth is increased [108]. A direct solution is to limit the inner current control bandwidth, which may sacrifice the current control dynamics. Apart from this, a multisampling approach can be used [109]. But harmonic instability driven by switching actions would be introduced, causing a distorted grid current with low-frequency aliasing. Hence, a repetitive filter to eliminate the multi-sampling-induced harmonics is needed.

3) Converter Switching Actions

For parallel converters with asynchronous carriers, the pulse-width-modulation (PWM) block generates sideband harmonics which may cause system harmonic instability [110, 111]. Figure 2-18 shows the harmonic current waveforms in a system with two-parallel current-type VSCs. To eliminate the f_{sw} sideband harmonics, a global synchronization of all PWMs through a communication-based central controller is needed. Another way is to add active damping or passive damping into the system to damp the high-frequency oscillations. Plus, the increasing parasitic resistance at a higher frequency due to the skin effect of the output inductor *L* can provide additional passive damping which is good for system stability. Therefore, the effects of controllers on system stability above Nyquist frequency (f_{sw}/2) may be negligible in some cases [112].

4) Outer Loop Control

Slow-interaction converter-driven instabilities are also observed in power systems as shown in Figure 2-19 and Figure 2-20, which are also called sub-synchronous oscillations (SSO) [43]. The main reason for SSO has been identified as the interactions between the outer control loops of the converters and grid strength (defined by short circuit ratio - SCR).

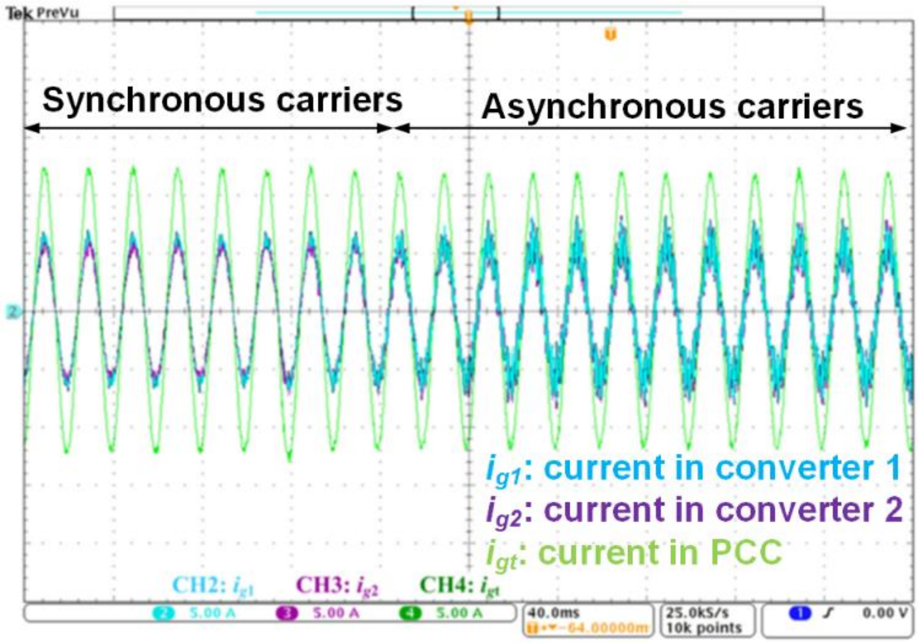

Figure 2-18. Current waveforms with varying carriers for two-paralleled inverters [110].

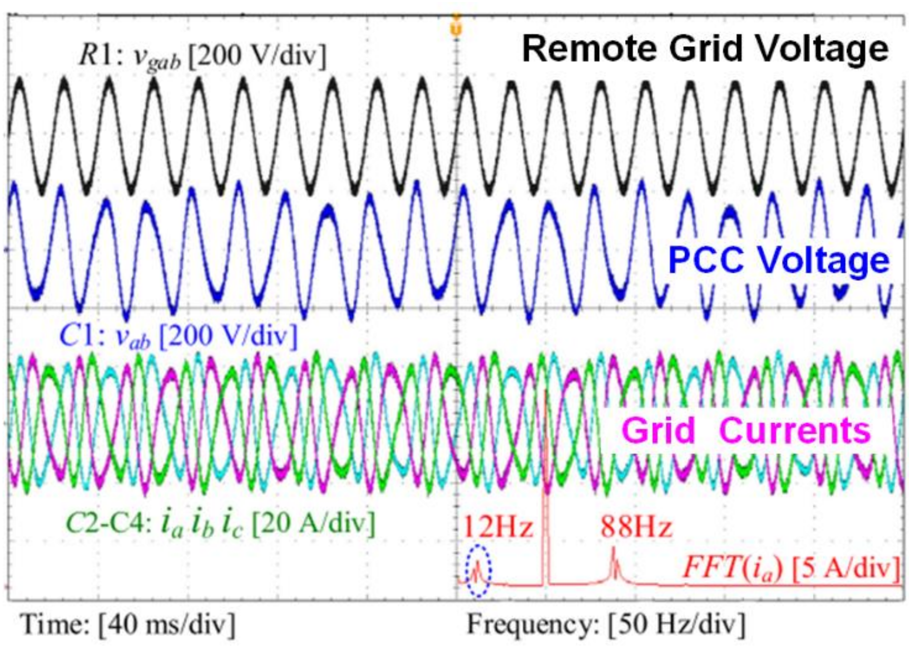

Figure 2-19. Small-signal synchronization stability issues of current-type VSCs in weak grid with SCR = 2 [113].

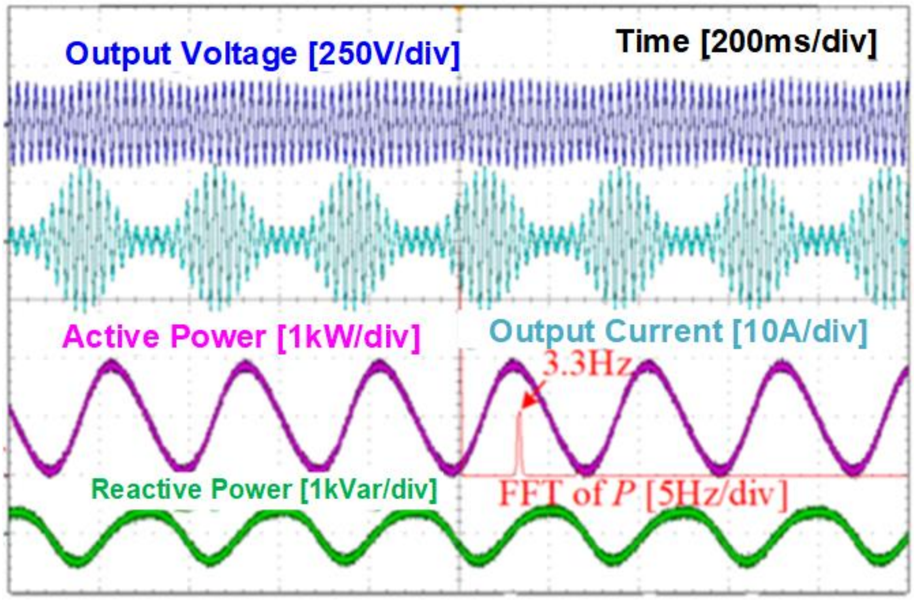

Figure 2-20. Small-signal synchronization stability issues of voltage-type VSCs in a strong grid with SCR ≈10 [114].

For current-type VSCs, the slow-interaction converter-driven instability is mainly due to the asymmetrical PLL dynamics, i.e., only regulating *q*-axis PCC voltage introducing positive feedback into the system [28, 115, 116]. By examining the closed-loop poles of current-type VSCs, it is found that there is one pair of complex poles ($P_{1,2}$) that have low-frequency dynamics related to system fundamental frequency sideband oscillations [115]. The root-locus approach is applied to analyze the locations of the poles to study the impact of the PLL (proportional gain K_{pll_P} and integral gain K_{pll_I}) as shown in Figure 2-21. For the PLL control parameters, a decrease of proportional gain K_{pll_P} (star line in Figure 2-21) and an increase of integral gain K_{pll_I} (circle line) will move the SSO mode-related pole to the unstable region. Also, reduction of the ACC integral gain K_{CC_I} (square line) will have minor impacts on system SSO stability. But the impact of ACC proportional gain K_{CC_P} on system SSO is negligible. Using the impedance-based Nyquist stability analysis approach can draw the same conclusions as discussed in [28, 116]. Additionally, the ACC loop may accelerate the equivalent motion of PLL in the first swing, which will worsen system transient stability by enlarging the mismatch between the accelerating and decelerating area in the power angle curve of the analogized synchronous machine model of the current-type VSC [117].

The PLL control blocks in LCC-HVDC and VSC-HVDC have similar impacts on system stability. For the LCC-HVDC, a study was conducted based on the small-signal model and eigenvalue analysis to investigate the impacts of PLL and LCC controllers in [99]. First, the PLL bandwidth has a significant impact on system stability. Too large PLL control bandwidth will cause system SSO, especially under weak ac grids. Considering the PLL gain stability boundary with different types of LCC controls, the stable region of PLL gain is larger with CDVC than with CEAC. Second, in CEAC controller G_γ, smaller proportional gain K_p and larger integral gain K_I

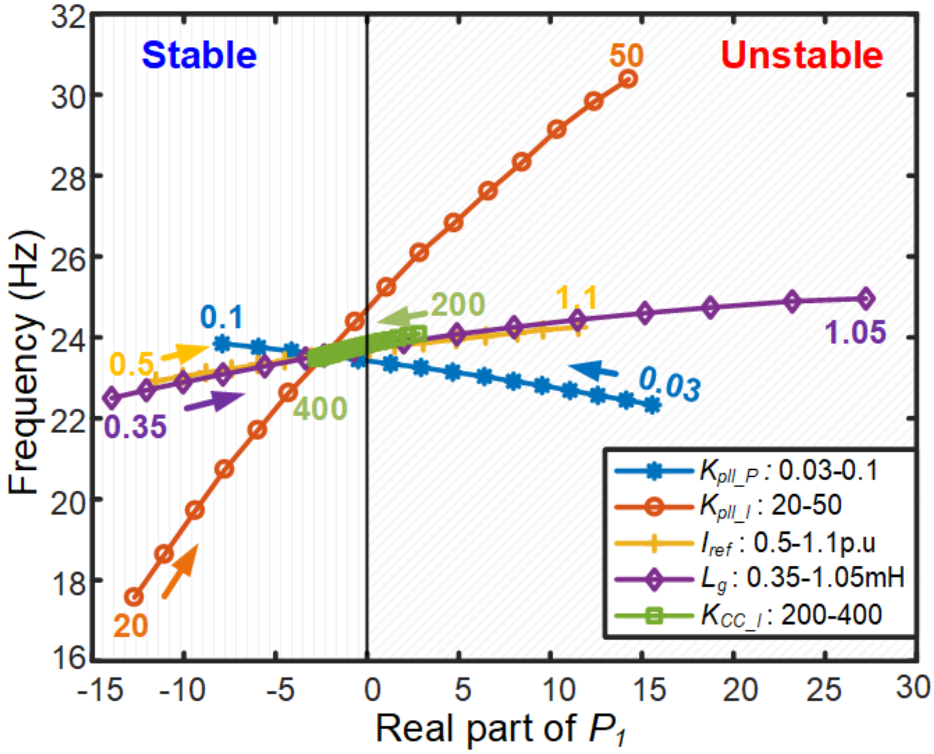

Figure 2-21. The real part of P_1 under different conditions in current-type VSCs [115].

can help improve system stability. While in CDVC controller $G_{dcv,}$ larger K_p and smaller K_I can enhance system stability. Third, there is a close coupling between PLL and LCC control loops, which indicates that the instability caused by larger PLL gain can be eliminated by properly tuning LCC controllers.

For the VSC-HVDC, based on the eigenvalue analysis of the corresponding small-signal model, the PLL impacts on system stability can be obtained as shown in Figure 2-22. It is seen that when the SCR is larger than 1.32, there will be no stability issues for any value of K_{pll_P}. However, in a system with lower SCR, there will be a maximum K_{pll_P} limitation for system stability. Note that the K_{pll_I} is assumed as c times of K_{pll_P} for simplicity. Another study on a windfarm-connected HVDC transmission is conducted with the impedance-based stability analysis in [100]. It is also found that increasing the voltage loop crossover frequency or reducing the PLL control bandwidth can improve system slow-interaction converter-driven stability.

The PLL-related converter-driven instabilities can be directly solved by tuning PLL control parameters, e.g., reducing PLL bandwidth to limit the effective frequency range of the harmful positive feedback. Another approach is to add active damping, e.g., virtual impedance [95, 118] or feedforward control [113, 119].

In voltage-type VSCs, droop control is normally adopted for power regulation and system synchronization. A complex-value-based output impedance model in the stationary frame is built [114] to study the impacts of the control loops. The interactions between the control loops (droop control and voltage control) and the grid tend to cause system instability issues. Moreover, a comparative study is conducted in [120] to investigate the differences between multi-loop droop (with inner *V-I* loop) and single-loop droop (without inner *V-I* loop). Figure 2-23 shows the stability boundaries under different grid equivalent impedances [120]. The voltage loop will make

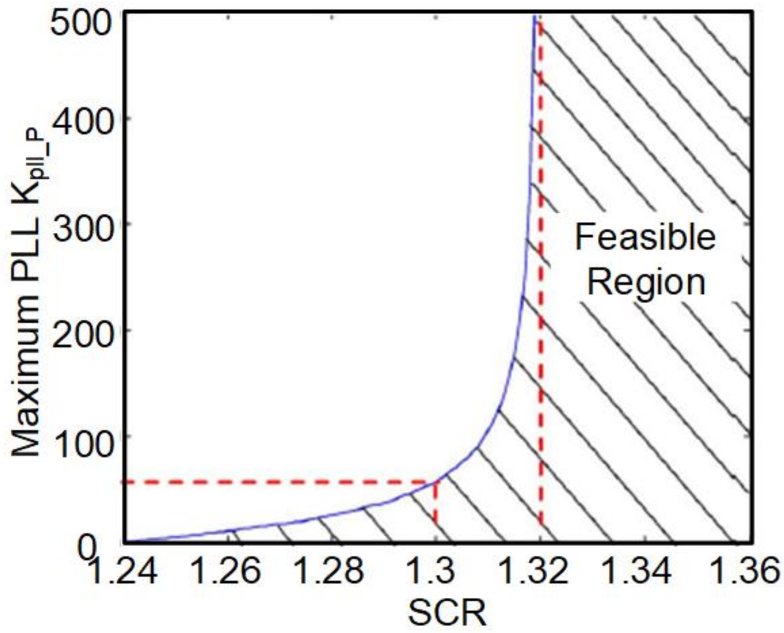

Figure 2-22. System SCR versus K_{pll_P} in VSC-HVDC [98].

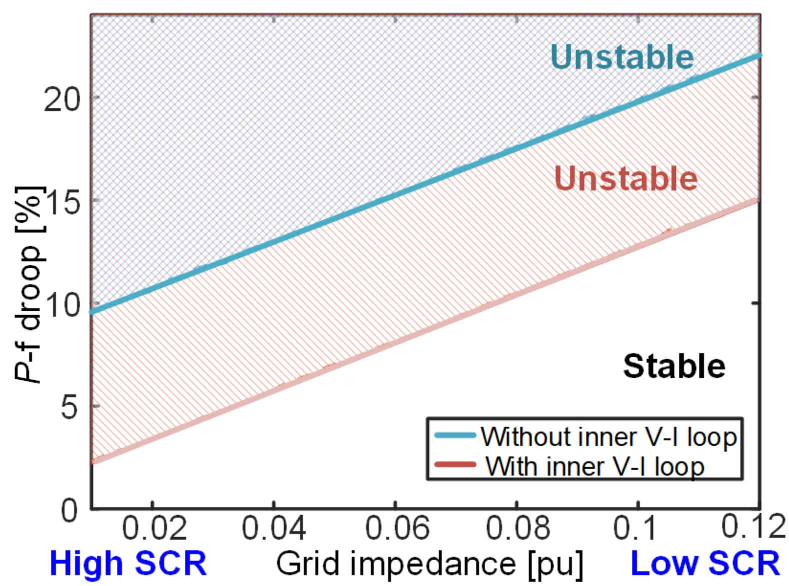

Figure 2-23. Stability boundary of *P-f* droop vs. grid impedance [120].

the converter prone to be less damped and lose system stability more easily since the stable region is reduced with inner *V-I* control. Also, Ref. [31] shows that a larger voltage control bandwidth may enhance system SSO stability. Additionally, the *Q-v* droop impact on system stability is weaker than the *p-f* droop. Accordingly, the droop-induced small-signal instability can be eliminated by tuning the more sensitive control blocks, i.e., *p-f* droop and voltage control.

In addition to various converter control loops, PEC-induced stability issues are also dependent on system interactions and operating conditions.

1) Grid Strength

As shown in Figure 2-21, Figure 2-22, and Figure 2-23, the slow-interaction converter-driven stability not only relies on the converter control loops but also depends on the grid strength. In converters with a PLL control block, the instabilities would be more likely to be stringent under weak grid conditions. As shown in Figure 2-21, an increase of L_g (diamond line), i.e., a weaker grid, will also make P_1 an RHP pole and cause SSO instability. Note that a weak grid is defined as an ac power system with a low SCR and/or inadequate mechanical inertia by IEEE standard 1204-1997 [121]. It is also worth mentioning that in the LCC-HVDC system, a weak system means an SCR < 2.5. While in VSC-HVDC systems, the SCR for "weak" or "strong" system boundary is suggested to be 1.3-1.6 as implied by Figure 2-22 [98]. However, in converters with droop control, the smaller the grid impedance is, the smaller the allowed maximum *p-f* droop gain would be as shown in Figure 2-23. That means the SSO instability tends to happen in a strong grid under the same droop gains in voltage-type VSCs, which coincides with results in [31, 114].

The fast-interaction stability may also be affected by the grid strength. For example, if the magnitude of the grid-side impedance intersects with that of the converter impedance in the HF-NPR, and the phase difference at the intersection does not meet the stability criterion, then harmonic instability issues will appear [54]. A grid impedance away from the HF-NPR can help eliminate the harmonic instability issues.

2) PEC-Interfaced Loads

The converter-interfaced loads (CILs) will have very different frequency and voltage characteristics from conventional resistive loads or motor loads. Under some circumstances, the CILs can be considered as current-type VSCs. It is revealed for simplicity that the CILs exhibit constant power characteristics when the control bandwidth is high enough in some studies [122-124]. Therefore, negative incremental impedances will be introduced by the constant power loads (CPLs) across the entire frequency range, and both fast- and slow-interaction converter-driven stability will be affected by this negative damping. Similar findings have been obtained by a microgrids study in [125] with different solutions such as using passive damping, active damping, or more advanced control strategies. One should note that although the CPL assumption is dynamic-wise (i.e., simplifying the load dynamics), it may not always be the worst-case condition for system stability from a control standpoint [126].

3) Operating Conditions

System operating conditions also affect the converter-driven stability, including both fast- and slow- interactions. For example, a theory for harmonics created by resonance in [127] shows that the harmonics may not happen in normal mode, but may suddenly occur and grow before it reaches a certain value if operating conditions change as shown in Figure 2-24. The main reason for this phenomenon is that the converter impedance depends on both the operating points and harmonic components. To solve this kind of issue, the focus should be on utilizing passive elements or control strategies to provide more damping to reshape the system impedance.

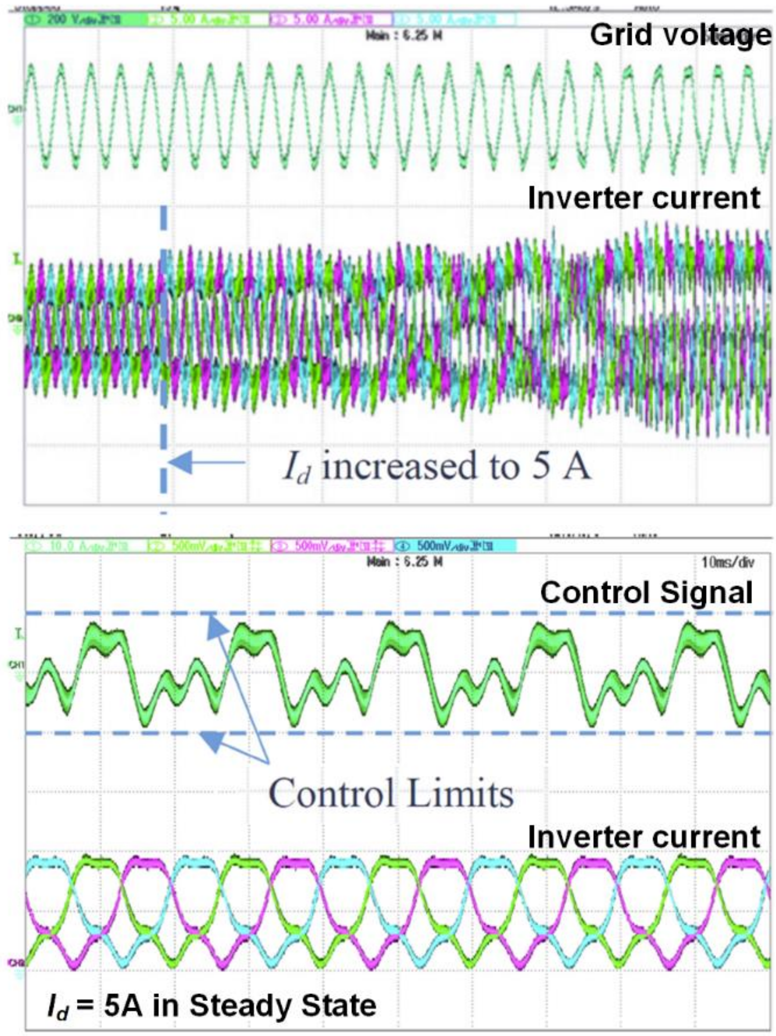

Figure 2-24. Phenomena of harmonics created by resonance in a converter-grid system [127].

Moreover, slow-interaction converter-driven stability will also be affected by system operating conditions as shown in Figure 2-21 that a larger current I_{ref} (bar line) will induce SSO with higher oscillation frequency. Hence, a proper design of converter impedance characteristics under different operating conditions should be examined to guarantee system stability.

In summary, PEC-induced stability issues may arise due to different reasons, including converter-control-induced issues (i.e., control delay, inner and outer control loops, and PEC switching actions) as shown in Figure 2-25 with the effective time ranges of different control functions and the working-condition induced issues (i.e., grid strength, loading conditions, and system operating conditions) [128]. The corresponding stability enhancement solutions can be developed based on these root causes, such as tuning the control parameters of PECs, adding active or passive damping components into the system, or reducing control delays in PECs.

B. Control design for unknown systems

However, with the utilization of many PECs, including wind turbine generators, photovoltaic generators, electric vehicles, and energy storage systems, it is highly possible that the entire system information is unknown to the PEC design. Therefore, a smart PEC integrated with the plug-and-play capability of system stabilization in a local way is expected to be developed [43], such that the PECs can be stably integrated into any existing unknown power grids. To address this issue, the PBSC approach can be applied so that the PECs can be stably connected to any passive grid, such as the linear PBC methods for dc/dc converters in [129], for current-type 2L-VSCs in grid-connected mode introduced in [16, 55, 56, 58, 96, 102, 107, 130], for MMCs in [131], and voltage-type 2L-VSCs introduced in [54, 105]. However, as shown in Figure 2-17, these PBC methods for VSCs only intend for HF harmonic instability issues in the system and ignore the LF dynamics.

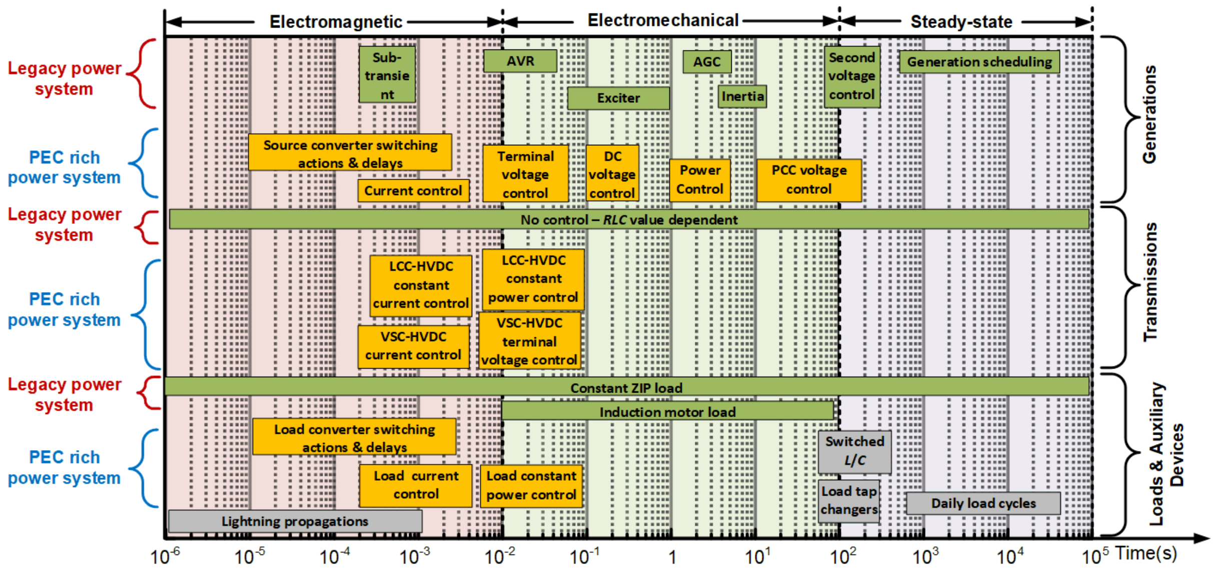

Figure 2-25. Dynamic characteristics based on timescale decomposition for legacy power systems and PEC-rich power systems [132-135].

The low-frequency band is mainly influenced by the synchronization control loops with slow dynamics, such as traditional PLL control as shown in Figure 2-12 or conventional droop control as shown in Figure 2-13.

Specifically, for traditional PLL control loops, the disturbances in the grid voltage will be introduced to the current controller and cause low-frequency non-passive regions of the *qq*-channel output impedances [136] which might cause some synchronization stability issues. While the smaller the control bandwidth of PLL loops is, the narrower the low-frequency non-passive regions in the impedance model of PECs will be, and the system will be more stable [137]. Besides, extra control blocks can be added to compensate for the impacts of PLL control, such as the compensation term G_H which is from grid voltage to converter control voltage directly in [136], or modified PLL with a pre-filter and a phase regulator in [138]. But these PLL compensation methods in [136, 138] can only passivate the *qq*-channel impedance, whilst the *dq*-channel and *qd*-channel impedances are still non-passive though they might have a minor impact on system stability.

For traditional droop control, due to the integrator in the active power control loop, a right-half-plane pole will appear at the system fundamental frequency and a non-passive frequency band can be observed in the converter output impedance [31]. A combination of passivity and small-gain stability criterion can be used to enhance the system stability in the non-passive region of the impedance; however, no control solutions have been reported to eliminate the non-passive regions of the impedance model around the system fundamental frequency. Note that the passivity-based analysis and control design approaches reviewed above are all based on impedance models of PECs. That is because the power networks can be considered passive in terms of bus impedance since the power networks consist of only passive RLC components [139] and as long as each device connected to the bus is passive, system stability can then be guaranteed. To enhance system small-signal synchronization stability, a control approach is proposed by passivating the frequency-power transfer function from system frequency to converter output active power instead of the converter output impedance model [140]. However, this approach might not be general enough since the power network might not be passive in terms of the frequency-power transfer function.

Hence, the challenges become how to design control strategies for PECs so that they can be small-signal stably connected to any unknown power system considering low-frequency dynamics, especially for voltage-type VSCs.

2.4 Review of Analysis and Control Design of PECs for System Large-Signal Stability

2.4.1 Modeling and Analysis for System Large-Signal Stability

The large-signal stability analysis of PEC-rich power systems can be accomplished by Lyapunov-based mathematical methods. Estimating the region of attraction of a stable operating point can provide the estimated size of disturbances, though often conservative, that the system can tolerate [69, 141]. Studies have explored the Lyapunov-based stability analysis of dc/dc converters [142], ac/dc rectifiers [143], and dc/ac inverters [144-150]. Specifically, for the dc/dc converter [142] or the inner loop (e.g., *dd*, *dq*, *qd*, and *qq* channels) of ac/dc [143] and dc/ac converters [144], the issues can be considered as a fixed-point tracking issue, so the Lyapunov function for stability analysis can be constructed from the system state-space model that is based on the state variables (e.g., capacitor voltage and inductor current). However, for the dc/ac converters with droop control or PLL control, since the voltage amplitude and phase angle are non-constant, it might be difficult to construct a Lyapunov function directly based on circuit voltage and current relationships. Instead, the swing-equation-like equations describing relationships between the power and phase angles can be referred to build the energy function of the inverters, such as the analysis in [145-150]. However, these Lyapunov models usually assume constant voltage amplitude and only focus on the phase dynamics.

2.4.2 Control Design to Enhance System Large-Signal Stability

A. Control design for known systems

For dc/dc converters, ac/dc rectifiers, or inner loop design of dc/ac inverters, if there are large-signal stability issues in the system, both hardware-based solutions and control-based solutions can be applied. The hardware-based methods add extra damping resistors or capacitor banks to provide more damping to the system. For example, storage systems can help improve system large-signal stability if the charging and discharging power of storage systems meet the stability criteria [151]. Nevertheless, the added physical elements will reduce efficiency and increase the weight and size of the system, which may not be applicable for some size/weight-sensitive applications, such as the shipboard MVDC power system. The control-based methods adopt different control strategies on the load side or source side to stabilize the system [152, 153]. The load-side stabilizing control strategies usually include the state of the bus voltage to generate reference power for the system, in which the basic principle is state variable-dependent adaptive virtual impedance control (i.e., virtual capacity or virtual resistance). The stabilization from the load side can also be obtained by real-time load shedding since load shedding is also an important backup solution during inadequate generation or voltage swings to ensure stable and continuous operation of the online loads. For the load-side control, since each load normally needs a special converter, stabilizing control methods need to be designed accordingly and may have to be recalculated if the system is reconfigured. In addition, in some applications such as systems with pulse loads, a stiff bus voltage is important for system operation. Therefore, the stabilization control needs to be implemented on the source side to save efforts on developing the control methods for all different types of loads and help enhance bus voltage regulation capability. The large-signal stability stabilization control methods on the source side have been developed based on nonlinear control theorems, such as sliding-mode control [154], active damping control [68], state-feedback control [155], boundary control [156], etc.

To enhance system transient stability, the parameters in the synchronization control loops (e.g., the PLL control as shown in Figure 2-12, or the conventional droop control as shown in Figure 2-13) should be properly designed to provide positive damping for the system. Specifically, based on the analysis in [150, 157], the PLL control provides a phase angle-dependent damping, and once the equivalent damping is negative, the system energy will gradually increase to be larger than the energy at the unstable equilibrium point and cause instability issues. The conventional droop control can provide positive damping to the system which is only affected by the frequency-power droop gain [150], but if the damping is not sufficient (i.e., too large droop gain), it might also destabilize the system [158]. While if there is no LPF in the active power-frequency droop loop or the cut-off frequency of the LPF is high enough, the system can then be considered a heavily damped system, and it will remain in stable operation as long as an equilibrium point exist. Also, the voltage-type VSC with dispatchable virtual oscillator control (dVOC) instead of conventional droop control is stable as long as an equilibrium point exists after the large disturbances are cleared [149]. If the impact of the reactive power-voltage droop control loop on system transient stability is considered, the conclusions about the droop control and dVOC approach, which are obtained under the assumption of a tight-regulated voltage, will not be valid anymore. This is because under large disturbances, there might be a sharp voltage dip and the system transient stability might be deteriorated [149, 158].

B. Control design for unknown systems

The reviewed stabilization methods for system large-signal stability require the knowledge of the entire system. There is still a challenge for the control design of PECs to be stably connected to an unknown system under large disturbances.

Passivity-based control approaches have been applied for the controller design of grid-connected PECs, such as the Buck-Boost converter with unknown constant power loads [159], the current-type 2L-VSCs in grid-connected mode [160], and the voltage-type 2L-VSC in grid-connected mode [161]. But for the current-type or voltage-type 2L-VSCs, they only considered the inner fast control loop dynamics to have a better transient response [160] or to improve the power quality [161] in the system, while the outer slow control loop, i.e. PLL loop or droop control loop, is neglected. A passivity-based plug-and-play voltage and frequency control has been proposed in [162] to enable stable operation of islanded inverter-based ac microgrids. However, the converters are only considered with constant impedance and constant power load, and the grid-connected condition is not discussed. A distributed stability criterion was developed in [163] for the control parameter design of GFMs based on the output-differential passivity in terms of bus voltage and bus power, but the power flow data is required for the evaluation of the passivity index of the power networks. In [164], a pH-based generic control strategy without the need of assuming constant voltage and constant frequency was proposed. The control approach has three channels to render the power electronic system passive, including a *torque-frequency* channel to generate the frequency reference, a *quorte-flux* channel to produce the flux reference, and a third channel to realize a lossless interconnection. Inverters with such a control structure can behave like a virtual synchronous machine and maintain system stability when they are connected to another passive system. However, the three-channel structure is quite obscure when these control variables are mapped to the physical components in the real system, for example, the '*quorte*' is a new word created in [165] which is dual to '*torque*' and the third channel is only created for mathematical correctness.

Therefore, it is desirable to have a simpler two-channel control structure that not only preserves the inverter passivity but also preserves physical meaning, in other words, using more well-accepted control variables, like the active power and reactive power in conventional droop control. In addition, it is expected that the control approach not only works for passive systems but is also able to work with non-passive systems since the existing power grids are normally non-passive.

2.5 Research Objectives

According to the survey above, there are many unsolved issues on the stability analysis and design of PEC-rich power systems. The main challenges include:

(1) Lack of an accurate dc impedance modeling for MMC with consideration of the important dynamic behavior in the control loops, such as submodule capacitor voltages and circulating currents.

(2) Lack of a simple setup for dc impedance measurement in medium- or high-voltage, high-power applications.

(3) Linear control design of PECs to connect to an unknown power system with ensuring system small-signal stability, including both high-frequency harmonic stability and low-frequency synchronization stability.

(4) Nonlinear control design of PECs to connect to an unknown power system with ensuring system stability under large disturbances (e.g., transient stability).

(5) For either the small-signal stability or the large-signal stability of a PEC-rich power system, if there is an instability problem, the common approach is to have a control solution to eliminate the instability phenomena. However, the intrinsic limitations of these stability requirements on system design are still unknown.

Corresponding to the challenges listed above, the research objectives of this dissertation are as follows:

(1) Develop a refined dc impedance model of MMC considering the dynamics of submodule capacitor voltage and circulating currents.

(2) Propose a simple and effective setup for dc impedance measurement of high- or medium-voltage, high-power applications by using an existing converter connected in a paralleled structure.

(3) Propose a passivity enhancement approach of GFMs to enhance system high-frequency harmonic stability.

(4) Propose a control approach for GFMs considering the impacts of virtual impedance control to enhance system low-frequency synchronization stability.

(5) Propose a nonlinear control approach for GFMs to ensure global asymptotic stability when connecting to an existing power grid with the grid either being passive or non-passive.

(6) Conduct a comparative study of dynamic requirement impacts on system design of notional aircraft dc and ac electric power systems.

Chapter 3. Dc Impedance-based Modeling, Stability Analysis, and Control Design of Modular Multilevel Converters

The modular multilevel converter (MMC), which was originally invented for HVDC applications in PEC-rich power systems, has also become a promising topology in MVDC systems due to the benefits of high efficiency, modularity for manufacturing, and low harmonics [166-170]. However, the dc-side system stability with MMCs has not been thoroughly investigated since there is no accurate dc impedance model of MMCs when applying the impedance-based stability analysis approach with the Nyquist stability criterion. A few MMC dc impedance models have been proposed, but their accuracy is limited by the assumption of ideal submodule voltage or neglecting the circulating current control [89, 90]. Therefore, in this chapter, a refined MMC dc impedance model is developed considering both the submodule capacitor voltage and circulating current dynamics.

3.1 Operation Principles and Control Strategies of MMCs

Figure 3-1 shows the structure of a typical three-phase modular multilevel converter, where there are two arms (one upper arm and one lower arm) in each phase. There are N submodules (SMs) connected in series in each arm, together with an arm inductor L_{arm} and its parasitic resistance R_{arm}. Typically, each submodule can be a half-bridge circuit or a full-bridge circuit as shown in Figure 3-2.

Normally, there are three control blocks in MMCs. One is the converter function control block; one is the circulating current suppression control block; another is the submodule dc voltage balance control block [171].

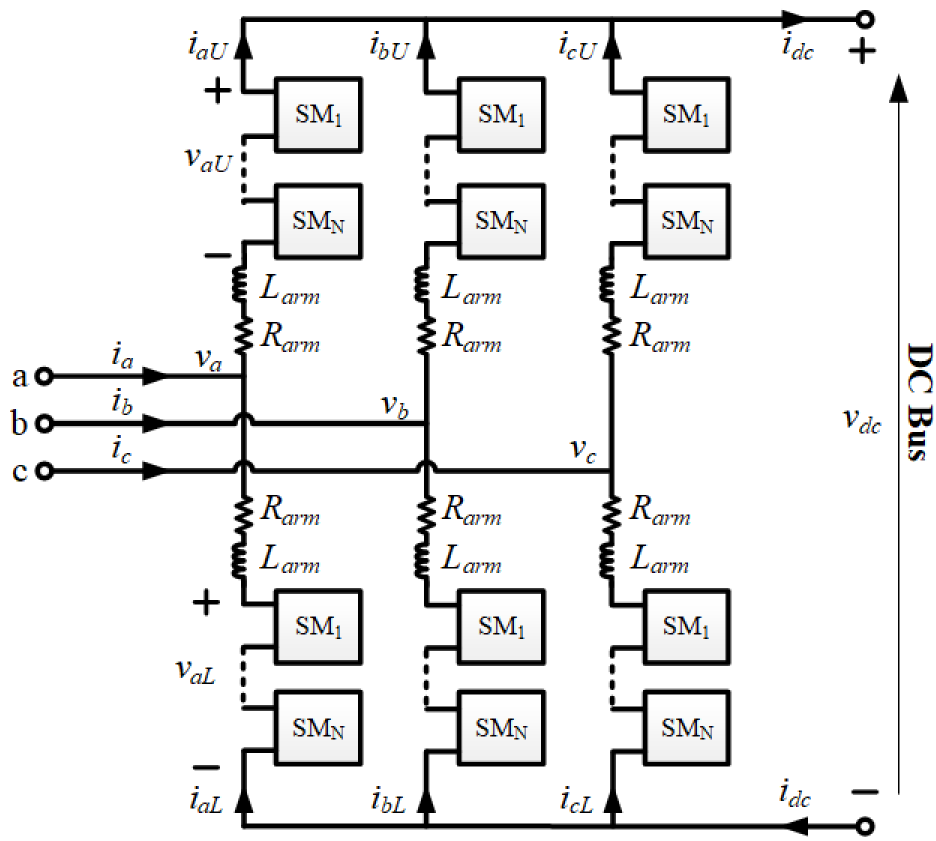

Figure 3-1. Topology of MMC.

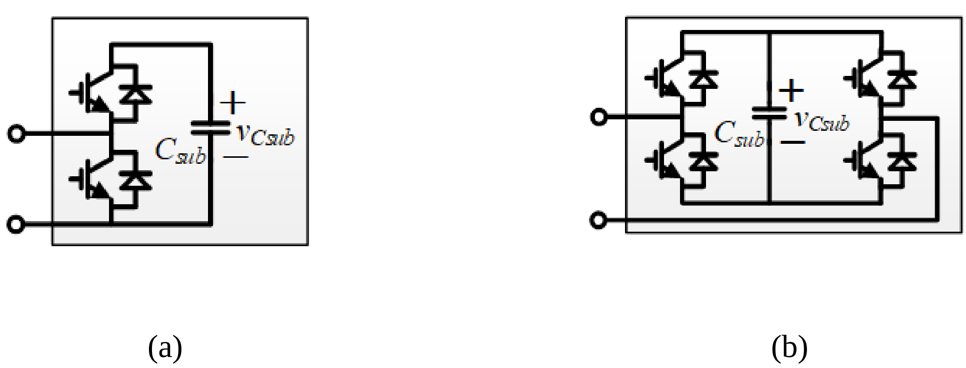

Figure 3-2. Circuits of submodules: (a) half-bridge circuit and (b) full-bridge circuit.

The converter function control is a double-loop controller which includes the outer dc voltage and power control loop, and the inner current control loop [172-174]. In this chapter, a dc voltage-controlled MMC with a unity power factor is illustrated as an example and the function control block is shown in Figure 3-3. The outer dc voltage controller generates the *d*-axis current reference I_{dref}. The *q* axis current reference I_{qref} is set to be 0 because of the assumptions of unity power factor. The inner current loop controls *d*-*q* axis currents using the proportional integrator (PI) controllers and decoupling terms, respectively. Therefore, the *abc*-frame duty cycle d_a, d_b, and d_c can be generated.

A circulating current suppression control is implemented in MMC to eliminate the second-order circulating current as shown in Figure 3-4 [175, 176]. The circulating current is controlled through a proportional resonance (PR) controller. The circulating current control duty cycle d_{xcir} is subtracted from the function control duty cycle d_x obtained in Figure 3-3 to generate the upper arm duty ratio d_{xU} and lower arm duty ratio d_{xL} in phase x (x=a, b, c).

Additionally, the submodule capacitor dc voltage is balanced with a sorting method as shown in Figure 3-5. By sorting the sensed submodule voltage, each SM module can be assigned a corresponding duty cycle [166, 177]. In this chapter, the submodule capacitor dc voltages are assumed to be well-balanced with this control.

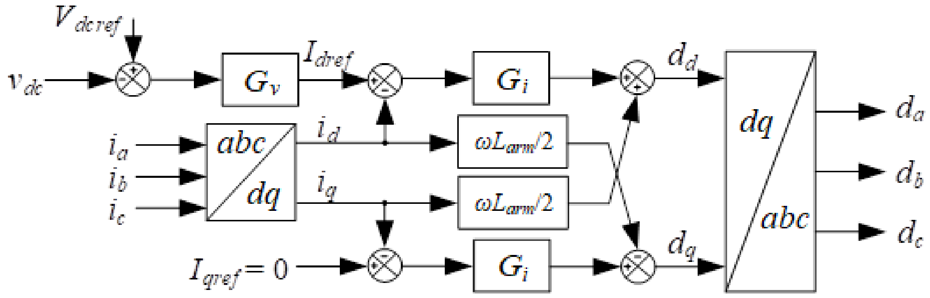

Figure 3-3. Converter function control block of MMC.

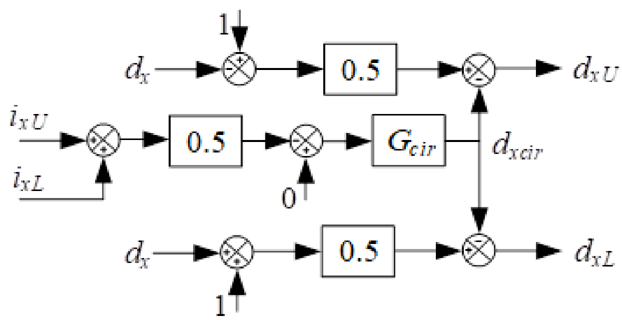

Figure 3-4. Circulating current suppression control block of MMC.

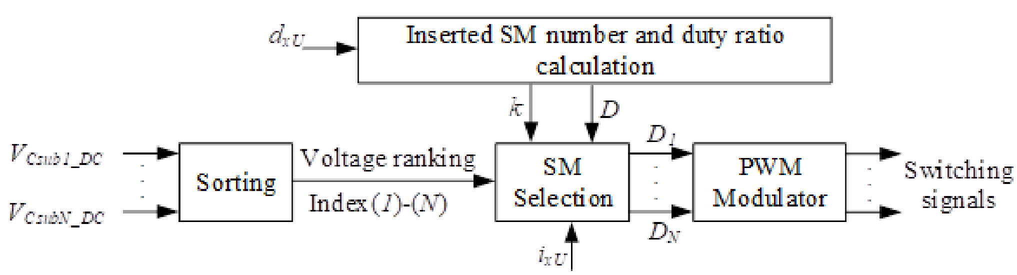

Figure 3-5. SM voltage balance control block of MMC.

3.2 Dc Impedance Models of MMCs

3.2.1 Existing Dc Impedance Models of MMCs

The mathematical representation of MMC can be obtained as follows. First, the real switching function of each arm is a stepped waveform which indicates when the submodules are connected or bypassed. In this chapter, it is regarded as a continuous waveform for simplicity. Therefore, the average switching function is considered, which is defined as $S_{xU(L)}$. Also, the submodule voltages in each arm are assumed to be identical. Hence, the relationships among the arm voltage $v_{xU(L)}$, arm current $i_{xU(L)}$, SM capacitor voltage $v_{CsubU(L)}$, and average switching function $S_{xU(L)}$ can be obtained as (3. 1) and (3. 2). In addition, the line current i_x, phase voltage v_x, dc current i_{dc}, and dc voltage v_{dc} can be obtained as (3. 3)-(3. 6). Note that the currents are defined with the respective flow path as in Figure 3-1.

$$\begin{cases} v_{xU} = NS_{xU}v_{CsubU} \\ v_{xL} = NS_{xL}v_{CsubL} \end{cases} \tag{3. 1}$$

$$\begin{cases} S_{xU}i_{xU} = -C_{sub}\dfrac{dv_{CsubU}}{dt} \\ S_{xL}i_{xL} = -C_{sub}\dfrac{dv_{CsubL}}{dt} \end{cases} \tag{3. 2}$$

$$i_x = i_{xU} - i_{xL} \tag{3. 3}$$

$$v_x = \frac{1}{2}[L_{arm}\frac{di_x}{dt} + R_{arm}i_x - (v_{xU} - v_{xL})] \tag{3. 4}$$

$$i_{dc} = \sum_{x=a,b,c} i_{xU} = \sum_{x=a,b,c} i_{xL} \tag{3. 5}$$

$$v_{dc} = (v_{xU} + v_{xL}) - R_{arm}(i_{xU} + i_{xL}) - L_{arm}\frac{d(i_{xU} + i_{xL})}{dt} \tag{3. 6}$$

Based on (3. 1) - (3. 6), the relationships between v_{dc} and i_{dc} represented by switching functions could be obtained as (3. 7).

$$v_{dc} = \frac{1}{3}\sum\nolimits_{x=a,b,c} N(S_{xU}v_{CsubU} + S_{xL}v_{CsubL}) - \frac{2}{3}R_{arm}i_{dc} - \frac{2}{3}L_{arm}\frac{di_{dc}}{dt} \tag{3. 7}$$

A. Model I

The modeling method in [89] is referred to as model I in this study. In model I, the submodule capacitors are assumed to be large enough and their voltages are assumed to be identical and constant, which are V_{dcref}/N. The average switching function $S_{xU(L)}$ is equivalent to $d_{xU(L)}$. Therefore, (3. 7) can be reformed as (3. 8).

$$v_{dc} = \frac{1}{3}\sum\nolimits_{x=a,b,c}(d_{xU} + d_{xL}) \cdot V_{dcref} - \frac{2}{3}R_{arm}i_{dc} - \frac{2}{3}L_{arm}\frac{di_{dc}}{dt} \tag{3. 8}$$

According to the control block in Figure 3-4, the sum of d_{xU} and d_{xL} can be represented by (3. 9). Therefore, the dc impedance model is derived as (3. 10), and its corresponding dc terminal equivalent circuit is shown in Figure 3-6. This model ignores the submodule capacitor voltage ripple. Therefore, it has some limitations as shown later in Section 3.2.3 and Section 3.3.

$$d_{xU} + d_{xL} = 1 - 2d_{xcir} \tag{3. 9}$$

$$Z_{dc\_model\_I}(s) = \frac{2}{3}(G_{cir}V_{dcref} + R_{arm} + sL_{arm}) \tag{3. 10}$$

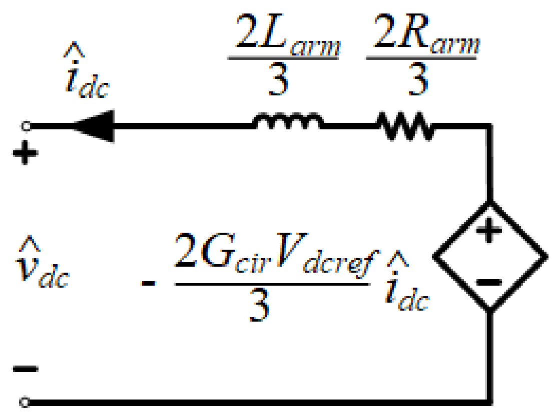

Figure 3-6. Equivalent circuit of model I [89].

B. Model II

The modeling method in [90] is referred to as model II in this chapter. It considers the capacitor voltage ripple and proposes an equivalent two-level VSC control model as shown in Figure 3-7, with equivalent dc impedance and ac impedance as in (3. 11) and in (3. 12), where the voltage across C_{ac} as in (3. 13) contains the voltage information of the capacitors. The dc impedance equation in (3. 11) is derived based on the energy conservation of the sub-module capacitors. However, the dynamics are not revealed. Therefore, to analyze the system stability considering the internal dynamics of a MMC, the equivalent circuit in Figure 3-7 has to be used. Because there is no complete mathematical expression for the equivalent circuit, this model is difficult to be adopted for stability analysis. In addition, the circulating current control effect cannot be revealed by this model.

$$Z_{dc\_model\_II}(s) = \frac{2}{3}R_{arm} + \frac{2}{3}sL_{arm} + \frac{N}{6sC_{sub}} \tag{3. 11}$$

$$Z_{ac}(s) = \frac{1}{2}R_{arm} + \frac{1}{2}sL_{arm} + \frac{1}{sC_{ac}} \tag{3. 12}$$

$$C_{ac} = 8C_{sub}/[N\left(1 - \frac{3k^2}{8}\right)] \qquad \text{where, } k = \frac{V_d}{V_{dc}/2} \tag{3. 13}$$

3.2.2 Proposed Dc Impedance Model of MMCs

Considering the limitations of the existing models, this chapter proposes a dc impedance model considering the MMC internal dynamics: submodule capacitor voltage ripple and circulating current suppression control. By defining d_{dc} as in (3. 14) and assuming all the

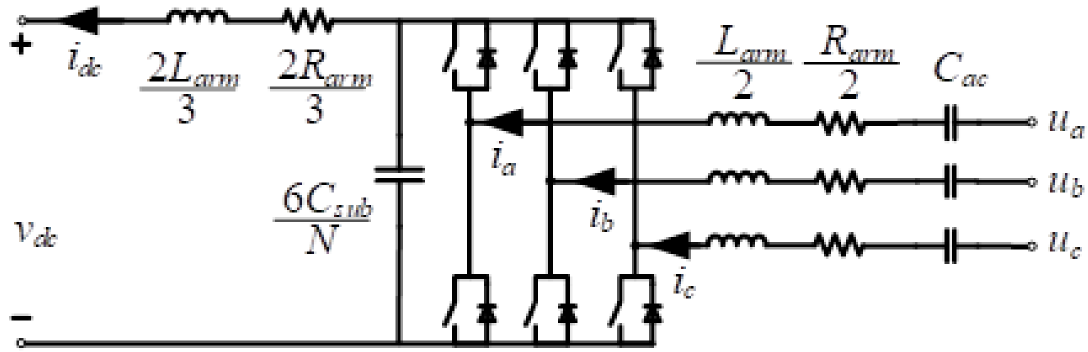

Figure 3-7. Equivalent circuit of model II [90].

submodule capacitor voltages are the same, (3. 7) can be written as (3. 15). Accordingly, the linearized small-signal equivalent circuit of the MMC dc terminal can be illustrated as shown in Figure 3-8.

$$d_{dc} = \frac{1}{3}\sum\nolimits_{x=a,b,c}(d_{xU} + d_{xL}) \tag{3. 14}$$

$$v_{dc} = N d_{dc} v_{Csub} - \frac{2}{3} R_{arm} i_{dc} - \frac{2}{3} L_{arm} \frac{di_{dc}}{dt} \tag{3. 15}$$

From Figure 3-8, it can be noted that if $\hat{d}_{dc}$ and $\hat{v}_{Csub}$ can be represented by $\hat{\imath}_{dc}$ and $\hat{v}_{dc}$, respectively, the dc impedance model of MMC can then be derived. Therefore, to develop the model, four transfer functions are defined first as in (3. 16).

$$\begin{aligned} G_{di}(s) &= \frac{\hat{d}_{dc}(s)}{\hat{\imath}_{dc}(s)} \\ G_{dv}(s) &= \frac{\hat{d}_{dc}(s)}{\hat{v}_{dc}(s)} \\ G_{vi}(s) &= \frac{\hat{v}_{Csub}(s)}{\hat{\imath}_{dc}(s)} \\ G_{vv}(s) &= \frac{\hat{v}_{Csub}(s)}{\hat{v}_{dc}(s)} \end{aligned} \tag{3. 16}$$

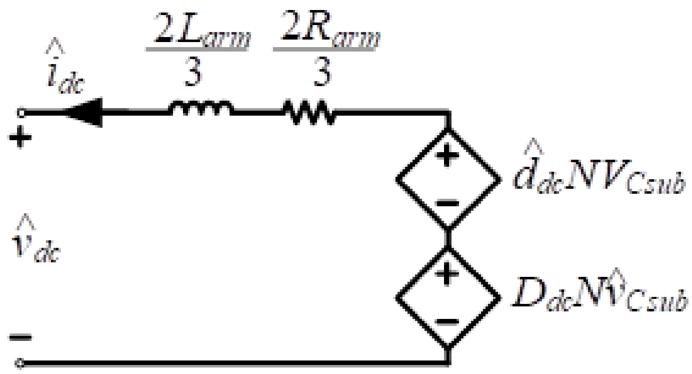

Figure 3-8. Small-signal equivalent circuit of MMC dc terminal.

Based on (3. 5) and according to Figure 3-4, the transfer functions of $\hat{i}_{dc}$ to $\hat{d}_{dc}$ and $\hat{v}_{dc}$ to $\hat{d}_{dc}$ can be obtained as shown in (3. 17).

$$G_{di}(s) = -\frac{2}{3}G_{cir}(s)$$
$$G_{dv}(s) = 0 \tag{3. 17}$$

In addition, the expression of submodule capacitor voltage v_{Csub} is the foundation to derive the transfer functions $G_{vi}(s)$ and $G_{vv}(s)$. According to (3. 2), the submodule capacitor voltage can be represented by $S_{xU(L)}$ as shown in (3. 18) and $i_{xU(L)}$ as shown in (3. 19), where $M = 2V_d/V_{dc}$ is the modulation index, $I_s = \frac{I_d}{\sin\beta}$ is the magnitude of the fundamental-frequency component, α, β, φ and γ are phase angles, and v_{cir} and i_{cir} are the second order circulating current related voltage and current. In this chapter, assume a unity power factor application, so $\sin\alpha = 1$ and $\sin\beta = 1$. In addition, circulating current is assumed to be well suppressed by the control in Figure 3-4. Therefore, $v_{cir} = 0$ and $i_{cir} = 0$.

$$S_{xU} = \frac{\frac{1}{2}V_{dc} - \frac{1}{2}V_{dc}M\sin(\omega t + \alpha) + v_{Cir}\sin(2\omega t + \varphi)}{V_{dc}}$$
$$S_{xL} = \frac{\frac{1}{2}V_{dc} + \frac{1}{2}V_{dc}M\sin(\omega t + \alpha) + v_{Cir}\sin(2\omega t + \varphi)}{V_{dc}} \tag{3. 18}$$

$$i_{xU} = \frac{1}{3}i_{dc} - \frac{1}{2}I_s\sin(\omega t + \beta) + i_{cir}\sin(2\omega t + \gamma)$$
$$i_{xL} = \frac{1}{3}i_{dc} + \frac{1}{2}I_s\sin(\omega t + \beta) + i_{cir}\sin(2\omega t + \gamma) \tag{3. 19}$$

By substituting (3. 18) and (3. 19) into (3. 2), the upper arm SM capacitor voltage can be expressed as (3. 20). It consists of a quasi-dc component, fundamental frequency component, and second-order frequency component with neglecting the higher-order frequency components [178, 179]. The lower arm SM voltages have the same frequency components, whereas the fundamental frequency has the opposite sign. In this chapter, all the submodule capacitor voltages are assumed to be the same. Therefore, the lower arm submodule voltage v_{CubL} is assumed as (3. 20).

$$\begin{aligned}\frac{dv_{Csub}}{dt} = &-\frac{1}{6C_{sub}}i_{dc} - \frac{1}{8C_{sub}}MI_s\cos(\alpha-\beta) \\ &+\frac{1}{4C_{sub}}I_s\sin(\omega t+\beta) + \frac{1}{6C_{sub}}Mi_{dc}\sin(\omega t+\alpha) \\ &+\frac{1}{8C_{sub}}MI_s\cos(2\omega t+\alpha+\beta)\end{aligned} \tag{3. 20}$$

By substituting all the values, (3. 20) can then be written as (3. 21).

$$\frac{dv_{Csub}}{dt} \approx -\frac{1}{6C_{sub}}i_{dc} - \frac{MI_d}{8C_{sub}} + \frac{I_d}{4C_{sub}}cos(\omega t) + \frac{Mi_{dc}}{6C_{sub}}cos(\omega t) \tag{3. 21}$$

By performing Laplace transformation on the differential equation of v_{Csub} in (3. 21) based on (3. 22) and (3. 23), and neglecting the higher-order differential components, the transfer function $G_{vi}(s)$ can be obtained as in (3. 24).

$$\cos x = \sum_{n=0}^{\infty}\frac{\cos(\frac{n\pi}{2})}{n!}x^n \tag{3. 22}$$

$$\mathcal{L}[x^n f(x)] = (-1)^n\frac{d^n}{ds^n}\mathcal{L}[f(x)] \tag{3. 23}$$

$$G_{vi}(s) = -\frac{1}{2C_{sub}s} + \frac{M}{6C_{sub}s} \tag{3. 24}$$

Similarly, the transfer function $G_{vv}(s)$ can be obtained as shown in (3. 27) based on (3. 21) - (3. 23), (3. 25), and (3. 26), where, $T_i(s) = \frac{G_i(s)V_{dcref}}{sL_{arm}+R_{arm}}$.

$$v_d(s) = \frac{V_{dcref}}{2} G_v(s) G_i(s) v_{dc}(s) \tag{3. 25}$$

$$i_d(s) = G_v(s) \frac{T_i(s)}{1 + T_i(s)} v_{dc}(s) \tag{3. 26}$$

$$\begin{aligned} G_{vv}(s) = & \frac{\left(\frac{I_d G_v G_i V_{dcref}}{2} + \frac{V_d G_v T_i}{1 + T_i}\right) V_{dcref} - V_d I_d}{4C_{sub} V_{dcref}^2 s} - \frac{G_v T_i}{4C_{sub}(1 + T_i)s} \\ & - \frac{\left(\frac{G_v G_i V_{dcref}}{2} - V_d\right) I_{dc}}{3C_{sub} V_{dcref}^2 s} \end{aligned} \tag{3. 27}$$

Therefore, the dc impedance model of MMC could be obtained as (3. 28), where $G_{di}(s)$, $G_{vi}(s)$, and $G_{vv}(s)$ can be seen in (3. 17), (3. 24), and (3. 27), respectively.

$$Z_{dc}(s) = \frac{\frac{2}{3}(L_{arm}s + R_{arm}) - G_{di}(s)V_{dcref} - NG_{vi}(s)}{1 - NG_{vv}(s)} \tag{3. 28}$$

3.2.3 Comparison of Existing and Proposed Dc Impedance Models of MMCs

In order to validate the accuracy of the proposed dc impedance model of MMC, a circuit-based simulation is conducted in MATLAB/Simulink with the parameters and working conditions listed in Table 3-1. The simulation model is built based on the switching circuit of MMC. The dc impedance simulation results are obtained by injecting a small current perturbation (frequency

Table 3-1. Components and Working conditions of the MMC.

Parameters	Value	Parameters	Value
DC bus voltage V_{dcref}	21 kV	Submodule DC voltage V_{Csub}	7 kV
Power rating P	1 MW	Submodule capacitor C_{sub}	70 μF
AC voltage $V_{LL,rms}$	13.8 kV	DC voltage PI controller	K_{pv} = 0.01, K_{iv} = 4
AC grid frequency f_o	60 Hz	AC current PI controller	K_{pi} = 0.0029, K_{ii} = 0.01
Arm inductor L_{arm} Parasitic resistance R_{arm}	17 mH 1 mΩ	Circulating current PR controller	K_{pr}=0.3, K_{sr}=30
Submodule number per arm N	3	Switching frequency f_{sw}	5 kHz

range in the simulation: 1 Hz – 10 kHz) at the MMC dc side, and performing FFT analysis on the measured dc current and dc voltage at the perturbation frequency.

The comparisons among the dc impedance models and simulation results are shown in Figure 3-9. The blue-star curve is the circuit-based simulation result. It can be seen that model I (black curve) cannot predict the low-frequency (around 1-50 Hz) characteristics which are mainly caused by the neglect of capacitor voltage dynamics. Model II (green curve) cannot reveal the middle-frequency (around 12-1200 Hz) behavior which is related to the circulating current suppression control. The proposed model (red curve), considering both capacitor voltage dynamics and circulating current control effects, can match the simulation results. Though due to the simplifications and linearization process of the submodule capacitor voltage, such as assuming $v_{cir} = 0$ and $i_{cir} = 0$ and ignoring high-order components, there is still a small dc offset of the proposed model compared with the circuit-based simulation. This small dc offset will not affect the prediction of the dc system stability as shown in Section 3.3.

3.3 Dc Impedance-based Stability Analysis of Power Systems with MMC

With the proposed dc impedance model, if connecting a standalone-stable MMC on a dc bus, the overall system stability can be predicted by analyzing the relationships of the impedances between the interconnected converters with the Nyquist stability criterion.

A dc system consisting of the MMC feeding a CPL through the dc-link is studied as shown in Figure 3-10, where the well-controlled MMC (in the simulation) or a two-level VSC (in the experiment) is regarded as a CPL.

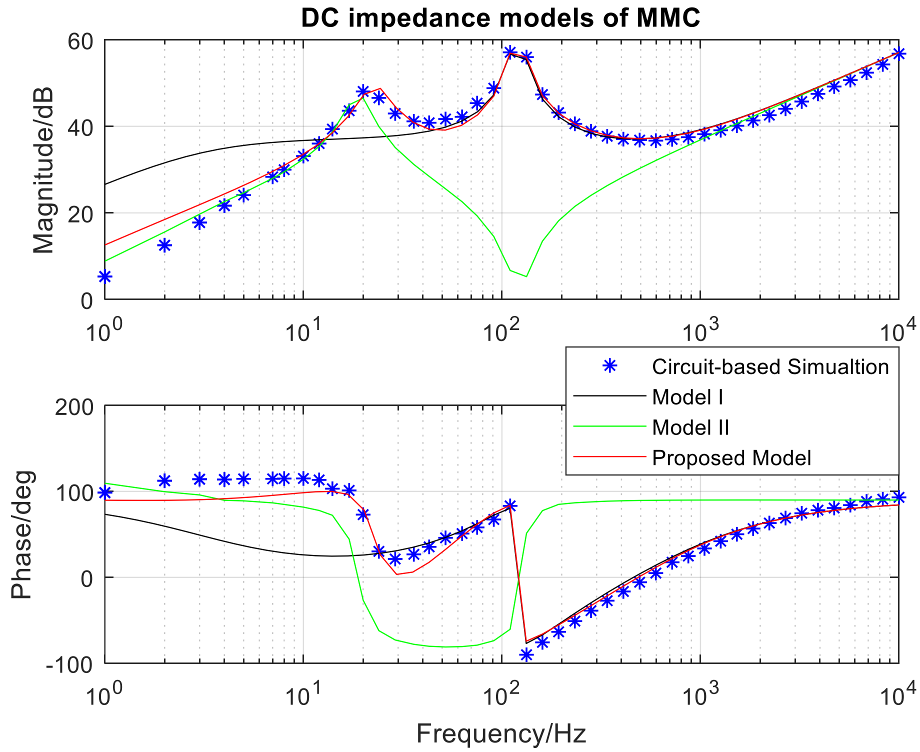

Figure 3-9. Comparisons of the existing and proposed DC impedance models of the MMC.

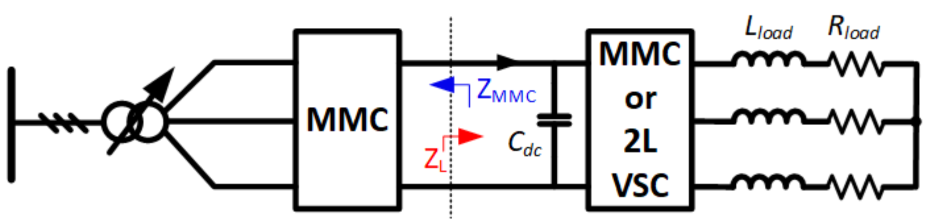

Figure 3-10. Configuration of a system with an MMC feeding a CPL.

3.3.1 Simulation Results

Three cases with different control parameters have been studied to validate the effectiveness of the proposed MMC dc impedance model for system stability analysis. Note that the MMC and the load converter have been designed to be stable in the standalone operation, so if there were unstable phenomena, they should be caused by the interactions between the source-side MMC and the load converter. In addition, the minor loop gain T_{minor} is defined as $T_{minor} = Z_L/Z_{MMC}$ in the analysis for these three simulations.

Simulation I: same parameters as listed in Table 3-1

In simulation I, the circuit uses the same parameters as listed in Table 3-1. Figure 3-11(a) shows the Nyquist stability analysis diagram using model I and the proposed model. It can be observed that both model I and the proposed model predict that the RHP zero of T_{minor} N_Z is 0, which means that the system would be stable. Figure 3-11(b) shows the bus voltage predicted by model II. As mentioned in Section 3.2.1, model II does not have a mathematical expression of closed-loop dc impedance, the stability analysis using model II is conducted by time-domain simulation in MATLAB/Simulink with the equivalent circuit in Figure 3-7. Figure 3-11 (c) shows the circuit-based simulation results of dc bus voltage, it can be seen that the system is stable. Therefore, the stability analysis results using the proposed model and existing models correspond with the simulation results.

Simulation II: change of ac current PI controller.

In simulation II, the ac current controller G_i is changed to k_{pi} = 0.00029 and k_{ii} = 0.001. Note that the standalone operation of MMC (MMC with a current load, instead of CPL) is kept stable.

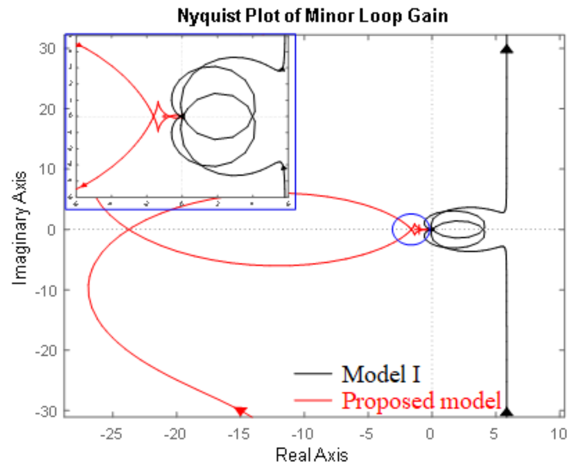

(a)

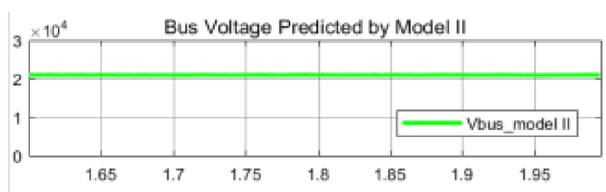

(b)

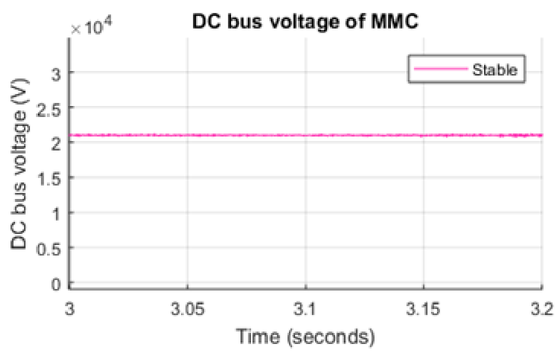

(c)

Figure 3-11. Simulation I: (a) Nyquist stability analysis using model I and the proposed model, (b) stability analysis using model II, and (c) simulated dc bus voltage.

Figure 3-12 (a) shows the system stability analysis results using the proposed model and model I. It can be seen that the proposed model predicts that the system would be unstable due to the RHP zero (i.e., $N_Z = N_P + N_{CW} = 0 + 4 = 4$). But model I predicts it to be stable since there are no encirclements of the critical point (-1+j0). Model II predicts the system to be unstable as shown in Figure 3-12 (b). The simulation of dc bus voltage as shown in Figure 3-12 (c) indicates that the system is unstable.

Therefore, the proposed model and model II can predict the system stability correctly in this case, while model I is ineffective in this case because it neglects submodule capacitor voltage dynamics in its modeling process.

Simulation III: change of circulating current PR controller

In simulation III, the circulating current parameters are changed to $k_{pr} = 0.5$ and $k_{sr} = 1$. From the analysis results, it can be observed that the proposed model shows that the system would be unstable ($N_Z = N_P + N_{CW} = 0 +2 = 2$). This prediction as shown in Figure 3-13(a) agrees with the simulated unstable dc bus voltage as shown in Figure 3-13(c).

However, both model I and model II predict the system would be stable which are opposite of the dc bus voltage simulation results. Model I is inaccurate because of the lack of information on the voltage dynamics of submodule capacitors. Model II cannot model the effects of the circulating current suppressing control; therefore, it cannot reveal the second-order frequency component in dc bus voltage.

Note that the part of the Nyquist contours not shown in the *GH*-plane in Figure 3-11 (a), Figure 3-12(a), and Figure 3-13(a) all go through the right half plane which will not affect the (-1, j0) encirclement counting for stability analysis.

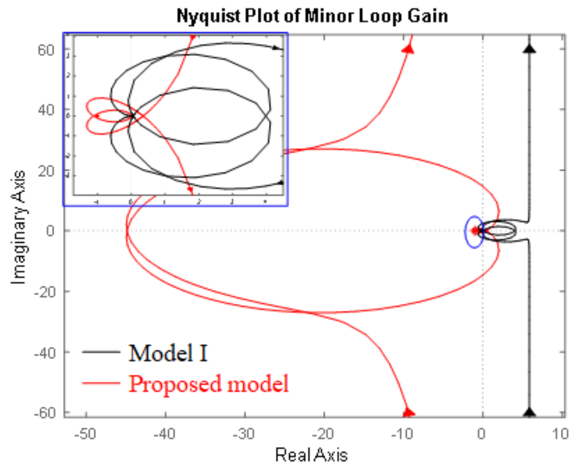

(a)

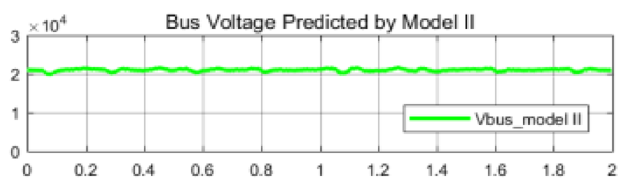

(b)

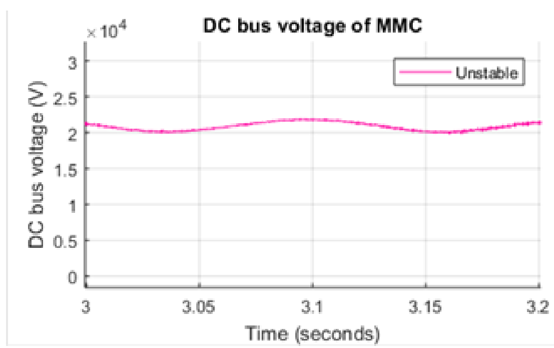

(c)

Figure 3-12. Simulation II: (a) Nyquist stability analysis using model I and the proposed model, (b) stability analysis using model II, and (c) simulated dc bus voltage.

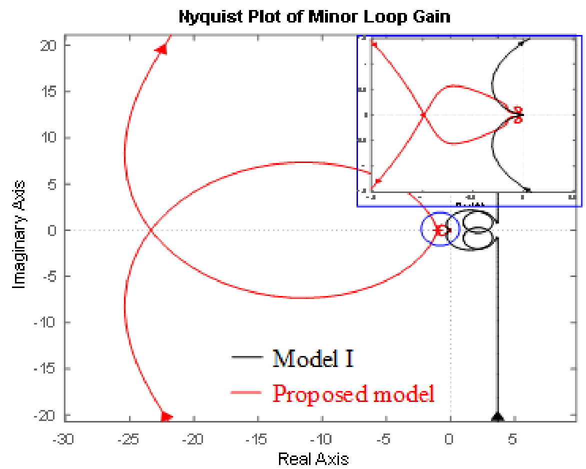

(a)

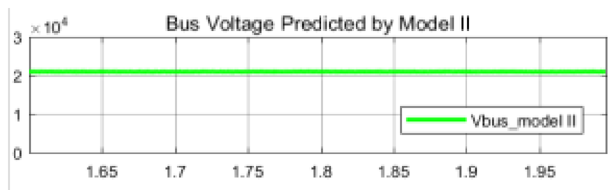

(b)

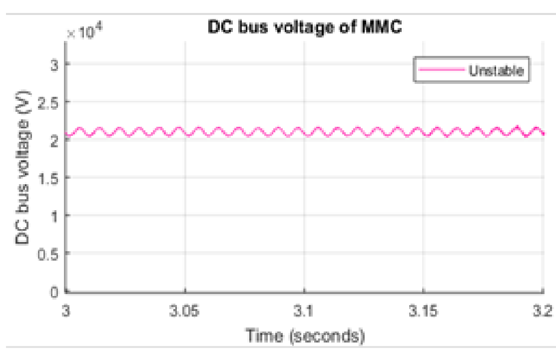

(c)

Figure 3-13. Simulation III: (a) Nyquist stability analysis using model I and the proposed model, (b) stability analysis using model II, and (c) simulated dc bus voltage.

3.3.2 Experimental Results

The experiments are carried out with a flexible MMC test-bed as introduced in [171] and a two-level VSC working as CPL as shown in Figure 3-14. The MMC has 10 SMs on each arm and the working conditions and control parameters are listed in Table 3-2. The stability analysis of the dc system is conducted using the proposed model and existing models first. And then the dc bus voltage is measured on the MMC-2LVSC testbed to validate the analysis results.

Test I: same parameters as listed in Table 3-2

The MMC hardware uses the same parameters as listed in Table 3-2. Figure 3-15(a) shows the Nyquist stability analysis diagram. It can be observed that model I ($N_Z = N_P + N_{CW} = 0 -1 = -1$ predicts the system to be unstable, and the proposed model reveals that the RHP zero of T_{minor} N_Z is 0 ($N_Z = N_P + N_{CW} = 0 – 0 = 0$), which means that the system is predicted to be stable. The simulation using model II as in Figure 3-15 (b) shows that the system is stable. Figure 3-15(c) shows the measurement of a stable dc bus voltage and current. Therefore, in test I, the stability analysis results using the proposed model and model II match with the measurement, while model I cannot predict the system stability correctly.

Test II: change of ac current PI controller

In test II, the ac current controller G_i is changed to $k_{pi} = 0.005$ and $k_{ii} = 0.1885$. Still, the standalone operation of MMC is kept stable. Figure 3-16(a) shows the system stability analysis results using the proposed model and model I. The proposed model predicts that the system would be unstable since the RHP zero N_Z is found to be $N_P + N_{CW} = 0 + 2 = 2$. Model I predicts it to be unstable because the RHP zero $N_Z = N_P + N_{CW} = 0 - 1 = -1$. The simulation of dc bus voltage using

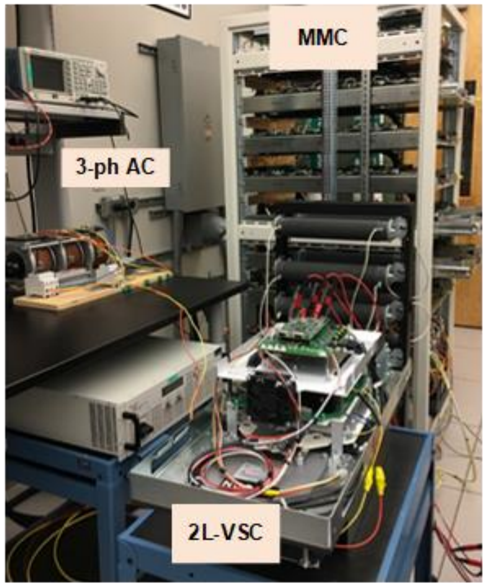

Figure 3-14. Experimental setup.

Table 3-2. Parameters of MMC.

Parameters	**Value**	**Parameters**	**Value**
DC bus voltage V_{dcref}	200 V	Power rating P	1.7 kW
AC voltage $V_{LL,rms}$	110 V	Submodule capacitor C_{sub}	2.2 mF
AC grid frequency f_o	60 Hz	Arm inductor L_{arm}	3 mH
Submodule number N	10	AC current PI controller	K_{pi}=0.05, K_{ii}=1.885
DC voltage PI controller	K_{pv}=0.4, K_{iv}=12	Circulating current PR controller	K_{pr}=0.4, K_{sr}=20

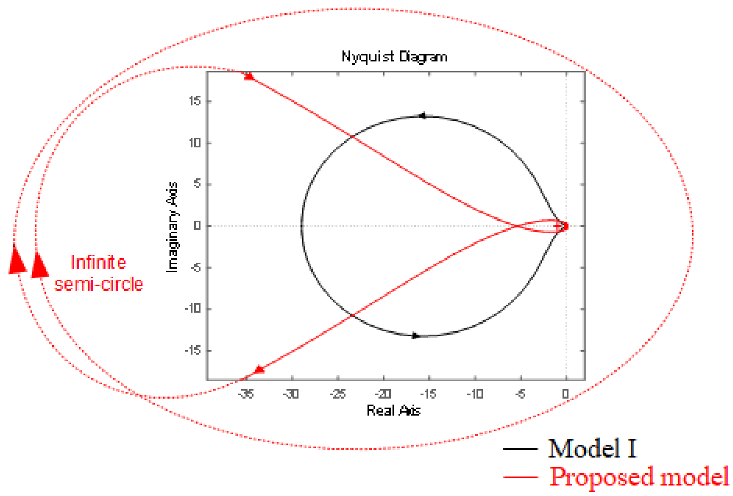

(a)

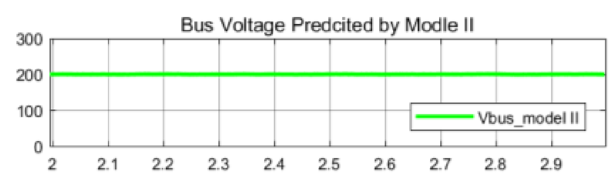

(b)

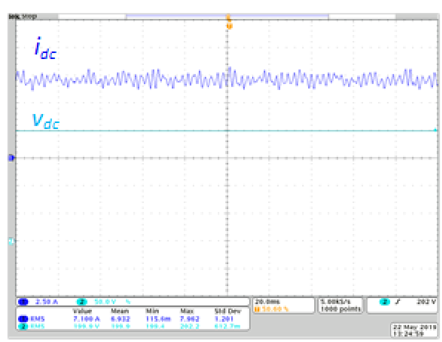

(c)

Figure 3-15. Test I: (a) Nyquist stability analysis using model I and the proposed model, (b) stability analysis using model II, and (c) measurement of dc bus voltage.

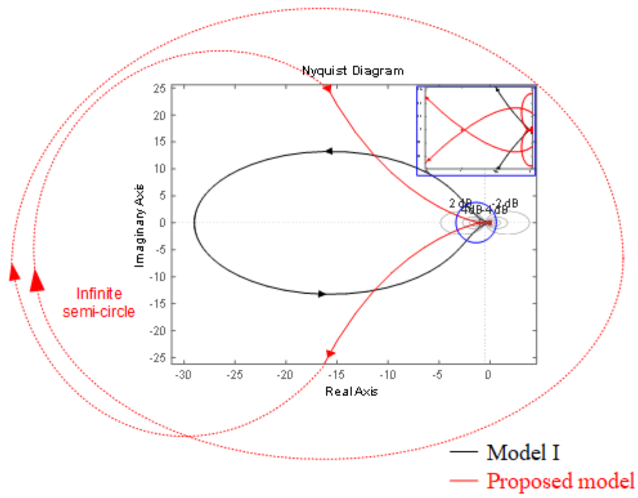

(a)

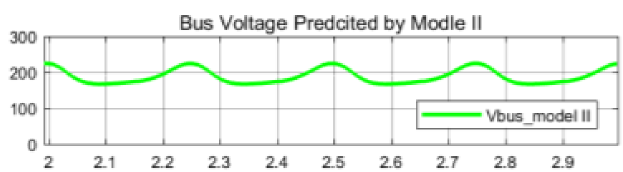

(b)

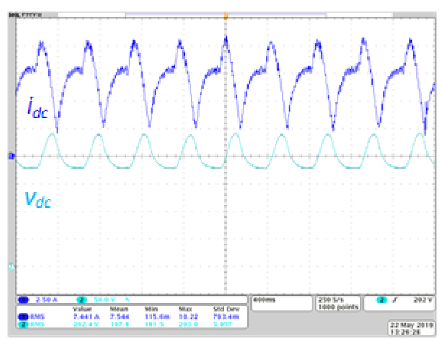

(c)

Figure 3-16. Test II: (a) Nyquist stability analysis using model I and the proposed model, (b) stability analysis using model II, and (c) measurement of dc bus voltage.

model II as shown in Figure 3-16(b) also indicates that the system is unstable. And the measurement results in Figure 3-16(c) also show that the system is unstable. Therefore, it can be concluded that all the models can predict the system stability correctly in this case.

In both test I and test II, model II can predict the system stability correctly. This is because the control parameters of the circulating current loop can only be changed within a small range due to the effects of control delays in the MMC testbed [180]. However, the limitations of model II which is caused by neglecting the effects of circulating current control cannot be overlooked as shown by the simulations.

3.4 Control Parameter Design of MMCs Considering System Small-Signal Stability

To guarantee system stability when connecting an MMC to the dc bus, the parameters in these three control loops of the MMC should be carefully designed according to the impedance model. Take the system in Figure 3-14 as an example. Since the information of the entire system is available, the system stability can then be determined by the NSC with the equivalent circuit as shown in Figure 3-17. The minor loop gain T_{minor} is derived as in (3. 29), where Z_{dc_MMC} is given in (3. 28), and Z_{dc_CPL} is given in (3. 30).

$$T_{minor} = \frac{Z_{dc\_MMC}}{Z_{dc\_CPL}} \tag{3. 29}$$

$$Z_{dc\_CPL} = \frac{-V_{dc}^2}{P - \frac{sC_{dc}V_{dc}^2}{sC_{dc}R_{dc}+1}} \tag{3. 30}$$

System stability can then be determined by the phase angle at the crossover frequency of T_{minor} as being mapped from the Nyquist diagram to the Bode diagram with GBC in Figure 3-18. That

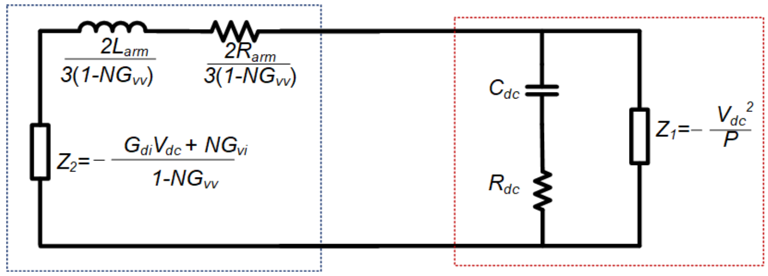

Figure 3-17. Small-signal equivalent circuit of the system consisting of an MMC and a CPL.

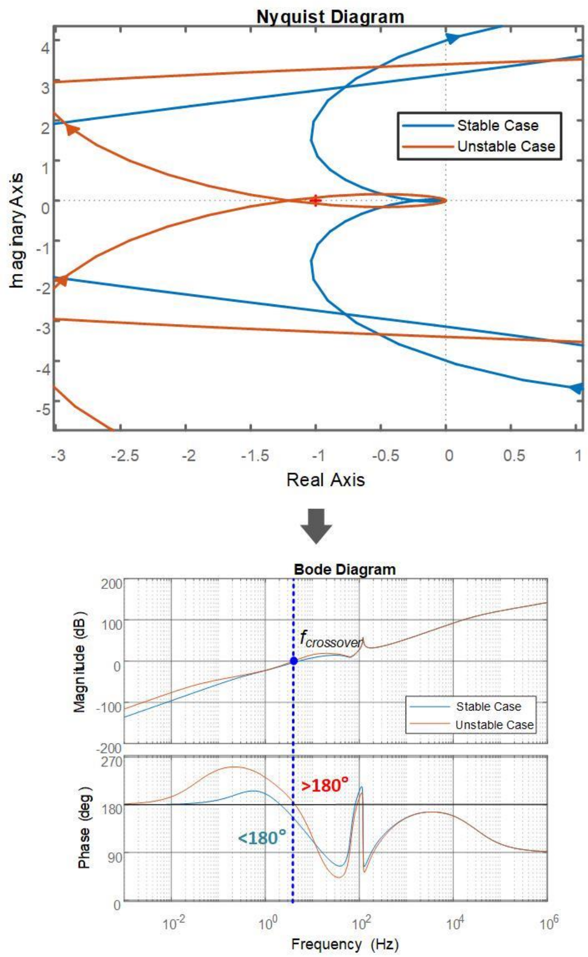

Figure 3-18. Nyquist diagram and Bode diagram of $T_{minor.}$

is, if before the crossover frequency $f_{crossover}$, the magnitude of Z_{dc_MMC} is smaller than Z_{dc_CPL} ($|Z_{MMC}| < |Z_{CPL}|$), and the derivation of the phase angle of Z_{dc_MMC} is smaller than that of Z_{dc_CPL} at the crossover frequency ($(\angle Z_{MMC})' < (\angle Z_{CPL})'$), then the system is unstable if the phase angle of T_{minor} is larger than 180°, where the phase angle of T_{minor} is within [0°, 360°).

To see the impacts of different control loops, including the inner ac current loop, outer dc voltage loop, and circulating current loop, on system stability, it is assumed in this study that each control loop is decoupled from the others. Specifically, when analyzing one of the control loops by sweeping the control parameters in a certain range, keep the other loops unchanged. Note that the ranges for the control parameters are determined by the stable operation of the MMC in an ideal load condition.

The impact of ac current control parameters on system stability is investigated by sweeping the proportional gain K_{pi} from 0 to 0.06 and the integral gain K_{ii} from 0 to 2, with keeping the outer dc voltage control and circulating current control unchanged as shown in Figure 3-19. It is seen that a smaller K_{pi} and a smaller K_{ii} will tend to destabilize the system with the phase angle at $f_{crossover}$ being larger than 180°.

Following the same approach, the impact of the dc output voltage is investigated as shown in Figure 3-20, and the impact of circulating current control is investigated as shown in Figure 3-21. A small proportional gain of voltage control loop K_{pv}, or a large resonance gain of circulating current control loop K_{sr} will have a significant impact on system stability.

The impedance model-based analytical results are also compared with simulation and experimental results as shown in Figure 3-22, Figure 3-23, and Figure 3-24, separately. It can be seen that the analytical boundary for the system stability is close to the simulation boundary. While

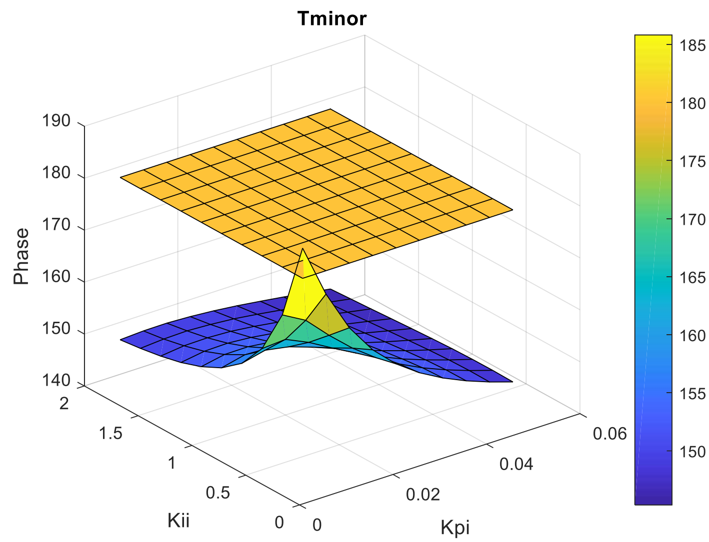

Figure 3-19. Impact of ac current control parameters on system stability with $K_{pv} = 0.4$, $K_{iv} = 12$, $K_{pr} = 0.4$, and $K_{sr} = 20$.

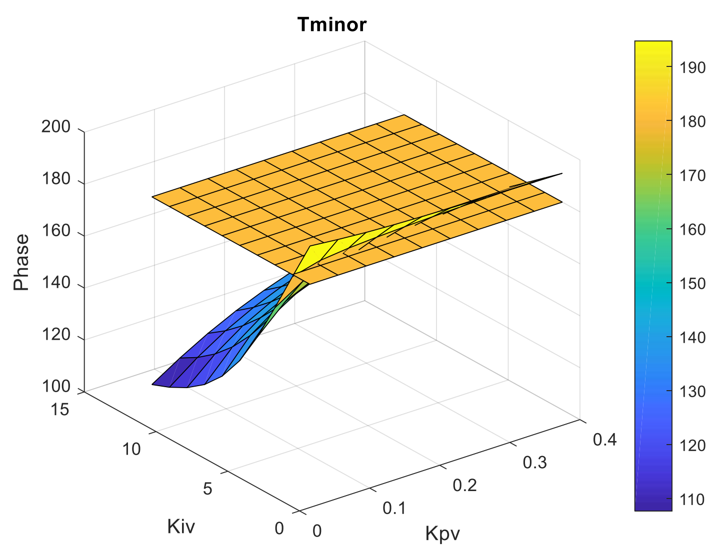

Figure 3-20. Impact of dc voltage control parameters on system stability with $K_{pi} = 0.05$, $K_{ii} = 1.885$, $K_{pr} = 0.4$, and $K_{sr} = 20$.

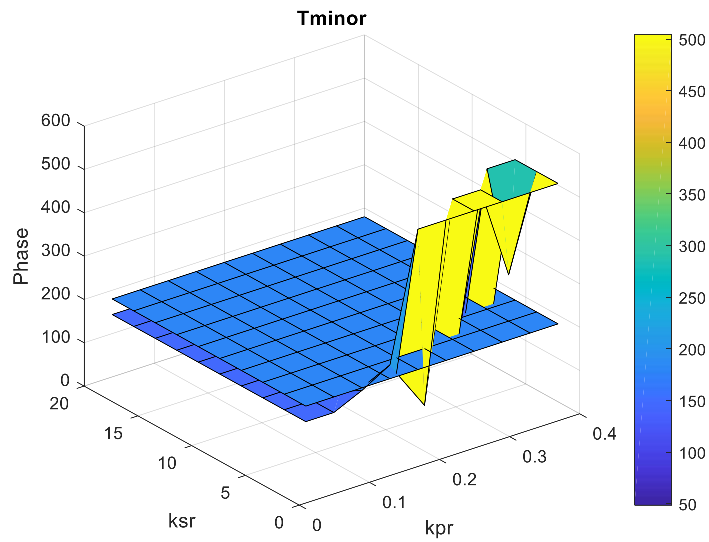

Figure 3-21. Impact of circulating current control parameters on system stability with K_{pi} = 0.05, K_{ii} = 1.885, K_{pv} = 0.4, and K_{iv} = 12.

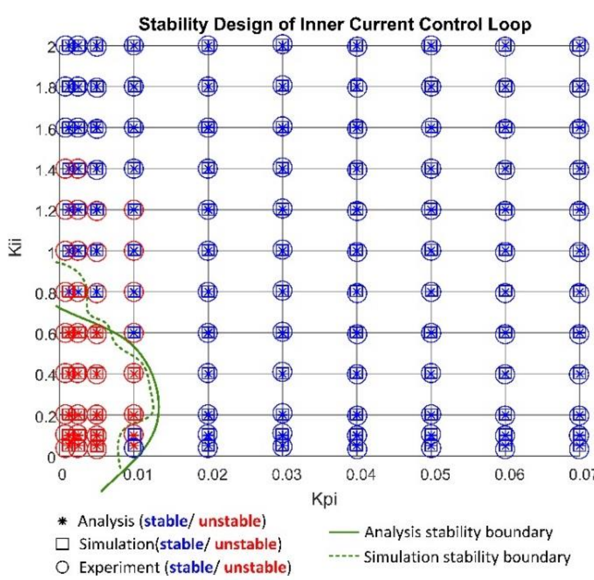

Figure 3-22. Inner ac current control loop design for system stability with K_{pv} = 0.4, K_{iv} = 12, K_{pr} = 0.4, and K_{sr} = 20.

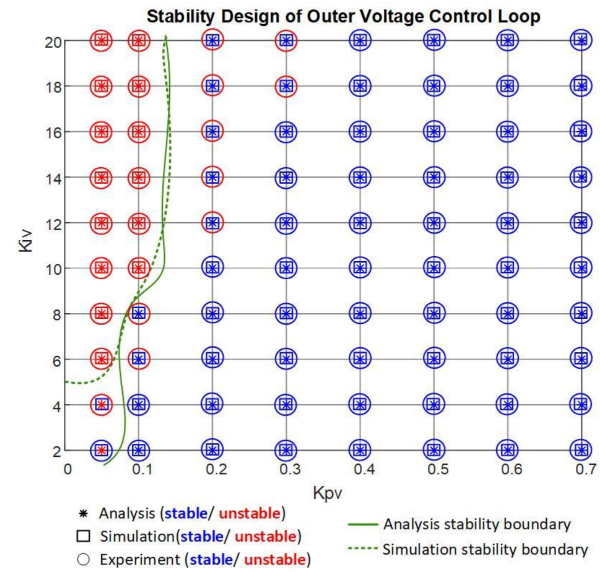

Figure 3-23. Outer dc voltage control loop design for system stability with $K_{pi} = 0.05$, $K_{ii} = 1.885$, $K_{pr} = 0.4$, and $K_{sr} = 20$.

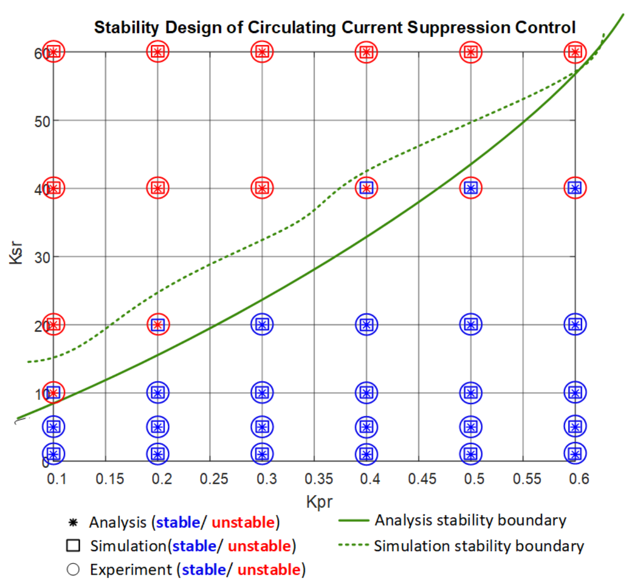

Figure 3-24. Circulating current control loop design for system stability with $K_{pi} = 0.05$, $K_{ii} = 1.885$, $K_{pv} = 0.4$, and $K_{iv} = 12$.

there are some deviations between the experimental results and simulation results. This might be caused by the parameter mismatch between the real hardware setup and the simulation circuits. To avoid this issue, when applying the stability analysis approach, it would be better to leave some stability margin for the parameter selection.

3.5 Conclusions

A dc impedance model of MMCs is proposed and used to conduct the stability analysis of a power system. Compared with the prior-art MMC models, the proposed dc impedance model can match the simulated results well and can predict the dc system stability correctly, due to the consideration of both the cell capacitor voltage ripple and circulating current dynamics. In addition, control parameters in MMCs are also investigated to see the impact on system stability with the proposed impedance model. Simulation and experimental results have proven the effectiveness of the proposed MMC impedance model for dc stability analysis.

Chapter 4. Dc Impedance Measurement using Existing Converter in the System

Starting with the discussion of different types of small-signal stability analysis approaches in Chapter 2, it is shown that the terminal impedance characteristics of each subsystem or equipment in a system seen from the common bus is one of the most important indicators for system stability. The subsystem or equipment impedance can be obtained by mathematical modeling or measurement. However, unlike dc systems of low voltage and low power (e.g., a notebook computer power system) in which impedances can generally be measured with commercially available instrumentation, it is difficult to use the commercial instrument in direct impedance measurement for medium- or high- voltage, high power systems (e.g., medium voltage dc distribution system or high-voltage dc transmission system). In this chapter, a simple-to-use approach is proposed to measure the dc impedance of PECs in power systems.

4.1 Proposed 2L-VSC-based Dc Impedance Measurement Unit

To minimize the efforts on building a new circuit to measure the impedance, an easy setup is proposed. In PEC-rich power systems with hybrid dc grids (paralleled structure or multi-terminal structure) as shown in Figure 4-1, a 2L-VSC is usually available, therefore, the proposed impedance measurement unit can be developed based on it. Compared with the existing impedance measurement methods, the contributions of this study can be summarized as follows:

(1) There is no need for dedicated equipment, such as a frequency response analyzer or a power amplifier.

(2) There is no extra dc power supply or ac source required.

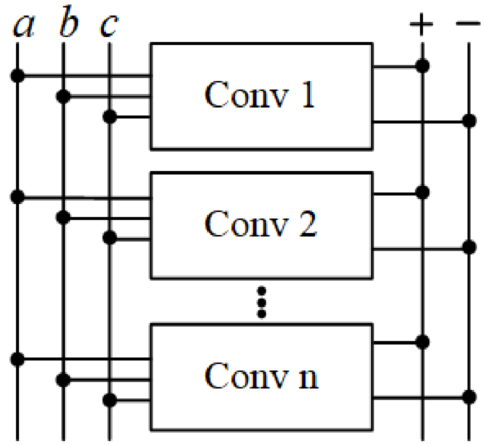

(a)

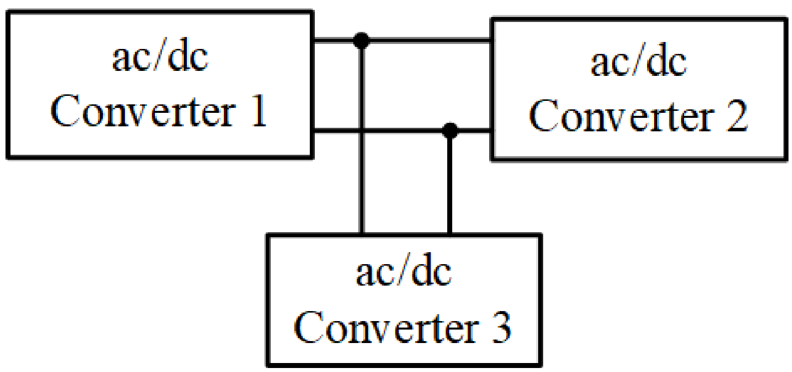

(b)

Figure 4-1. Scenarios for the proposed IMU: (a) a paralleled converter structure and (b) a multi-terminal dc grid.

(3) It is suitable for systems with paralleled structures or a multi-terminal dc grid.

4.1.1 Concept, Structure, and Flowchart of the Proposed IMU

In order to measure the small-signal dc impedance of an ac/dc converter, small sinusoidal disturbances are usually injected into the system, such as a shunt current perturbation injection as shown in Figure 4-2(a) or a series voltage perturbation injection as shown in Figure 4-2(b). Then by analyzing the response waveforms under the perturbations, small-signal models can be obtained. Usually, the current or voltage perturbation signals are generated by an FRA with a PA.

Also, the amplitude of the injection signal should be small enough to avoid affecting the system's steady-state operation. The injected low-frequency perturbation magnitude is usually selected to be smaller than 10% of the normal operating points. For high-frequency injections, the amplitude can be around 20%-30% of the steady-state operating point to compensate for the low-pass filter impacts and increase the high-frequency noise immunity [33].

In this chapter, to avoid using any dedicated equipment like an FRA or a PA, an impedance measurement method is proposed based on a 2L-VSC since a 2L-VSC can be easily obtained in most hybrid dc systems. The schematic of the impedance measurement setup is shown in Figure 4-3. There are three types of converters in the system: one is a source-side converter; one is a load-side converter; and another is an IMU converter. A three-phase voltage source is connected to the system to provide power for both the source converter and IMU converter. And the IMU generates the perturbation signals to the dc link in the system under test which will be discussed in detail in Section 4.1.2. In the IMU setup, probes and oscilloscopes are required for waveform measurement and data acquisition. The MATLAB environment is also needed for data processing to obtain the small-signal model as will be further introduced in Section 4.1.3.

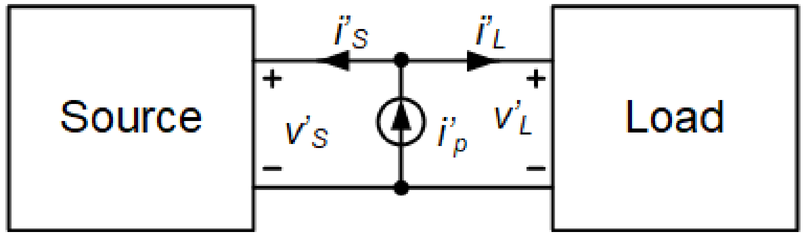

(a)

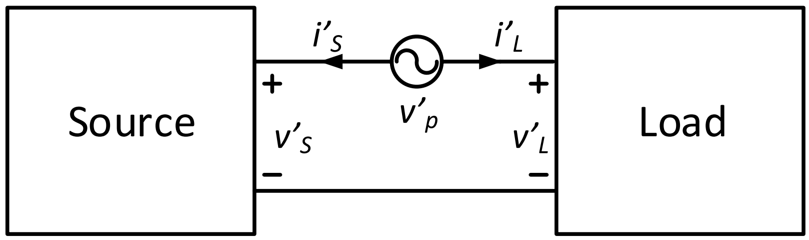

(b)

Figure 4-2. Small-signal injections: (a) shunt current perturbation injection and (b) series voltage perturbation injection.

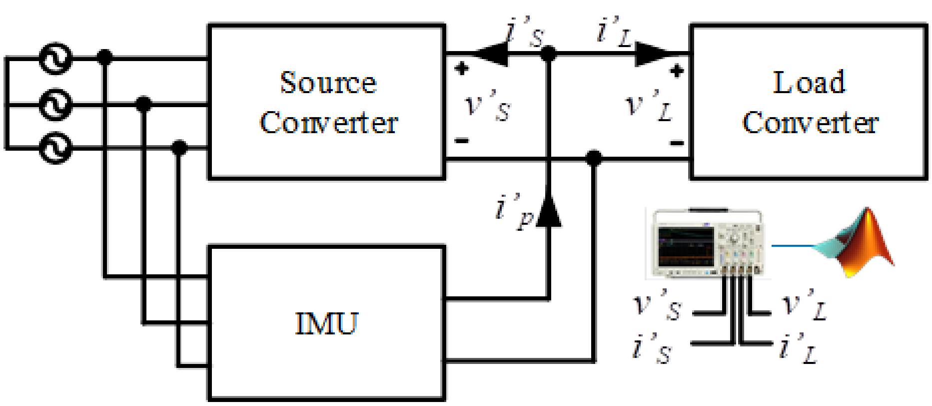

Figure 4-3. Structure of the proposed IMU.

Figure 4-4 shows the flowchart of the impedance measurement process. First, the test frequency range and the test points should be defined. The identifiable perturbation frequency can be up to half of the switching frequency of SUT which is f_{max}. The lowest frequency f_{min} can start from 1 Hz. Since the terminal voltages (v'_S, v'_L) and currents (i'_S, i'_L) at the source side and load side at each frequency are measured by probes and the data are acquired through an oscilloscope, if a lower-frequency (< 1 Hz) perturbation is injected, the oscilloscope may not have enough memory to store all data. The sampling rate of the oscilloscope is set to be 1 MS/s (i.e., millions of samples per second). In addition, the number of testing points N is selected by the user. The larger N is, the more impedance data can be obtained. With the predefined frequency range and number of test times, the perturbation frequency test points can be selected. For example, the N test points can be equally scattered within the identifiable frequency range in the logarithmic scale.

Then, it can be started to test from the first testing point to the given last testing point. Considering the accuracy of data measurement and FFT calculation, multiple periods of the injected sinusoidal perturbations should be guaranteed. The lower the injection frequency is, the longer the injection time should be. For example, 4 seconds of perturbation injection is used for 1 Hz disturbance and 0.2 seconds of perturbation injection is used for 50 Hz disturbance.

After finishing frequency sweeping at all the test points, the measured waveforms are imported into MATLAB for further analysis. By doing FFT and system identification using toolbox in MATLAB, Z_S and Z_L can be achieved with $Z_S(s) = v'_S(s)/i'_S(s)$ and $Z_L(s) = v'_L(s)/i'_L(s)$.

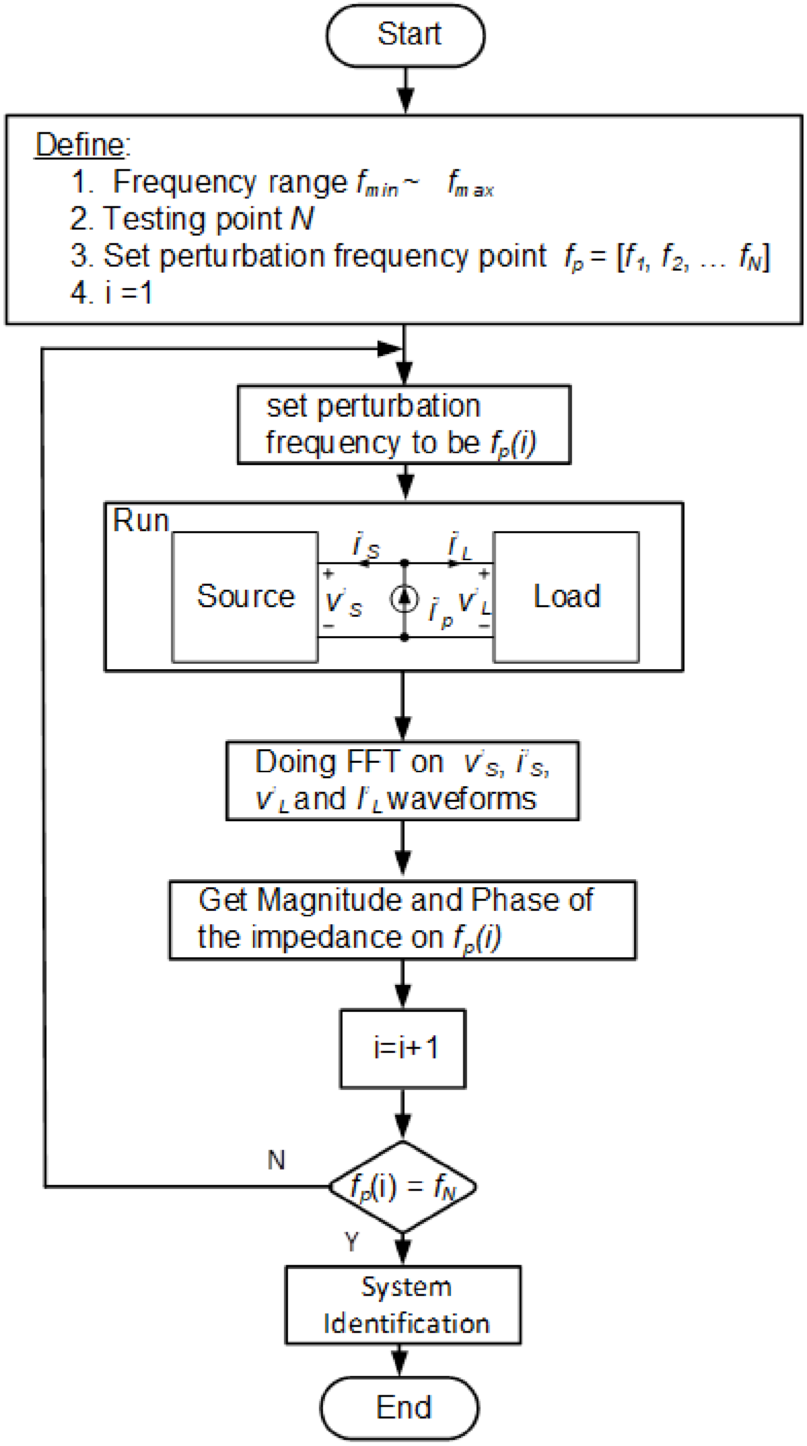

Figure 4-4. Flowchart of the proposed impedance measurement method.

4.1.2 Circuit Diagram and Control Structure of the Proposed IMU

One of the most important steps of the proposed impedance measurement method is the generation of perturbation signals using a 2L-VSC. Figure 4-5 shows the circuit diagram of the proposed current perturbation injection circuit. Compared with the conventional 2L-VSC structure, a resistor R_{dc} with a paralleled switch *S2* is connected on the dc link and a switch *S1* is connected in series with the large dc-link capacitor C_{dc2}. This proposed IMU structure can have two working modes: one is a conventional rectifier and the other is an impedance measurement unit. If working as a conventional 2L-VSC rectifier, the switch *S1* and *S2* are both "on" to obtain a large equivalent dc-link capacitor (C_{dc1} + C_{dc2}) and bypass the resistor R_{dc} on the dc link. But when working as the perturbation current injection circuit, the switch *S1* is "off" to have a smaller dc-link capacitor C_{dc1} which can filter out the high-frequency noise but keep the perturbation component. And the switch *S2* is also "off" to decouple the dc bus of SUT v_{bus} and dc output of IMU v_t. The decoupling resistor R_{dc} is designed based on the perturbation amplitude. For example, if i_p is designed to be 10% of i_{nom} and v_t is designed to be 1.1v_{bus}, then R_{dc} would be selected as v_{bus}/i_{nom}. The losses introduced by this resistor are very small due to the small-magnitude current perturbation injection.

Based on the circuit diagram in Figure 4-5, the relationships between the dc bus voltage v_{bus} and the IMU dc terminal voltage v_t are determined by the perturbation current i_p and decoupling resistor R_{dc}, which can be expressed as in (4. 1). And the current flowing out of the dc terminal of the IMU i_t can be determined as shown in (4. 2), which is the sum of the dc capacitor current i_{Cdc1} and perturbation current i_p. Then, according to the ac and dc power balance concept, the *d*-axis reference current i_{dref} can then be estimated as in (4. 3) in the synchronous control frame. This calculated reference value i_{dref} can be used to generate the control signals of the IMU through an open-loop control block to avoid the limitations of the closed-loop control bandwidth. Also,

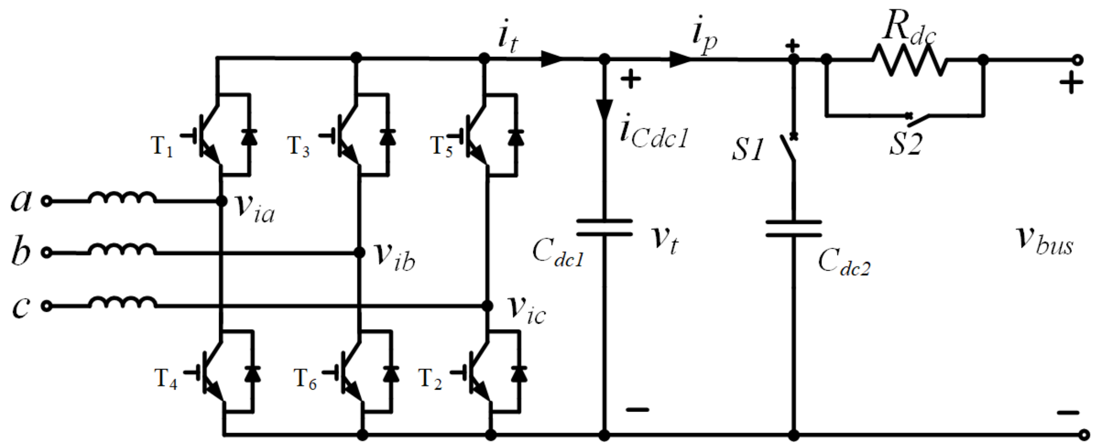

Figure 4-5. Circuit diagrams of the proposed IMU.

the reactive power is controlled to be 0 through a closed-loop PI controller for better accuracy because reactive power will only have a slight impact on the dc side current so that *q*-axis control bandwidth limitations can be ignored. Besides, the desired current perturbation i_p is a sinusoidal signal, where the perturbation frequency f_p and perturbation amplitude A_p are given by the user to the controller through a LabVIEW interface. Therefore, this open-loop active power and closed-loop reactive power control diagram can be obtained as shown in Figure 4-6. With the duty cycle generator, the corresponding three-phase duty cycles D_a, D_b, and D_c can be obtained for the gate control signals for the switches in the proposed IMU. In addition, the sinusoidal pulse width modulation technique is adopted in this study.

$$v_t = v_{bus} + i_p R_{dc} \tag{4. 1}$$

$$i_t = C_{dc1}\frac{dv_t}{dt} + i_p \tag{4. 2}$$

$$i_{dref} \approx \frac{v_t i_t}{v_d} \tag{4. 3}$$

4.1.3 Identification of Impedance Models

With different perturbations, a group of terminal voltage and current data can be obtained by oscilloscopes. By importing these data to MATLAB and performing Fast Fourier Transform (FFT), a set of discrete impedance data (frequency, magnitude, and phase) can be calculated. However, these discrete data cannot be directly used to analyze system stability. To further use these data, they need to be transferred to continuous transfer functions. To do so, *System Identification Toolbox* in MATLAB can be adopted.

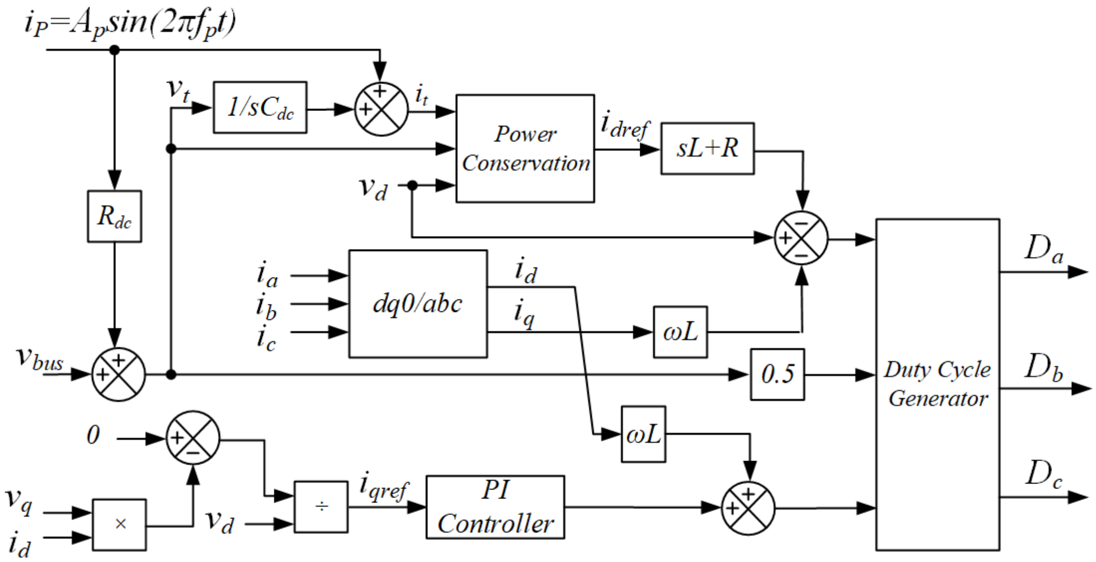

Figure 4-6. Control blocks of the proposed IMU.

The system identification process requires a model structure first and estimation methods will then be applied to determine the numerical values of the model parameters. We know that any transfer function can be expressed by an l^{th}-order ($l = \max\{m, n\}$) expression as shown in (4. 4), which can also be used as the model structure in our case. By increasing the order number until an accurate model is found through this iterative process, the corresponding impedance transfer functions can finally be achieved. Then with the estimated impedance models, system stability can be analyzed using either the Nyquist stability criterion or the passivity-based stability criterion.

$$Z(s) = \frac{b_m s^m + b_{m-1} s^{m-1} + \cdots + b_o}{a_n s^n + a_{n-1} s^{n-1} + \cdots + a_o} \tag{4. 4}$$

Although this non-parametric model cannot tell the direct impact of the converter hardware and controller design on its terminal characteristics, it can be used to analyze system stability and to check the accuracy of the derived mathematical model.

4.2 Simulation Results and Analysis

To verify the proposed IMU, a dc test system consisting of a modular multilevel converter (MMC) which is working as the source converter and a 2L-VSC which is working as the load converter is built. Also, the 2L-VSC-based IMU is connected in parallel with the MMC for the source converter output impedance measurement and load converter input impedance measurement. Figure 4-7 shows the simulation schematic of the test system. There are two sets of simulations conducted for comparison: one is perturbation injection with the proposed IMU, and the other is perturbation injection with an ideal current source which can be regarded as the benchmark. The comparisons are designed to see the effectiveness of the perturbation signals generated by the proposed IMU.

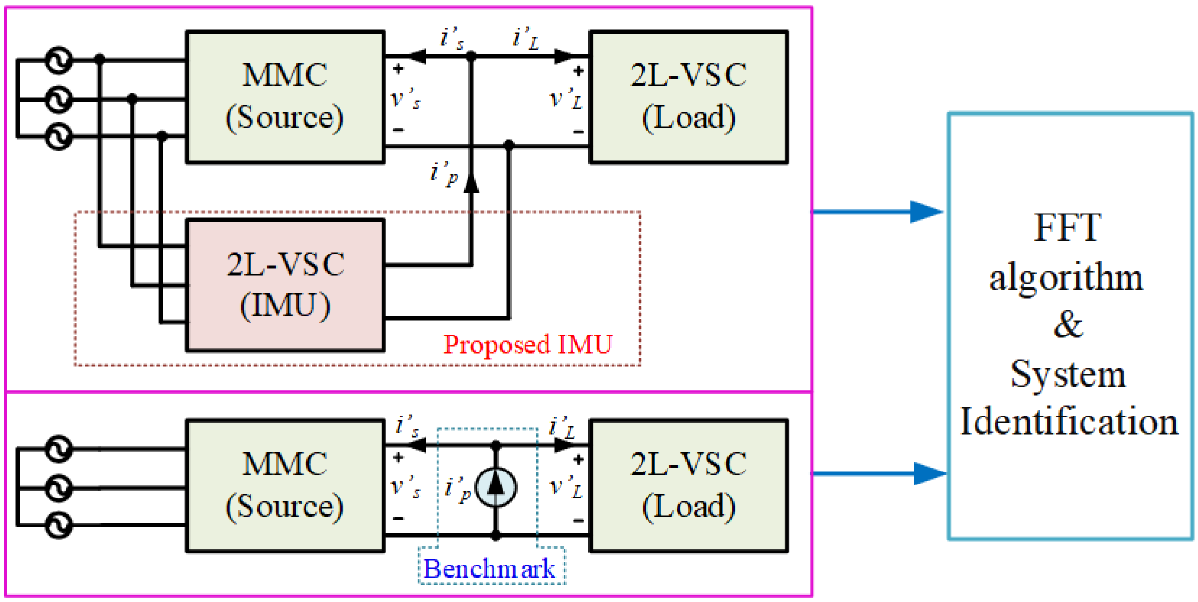

Figure 4-7. Simulation circuit diagram in MATLAB/Simulink.

The simulation results of the source converter output impedance and load converter input impedance are shown in Figure 4-8 separately. The results are in the frequency range of [1 Hz, 1 kHz]. The blue squares are the benchmark simulation results, the red stars are the discrete simulation data with the proposed IMU, and the black line is a continuous model identified from the simulated discrete data. The source output impedance can be modeled as a 10^{th}-order transfer function, and the load input impedance is estimated as a second-order transfer function. Taking the load converter input impedance $Z_{L\_SI\_SIMU}(s)$ as an example, the system identification result can be obtained as shown in (4. 5). From the Bode diagrams in Figure 4-8, it can be seen that, for both source converter impedance and load converter impedance, the measured discrete data and the system identification results match well with the benchmark simulations. It indicates that the results of perturbation injection generated by the proposed IMU are the same as the injection by the ideal current source and the system identification technique can estimate the impedance model correctly. Also, with more simulation points, the more accurate the system identification model would be.

$$Z_{L\_SI\_SIMU}(s) = \frac{0.005017s^2 + 182.1s - 2309}{s^2 - 17.86s + 64.46} \tag{4. 5}$$

4.3 Experimental Platform and Results

To further demonstrate the effectiveness of the proposed IMU, an experimental platform is constructed with the same dc system structure as in the simulation. Figure 4-9 shows the hardware setup in the lab. A three-phase MMC with 10 submodules in each arm is working as the source converter and 2L-VSC converts dc to ac which can be regarded as a constant power load (CPL). By connecting another 2L-VSC (similar design and power rating as CPL in SUT) in parallel with the MMC and controlling it to work as an IMU, small current perturbations can be injected into

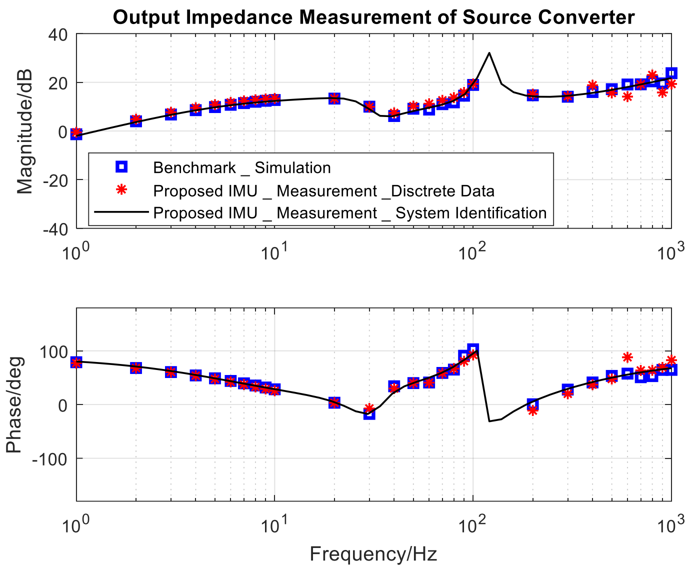

(a)

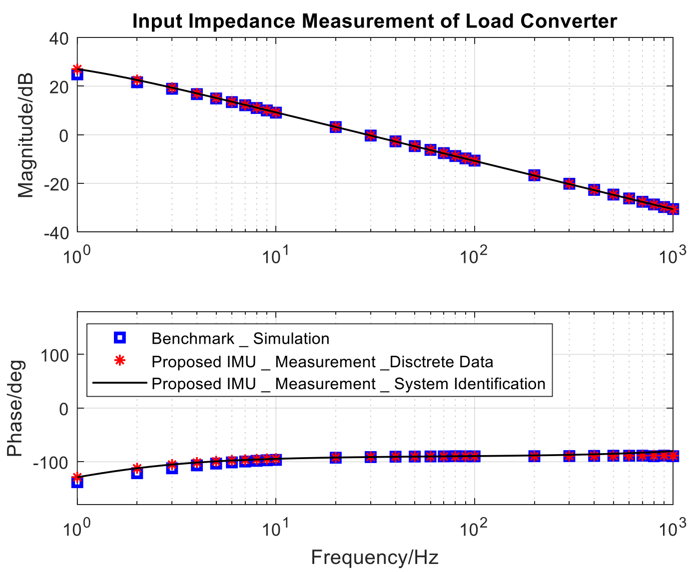

(b)

Figure 4-8. Simulation results of impedance measurement: (a) source output impedance and (b) load input impedance.

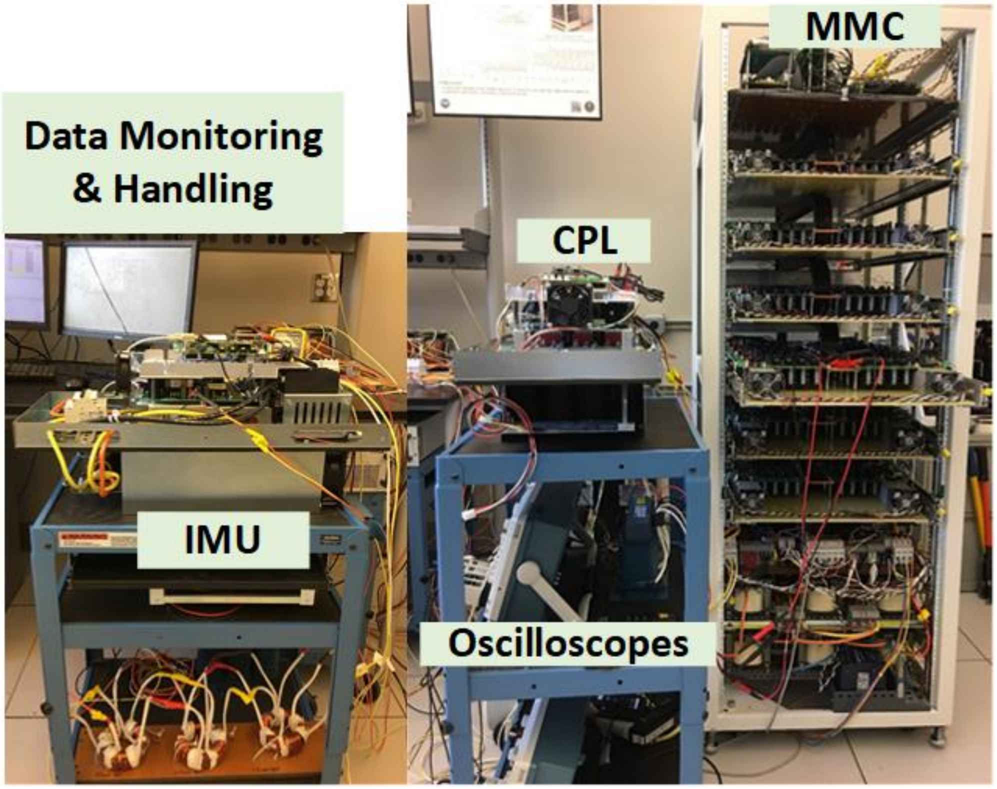

Figure 4-9. The hardware setup of converter impedance measurement using the proposed IMU.

the dc-link of the SUT. The three-phase ac voltage input of MMC and IMU is connected to the wall power. Tektronix oscilloscopes are used to measure and store the response waveforms under perturbations. Then the data are transmitted to personal computers (PCs) for monitoring and handling. By doing data processing offline, the MMC output impedance and CPL input impedance models can then be estimated.

A. Practical Considerations

Unlike the conceptual design, there will be some practical issues when doing hardware tests, such as circulating current, control delay effects, and operation sequence. These practical considerations will be discussed as follows.

1) Elimination of circulating currents

There are different types of circulating currents in the common-ac and common-dc parallel structure which will affect the impedance measurement results. And there are also some solutions by adding extra control blocks or some hardware to suppress these circulating currents as introduced in [181-183]. In this test platform, circulating current among the paralleled structure is suppressed by adding a three-phase transformer at the ac input side of the IMU for simplicity.

2) Minimization of control delay effects

There will be time delays in digital signal processing controllers (DSP). To eliminate the control delay effects, the controller structure needs to be designed efficiently to minimize the time delay. In addition, some delay compensation methods (e.g., linear predictor, first-order-filter compensation, or shifting sampling instant) can also be implemented in the control loop as introduced in [184]. In this study, a first-order filter (FOF) compensation is adopted in the control loop.

3) Design of operation sequence

For such a three-converter system, an appropriate operation sequence is also important. If not starting up or shutting down properly, there may be a huge inrush current which may cause a trip or even damage the whole system, especially under high voltage and high-power conditions. The key to the start-up and shutdown process is to minimize the voltage difference. Therefore, the recommended start-up and shut-down sequences are shown below.

a. Start-up sequence:

(1) Pre-charge source side MMC submodules capacitors and dc bus capacitors (If the source converter is also a 2L-VSC, only the dc bus capacitor needs to be pre-charged).

(2) Turn on the ac voltage source.

(3) Enable source-side converter control to regulate dc bus voltage with no load condition.

(4) Enable load converter control.

(5) Enable IMU control to start injecting perturbation signals.

b. Shut-down sequence:

(1) Disable IMU control.

(2) Disable load converter control.

(3) Disable source-side control.

(4) Shutdown ac voltage source.

B. Experimental Results

Considering all the practical issues in the hardware platform, the experimental results can then be examined. First, the perturbation signals generated by the proposed IMU are monitored. Following the instructions given through the LabVIEW interface with the frequency range defined from f_{min} to f_{max}, the perturbation current waveforms can be measured. For example, a 1 Hz small perturbation current i_p is injected into the dc-link of the SUT which is shown as the green waveforms in Figure 4-10. The blue waveform shows the line-to-line voltage v_{ab} of the IMU, and the magenta waveform is the IMU dc terminal voltage v_t. As seen from the waveforms, 4 seconds of perturbations are injected into the SUT to have 4 periods of response data so that FFT calculation accuracy can be guaranteed.

With the proper perturbation signals over the desired frequency range (f_1, f_2, ..., f_N), the waveforms under different perturbations can be obtained. Then with data processing technology, the source and load impedances can be acquired.

Figure 4-11 shows the Bode diagram of the measured results, where Figure 4-11 (a) is for the source converter output impedance and Figure 4-11 (b) is for the load converter input impedance. The blue squares are the benchmark simulation results as introduced in Section 4.2, the magenta circles are the discrete measured data with the proposed IMU, and the light green line is a continuous model identified from the measured discrete data. The estimated results from the measured data of the source impedance are also a 10th-order non-parametric model and the load converter impedance from the measurement data is also a 2nd-order model which is shown in (4. 6) as an example. From the Bode diagrams, it can be seen that the measured results (both the measured discrete data and estimated transfer functions by system identification) by the proposed IMU agree well with the simulation results with the benchmark simulation. Therefore, it can be concluded that the proposed IMU can be used to measure converter dc impedance correctly.

$$Z_{L\_SI\_MEAS}(s) = \frac{0.02989s^2 + 189.1s + 838}{s^2 - 2.565s - 27.6} \tag{4. 6}$$

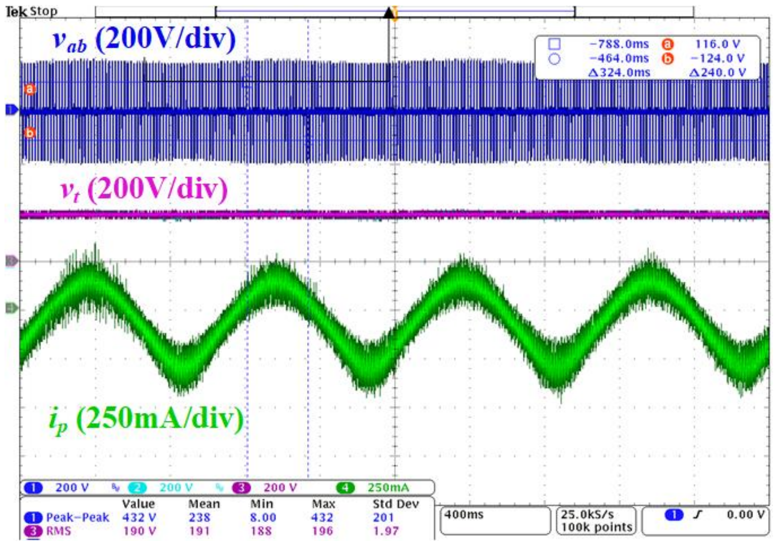

Figure 4-10. Measurement of current perturbation injection at f_p = 1 Hz.

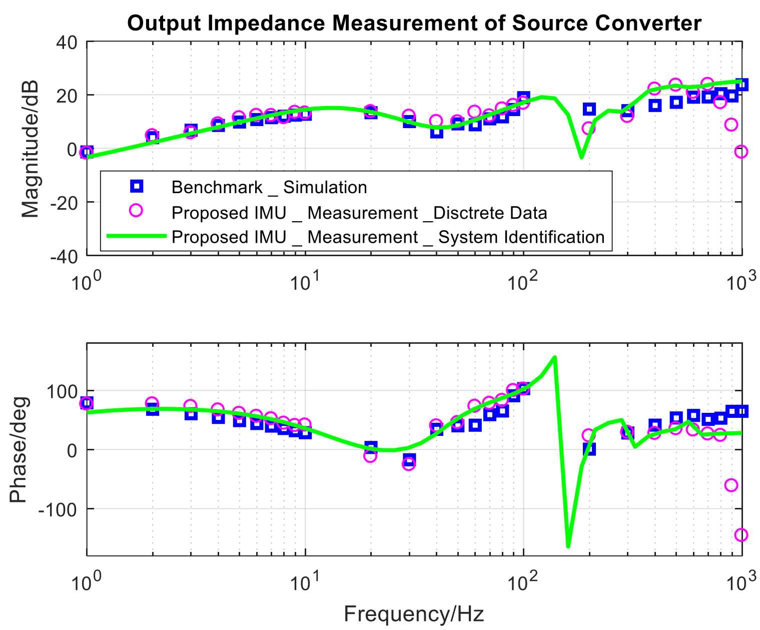

(a)

Figure 4-11. Experimental results of impedance measurement: (a) source output impedance and (b) load input impedance.

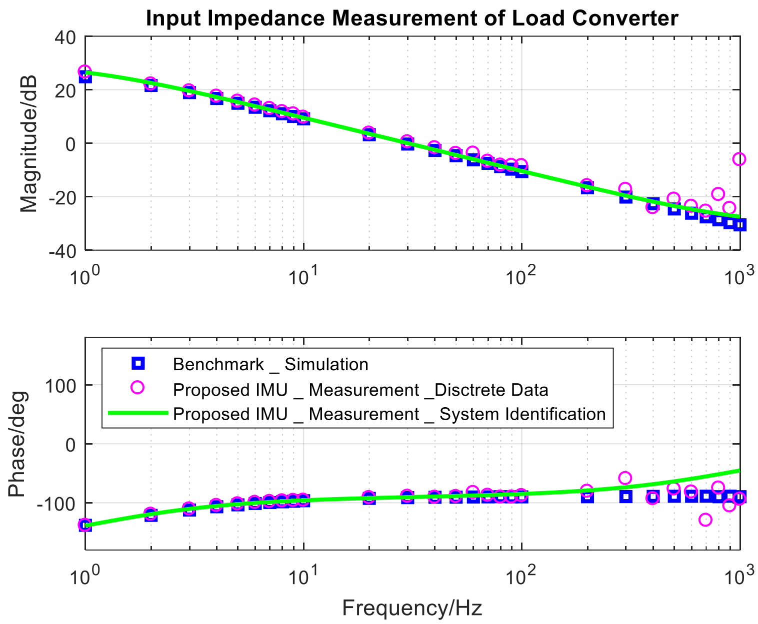

(b)

Figure 4-11. (continued).

4.4 Conclusions

In this chapter, a practical and easy-to-use dc impedance measurement unit based on a 2L-VSC for the dc terminal of PEC-rich power systems is proposed. The impedance measurement unit is controlled to generate small current perturbations on the dc bus of the system under test. The terminal voltage and current response waveforms under the perturbations are measured and stored by oscilloscopes. Data processing, including Fast Fourier Transform and System Identification, is then conducted in MATLAB with the measured data to obtain non-parametric models of converter dc impedances for system stability analysis. This method can also be extended to control other types of ac/dc converters to be the IMU in the system.

Chapter 5. Linear Control Design of Grid-Forming Inverters to Enhance System Small-Signal Stability

In this chapter, the impact of the existing passivity-based control of grid-forming inverters on system stability is investigated. It is found that to design the converter to be passive at the high-frequency (HF) region for fast-interaction stability issues, both a voltage feedforward control block (H_v) and a virtual impedance control block (Z_v) need to be added to the converter. However, it is also found that the low-frequency (LF) slow-interaction stability will be affected by the added Z_v block. Two solutions are then proposed accordingly. One is that instead of using the conventional passivity-based control method, a harmonic-detection-based adaptive stability enhancement control is adopted without the use of Z_v. The other is to use angle droop control to compensate for the negative effect of Z_v on the LF behaviors of converters.

Note that the controller for GFMs in Chapters 5, 6 and 7 are all designed based on the assumption that the dc voltage is ideal and there are no limits (e.g., power limits, current limits, etc.) on the inverter capacity. If the dc side voltage is nonideal, the dc dynamics might be coupled to the ac terminal and affect system stability, especially the low-frequency stability performance. And if the capacity limits of the inverter are considered, the controller design and expected control performance might need to be modified accordingly. In this dissertation, the focus is on the theory development and intrinsic natural response of the proposed control approaches, these assumptions can be further considered to make the proposed approaches more realistic in the future.

5.1 Introduction and Background

Different types of voltage-controlled PECs, which are also termed grid-forming inverters (GFMs), have been developed to generate system frequency and voltage autonomously, including droop control, virtual synchronous control, virtual oscillator control, etc. [120, 185-187]. Among them, the most well-developed grid-forming approach is droop control, which was first proposed in the 1990s [188]. It enables multiple GFMs to share and deliver desired active and reactive power into the system through local control in a stable manner. A typical droop control includes an active power-frequency (*P*-*f*) droop and a reactive power-voltage (*Q*-*v*) droop. The general circuit diagram of the conventional droop-control-based GFM is shown in Figure 2-13 [30, 120, 186, 189]. The outer power loop is to provide a well-defined voltage reference with proper amplitude and phase angle. Additionally, the inner voltage-current control loops are designed to regulate the output voltage, provide damping for the *LC* resonance, and limit the converter overcurrent. These control blocks can be implemented in either $\alpha\beta$ or dq frames. The controllers used in this study are implemented in $\alpha\beta$ frame.

To study the dynamic characteristics of droop-control-based GFMs and their impacts on system stability, both impedance-based Nyquist stability criterion and passivity-based stability analysis approaches have been adopted in the literature. Generally speaking, the impacts of droop-controlled GFMs on system stability can be roughly categorized into two types: slow-interaction grid-synchronization stability (in the low-frequency range near fundamental frequency) and fast-interaction harmonic stability (in the high-frequency range about several hundred Hz to several kHz). For the analysis of system synchronization stability, the Nyquist stability criterion with a full-order complex-value-based output impedance as shown in (5. 1) has been used [43, 54], where $\boldsymbol{G_{ref}}$ is the output voltage to reference voltage, $\boldsymbol{Z_{ref}}$ is the output current to reference voltage, $\boldsymbol{Z_o}$

is the transfer function considering the inner voltage and current loops, and $\boldsymbol{G_{vv}}$ is the transfer function matrix from voltage reference to output.

$$\boldsymbol{Z_{o\_GFM}}(s) = (\boldsymbol{I} + \boldsymbol{G_{vv}}\boldsymbol{G_{ref}})^{-1}(\boldsymbol{Z_o} + \boldsymbol{G_{vv}}\boldsymbol{Z_{ref}}) \tag{5. 1}$$

GFMs tend to induce sub-synchronous oscillations (SSO) under strong grid conditions because the smaller the grid impedance is, the larger damping will be needed, which means that a smaller *p-f* gain *m* is allowed. Hence, to ensure stable operation of systems in the low-frequency range, the droop gains (*m* and *n*) in the outer power loop should be designed according to the grid conditions. In this chapter, the droop gains are assumed to be well designed for system LF SSO stability. For the analysis of system harmonic instability issues, the PBSC has been used to identify the root causes of the possible instability issues. Since the high-frequency harmonic instabilities are investigated here, the LF dynamic behaviors can be assumed to be well designed and ignored. Therefore, (5. 1) can be further simplified as (5. 2). Also, due to the identical dynamics in the α and β axes, the impedance model can be represented by a single-input-single-output model $Z_{ov}(s)$, where, G_i is the current controller, G_v is the voltage controller, and G_d is control delay.

$$Z_{ov}(s) = \frac{sL + G_i G_d}{LCs^2 + G_i G_d Cs + G_v G_i G_d + 1} \tag{5. 2}$$

As long as the simplified $Z_{ov}(s)$ can represent the same dynamics as $\boldsymbol{Z_{o\_GFM}}(s)$ in the high-frequency region, it can then be used for the system harmonic stabilization design since it is more design-oriented. Therefore, the linearized PBSC is examined on impedance models in (5. 1) and (5. 2), separately. Figure 5-1 shows the results of the minimum eigenvalue λ_{min} derived from $\boldsymbol{Z_{o\_GFM}}(s)$ and $phase\{Z_{ov}(j\omega)\}$ where the impedance models are derived based on the circuit parameters as listed in Table 5-1. Since the LF dynamics (around the fundamental frequency 60

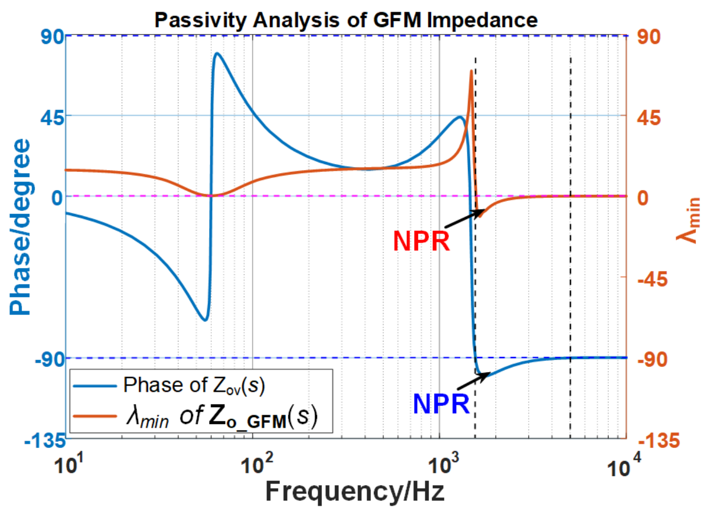

Figure 5-1. Analysis of GFMs with the full-order model $Z_{o\_GFM}(s)$ and the simplified model $Z_{ov}(s)$ with linearized PBSC.

Table 5-1. Circuit and control parameters of GFMs in the analysis model.

Variables	**Value**	**Variables**	**Value**
GFM voltage RMS value V_o	50 V	Fundamental frequency f_0	60 Hz
Dc voltage V_{dc}	130 V	Switching frequency f_{sw}	10 kHz
LC filter capacitance L, C	2.4 mH,10 μF	Power references P_0, Q_0	600 W, 0 Var
Control delay T_d	$1.5/f_{sw}$	Current control G_i	8
Voltage control G_v	$0.01+\dfrac{50s}{s^2+7.5398s+142122}$		

Hz) have been assumed to be stable first, only the characteristics at HF ranges are checked. From Figure 5-1, it can be observed that the non-passive region (NPR) indicated by the phase angle of $Z_{ov}(s)$ is the same as by λ_{min}, which, in a way, validates one claim that the high-frequency dynamics will not be affected by the outer power control loops, so $Z_{ov}(s)$ is adopted for the study of HF dynamics.

As indicated by the impedance model, the converter control delays will cause an NPR in the output impedance at high frequencies, within which the negative damping will be introduced to the current control and destabilize the system. Accordingly, passivity-based control solutions have been proposed, such as adding both virtual impedance control function Z_v and the voltage feedforward control function H_v to the inner voltage-current loop as shown in Figure 5-2 [54]. With these two blocks Z_v and H_v, the output impedance of GFMs is modified to be $Z_{ov\_c}(s)$ as shown in (5. 3), where Z_{ol} is the open-loop output impedance, G_{ui}, G_{uv}, and G_{ii} are the transfer functions from converter-side voltage to inductor current, converter-side voltage to output voltage, and grid-side current to inductor current separately. The Bode diagrams of the output impedance with and without the passivity compensation blocks (Z_v and H_v) are given in Figure 5-3. It is seen that the HF-NPR below Nyquist frequency can be removed with the help of the Z_v and H_v compensation blocks. Therefore, the system harmonic instability issues caused by converter control delays can be eliminated regardless of the strength of the grid impedance.

Note that both Z_v and H_v need to be added to achieve the passivation of the GFMs up to the Nyquist frequency. If with H_v only, the system stability margin could be improved, but system harmonic instability issues cannot be solved thoroughly since the inverter still has some non-passive regions. Once the grid condition changes, harmonic instability might still happen. One can see more case studies later in Section 5.2.

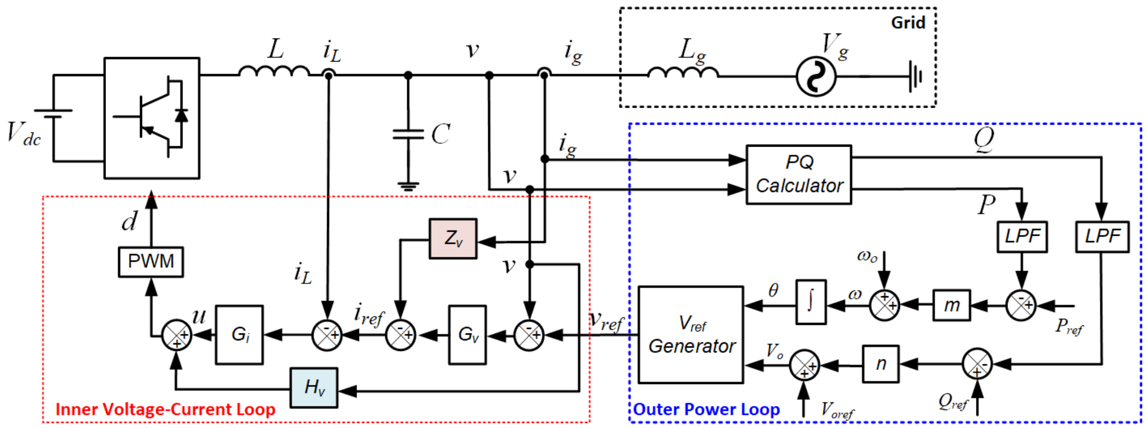

Figure 5-2. Circuit diagrams of droop-control-based GFMs with passivity-based control blocks Z_v and H_v.

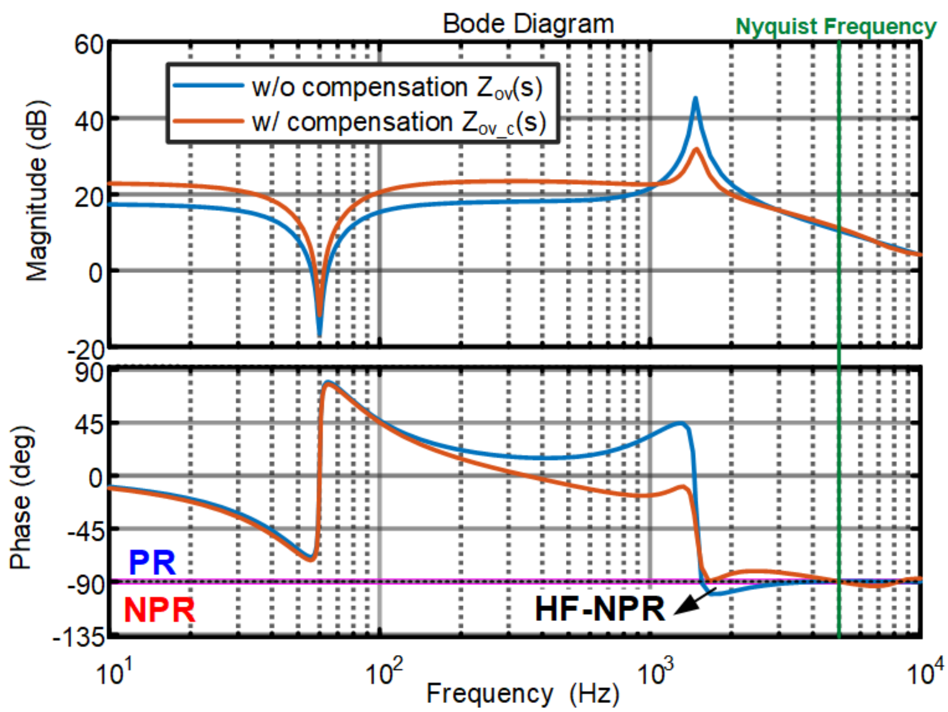

Figure 5-3. Bode diagrams of impedance model of GFMs w/o and w/ passivity compensation blocks (Z_v and H_v).

$$Z_{ov\_c}(s) = \frac{Z_{ol}(1 + G_{ui}G_iG_d) + G_{uv}G_dG_i(G_{ii} + Z_v)}{1 + G_{ui}G_iG_d + G_{uv}G_d(G_vG_i - H_v)} \tag{5. 3}$$

5.2 Negative Impacts of Z_v Control on System LF Stability

A. Simulation Investigation

To see the negative impacts of the Z_v block on system synchronization stability, a simulation testing platform is built in MATLAB/Simulink following the circuit structure as shown in Figure 5-2 with the parameters listed in Table 5-2.

In these cases, the grid inductor L_g ranges from 8 mH to 2 mH (i.e., SCR from 6 to 24) to emulate weak grid and strong grid conditions. The *p*-*f* droop gain *m* and *Q*-*v* droop gain *n* are then designed respectively based on the grid conditions using the Nyquist stability criterion assuming the converter control delay is ideally small enough, i.e., T_d = 0.5T_{sw}. This guarantees that under ideal situations, there are no HF harmonics and no LF SSO. Then, a larger control delay (1.5T_{sw}), which is also a typical and practical value in most cases, is taken into consideration.

Simulations with different control structures (CI: w/o Z_v and w/o H_v, CII: w/o Z_v and w/ H_v, CIII: w/ Z_v and w/ H_v) are investigated. For example, when SCR = 8, the frequency droop gain is designed as 2% ω_0/P_0 and the voltage droop gain is 10% V_0/P_0 (for simplicity, only the ratio will be given in the following text), and the simulation results show that with CI, there will be high-frequency harmonic instability issues with the harmonics component to be around 1.5 kHz as shown in Figure 5-4. If there is no Z_v, but H_v is added, that is with CII, the system is stable as shown in Figure 5-5. While with CIII, high-frequency harmonics can be eliminated, but low-frequency SSO (57.6 Hz and 62.4 Hz) will be introduced into the system as shown in Figure 5-6.

Table 5-2. Circuit and control parameters of GFMs in simulations.

Variables	**Value**	**Variables**	**Value**
Grid voltage RMS value V_g	190 V	Fundamental frequency f_0	60 Hz
GFM voltage RMS value V_o	190 V	Switching frequency f_{sw}	10 kHz
LC filter capacitance *L*, *C*	2 mH, 10 μF	Power references P_0, Q_0	2 kW, 0 Var
Grid impedance L_g (mH)	8 / 6 /4 / 2	Short circuit ratio SCR	6 / 8 /12 / 24
Control delay T_d	1.5/f_{sw}	Current control G_i	8
Voltage control G_v	$0.01+\frac{50s}{s^2+7.5398s+142122}$		

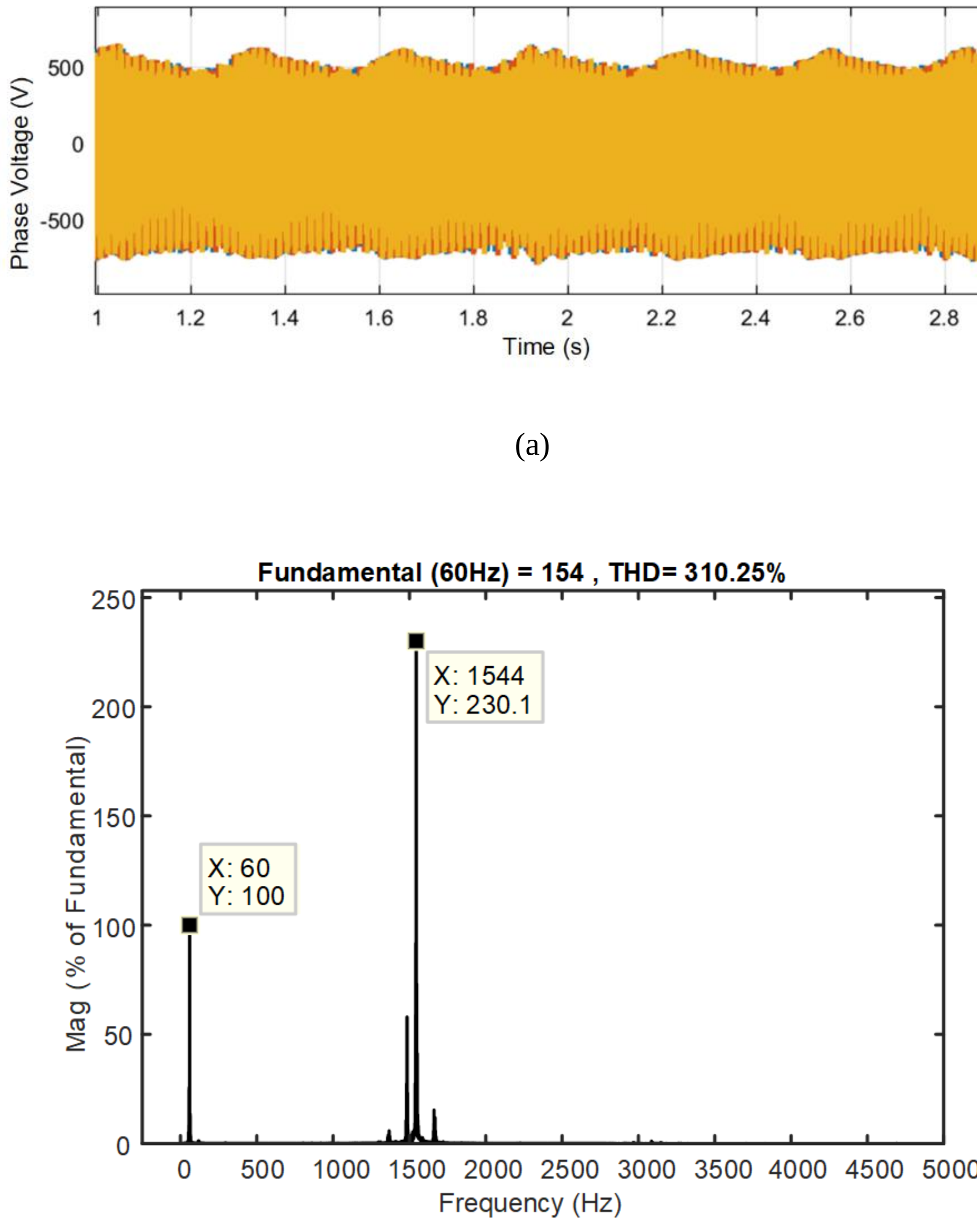

(b)

Figure 5-4. Harmonic instability issues with CI when SCR = 8 (m = 2% and n = 10%): (a) simulation waveforms of phase voltage and (b) FFT analysis of phase voltage.

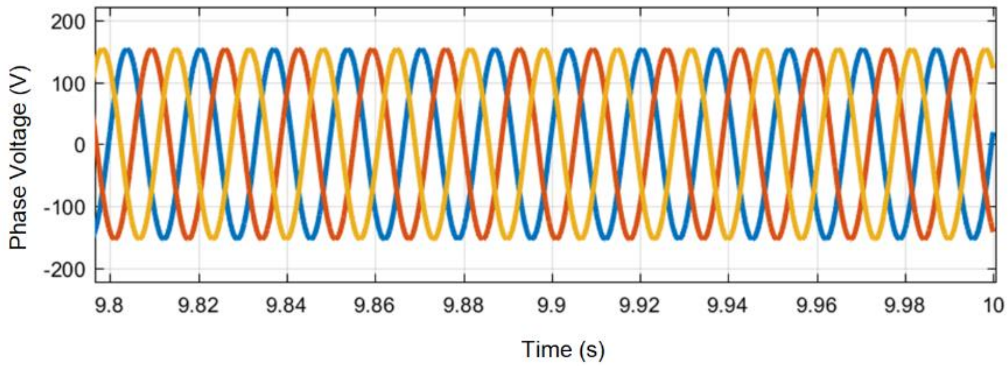

Figure 5-5. Simulation waveforms of phase voltage in a stable system with CII when SCR = 8 (*m* = 2% and *n* = 10%).

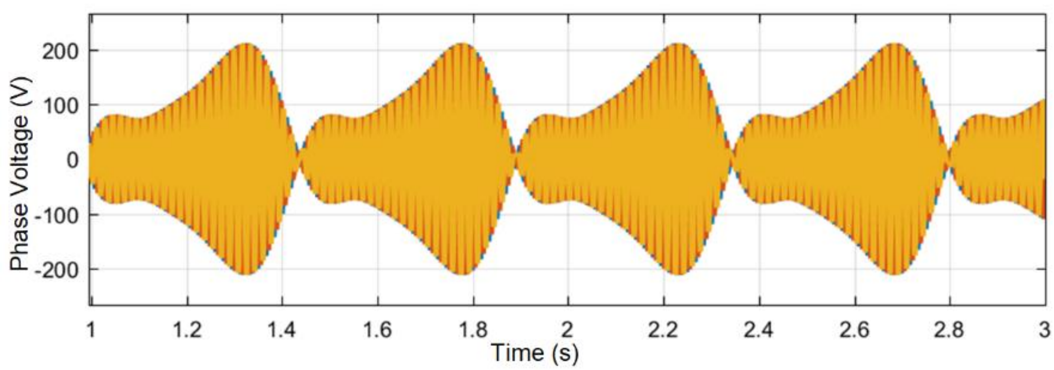

(a)

Figure 5-6. SSO issues with CIII when SCR = 8 (*m* = 2% and *n* = 10%): (a) simulation waveforms of phase voltage and (b) FFT analysis of phase voltage.

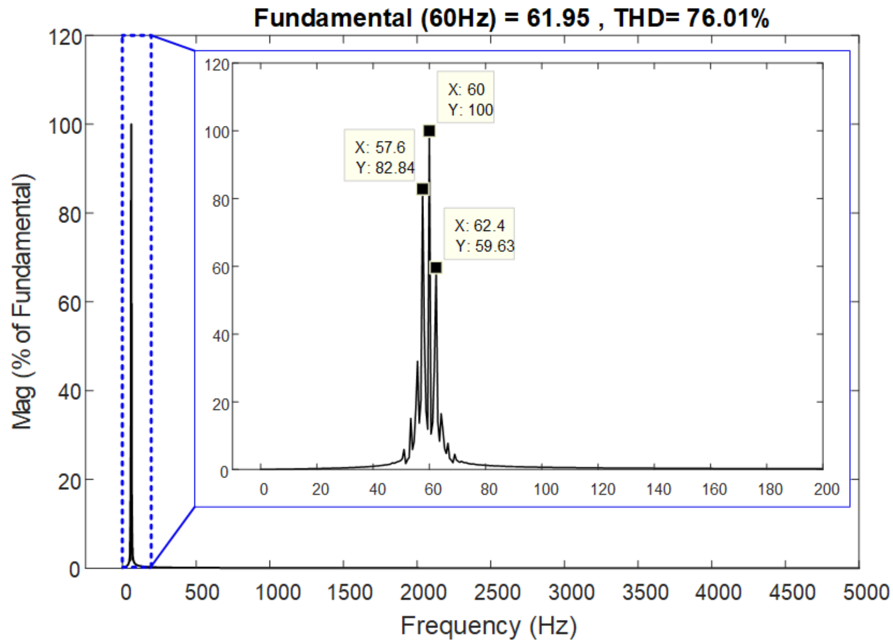

(b)

Figure 5-6. (continued).

More cases under different grid conditions are summarized in Table 5-3, where HF Harmonics refer to the unstable phenomena similar to that in Figure 5-4 and LF SSO refers to instabilities similar to that in Figure 5-6. Several findings can be summarized in Table 5-3. First, it is seen that without the passivity compensation blocks (CI: w/o Z_v and w/o H_v), the system will have high-frequency harmonic instability issues when SCR is large (SCR = 8, 12, and 24). Second, with H_v only (CII), system stability can be improved (stable under SCR = 8 or 12), but it still has harmonic instability issues when SCR = 24. Third, with both Z_v and H_v compensation blocks (CIII), there will be no HF harmonic issues in the system; however, LF SSO will be introduced instead. Therefore, it can be concluded that the Z_v compensation block can improve system high-frequency stability, but it may negatively impact system low-frequency resonance as well.

B. Theoretical Analysis

To analyze the fundamental mechanism of Z_v impacts on system synchronization stability, an equivalent virtual impedance Z_{veq} is obtained first by moving the Z_v block to the input side of the voltage controller G_v as shown in Figure 5-7, which can be expressed as in (5. 4) with an equivalent frequency-dependent virtual resistance R_{veq} and a virtual reactance X_{veq}.

The values of the equivalent virtual impedance in this study are calculated as shown in Figure 5-8. It can be seen that the equivalent R_{veq} is large enough ($R_{veq} >> X_{veq}$) in both LF and HF ranges to provide enough damping for the system, but near the fundamental frequency f_{fund} (shaded area in Figure 5-7), the R_{veq} is almost 0 which means there is no resistive damping provided for the system in this frequency range.

Then, assuming the inner voltage-current loop to be 1 since LF SSO is under investigation, the system equates to a grid-connected voltage source with Z_{veq} as shown in Figure 5-9. This equaivlent virtual impedance Z_{veq} will reduce the output voltage reference proportionally to the

Table 5-3. Simulation results under different grid conditions with different control structures.

Grid Conditions	**CI**	**CII**	**CIII**
SCR = 6 (m = 2% & n = 10%)	Stable	Stable	Stable
SCR = 8 (m = 2% & n = 10%)	HF Harmonics	Stable	LF SSO
SCR = 12(m = 0.5% & n = 2.5%)	HF Harmonics	Stable	LF SSO
SCR = 24 (m = 0.2% & n = 1%)	HF Harmonics	HF Harmonics	LF SSO

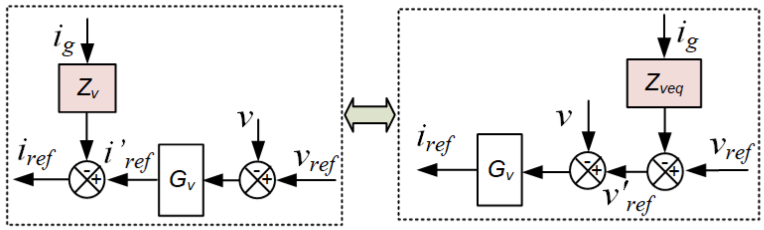

Figure 5-7. Equivalent virtual impedance in the control diagrams.

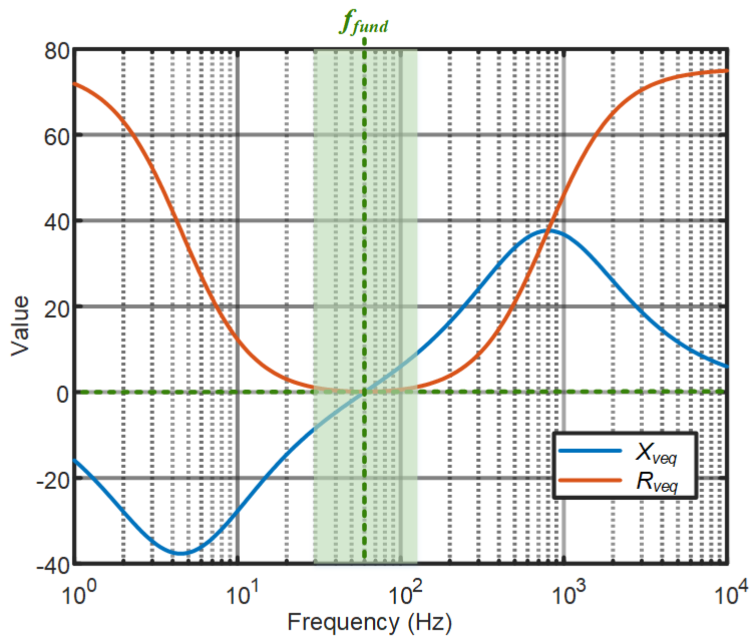

Figure 5-8. Frequency-dependent values of equivalent impedance.

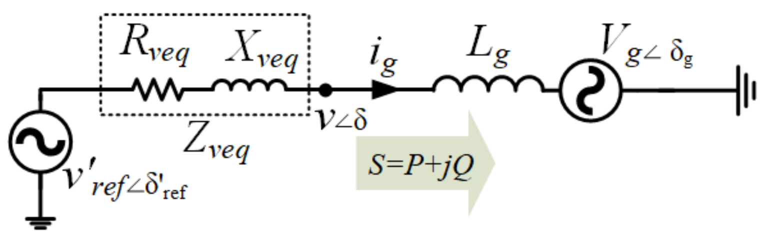

Figure 5-9. Equivalent virtual impedance in the entire system.

output current as shown in (5. 5). Accordingly, the power flow S can be calculated as (5. 6). Based on (5. 5) and (5. 6), the equations about magnitude and phase angle of the reference voltage v'_{ref} and output voltage v are obtained as (5. 7) and (5. 8) [190, 191].

$$Z_{veq}(\omega) = Z_v / G_v(j\omega) = R_{veq}(\omega) + jX_{veq}(\omega) \tag{5. 4}$$

$$V'_{ref} = V_{ref} - Z_{veq} i_g \tag{5. 5}$$

$$S = P + jQ = v\angle\delta\left(\frac{v'_{ref}\angle\delta'_{ref} - v\angle\delta}{R_{veq} + jX_{veq}}\right)^* \tag{5. 6}$$

$$\Delta v = v'_{ref} - v \cong \frac{R_{veq}P + X_{veq}Q}{v} \tag{5. 7}$$

$$\delta_v = \delta'_{ref} - \delta \cong \frac{X_{veq}P - R_{veq}Q}{v'_{ref}v} \tag{5. 8}$$

Assume v'_{ref} and v are equal to V_o for simplicity, which is true for most conditions since the voltage magnitude should be limited within a narrow range. Besides, it is seen from Figure 5-8 that the calculated value of R_{veq} is almost 0 around f_{fund}. Equations (5. 9) and (5. 10) can then be obtained, where, $m_e(f) = \frac{X_{veq}(f)}{V_o^2}$ and $n_e(f) = \frac{X_{veq}(f)}{V_o}$.

In the P-f control loop, the virtual impedance control Z_v adds an equivalent power-angle droop gain m_e, and in the Q-v control loop, Z_v adds an equivalent voltage droop gain n_e. The Q-v loop dynamics expressed in (5. 10) can be ignored as long as $n + n_e$ is larger than 0 since it has little impact on system stability [114, 150]. The Z_v-induced m_e as expressed in (5. 9) turns out to be the cause of the LF SSO issues in the system as analyzed below.

First, the small-signal stability analysis on the active power-frequency loop is conducted with the linearized model derived in (5. 11), which is based on the equivalent circuit as shown in Figure 5-10 [190, 191], where the cut-off frequency of the low-pass filter ω_{LPF} is 2π rad/s, $G = \partial P/\partial \delta_l$, $\delta_l = \delta - \delta_g$.

According to the characteristics equation of (5. 11), it can be concluded that the Z_v block does not cause any right-half-plane poles to affect system stability since all the eigenvalues locate in the LHP.

$$\omega \approx \omega_o - mP_{LPF} - m_e(f)\frac{dP}{dt} \tag{5. 9}$$

$$V_o \approx V_{ref} - nQ_{LPF} - n_e(f)Q \tag{5. 10}$$

$$\Delta P = \frac{G(s+\omega_{LPF})}{(1+m_eG)s^2 + \omega_{LPF}(1+m_eG)s + \omega_{LPF}mG}(\Delta\omega - \Delta\omega_g) \tag{5. 11}$$

Second, the analysis is extended to the transient stability of the system. The swing equation which describes the behaviors of the active power loop can be derived as shown in (5. 12), where H is the inertia time constant as shown in (5. 13), and D is the damping coefficient as shown in (5. 14) [150].

$$H\ddot{\delta} = P_{ref} - P_{max}sin\delta - D\dot{\delta} \tag{5. 12}$$

where,

$$H = \frac{1 + m_eP_{max}}{\omega_{LPF}m} \tag{5. 13}$$

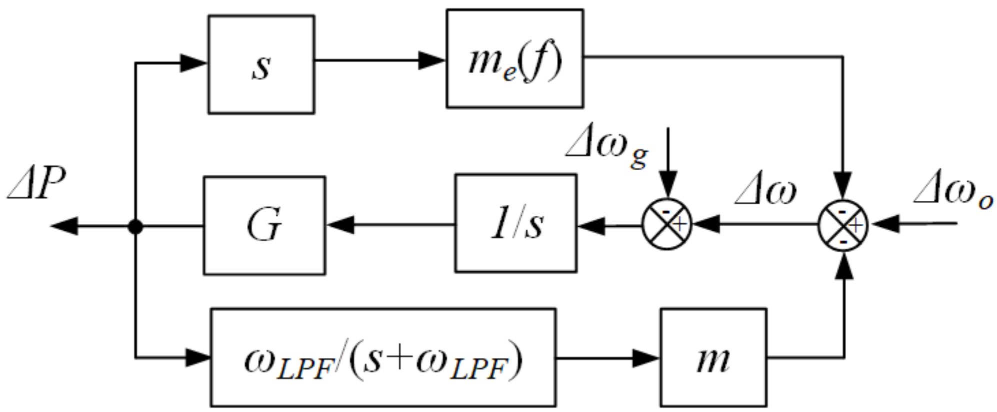

Figure 5-10. Small-signal model of active power loop considering virtual impedance impact.

$$D = \frac{1 + m_e P_{max}}{m} \tag{5. 14}$$

$$P_{max} = \frac{V_o^2}{X_g} \tag{5. 15}$$

It can be observed that the equivalent m_e term will add m_eP_{max} on both system inertia and damping. As seen from Figure 5-8, X_{veq} is a negative value below f_{fund} which means m_e will also be negative below f_{fund}. Though it is difficult to quantify the damping and inertia value and to draw the phase portrait for the analysis of system stability since m_e is a variable frequency-dependent value, the negative impacts can still be observed in Figure 5-11, where H_0 and D_0 are the original system inertia and damping without Z_v, and H and D are the ones considering Z_v impacts. Hence, it can be inferred that the system stability will be affected since a system with less damping is more likely to have LF SSO issues as shown in Table 5-3. Finally, it can be concluded that the virtual impedance control block, which is intended to eliminate the system harmonic instability issues, might reduce the system damping near f_{fund} and cause LF SSO issues in the system.

Although the analysis method introduced here is only valid near f_{fund} (30 Hz to 100 Hz) since R_{veq} can only be assumed to be 0 in this region, it is already good enough for the synchronization stability analysis. In addition, in either the low-frequency or high-frequency ranges, R_{veq} would be large enough to provide damping for the system and can help to maintain system stability.

5.3 Method I: Proposed Online Harmonic Detection-Based Stabilization Method

To avoid the negative impact of the Z_v block on system LF stability, a direct solution is to avoid using the Z_v block. Then HF stability of the system is achieved with an online harmonic detection-based system stabilization function.

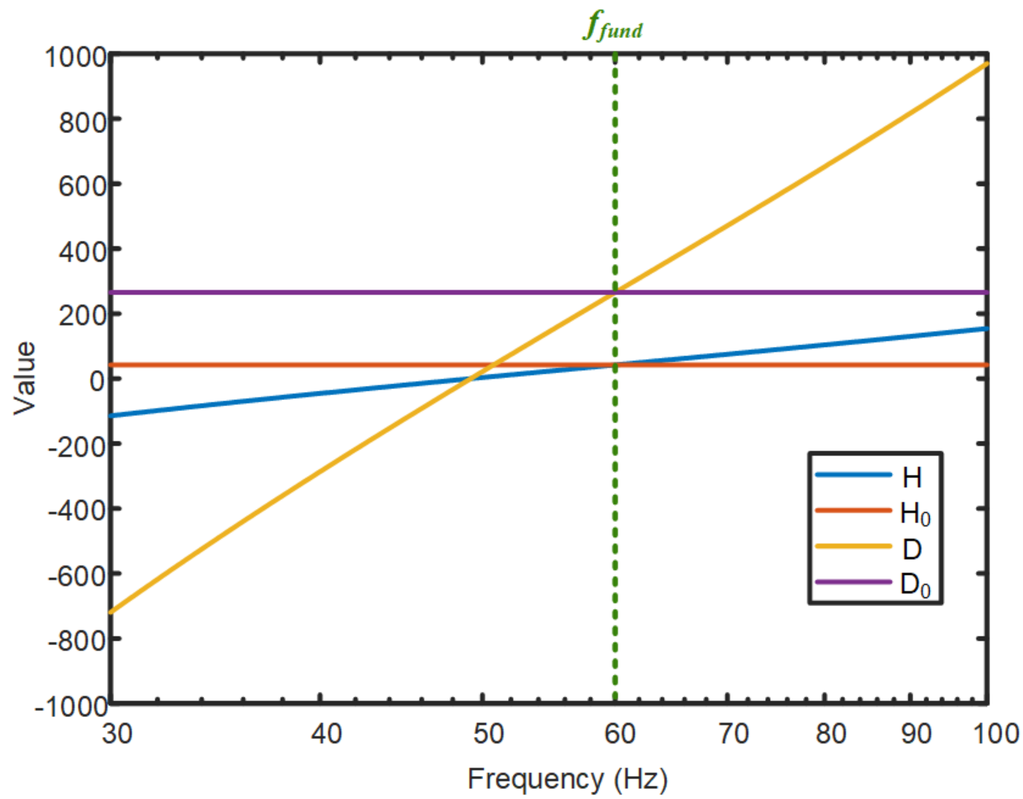

Figure 5-11. Impacts of Z_v on system inertia and damping constant.

5.3.1 Proposed System Stabilization Function

As indicated by the impedance model in (5. 2), there is an HF-NPR in GFMs, within which, there is a possibility that the harmonic instability might occur under some grid conditions. Therefore, a system stabilization function (SSF) block is needed to compensate for this NPR ifthere are harmonic stability issues. The expected SSF should be able to adaptively adjust the controller to eliminate the harmonic instability phenomena without affecting the predefined system in the low-frequency region. Specifically, when connecting the GFM into an existing grid, if the system is stable, no action will be needed; but if there are harmonic instability issues, the system stabilization function embedded in the controller of GFMs should start to passivate the converter and modify the impedance characteristics at the harmonic resonant frequency.

Accordingly, the system stabilization function of GFMs is proposed as shown in Figure 5-12, where an adaptive voltage feedforward gain K_{FF} that is calculated based on the online harmonic detection technique is added to the inner voltage and current loops. In the proposed SSF block, an online harmonic detection module is implemented with a Fast Fourier Transform (FFT) block to analyze the harmonic component in the output voltage of the GFMs. If there is no harmonic or the magnitude of the harmonic component V_{res} is smaller than the threshold voltage V_{th}, then the K_{FF} block will be disabled. If there are harmonics with V_{res} larger than V_{th}, the K_{FF} block will be enabled and calculated with the harmonic resonant frequency ω_{res} based on (5. 16), where K_{pi} or K_{pv} is the current or voltage controller proportional gain, K_{rv} is the voltage controller resonance gain, T_d is converter control delay, and K_{mar} is the reserved margin.

$$K_{FF} = K_{mar}\left(K_{pi}K_{pv} + \frac{K_{pi}(1 - K_{rv}L)\cos(\omega_{res}T_d)}{-\omega_{res}L\sin(\omega_{res}T_d) + K_{pi}}\right) \tag{5. 16}$$

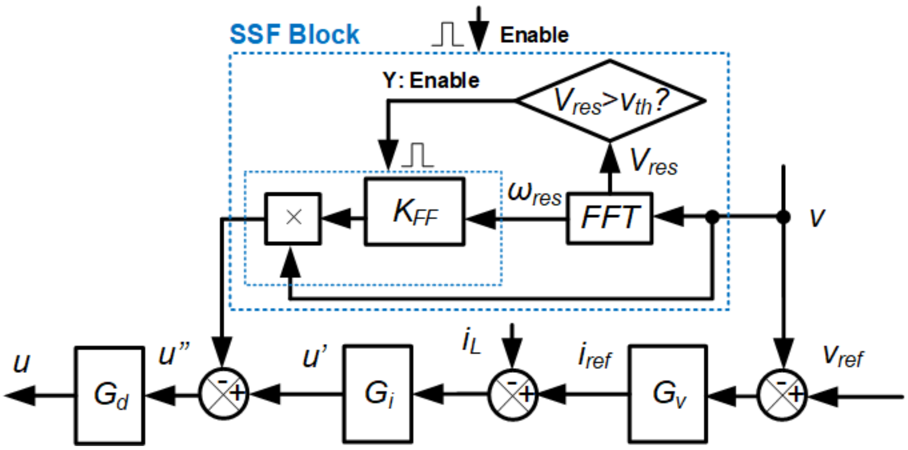

Figure 5-12. Proposed system stabilization function of GFMs.

The mechanism of the SSF block can be explained through the impedance vector in a complex plane at the harmonic resonant frequency ω_{res} as shown in Figure 5-13. It is seen that without K_{FF} compensation, Z_{ov} is in the non-passive region, and when K_{FF} is added, Z_{ov} can be improved to be passive at this resonant frequency while keeping the same magnitude. Also, since K_{FF} is onlyeffective in the high-frequency region of the inverter impedance model, it will not affect the pre-defined low-frequency dynamics.

5.3.2 Simulation and Experimental Validations

A. Simulation Verification

A GFM connecting to a bulk grid with the parameters listed in Table 5-1 is built in MATLAB/Simulink. It is an unstable setup with harmonic instability issue first, then the proposed SSF control block is implemented. The system harmonic resonant frequency is identified by the FFT block embedded in the controller to be 1.45 kHz (with 10 Hz as the base frequency) as shown in Figure 5-14. Then, the SSF block is enabled with the K_{FF} calculated under this resonant frequency. The whole process can be seen in Figure 5-15. At t = 0.1 s, the GFM is connected to the grid, and due to the impedance interaction between the GFM and the grid, there are some harmonic instability issues. Then, at t = 0.5 s, the SSF control is enabled, and the output voltages of the GFM are converged and stabilized.

The simulation results can be further proved with the theoretical model. The impedance model with the proposed SSF can be checked by substituting the automatically calculated K_{FF} value into the $Z_{ov}(s)$. As shown in Figure 5-16, the converter becomes passive around the resonant frequency ω_{res}, and then the system is stabilized.

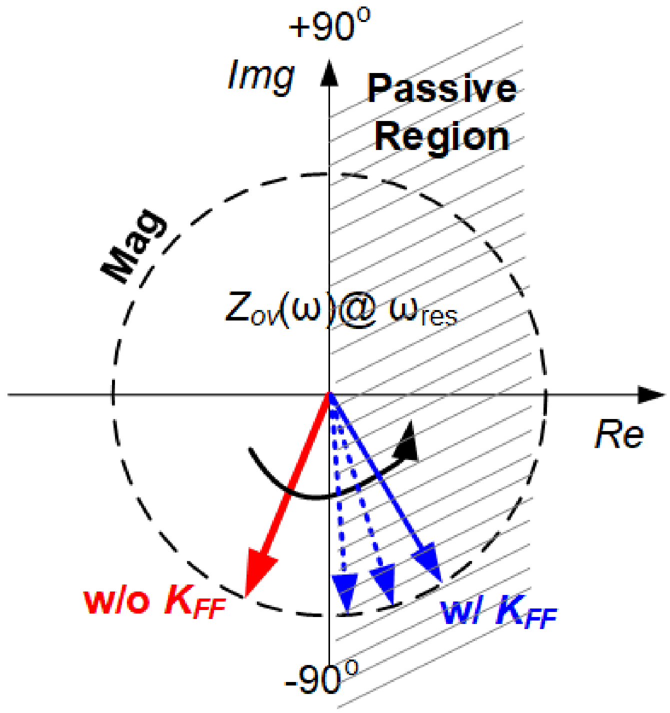

Figure 5-13. Z_{ov} in a complex plane with and without K_{FF}.

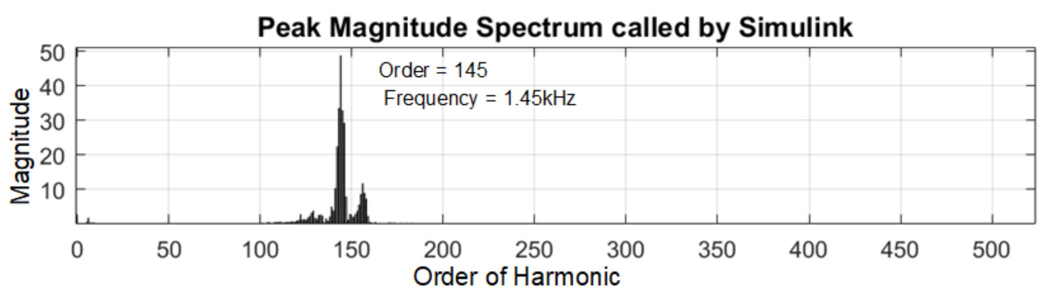

Figure 5-14. Peak magnitude spectrum called by Simulink.

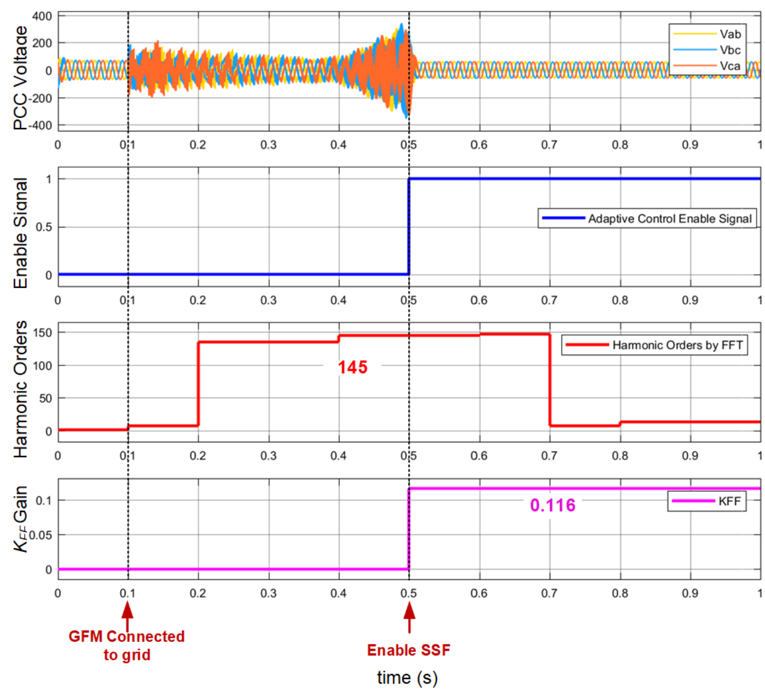

Figure 5-15. Output voltages of GFMs with the proposed SSF Method.

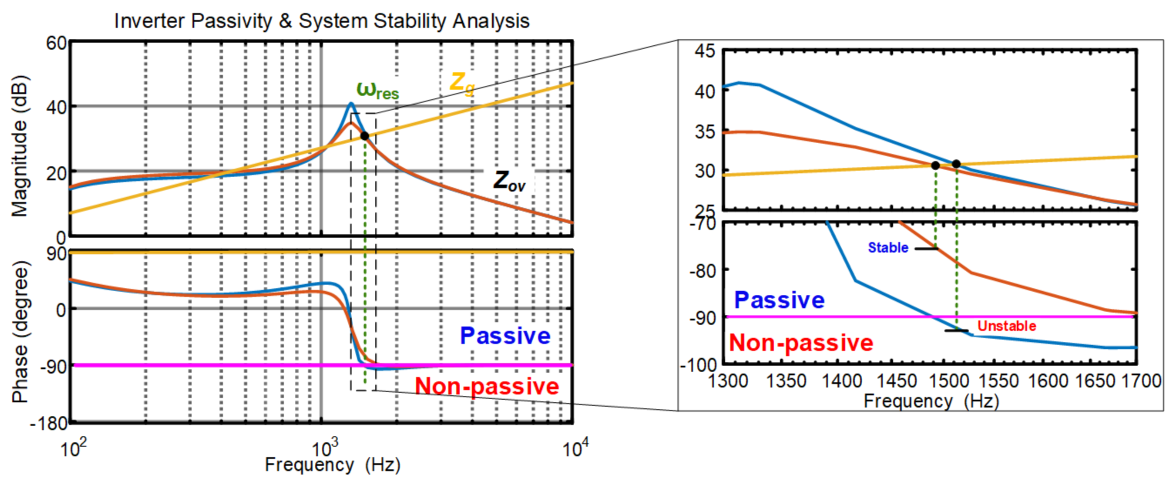

Figure 5-16. Analysis of Z_{ov} and system stability w/ and w/o SSF.

B. Experimental Verification

An experimental setup is also built as shown in Figure 5-17 for further verification. Two converters are connected, with one converter working as the grid emulator with open-loop control, and the other converter works as a GFM with the proposed SSF. The output filter of the GFM consists of 1.2 mH inductors and 10 μF capacitors, the grid-side impedance L_g = 4.8 mH, and the current control K_{pi} = 6.9. The rest of the parameters including system working conditions and voltage control parameters are the same as listed in Table 5-1. Also, when the external SSF is enabling signal is high, the SSF is disabled; when it is low, the SSF is enabled. From the testing results that are given in Figure 5-18, it can be concluded that when enabling the proposed adaptive control function, the high-frequency harmonic instability issues can be eliminated and the system stability can be enhanced.

5.4 Method II: Proposed Angle Droop Compensation Design

However, the proposed online harmonic-detection-based SSF allows harmonic instabilities to happen in the system. This may not be acceptable in some cases, where the Z_v block is unavoidable for the passivation of the impedance of GFMs. Therefore, an angle-droop design is proposed to compensate for the negative impact of Z_v in system LF regions.

5.4.1 Design Guidelines for Modified Outer Power Loop Considering Z_v Impacts

Based on the simulation studies and theoretical analysis above, a direct solution can be proposed to eliminate the negative damping impact of Z_v on active power droop control, that is adding corresponding droop compensation gains to compensate for the Z_v induced negative value of the equivalent angle droop gain $m_e(f)$ and voltage droop gain $n_e(f)$.

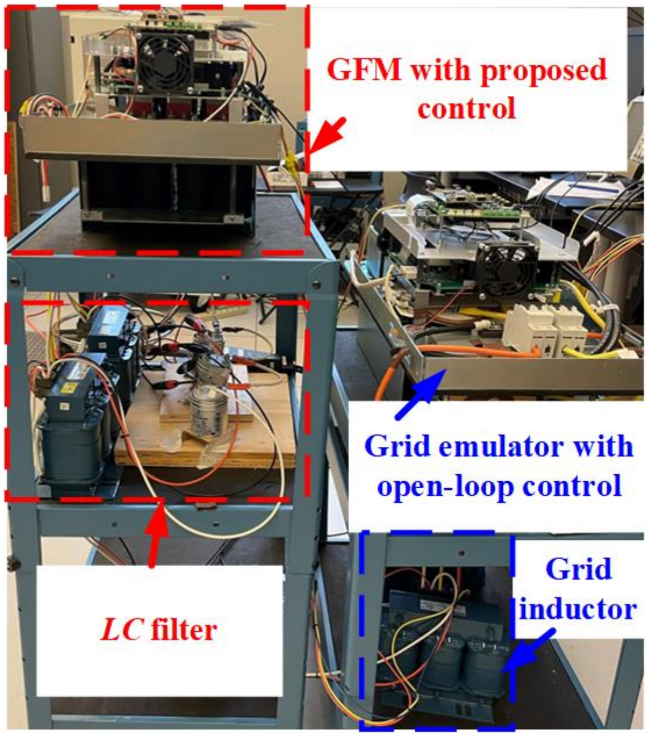

Figure 5-17. Experimental setup with proposed control methods.

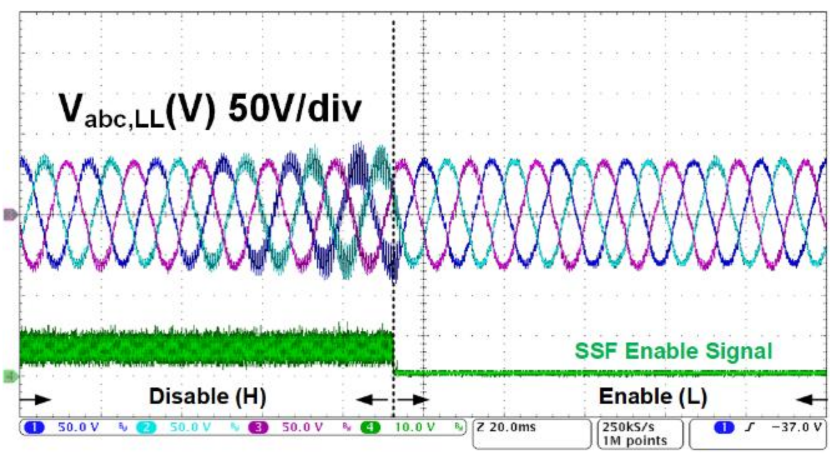

Figure 5-18. Experimental results with the proposed harmonic-detection-based system stabilization method.

Therefore, an angle droop gain k_1 (rad/W) is added to the outer active power loop, and a voltage droop gain k_2 (V/Var) is added to the reactive power droop loop as shown in Figure 5-19. This modified outer power loop (i.e., conventional droop plus angle droop) is not a new topology and has been proven to be able to improve the converter power-sharing capability [192].

But in this study, the modified droop controls are mainly designed for the consideration of the impacts of Z_v so that both LF SSO issues and harmonic instability issues can be eliminated. The design criteria for the droop gains k_1 and k_2 can be obtained as shown below.

To eliminate the low-frequency impacts caused by Z_v on the swing equation, the power-angle droop gains considering both k_1 and Z_v induced $m_e(f)$ should meet the criteria that is $m_e(f) + k_1 > 0$ (Criterion 1) to fully compensate for the negative damping impacts of Z_v within the studied frequency range. Note that like the analysis in (5. 11), adding k_1 will not introduce any RHP poles in the system from the aspects of system small-signal stability.

Based on Criteria 1, k_1 should be large enough so that it would be effective for the elimination of low-frequency resonance with good system dynamics. However, k_1 cannot be designed to be too large either to keep the passivity of the GFM at high frequency.

Based on the Bode plots shown in Figure 5-20, when k_1 is small (1.8×10^{-5} or 3×10^{-5}), the inverter output impedances stay unchanged compared with the baseline impedance when k_1 = 0. However, if increasing k_1 to be 7.5×10^{-5}, the inverter will show an HF-NPR as the phase value indicates.

Therefore, to maintain inverter passivity compensated by the Z_v block, R_{veq} should dominate the Z_{veq} characteristics at high frequencies, i.e., $R_{veq} >> X_{veq} + k_1 \times V_{nom}^2$ (Criteria 2), to avoid the impacts of k_1 on inverter passivity for system harmonic stability.

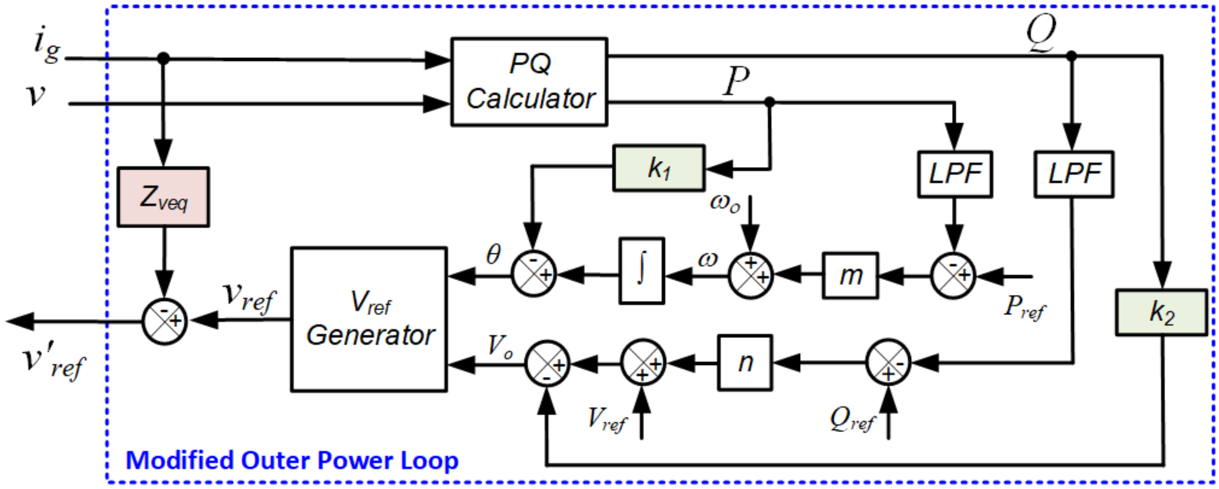

Figure 5-19. Control function blocks of the modified outer power loop with angle droop gain and compensated voltage gain.

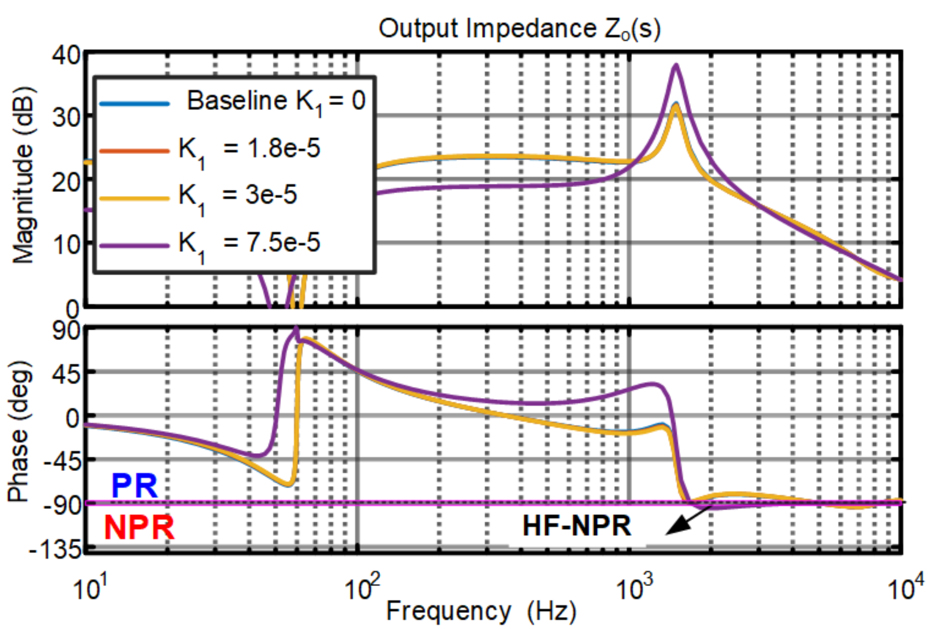

Figure 5-20. Passivity enhanced $Z_o(s)$ with different k_1.

Additionally, if considering the reactive power dynamics, the sum of the *Q-v* droop gains, including original gain n, Z_v induced $n_e(f)$, and k_2, should be larger than 0, i.e., $n + n_e + k_2 > 0$ (Criterion 3). As mentioned in Section 5.2, the active power droop is the dominant loop for system transition dynamics, therefore, k_1 is the key to system stability and k_2 is less important. For simplicity, k_2 can be designed as $V_{nom} \times k_1$ first and then checked with Criterion 3.

5.4.2 Simulation and Experimental Validations

A. Simulation Verification

1) System Stability Enhancement with Angle Droop Control

To eliminate the LF SSO of the cases studied in Table 5-3 with CIII, droop compensations are implemented at $t = 6$ s in the simulations. For SCR = 8, 12, and 24, k_1 is designed to be 6×10^{-5}. Figure 5-21 shows that all the LF SSO issues can then be eliminated when the angle droop compensation is enabled.

2) Impact of Different Angle Droop Gain Values on System Stability

Effects of the k_1 values on system performance have also been investigated under SCR = 8 as shown in Figure 5-22.

If k_1 is too small, the LF resonance will not be eliminated as in Figure 5-22(a). Within the proper design range, the system will be stabilized, and a larger k_1 will provide better dynamics as shown in Figure 5-22 (b) and Figure 5-22(c).

While if k_1 is too large, inverter passivity will be affected, and harmonic instability will happen as shown in the zoom-in view of Figure 5-22 (d).

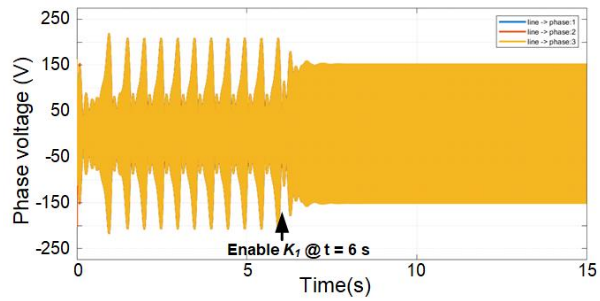

(a)

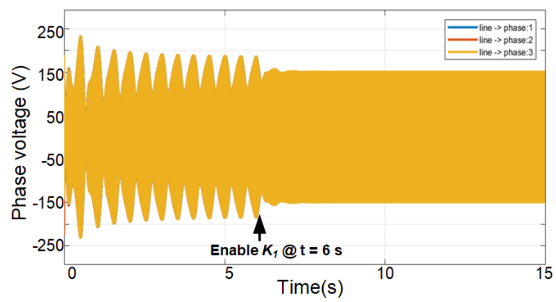

(b)

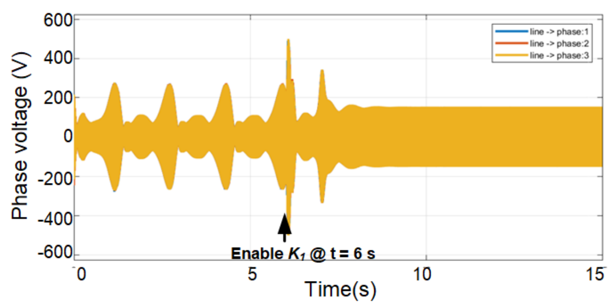

(c)

Figure 5-21. Simulation results under different cases: (a) SCR = 8 (b) SCR = 12, and (c) SCR = 24.

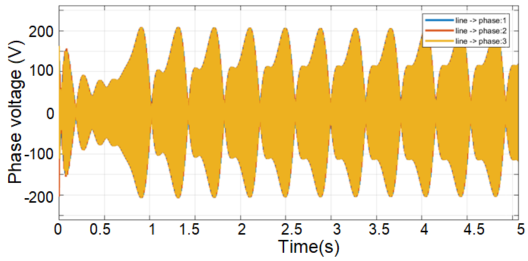

(a)

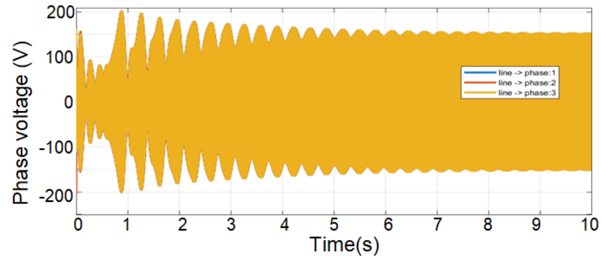

(b)

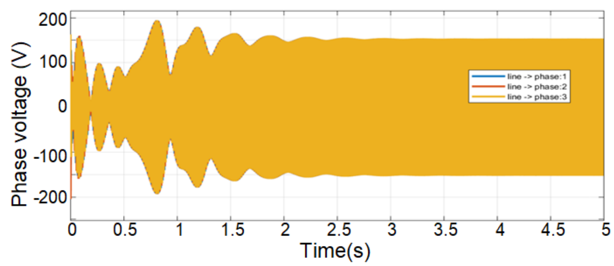

(c)

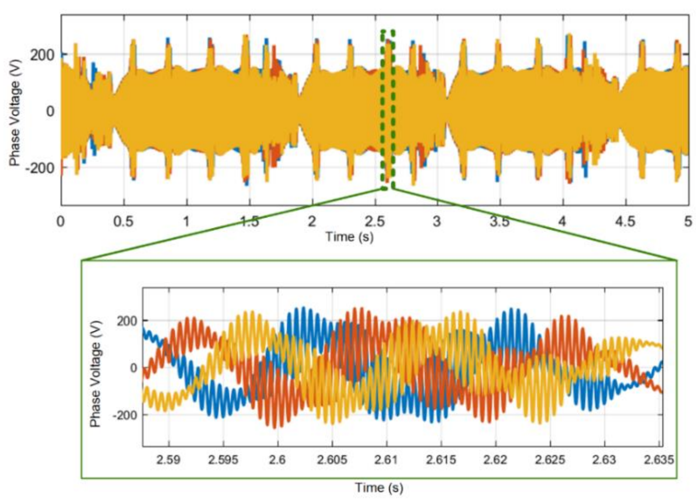

(d)

Figure 5-22. Simulation results with different k_1 under SCR = 8: (a) 1.2×10^{-5}, (b) 1.8×10^{-5}, (c) 3×10^{-5}, and (d) 3×10^{-4}.

B. Experimental Verification

To further validate the effectiveness of the angle droop gain on the compensation of the negative impact of Z_v on system synchronization stability, an experimental platform is built as shown in Figure 5-17.

Two converters are used to mimic the circuit connections in Figure 5-2. The first converter is a grid emulator using open-loop control with grid impedance (L_g = 3.6 mH), and the second converter is the droop-controlled GFM with output filters (L = 2.4 mH and C_f = 10 μF). The reference powers in the test are 600 W and 0 Var. In addition, the reference output voltage and grid voltage is 50 $V_{LL,rms}$. The control parameters are the same as those in Table 5-2.

The impact of Z_v on system stability is investigated first. From Figure 5-23(a), it can be seen that if the controller is implemented with CI (i.e., no Z_v and no H_v), there will be HF harmonic issues on the output voltage.

Then, if the controller is implemented with CIII (i.e., with Z_v and with H_v), it is seen from the full view of Figure 5-23 (b) that there will be low-frequency stability issues, while there are no HF harmonics as seen from the zoom-in view of Figure 5-23 (b). It should be noted that the controller implemented with CII (i.e., no Z_v but with H_v) will not be shown here since the system is stable.

In the end, it can be observed that the low-frequency oscillations caused by the negative impacts of Z_v can be removed with the proposed angle droop as shown in Figure 5-24.

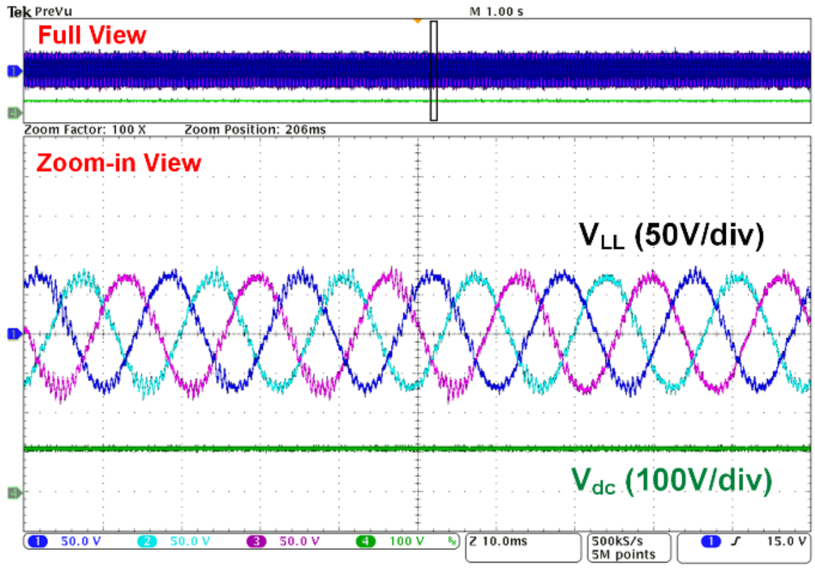

(a)

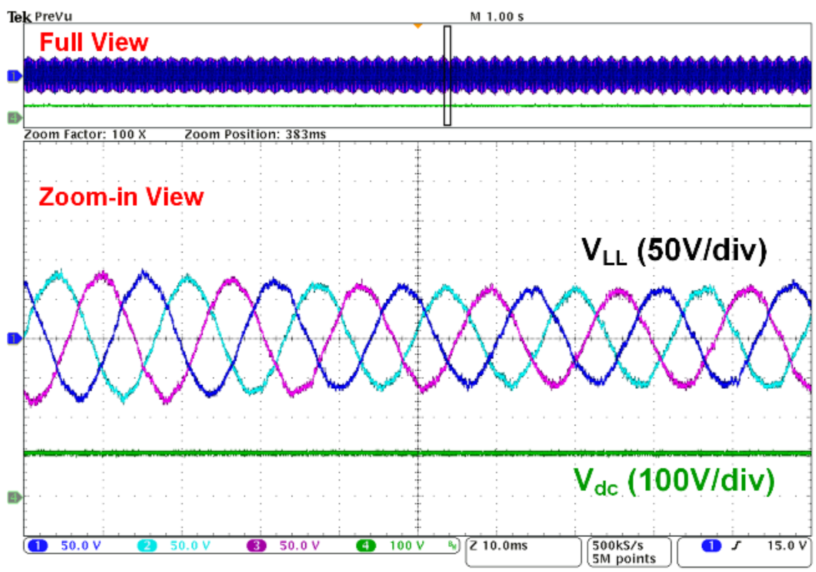

(b)

Figure 5-23. Impacts of Z_v on system stability: (a) with CI and (b) with CIII.

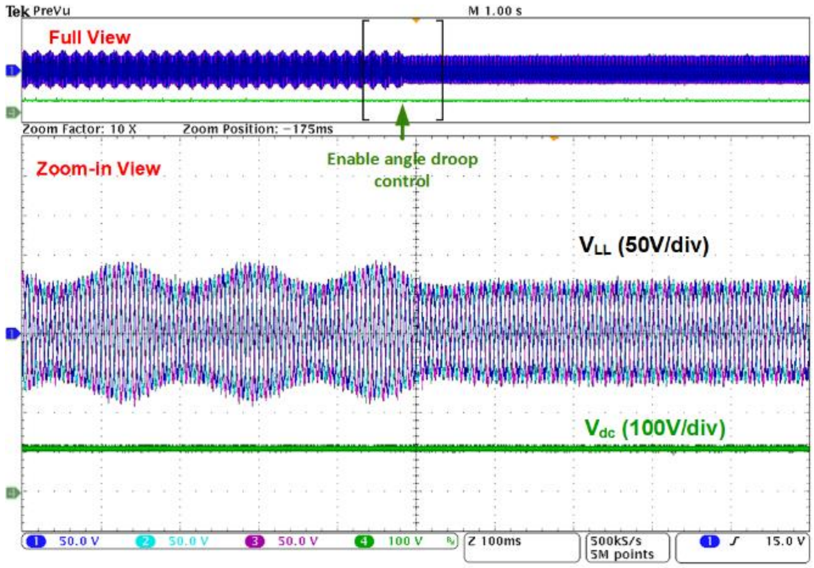

Figure 5-24. Elimination of Z_v –induced LF SSO with angle droop control.

5.5 Conclusions

In this chapter, the positive and negative impacts of passivity-based control for grid-forming inverters using virtual impedance control block Z_v on system stability are reviewed and investigated. With Z_v block, the inverter can be designed to be passive at high frequency, and therefore, the HF harmonic instability issues can be eliminated for all grid conditions.However, the Z_v block will also affect system LF stability by reducing the inertia and damping of the system. To solve this issue, two methods are proposed. Method I uses a system stabilization function or SSF for GFMs to eliminate the HF harmonic instability issues through an online harmonic detection technique. Once a harmonic resonance is detected, the SSF block will be enabled with K_{FF} being calculated based on the harmonic resonant frequency, then the inverter will be passivated at this resonant frequency to stabilize the system. Method II adds an angle droop control block to the *P*-*f* droop control to compensate for the negative impact of Z_v on the LF region. Corresponding design criteria for the gains are also proposed.

Chapter 6. A Port-Hamiltonian-based Control Framework to Render Grid-Forming Inverters Passive

In this chapter, a port-Hamiltonian (pH)-based control structure to achieve the passivity of grid-forming inverters (GFMs) without the presumptions of constant voltage and constant frequency is proposed. The key to the control dynamics is to mimic the behaviors of coupled harmonic oscillators together with an energy 'Pumping-or-Damping' block and a lossless interconnection framework to render the inverter passive. It is shown that the proposed control strategy can guarantee the passivity of GFMs so that it will facilitate the stable design of multi-inverter systems since interconnections of passive systems remain passive.

6.1 Proposed Control Framework and Passivity Analysis of GFMs

The system under consideration is a three-phase grid-connected GFM as shown in Figure 6-1. The inverter has an LC output filter with inductor current denoted as i_L and capacitor voltage denoted as v. The control input for the GFM is u and the external disturbance is grid current i_g. The system will be studied in the stationary $\alpha\beta$ reference frame transformed from the *abc* reference frame through Clarke transformation. Also, the switching effect of the power switches will be neglected based on the averaging theory.

6.1.1 Modeling of Open-Loop GFMs and Passivity Analysis

Given a constant control input u for this inverter, it will operate under open-loop conditions. The system pH model can then be written as (6. 1) with the inductor flux and capacitor charge as the state variables $x_P = [\varphi_{L\alpha} \quad \varphi_{L\beta} \quad q_\alpha \quad q_\beta]^T$ and the Hamiltonian function as given in (6. 2).

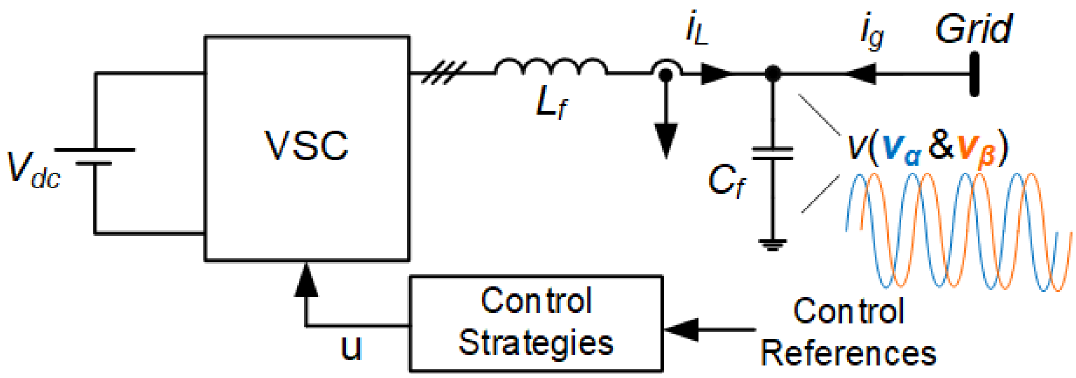

Figure 6-1. A grid-connected grid-forming inverter.

$$\Sigma_P: \begin{cases} \dot{x_P} = (\mathcal{J}_P - \mathcal{R}_P)\nabla H_P(x) + Gu + K\xi \\ \quad\quad y_{P1} = G^T \nabla H_P(x) \\ \quad\quad y_{P2} = K^T \nabla H_P(x) \end{cases} \tag{6. 1}$$

$$H_P(x) = \frac{1}{2}L_f i_{L\alpha}^2 + \frac{1}{2}L_f i_{L\beta}^2 + \frac{1}{2}C_f v_\alpha^2 + \frac{1}{2}C_f v_\beta^2 \tag{6. 2}$$

where, $\mathcal{J}_P = \begin{bmatrix} 0 & 0 & -1 & 0 \\ 0 & 0 & 0 & -1 \\ 1 & 0 & 0 & 0 \\ 0 & 1 & 0 & 0 \end{bmatrix}$, $\mathcal{R}_P = \begin{bmatrix} R_f & 0 & 0 & 0 \\ 0 & R_f & 0 & 0 \\ 0 & 0 & 0 & 0 \\ 0 & 0 & 0 & 0 \end{bmatrix}$, $G = \begin{bmatrix} 1 & 0 \\ 0 & 1 \\ 0 & 0 \\ 0 & 0 \end{bmatrix}$, $K = \begin{bmatrix} 0 & 0 \\ 0 & 0 \\ 1 & 0 \\ 0 & 1 \end{bmatrix}$, $u = \begin{bmatrix} u_\alpha \\ u_\beta \end{bmatrix}$,

and $\xi = \begin{bmatrix} i_{g\alpha} \\ i_{g\beta} \end{bmatrix}$.

It is obvious that the pH system in (6. 1) is passive with $H_P(x) \geq 0$ in terms of system inputs ($[u^T \quad \xi^T]^T$) and system outputs ($[y_{P1}^T \quad y_{P2}^T]^T$).

6.1.2 Proposed Control Block with Lossless Interconnection Framework

To render the closed-loop GFM passive, a control framework is proposed as shown in Figure 6-2 which follows the fundamental characteristics of the virtual oscillator control [193-195]. The proposed control scheme has three loops, including the outer power loop, the virtual oscillator loop, and the current loop. There are two channels in the outer power loop, where the reactive power channel is to adjust the oscillation magnitude of the virtual oscillator with a sign-indefinite gain $\pm|\xi_2|$ and the active power loop is to generate the frequency reference with a constant gain ξ_3. The virtual oscillator loop is to mimic the dynamics of coupled harmonic oscillators to achieve spontaneous synchronization of the inverter. And the inner current loop is to maintain lossless connections between the controller block and the plant block. Note that there is a '*Pumping or Damping'* motion in the outer reactive power loop, which will be explained later in Section 6.1.3.

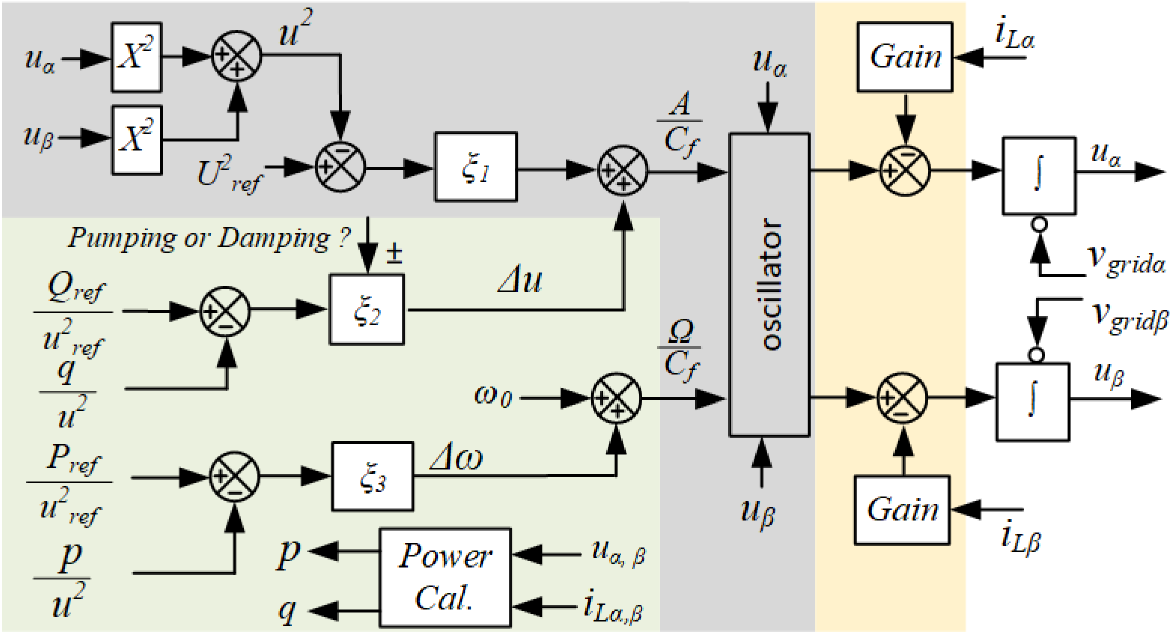

Figure 6-2. Proposed control scheme.

The control dynamics can be written as (6. 3), where the control state is selected as $x_C = [C_f u_\alpha \quad C_f u_\beta]^T$, the Hamiltonian function $H_C(x)$ is defined in (6. 4) with ε being a very small constant, a function Φ is defined in (6. 5), A is defined in (6. 6) and Ω is defined in (6. 7).

$$\textstyle\sum_C: \dot{x}_C = \left(\begin{bmatrix} -\varepsilon^2/\Phi & 0 & 0 & -\Omega \\ 0 & -\varepsilon^2/\Phi & \Omega & 0 \end{bmatrix} - \begin{bmatrix} 0 & 0 & -A & 0 \\ 0 & 0 & 0 & -A \end{bmatrix}\right)\begin{bmatrix} i_{L\alpha} \\ i_{L\beta} \\ u_\alpha \\ u_\beta \end{bmatrix} \tag{6. 3}$$

$$H_C(x) = \frac{1}{2}\frac{\Phi^2}{\varepsilon^2} \tag{6. 4}$$

$$\Phi = \frac{1}{2}C_f u_\alpha^2 + \frac{1}{2}C_f u_\beta^2 - \frac{1}{2}C_f u_{ref}^2 \tag{6. 5}$$

$$\mathrm{A} = C_f \xi_1 \left(u_{ref}^2 - u^2\right) + C_f \xi_2 \left(\frac{Q_{ref}}{u_{ref}^2} - \frac{Q}{u^2}\right) \tag{6. 6}$$

$$\Omega = \omega_o C_f + \xi_3 C_f \left(\frac{P_{ref}}{u_{ref}^2} - \frac{P}{u^2}\right) \tag{6. 7}$$

6.1.3 Modeling of Closed-Loop GFMs and Passivity Analysis

With the proposed control strategy, the closed-loop system can then be obtained in the pH framework as shown in Figure 6-3 which consists of a control block $\sum_C$, an interconnection block $\sum_I$, and an inverter hardware block $\sum_P$. Therefore, the closed-loop GFM can be modeled as (6. 8) with selecting the system storage function H as (6. 9). First, it can be seen that $\mathcal{J} = -\mathcal{J}^T$. Then, as long as $\mathcal{R} \geq 0$, then (6. 10) can be obtained, meaning that the closed-loop system Figure 6-3 is passive concerning the inputs $\xi = [i_{g\alpha} \quad i_{g\beta}]^T$ and outputs $y = [v_\alpha \quad v_\beta]^T$.

Since the proposed control structure is developed based on the mechanisms of coupled harmonic oscillators, it will have some similarities with the existing dispatchable virtual oscillator

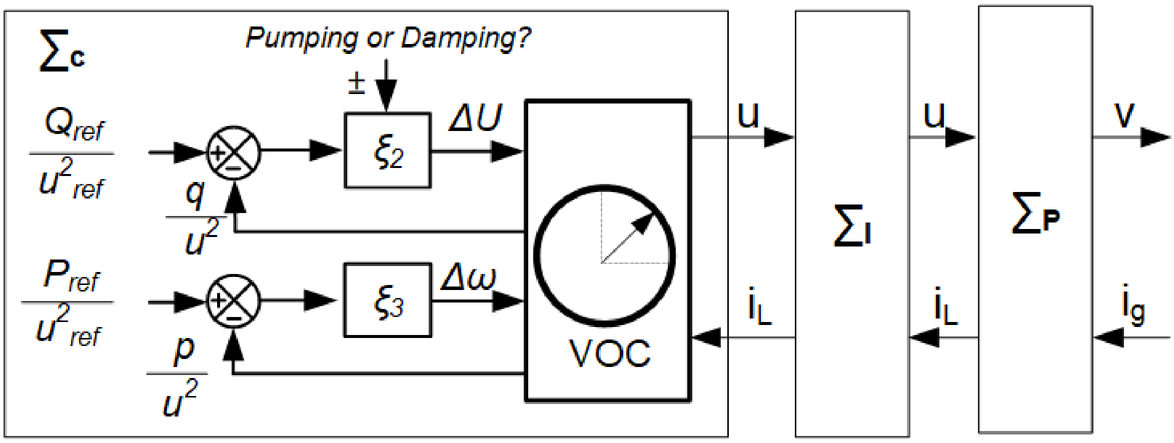

Figure 6-3. Closed-loop GFMs in pH Framework.

control (dVOC) approaches [187, 195-197]. For example, if neglecting the voltage amplitude dynamics and the inner current loops, the proposed control approach will have the same transient stability dynamics as the existing dVOC approaches [187, 195]. The main differences between the proposed approach and the existing dVOC approaches are: (1) the ‘*Pumping or Damping’* block in the reactive power loop which is to maintain a constant control voltage in any situation; and (2) the lossless interconnection in a pH structure which is achieved by the inner current loop. In other words, the proposed control approach renders the inverter passive, and thus will always guarantee system stability if an equilibrium operating point exists. Nevertheless, the existing dVOC approaches may lose synchronism under conditions when the voltage drop imposed by the reactive power regulation becomes significant [149].

$$\Sigma: \begin{cases} \begin{bmatrix} \dot{x}_P \\ \dot{x}_c \end{bmatrix} = (\mathcal{J} - \mathcal{R}) \nabla H(x) + L\xi \\ \qquad y = L^T \nabla H(x) \end{cases} \tag{6. 8}$$

$$H = H_P + H_c \tag{6. 9}$$

$$\dot{H} = \xi^T y - \frac{\partial H^T}{\partial x} \mathcal{R} \frac{\partial H}{\partial x} \leq \xi^T y \tag{6. 10}$$

where, $\mathcal{J} = \begin{bmatrix} 0 & 0 & -1 & 0 & \varepsilon^2/\Phi & 0 \\ 0 & 0 & 0 & -1 & 0 & \varepsilon^2/\Phi \\ 1 & 0 & 0 & 0 & 0 & 0 \\ 0 & 1 & 0 & 0 & 0 & 0 \\ -\varepsilon^2/\Phi & 0 & 0 & 0 & 0 & -\Omega\varepsilon^2/\Phi \\ 0 & -\varepsilon^2/\Phi & 0 & 0 & \Omega\varepsilon^2/\Phi & 0 \end{bmatrix}$, $\mathcal{R} = \begin{bmatrix} R_f & 0 & 0 & 0 & 0 & 0 \\ 0 & R_f & 0 & 0 & 0 & 0 \\ 0 & 0 & 0 & 0 & 0 & 0 \\ 0 & 0 & 0 & 0 & 0 & 0 \\ 0 & 0 & 0 & 0 & -A\varepsilon^2/\Phi & 0 \\ 0 & 0 & 0 & 0 & 0 & -A\varepsilon^2/\Phi \end{bmatrix}$,

and $L = \begin{bmatrix} 0 & 0 \\ 0 & 0 \\ 1 & 0 \\ 0 & 1 \\ 0 & 0 \\ 0 & 0 \end{bmatrix}$.

6.1.4 Controller Implementation Issues

As mentioned in Section 6.1.3, the damping matrix $\mathcal{R}$ should be non-negative to ensure that the closed-loop GFM is passive. In order to have $\mathcal{R} \geq 0$, $-A\varepsilon^2/\Phi$ or $-A/\Phi$ should be non-negative, which means A needs to be adjusted based on the change of Φ.

Define $K_P = -A/\Phi$, it can be further expressed as (6. 11) based on (6. 5) and (6. 6). Then, it can be seen that the first term $2\xi_1$ will always be non-negative as long as ξ_1 is designed positive. And ξ_2 should be sign-indefinite and the sign should be determined based on (6. 12). That is if $\Phi > 0$, ξ_2 should be tuned to damp the energy function; if $\Phi < 0$, ξ_2 should be tuned to pump the energy function. Though this is a conservative design, it can guarantee passivity of the inverter and thus the stability of the system.

$$K_P = 2\xi_1 - 2\xi_2\left(\frac{Q_{ref}}{u_{ref}^2} - \frac{Q}{u^2}\right)/\left(u^2 - u_{ref}^2\right) \tag{6. 11}$$

$$sgn(\xi_2) = -sgn\left(\left(\frac{Q_{ref}}{u_{ref}^2} - \frac{Q}{u^2}\right)/\left(u^2 - u_{ref}^2\right)\right) \tag{6. 12}$$

When implementing this sign-indefinite '*Pumping or Damping*' action as described in (6. 12) in the controller, a hysteresis block should be used, and the sign for ξ_2 can be generated based on the control mechanism as shown in Figure 6-4, where *h* is the preset hysteresis value. Instead of using a divider for $\frac{Q_{ref}}{u_{ref}^2} - \frac{Q}{u^2}$ and $u^2 - u_{ref}^2$ as in (6. 12), a multiplier is used in the real implementation due to two reasons. First, no matter whether it is a multiplication or division between these two terms, it will not affect the result for the sign determination. Second, the multiplication process is faster than the division process in digital controllers.

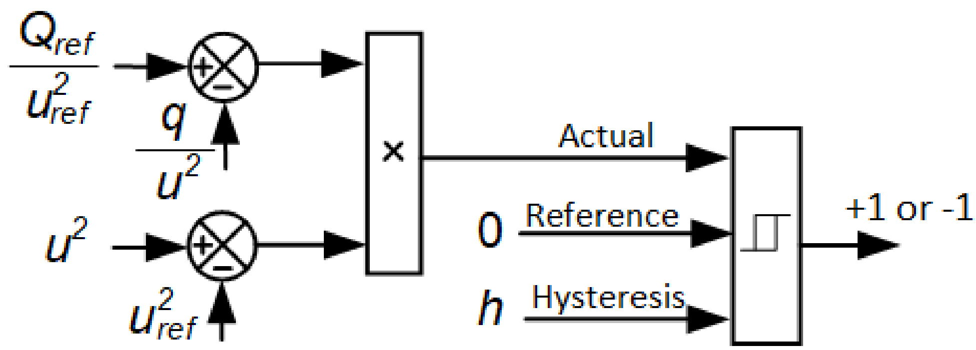

Figure 6-4. The control diagram of the '*Pumping or Damping*' block.

6.2 Case Study of Multi-inverter Systems with Proposed PVOC Approach

6.2.1 Simulation Tests

A. Three-bus system

To further validate the feasibility and effectiveness of the proposed approach in multi-inverter systems, simulations were carried out for a three-bus system as shown in Figure 6-5. Bus 1 is assumed to be a bulk power system, Bus 2 and Bus 3 are connected to Inverter 2 and Inverter 3. Both inverters are GFM implemented with the proposed PVOC approaches. All loads in the system are constant impedance loads.

The electrical and control parameters are given in Table 6-1. Four transient scenarios have been simulated, including the normal load transient, short-circuit fault, open-circuit fault, and bus voltage drop. Note that no system information (e.g., transmission line parameters) is required for the control parameters design for these inverters.

1) Normal Load Transient

In the first scenario, Inverter 2 works as a source and delivers 1 p.u. active power to the system. While Inverter 3 first works as a load with consuming 0.1 p.u. power; then the reference load power is increased to 1 p.u. at t = 3 s; at t = 6 s, it changes to generation mode with 1 p.u. output power.

As shown in Figure 6-6, the active power of Inverter 3 is regulated to the reference value in steady-state, and the active power of Inverter 2 is well regulated at pre-defined 1 p.u.. The steady-state output voltage of Inverter 2 and Inverter 3 slightly drop to meet the power requirements, while the frequencies all return to 60 Hz.

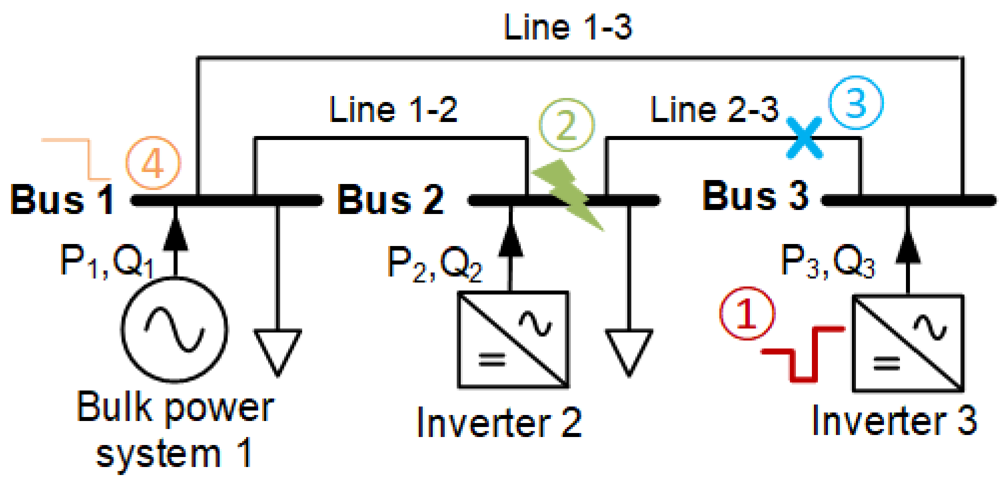

Figure 6-5. Test of system with multiple inverters.

Table 6-1. Electrical and control parameters in the multi-inverter test system.

Variables		Value	Variables	Value
Bus voltage (V)		50	Line 1-2 (pu)	0.18
Rated power (kVA)		1	Line 1-3(pu)	0.37
System frequency (Hz)		60	Line 2-3 (pu)	0.11
Output inductor (mH)		2.4	Output capacitor (μF)	10
Control parameters	ξ_1	0.0605	$\lvert\xi_2\rvert$	0.42
	ξ_3	6.28	ε	10^{-5}

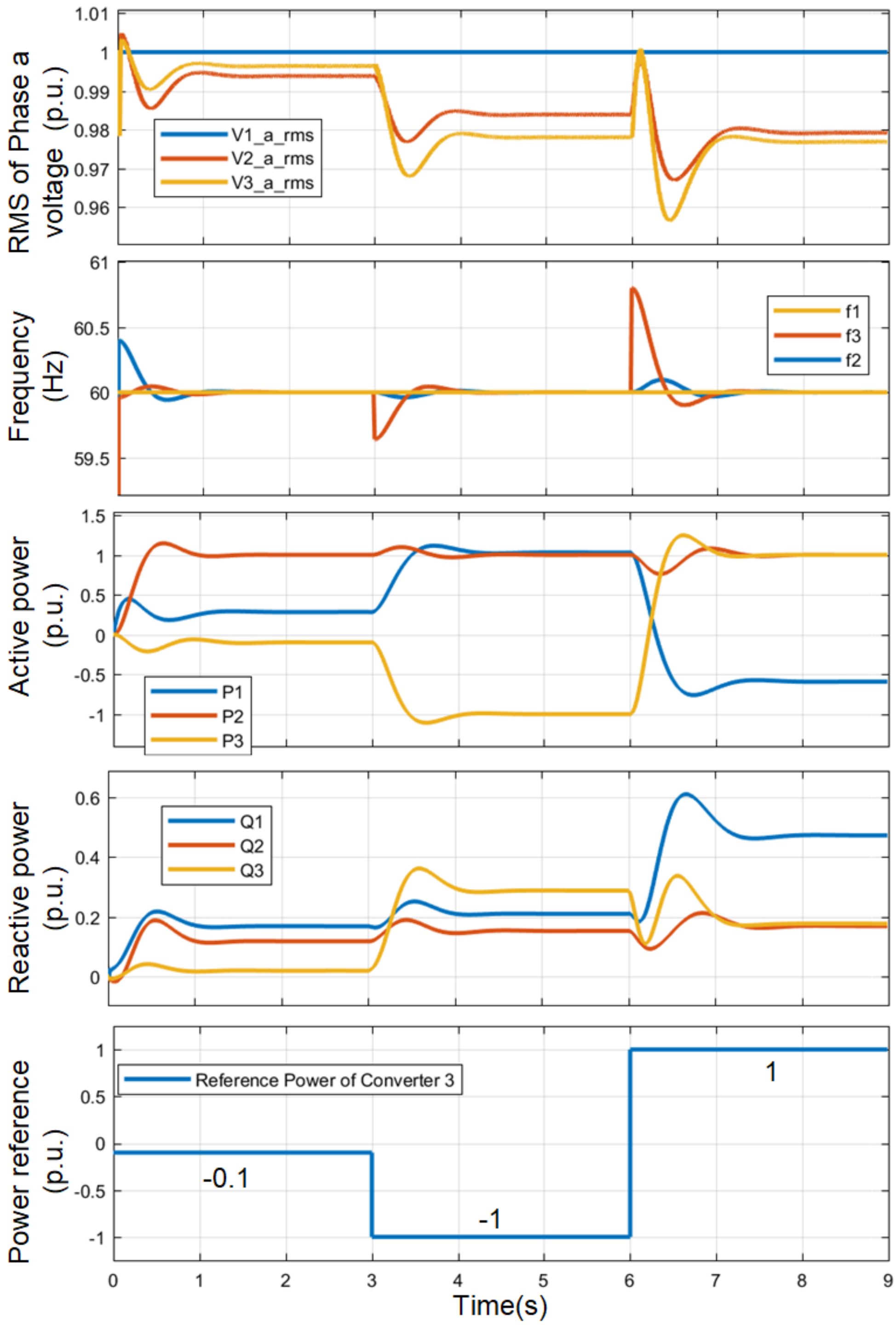

Figure 6-6. System response under load transient.

2) Short-Circuit Fault

In the second scenario, both Inverter 2 and Inverter 3 work as sources delivering 1 p.u. power to the rest of the system, then a short-circuit fault with 1 mΩ short resistance happens at Bus 2 at t = 2 s and lasts for 5 cycles. As shown in Figure 6-7, after the fault is cleared, the voltage, frequency, and power all return to the prespecified reference value. It can also be observed that Bus 1, as an ideal bulk power system, needs to maintain the bus voltage, so its reactive power is increased to more than 3 p.u. during fault.

3) Open-circuit Fault

In the third scenario, Inverters 2 and 3 still deliver 1 p.u. power to the system, then Line 2-3 has an open-circuit fault at t = 3 s and returns to service at t = 6 s. Two types of open-circuit faults occur, one is that Line 2-3 is totally out of service and disconnected from the system, and the other is that the impedance of Line 2-3 changes from 0.1 p.u. to 0.2 p.u..For the first type of open-circuit fault, as shown in Figure 6-8, the inverters can regulate the output power and frequency during the fault and after the fault is cleared. And the output voltage will self-adjust according to the power flow. For the second type of open-circuit fault, as shown in Figure 6-9, the system remains stable during the fault and returns to the pre-fault operating conditions after the fault is cleared.

4) Bus Voltage Drop

In this scenario, Inverters 2 and 3 deliver 1 p.u. power into the system separately, and it is assumed that the voltage on Bus 1 drops to 0.5 p.u. during a fault and the fault lasts for 3 seconds. As shown in Figure 6-10, Inverter 2 and Inverter 3 maintain synchronism with the grid and regulate the active power to 1 p.u. during the fault and after the fault is cleared. About 50% more reactive power is required for Inverters 2 and 3 to regulate voltage during the fault.

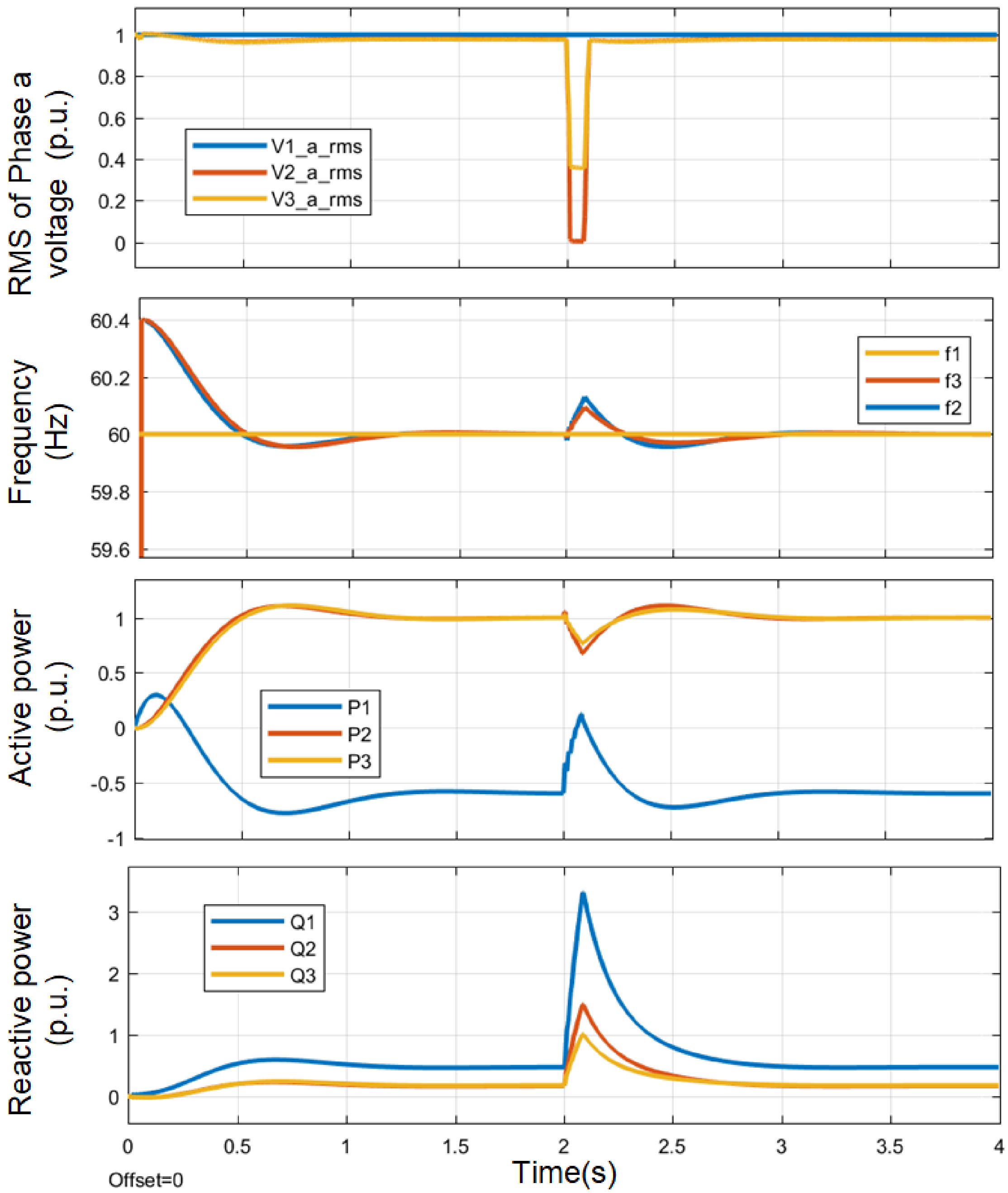

Figure 6-7. System response during short-circuit fault.

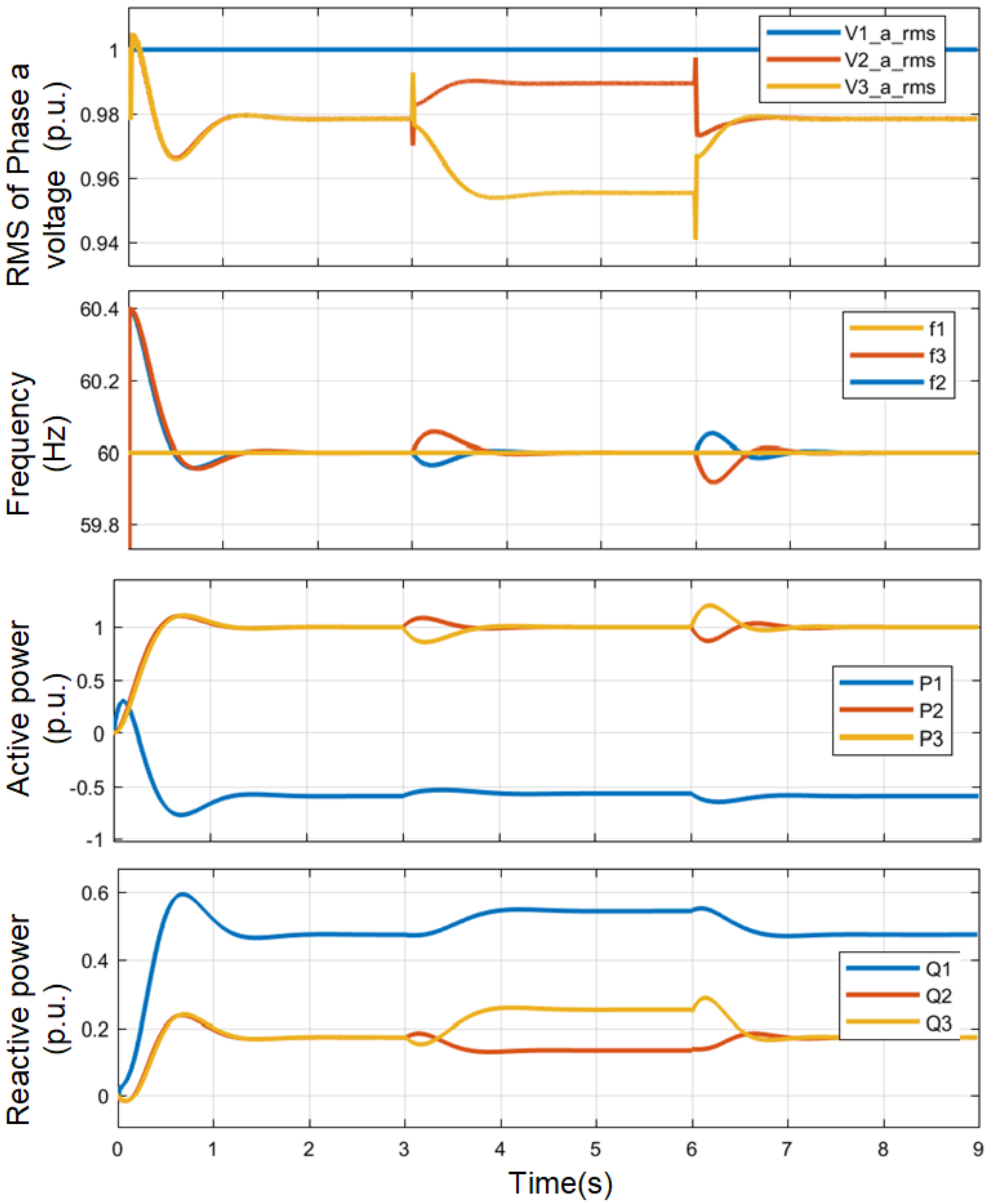

Figure 6-8. System response during an open-circuit fault (Line 2-3 disconnected).

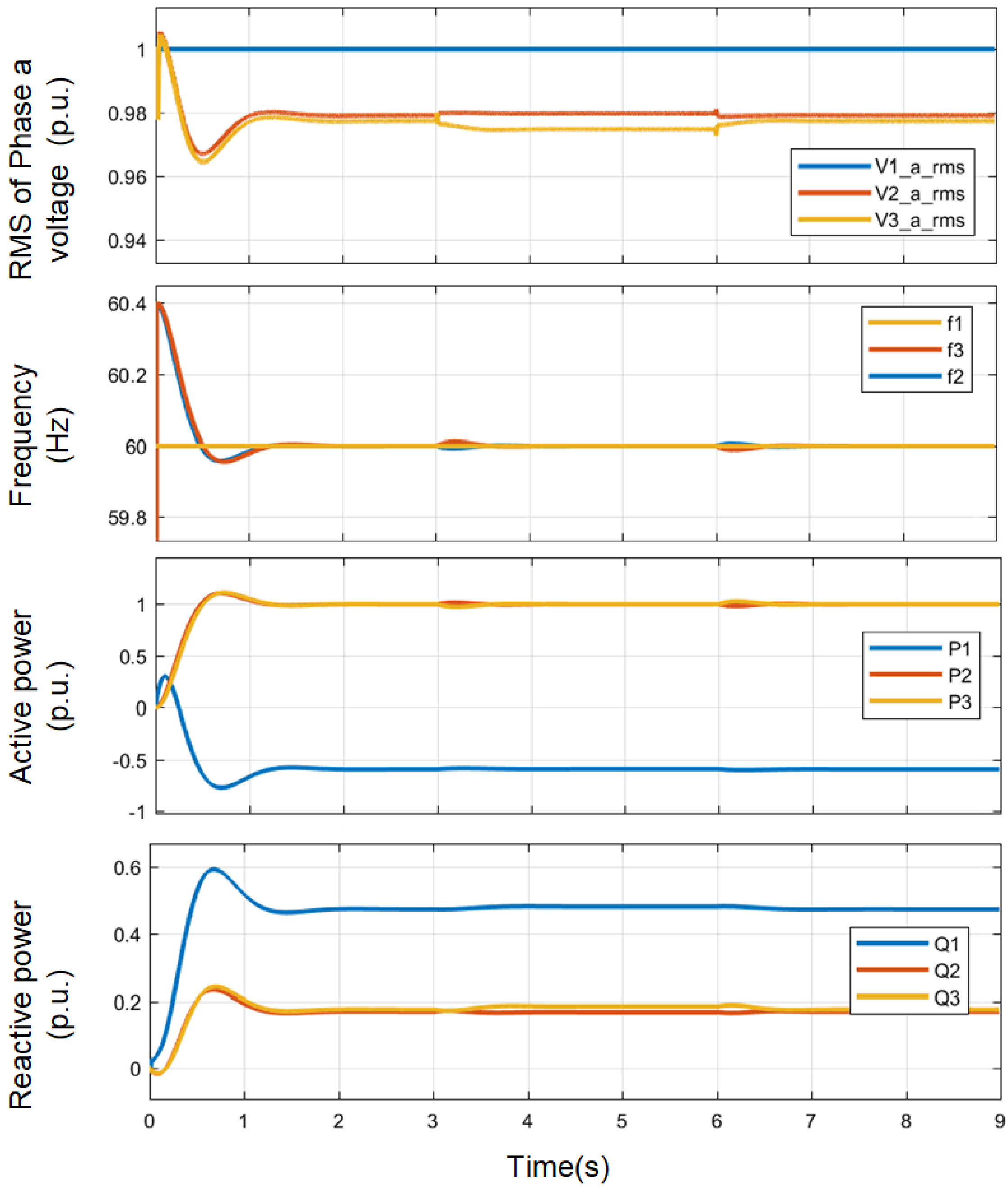

Figure 6-9. System response during an open-circuit fault (Impedance of Line 2-3 change from 0.1 pu to 0.2 pu).

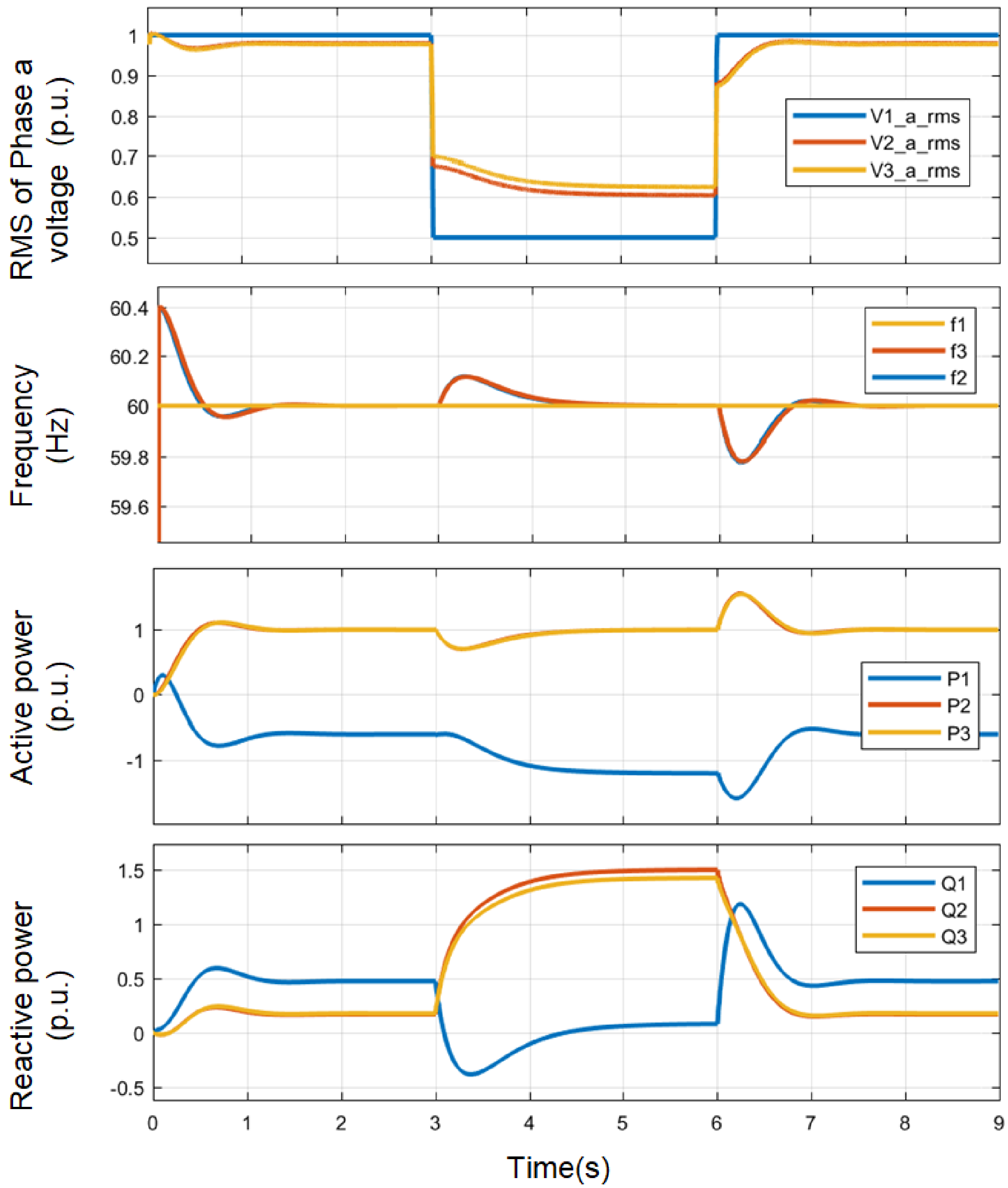

Figure 6-10. System response during voltage drop at Bus 1.

B. Six-converter system

A system with six converters as shown in Figure 6-11 is built for further validation under two transient scenarios: (1) change of line impedance and (2) change of load power. The working conditions and system parameters are listed in Table 6-2.

Scenario I: Change of Line Impedance

In this scenario, the impedances of Line 2 and Line 3 are assumed to be increased to emulate some out-of-service fault. It can be seen from Figure 6-12 that the change of line impedances at $t = 2s$ will not affect system stability, both the voltage and power will return to a stable value after the transient.

*Scenario II**:** Change of Load Power*

Power changes from 0.2 pu to 0.8 pu at $t = 2s$ and then to -0.2 pu at $t = 4s$ of G_{12} in this scenario. Note that the positive power means the converter is a load that is consuming power in the system, and the negative power means the converter is a source that is providing power to the system. As shown in Figure 6-13 during the load transient, the voltage can be kept stable, and the power can track the references well.

6.2.2 Experimental Tests

The above analysis and simulation results have already shown that the proposed PVOC has enhanced transient stability performance due to the '*Pumping or Damping*' motion in the reactive power loop.

As for the experimental validations of the proposed controller, it is difficult to repeat these severe system disturbances in the laboratory test due to hardware limitations. Therefore, in order

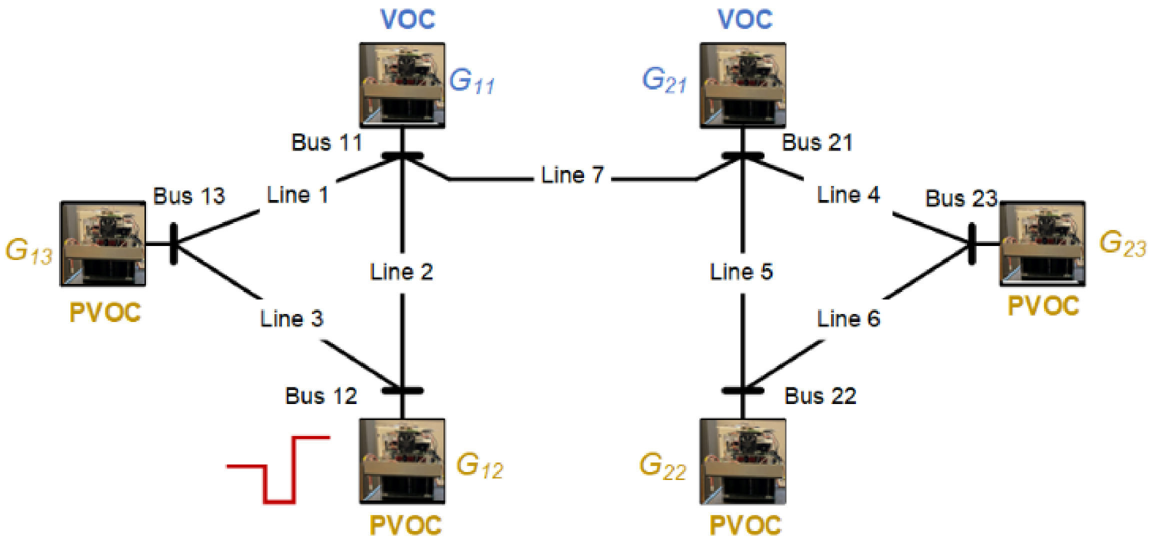

Figure 6-11. Circuit diagram of the six-converter test system.

Table 6-2. Working conditions and system parameters of the six-converter test system.

Variables	Value	Variables	Value
Dc voltage (V)	130	Line 1 (pu)	0.37
Ac voltage (V)	50	Line 2 (pu)	0.18 → 0.54
Rated power (kVA)	1	Line 3 (pu)	0.11 → 0.47
Real power of G_{12} (pu)	0.2 → 0.8 → -0.2	Line 4 (pu)	0.38
Real power of G_{13} (pu)	0.5	Line 5 (pu)	0.11
Real power of G_{22} (pu)	0.5	Line 6 (pu)	0.11
Real power of G_{23} (pu)	0.5	Line 7 (pu)	0.11

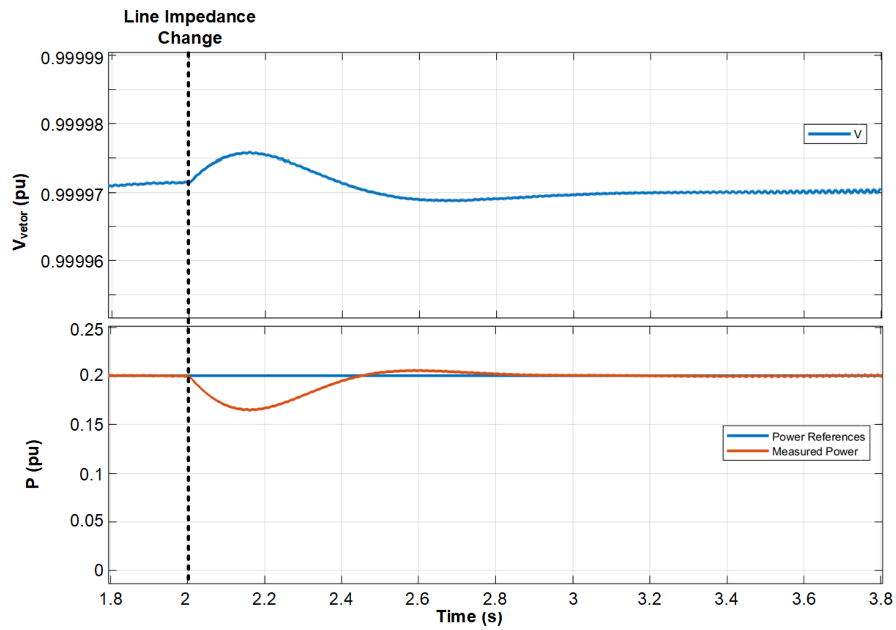

Figure 6-12. Simulation results of voltage vector and power of G_{12} with system line impedance change.

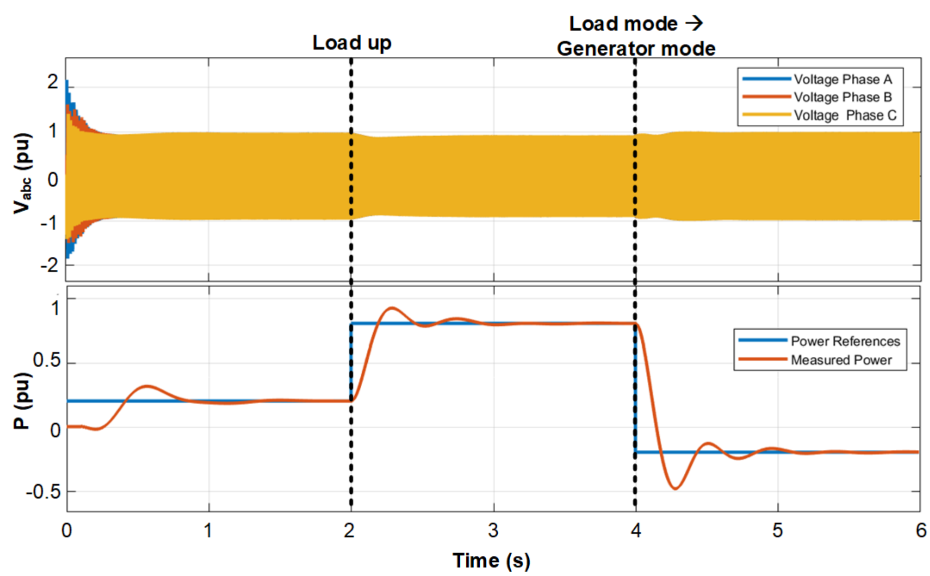

Figure 6-13. Simulation results of output voltage and power with load power change at G_{12}.

to verify that the proposed PVOC can function properly and facilitate the stability design of multi-inverter systems, a six-inverter system as shown in Figure 6-11 is constructed in the hardware testbed (HTB) in CURENT UTK [198] and a normal load-step transient is examined.

In this six-inverter system, G_{11} and G_{21} are implemented with a simple virtual oscillator control without any power dispatching loop; all the other inverters are implemented with the proposed PVOC approach with the control parameters in Table 6-2. Still, no network information is used in these control parameter designs. The underlying assumption is that the system can find an equilibrium point under its given working conditions. It is then assumed that inverter G_{12} works as a generator and delivers 0.2 p.u power to the system first; then it increases its output power to 0.8 p.u.; afterwards, it changes from generator mode to load mode and consumes 0.2 p.u. power.

Figure 6-14 and Figure 6-15 show the test results of the six-inverter system under the normal load transient. It can be seen that the inverters with the proposed control approach can function well as expected and maintain system stability under the load transient scenario.

6.3 Conclusions

In this chapter, a control framework has been proposed to ensure the passivity of the closed-loop grid-forming inverters based on the port-Hamiltonian system theory without the need for the assumption of constant voltage and constant frequency. This is a simple two-channel structure compared with the three-channel passivity-based VSM approach. It has also been proved by the simulation results and the preliminary results of experimental tests that this approach can facilitate the stability design of a multi-inverter system. This is because as long as each inverter follows the proposed passivity-based control strategy, the interconnected system will be naturally stable.

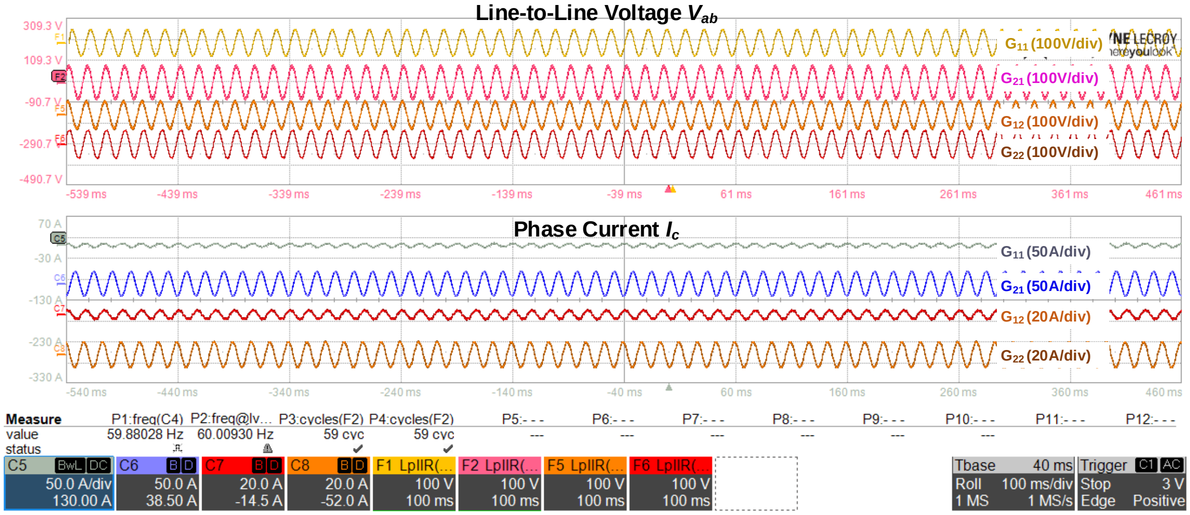

(a)

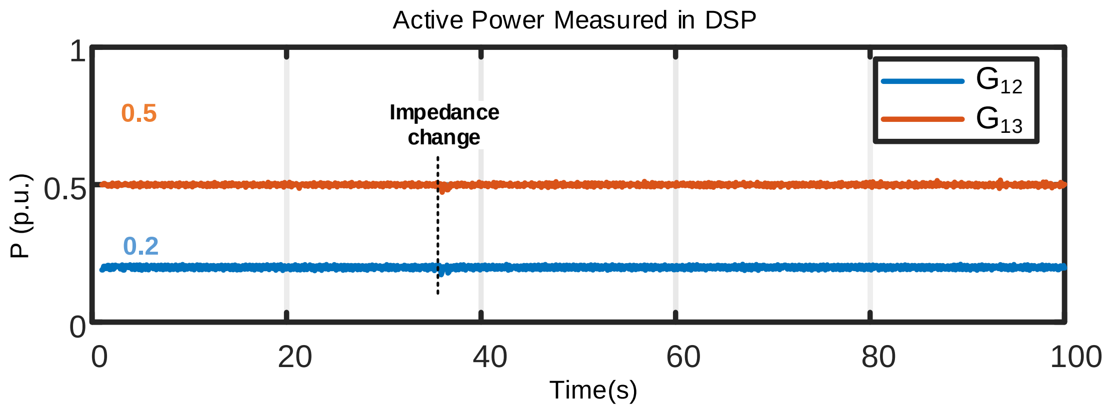

(b)

Figure 6-14. Experimental results with system line impedance change: (a) voltage and current and (b) power.

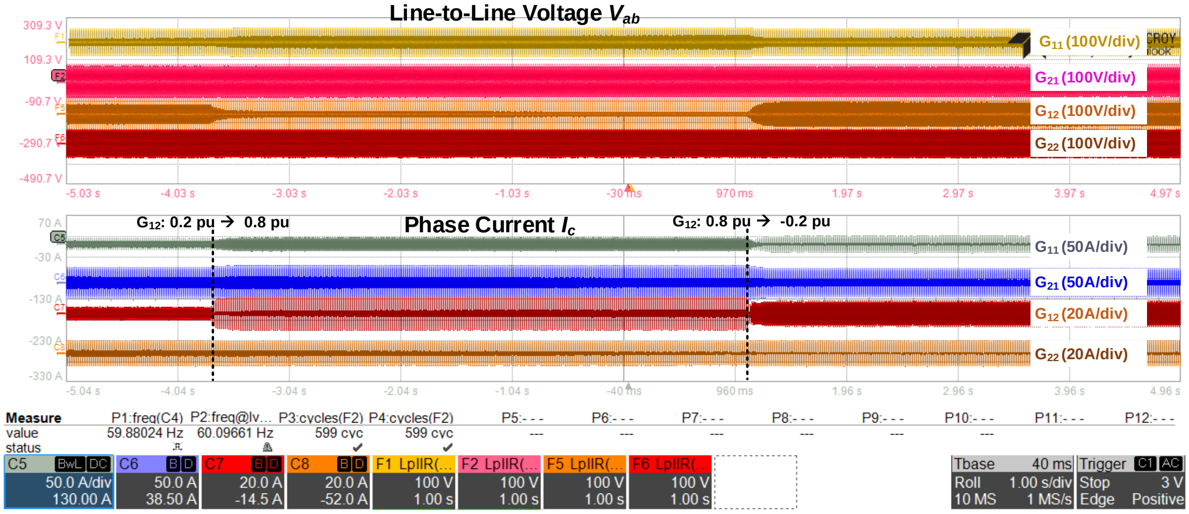

(a)

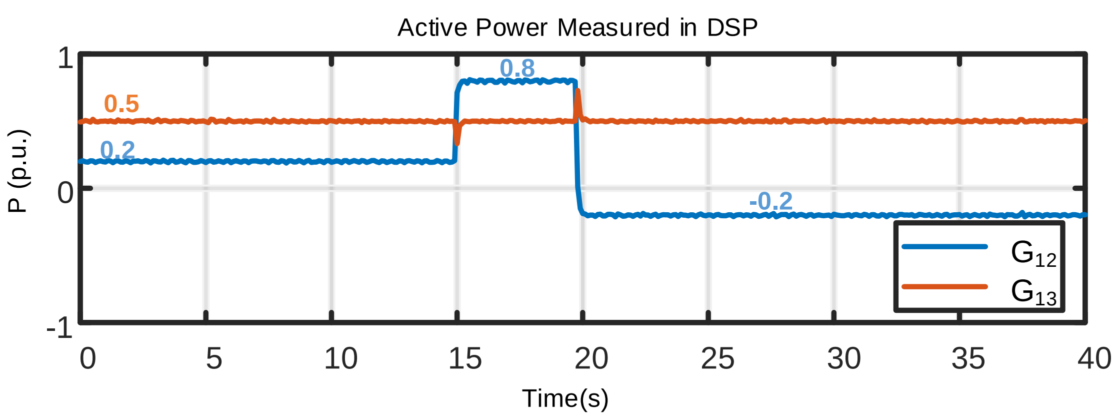

(b)

Figure 6-15. Experimental results with load power change: (a) voltage and current and (b) power.

Chapter 7. Extended Passivity-based Control for Grid-Forming Inverters in Non-Passive Power Systems

In Chapter 6, a passivity-based control approach has been proposed to render GFMs passive, so that they can stably operate with other passive systems. However, passivity is only an intermediate step for system stability design. The relationships between passivity and system stability remain unrevealed. Also, the control method in Chapter 6 for system stability requires a premise that the rest of the system is passive. But in real power systems, there are many non-passive components, such as synchronous generators or converters with some non-passive control. Therefore, in this chapter, an extended passivity-based control is developed, and the converter stability is analyzed from both Lyapunov stability and synchronization stability. Additionally, it is proven that the proposed GFM can be stably operated with a non-passive but stable power system, e.g., a legacy three-bus power system.

7.1 Modeling of GFMs with General VOC in pH Framework

7.1.1 GFMs with General VOC Approach

There is a close connection between coupled harmonic oscillators (CHOs) and the control of power inverters because of the synchronization of inverters pertaining to the synchronization of CHOs. Therefore, in this study, we rely on controlling the GFMs to behave like the Stuart-Landau (SL) oscillators owing to two considerations [199-202].

First, the harmonic oscillation pattern of the SL oscillator has a clear mapping to the voltage pattern in power systems. That is, the oscillators represented in Cartesian coordinates can describe the two voltage vectors (v_α and v_β) in power systems which are transformed from three-phase voltage through Clark Transformation.

Second, it is easy to develop coupling terms in an analytical form for multiple coupled SL oscillators using the ac power flow analysis results of the power grids.

Accordingly, the entire power grid can be modeled as (7. 1) in polar coordinates [201, 203], where, ω_k is the natural frequency of oscillator k, γ_{ki}/μ_{ki} is the dissipative/reactive coupling strength between interacting oscillators, v_{refk} is the reference value of the oscillation amplitude, and $v_k(= \rho_k e^{i\theta_k})$ is a complex variable with ρ_k being the amplitude of oscillator k and θ_k being its phase angle.

The model in (7. 1) can also be reformatted in Cartesian coordinates as given in (7. 2), where $v_k = v_{\alpha k} + jv_{\beta k}$. Furthermore, since this chapter is aimed to design a local control approach for GFMs to ensure the stability of the entire system without the knowledge of the rest of the system, the problem can then be simplified as two CHOs as shown in Figure 7-1 with a single-directional coupling that is from grid to GFM without loss of generality. This is because, in the design of grid-connected GFMs, the grid can be assumed as an ideal three-phase voltage source, which can be modeled as a coupled harmonic oscillator $v_{\alpha g}$ and $v_{\beta g}$ through Clarke transformation. And the GFM can be controlled as coupled harmonic oscillators v_α and v_β. Also, to have the power dispatching capability, the power flowing through interconnected lines between the grid and the inverter should be controlled, so the power flow can be considered as the coupling effect from the grid oscillator to the inverter oscillator.

In this oscillator-based model, there are two types of couplings in between: one is the internal coupling between v_α and v_β through the oscillation frequency, and the other is the external coupling between the inverter oscillator and grid oscillator which is physically coupled by the

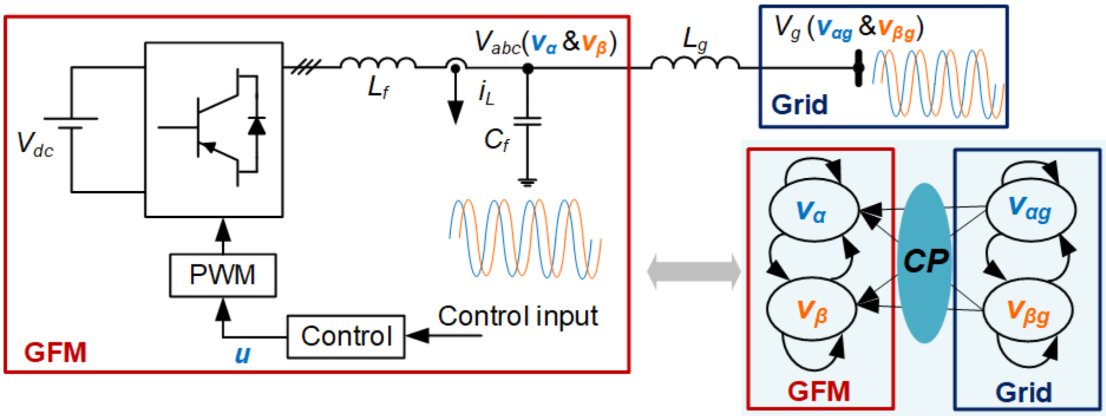

Figure 7-1. A grid-connected GFM with a general VOC approach.

power flow among the connecting lines. As shown in (7. 3), which is simplified from (7. 2) by considering two groups of coupled harmonic oscillators, ω_o is the system fundamental frequency, and the terms in the square brackets are the measure of coupling strength $CP_{\alpha,ref}$ and $CP_{\beta,ref}$ between the GFM and the grid. The coupling strength term can be further modeled by the power flow analysis results as given in (7. 4) for a well-synchronized system, where γ and μ is defined by the power system parameters as given in (7. 5) with L_g being the impedance and R being the equivalent resistance of the connecting line between GFM and grid.

More details on the derivation process can be seen in Appendix A.

$$\dot{v}_k = \left(v_{refk}^2 + \boldsymbol{i}\omega_k - |v_k|^2\right)v_k + \sum_{j=1}^{N}(\gamma_{kj} + \boldsymbol{i}\mu_{kj})(v_j - v_k) \tag{7. 1}$$

$$\begin{cases} \dot{v}_{\alpha k} = \left(v_{refk}^2 - v_k^2\right)v_{\alpha k} - \omega_k v_{\beta k} + \displaystyle\sum_{j=1}^{N}[\gamma_{kj}\left(v_{\alpha j} - v_{\alpha k}\right) - \mu_{kj}(v_{\beta j} - v_{\beta k})] \\ \dot{v}_{\beta k} = \left(v_{refk}^2 - v_k^2\right)v_{\beta k} + \omega_k v_{\alpha k} + \displaystyle\sum_{j=1}^{N}[\gamma_{kj}\left(v_{\beta j} - v_{\beta k}\right) + \mu_{kj}(v_{\alpha j} - v_{\alpha k})] \end{cases} \tag{7. 2}$$

$$\begin{cases} \dot{v}_\alpha = \left(v_{ref}^2 - v^2\right)v_\alpha - \omega_o v_\beta + [\gamma\left(v_{\alpha g} - v_\alpha\right) - \mu\left(v_{\beta g} - v_\beta\right)] \\ \dot{v}_\beta = \left(v_{ref}^2 - v^2\right)v_\beta + \omega_o v_\alpha + [\gamma\left(v_{\beta g} - v_\beta\right) + \mu\left(v_{\alpha g} - v_\alpha\right)] \end{cases} \tag{7. 3}$$

$$\begin{bmatrix} CP_{\alpha,ref} \\ CP_{\beta,ref} \end{bmatrix} = \begin{bmatrix} \gamma\left(v_{\alpha g} - v_\alpha\right) - \mu\left(v_{\beta g} - v_\beta\right) \\ \gamma\left(v_{\beta g} - v_\beta\right) + \mu\left(v_{\alpha g} - v_\alpha\right) \end{bmatrix} = \frac{1}{v^2}\begin{bmatrix} -Q_{ref} & P_{ref} \\ -P_{ref} & -Q_{ref} \end{bmatrix}\begin{bmatrix} v_\alpha \\ v_\beta \end{bmatrix} \tag{7. 4}$$

It can then be inferred that to mimic the behavior of CHOs, the controller of GFMs should follow the control structure as given in (7. 6), where ξ_1 is the Hopf bifurcation parameter that controls the convergence speed of the trajectory onto the attractor, ξ_2 is a tuning gain for the coupling strength of the reactive power loop, and ξ_3 is the tuning gain for the coupling strength of the active power loop. Note that the initial conditions for the first-order differential equations (7.

6) should avoid the origin point to initiate an oscillation. The control dynamics introduced in (7. 6) is a general form of the CHO-emulation control strategies with (7. 7) describing the amplitude dynamics and (7. 8) describing the frequency dynamics of the oscillator. For example, if the amplitude dynamics of the inner oscillations are ignored, it can be simplified as the conventional active *p*-*f* and reactive power-voltage (*Q*-*v*) droop control loops; if the external coupling effects from the active power and reactive power are ignored ($\xi_2 = \xi_3 = 0$), it can be simplified as the basic VOC method; while if the tuning gains of the coupling strength in the reactive and active power loop are the same ($\xi_2 = \xi_3$), it will be equivalent to the dVOC approach in [187, 195], furthermore, if the reference voltage is equal to the real voltage in the outer power coupling term ($v_{ref}^2 = v^2$), it can be further simplified as the dVOC method in [196, 197].

$$\begin{cases} \gamma = \dfrac{\omega_o L_g}{R^2 + (\omega_o L_g)^2} \\ \mu = \dfrac{R}{R^2 + (\omega_o L_g)^2} \end{cases} \tag{7. 5}$$

$$\begin{bmatrix} \dot{v}_\alpha \\ \dot{v}_\beta \end{bmatrix} = \begin{bmatrix} O_{C11} & O_{C12} \\ O_{C21} & O_{C22} \end{bmatrix} \begin{bmatrix} v_\alpha \\ v_\beta \end{bmatrix} \tag{7. 6}$$

where,

$$O_{C11} = O_{C22} = \xi_1 \left({v_{ref}}^2 - v^2 \right) + \xi_2 \left(\frac{Q_{ref}}{v_{ref}^2} - \frac{Q}{v^2} \right) \tag{7. 7}$$

$$O_{C21} = -O_{C12} = \omega_o + \xi_3 \left(\frac{P_{ref}}{v_{ref}^2} - \frac{P}{v^2} \right) \tag{7. 8}$$

7.1.2 Open- and Closed-Loop Models of GFMs in pH Framework

A. Open-Loop pH model

The open-loop pH model of the GFM in Figure 7-1 is derived as (7. 9) [79], where the state vector $x = [\varphi_{L\alpha} \quad \varphi_{L\beta} \quad q_\alpha \quad q_\beta]^T = [L_f i_{L\alpha} \quad L_f i_{L\beta} \quad C_f v_\alpha \quad C_f v_\beta]^T$ which are the inductor flux and capacitor charge, $\mathcal{J}_P = -\mathcal{J}_P^T$ is the interconnection matrix as in (7. 10), $\mathcal{R}_P = \mathcal{R}_P^T \geq 0$ is the damping matrix as in (7. 11), $G(x)$ is control matrix as in (7. 12), the u and y are the input and output pairs of the system, and ξ is the external interaction variables as in (7. 13). Note that u represents an ideal voltage source (control vectors in the closed loop) because the switching frequency of an inverter is much higher than the fundamental frequency, the switching effect can be ignored. In addition, the open-loop Hamiltonian function $H_o(x)$ is a smooth function of the states representing the total energy function as given in (7. 14) and its gradient called variable of co-energy $\nabla H_o(x) = \frac{\partial H_o}{\partial x} = [i_{L\alpha} \quad i_{L\beta} \quad v_\alpha \quad v_\beta]^T$.

$$\begin{cases} \dot{x} = (\mathcal{J}_P - \mathcal{R}_P)\nabla H_o(x) + G(x)u + \xi \\ y = G^T(x)\nabla H_o(x) \end{cases} \tag{7. 9}$$

$$\mathcal{J}_P = \begin{bmatrix} 0 & 0 & -1 & 0 \\ 0 & 0 & 0 & -1 \\ 1 & 0 & 0 & 0 \\ 0 & 1 & 0 & 0 \end{bmatrix} \tag{7. 10}$$

$$\mathcal{R}_P = \begin{bmatrix} R_f & 0 & 0 & 0 \\ 0 & R_f & 0 & 0 \\ 0 & 0 & 0 & 0 \\ 0 & 0 & 0 & 0 \end{bmatrix} \tag{7. 11}$$

$$G(x) = \begin{bmatrix} 1 & 0 \\ 0 & 1 \\ 0 & 0 \\ 0 & 0 \end{bmatrix} \tag{7. 12}$$

$$\xi = \begin{bmatrix} 0 & 0 \\ 0 & 0 \\ -1 & 0 \\ 0 & -1 \end{bmatrix} \begin{bmatrix} i_{g\alpha} \\ i_{g\beta} \end{bmatrix} \tag{7. 13}$$

$$H_o(x) = \frac{1}{2} L_f i_{L\alpha}^2 + \frac{1}{2} L_f i_{L\beta}^2 + \frac{1}{2} C_f v_\alpha^2 + \frac{1}{2} C_f v_\beta^2 \tag{7. 14}$$

B. Desired Closed-Loop pH Model

The desired closed-loop pH model combining the general VOC dynamics in (7. 6) is given in (7. 15), where $\mathcal{J}_d(x)$ is given in (7. 16) and $\mathcal{R}_d(x)$ is given in (7. 17) with b_{34} and b_{43} given in (7. 18), a_{11} and a_{22} given in (7. 19), a_{33} and a_{44} given in (7. 20), and ξ_4 is the current loop control gain. Also, the desired closed-loop Hamiltonian function $H_d(x)$ is given in (7. 21).

$$\dot{x} = (\mathcal{J}_d(x) - \mathcal{R}_d(x)) \nabla H_d(x) \tag{7. 15}$$

$$\mathcal{J}_d(x) = \begin{bmatrix} 0 & 0 & 0 & 0 \\ 0 & 0 & 0 & 0 \\ 0 & 0 & 0 & b_{34} \\ 0 & 0 & b_{43} & 0 \end{bmatrix} \tag{7. 16}$$

$$\mathcal{R}_d(x) = \begin{bmatrix} a_{11} & 0 & 0 & 0 \\ 0 & a_{22} & 0 & 0 \\ 0 & 0 & a_{33} & 0 \\ 0 & 0 & 0 & a_{44} \end{bmatrix} \tag{7. 17}$$

$$b_{43} = -b_{34} = C_f O_{C21} \tag{7. 18}$$

$$a_{11} = a_{22} = -L_f \xi_4 \tag{7. 19}$$

$$a_{33} = a_{44} = -C_f O_{C11} = -C_f O_{C22} \tag{7. 20}$$

$$H_d(x) = \frac{1}{2}L_f\left(i_{L\alpha} - i_{L\alpha ref}\right)^2 + \frac{1}{2}L_f\left(i_{L\beta} - i_{L\beta ref}\right)^2 + \frac{1}{2}C_f v_\alpha^2 + \frac{1}{2}C_f v_\beta^2 \tag{7. 21}$$

7.2 Extended Passivity-based VOC Control of GFMs

7.2.1 Passivity-based VOC Method in pH System

The control vector u can then be solved as given in (7. 22) by matching the open-loop pH model in (7. 9) and desired closed-loop pH model in (7. 15). The detailed derivation process can be seen in Appendix B.

$$u = \begin{bmatrix} u_\alpha \\ u_\beta \end{bmatrix} = \begin{bmatrix} -L_f\xi_4(i_{L\alpha ref} - i_{L\alpha}) + R_f i_{L\alpha} + v_\alpha \\ -L_f\xi_4(i_{L\beta ref} - i_{L\beta}) + R_f i_{L\beta} + v_\beta \end{bmatrix} \tag{7. 22}$$

Then, the passivity-based control theory can be applied to design the GFM to be stable with this control vector.

The conventional passivity-based design is based on the interconnection damping assignment (IDA) approach [204], which is to design the closed-loop pH model in (7. 15) to meet the following criteria:

(1) $\mathcal{R}_d(x) = \mathcal{R}_d^T(x) \geq 0$ is positive semi-definite.

(2) $\mathcal{J}_d(x) = -\mathcal{J}_d^T(x)$ is skew-symmetric.

(3) $H_d(x)$ is a local minimum at desired equilibrium point $x*$.

However, the IDA approach is mainly intended for a fixed-point regulation or tracking of a reference, it does not meet the design goal in this study, which is to achieve a stable orbit. Therefore, for orbital stabilization, a modified IDA passivity-based approach via energy pumping and damping motion is adopted as follows [205]:

First, the closed-loop Hamiltonian function $H_d(x)$ in (7. 21) is decomposed into two parts: $H_l(x_l)$ as given in (7. 23) which is to track the current reference following the conventional IDA approach and $H_p(x_p)$ as given in (7. 24) which is to push the state trajectory to the desired orbit.

Second, a function $\Phi(x_p)$ that defines the Jordan curve, a non-self-intersecting continuous loop in the plane is given in (7. 25), with the desired capacitor energy level $H_p^* = \frac{1}{2}C_f(v_{\alpha ref}^2 + v_{\beta ref}^2) = \frac{1}{2}C_f v_{ref}^2 > min\left(H_p(x_p)\right)$.

Third, the damping matrix $\mathcal{R}_\mathrm{d}(\mathrm{x})$ in (7. 17) is reformatted as (7. 26), where, $\mathcal{R}_{ll} = \begin{bmatrix} a_{11} & 0 \\ 0 & a_{22} \end{bmatrix}$, $\mathcal{R}_{pp} = \begin{bmatrix} a_{33} & 0 \\ 0 & a_{44} \end{bmatrix}$.

Then, as shown in Figure 7-2 when H_p is larger than H_p^*, i.e., $\Phi(x_p) > 0$, the corresponding energy function should be damped, i.e., $\mathcal{R}_\mathrm{pp} > 0$; when H_p is smaller than H_p^*, i.e., $\Phi(x_p) < 0$, more energy should be pumped into the energy function, i.e., $\mathcal{R}_\mathrm{pp} < 0$.

Therefore, with $\mathcal{R}_\mathrm{ll} > 0$ and $\mathcal{R}_\mathrm{pp}$ satisfying the damping-and-pumping conditions in (7. 27), the modified IDA passivity-based criteria can be obtained.

Note that several assumptions have been made to ensure that the system is asymptotically orbitally stable, including:

(H1) x_l^* is the largest invariant set in the set $\{x_l \in \mathbb{R}^{n-2} | \nabla^T H_l(x_l)\mathcal{R}_{ll}(x_l)\nabla H_l(x_l) = 0\}$;

(H2) $\mathcal{J}_d(x)$ satisfies $\nabla^T H_p(x_p)\mathcal{J}_{pl}(x) = 0$ and $\mathcal{J}_{(1,2)}(x) = \frac{c(x)}{\nabla x_0 H_{d0}(x_l, x_0)}|_{x_0=\Phi(x_p)} \neq 0$, where $0 < |c(x)| < \infty$;

(H3) for some $\varepsilon_* > 0$ and ε_* -neighborhood $B_{\varepsilon_*}(x_p^*)$, $\nabla^2 H_p|_{x_p \in B_{\varepsilon_*}(x_p^*)} > 0$ and $max_{B_{\varepsilon_*}(x_p^*)} H_p(x_p) > H_p^*$.

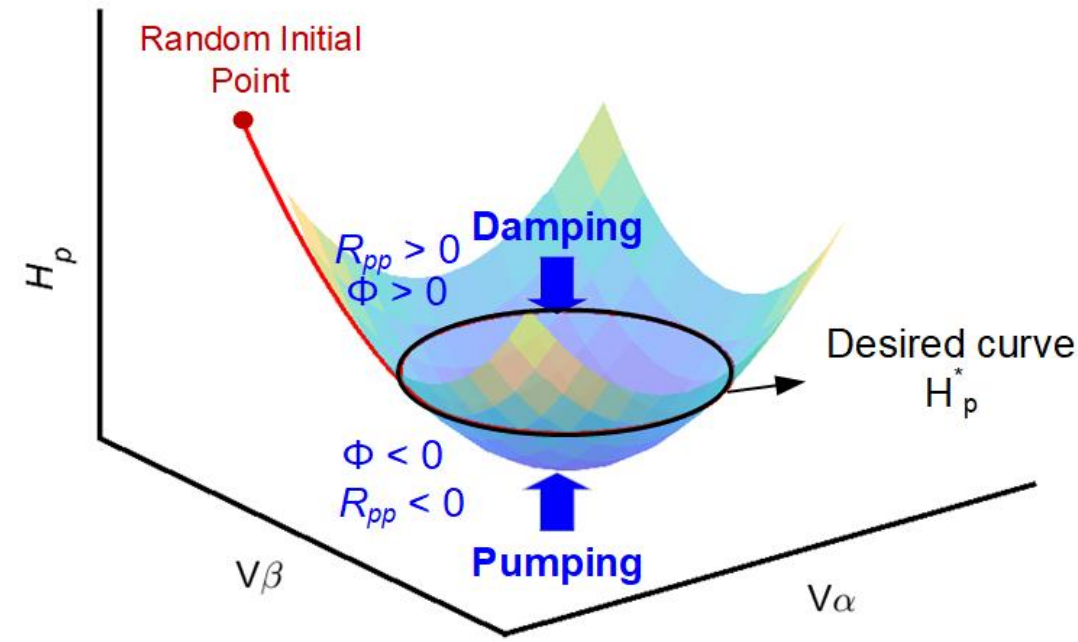

Figure 7-2. Desired energy level H_p^* and closed orbit through energy pumping and damping motion.

The assumptions H1 and H2 ensure that $\lim_{t\to\infty} x_l(t) = x_l^*$ which means the current can only converge to the reference current in the steady state, and the assumptions H2 and H3 guarantee that the voltage oscillator can only converge to the desired orbit.

$$H_l(x_l) = \frac{1}{2}L_f\left(i_{L\alpha} - i_{L\alpha ref}\right)^2 + \frac{1}{2}L_f\left(i_{L\beta} - i_{L\beta ref}\right)^2 \tag{7. 23}$$

$$H_p(x_p) = \frac{1}{2}C_f v_\alpha^2 + \frac{1}{2}C_f v_\beta^2 \tag{7. 24}$$

$$\Phi\left(x_p\right) = H_p(x_p) - H_p^* \tag{7. 25}$$

$$\mathcal{R}_d = \begin{bmatrix} \mathcal{R}_{ll_{2\times2}} & 0_{2\times2} \\ 0_{2\times2} & \mathcal{R}_{pp_{2\times2}} \end{bmatrix} \tag{7. 26}$$

$$\mathcal{R}_{pp}\Phi \geq 0 \text{ and } \mathcal{R}_{pp} = 0 \Leftrightarrow \Phi\left(x_p\right) = 0 \tag{7. 27}$$

7.2.2 Function Blocks of Proposed Control Approach

The detailed function block of the control vectors given in (7. 22) can be found in Figure 7-3 which consists of three parts:

1) the external coupling control to determine the coupling strength between the inverter and the grid to achieve system synchronization through the active and reactive power regulation;

2) the internal oscillation control to mimic the virtual oscillator behavior of three-phase output voltage in *αβ0* frame;

3) the inner current control to provide damping for the current loop.

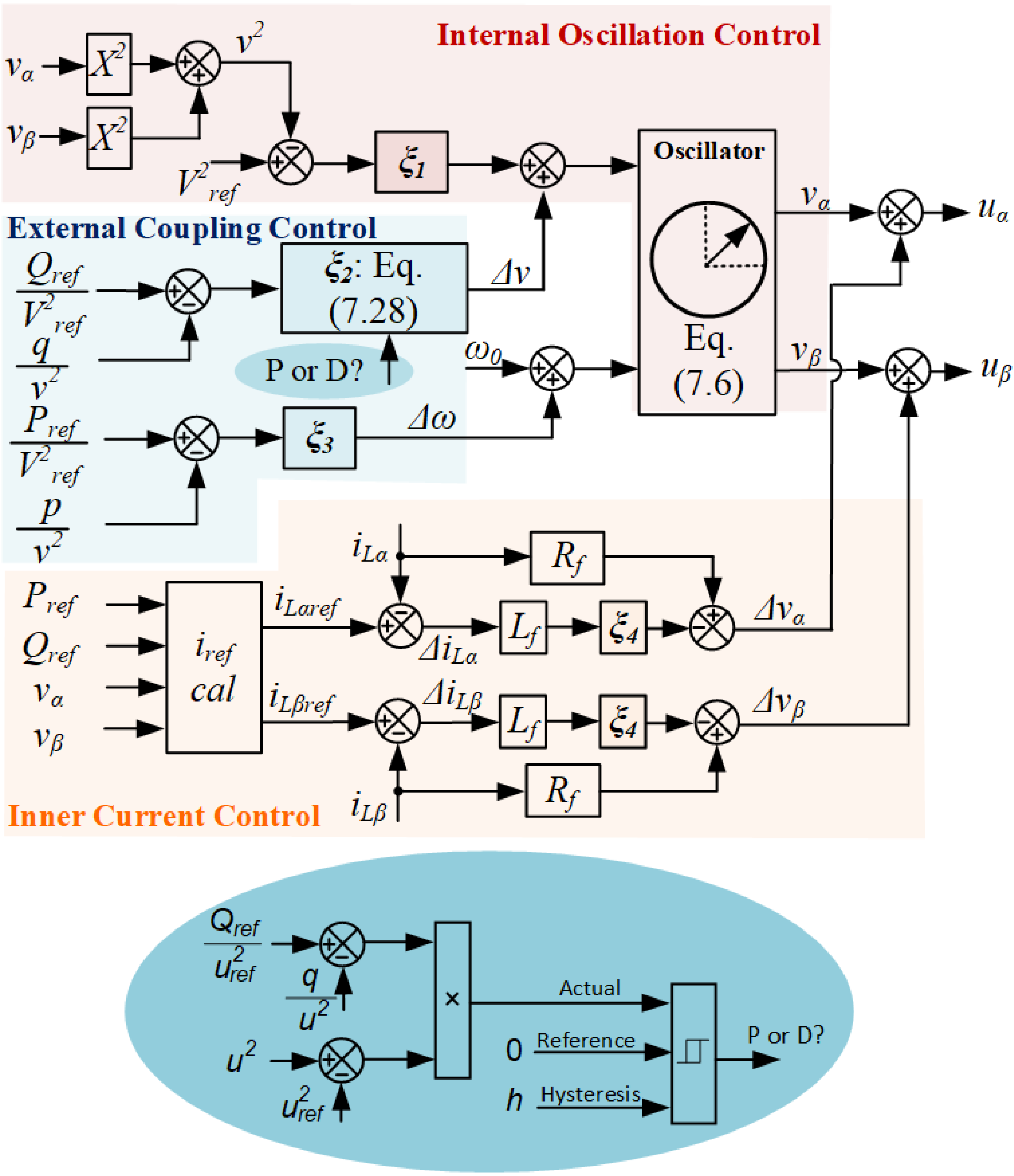

Figure 7-3. Function blocks of the proposed passivity-based VOC method for GFMs.

Applying the modified IDA criterion to the design of parameters, the following three requirements can be obtained.

(1) $b_{43} = -b_{34} \neq 0$. Also, ξ_3 should not be designed to be too large because the steady-state fundamental frequency of the inverter should be the same as the grid frequency so that the prespecified ac power flow solutions are still valid.

(2) to achieve $\mathcal{R}_{ll} > 0$, ξ_4 should be negative.

(3) to meet the criterion in (7. 27), the sign of ξ_2 should be adjusted following the rule in (7. 28) and ξ_1 should be positive. Note the pumping-and-damping motion is the same as the one in Figure 6-4.

$$sgn(\xi_2) = -sgn\left(\left(\frac{Q_{ref}}{v_{ref}^2} - \frac{Q}{v^2}\right)\left(v^2 - v_{ref}^2\right)\right) \tag{7. 28}$$

7.3 Stability Analysis of Extended Passivity-based VOC Approach

7.3.1 Lyapunov stability analysis

To further validate that the GFM with the proposed design is asymptotically stable, a Lyapunov energy function $V(x)$ can be constructed as (7. 29) based on the Hamiltonian functions. First, it can be easily proven that $\mathrm{V}(x) > 0$ for $\forall x \neq x_{ref}$. Then, taking the time derivative of $V(x)$, (7. 30) can then be obtained. According to $\mathcal{R}_{ll} > 0$ and (7. 27), it can be concluded that $\dot{V}(x) < 0$ for $\forall x \neq x_{ref}$. Also, when $||x|| \to \infty, V(x) \to \infty$. Therefore, based on the properties of Lyapunov's second method and LaSalle's theorem, it is proven that the system is GAS in the region of attraction which is defined as $\Omega = \{x \in R^n | \dot{V}(x) \leq 0\}$[206]. The derivation process can be seen in Appendix C.

$$V(x) = H_l(x_l) + \frac{1}{2}\Phi^2(x_p) \tag{7. 29}$$

$$\dot{V}(x) = -\nabla^T H_l R_{ll} \nabla H_l - \nabla^T H_p \left[R_{pp}\Phi\right] \nabla H_p \tag{7. 30}$$

Applying LaSalle's invariance principle, the state will ultimately converge into the largest invariant set $\mathcal{A}$ of the set $\{x \in R^n | x_l = x_l^*, \left[R_{pp}(x)\Phi(x)\right]\nabla H_p(x) = 0\}$. It has been proven in [205] that $\mathcal{A} = \mathcal{C} \cup col\left(x_p^*, x_l^*\right)$ and $\mathcal{C}$ is a non-empty attractive closed orbit. That means if the GFM meets the modified IDA passivity-based criterion, it can eventually approach the desired voltage oscillator and current equilibrium points starting from any initial state.

7.3.2 Comparisons of Proposed Control Method with Existing Approaches

The stability of the proposed control approach has been mathematically analyzed based on the Lyapunov stability theorem in Section 7.3.1. It has been proved that the inverter can reach the steady-state operating point from any initial conditions due to the passivity-based control.

To be more specific with the concept of power system stability, in this section, the synchronization stability will be investigated under the three scenarios:

(SC1): The inverters should be able to maintain synchronism in the grids with different grid short-circuit-ratios (SCRs) under small disturbances;

(SC2): The GFMs should maintain system *transient stability* under large disturbances, such as load dispatch, fault, line impedance variations, etc.;

(SC3): For systems with many small-to-medium and distributed GFMs, it is important to have a decentralized control method so that GFMs are capable of maintaining system *synchronization stability* in a local way [43].

First of all, it has already been shown in [149] that the dVOC approaches are superior to the conventional droop control in terms of system synchronization stability. Therefore, the proposed approach will not be compared with conventional droop control and will only be compared with the more advanced dVOC approaches.

Additionally, since the proposed control is developed based on the mechanism of coupled harmonic oscillators, it will have a similar structure as the existing dVOC approaches [187, 195-197]. Note that in the following discussion, the method in [196, 197] will be denoted as dVOC1, the method in [187, 195] will be denoted as dVOC2, and the proposed method will be denoted as PVOC.

The circuit diagrams of system synchronization stability-related control blocks of dVOC1, dVOC2, and PVOC (ignoring the inner current loop in Figure 7-3) can be obtained respectively as shown in Figure 7-4 where the voltage oscillators are built based upon the line-to-line RMS value of the output voltage.

The synchronization stability performance of the proposed PVOC can then be compared with the dVOC approaches.

For SC1 and SC3, comparison results between the dVOC and the proposed approach can be easily obtained. First, for SC1, it has been proved in [149] that the dVOC approach will always remain stable as long as an equilibrium operating point exists with constant voltage amplitude. The same conclusion can be reached for the proposed control approach since if neglecting the voltage amplitude dynamics, the proposed PVOC would be the same as dVOC1 and dVOC2. Second, for SC3, the proposed approach is developed based on the theorem of passivity-based control design, so the stability of interconnection of multiple inverters can be guaranteed, while the control parameters of the dVOC approaches need to be designed with the system information.

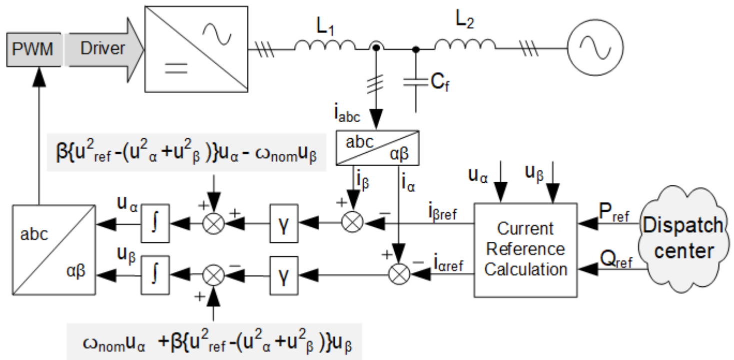

(a)

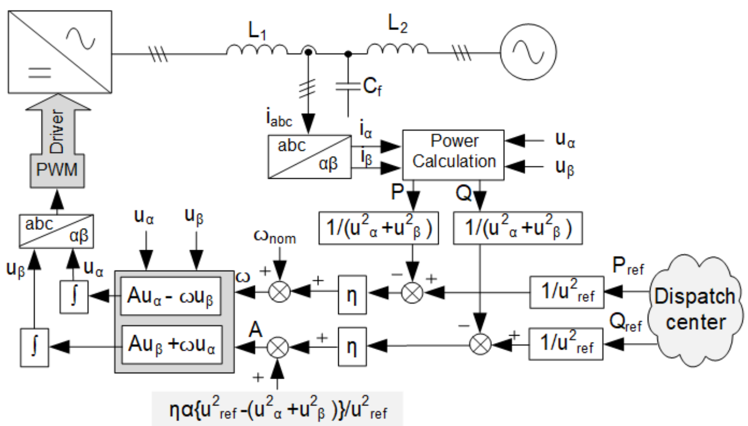

(b)

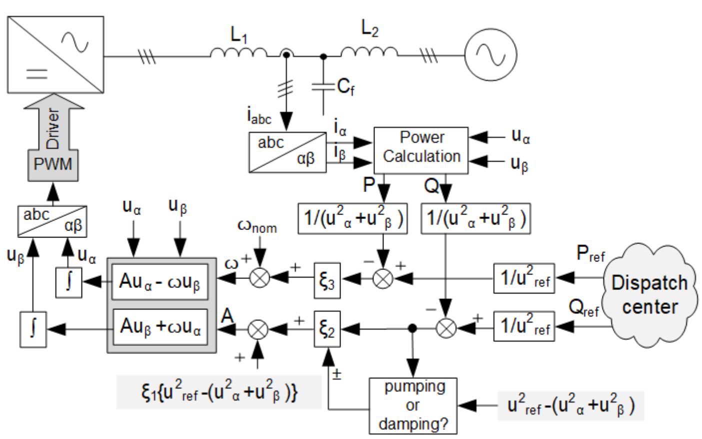

(c)

Figure 7-4. Function Control diagrams of different VOC approaches: (a) dVOC1[196, 197], (b) dVOC2 [187, 195], and (c) proposed PVOC.

While for SC2, a case study will be given below to illustrate the different performances between the proposed control and the existing dVOC approaches. A system of a GFM connected to an infinite bus through two paralleled transmission lines as shown in Figure 7-5 is adopted as an example for a comparison study of system transient stability. Two fault scenarios will be considered, including

(1) open-circuit fault (OCF) on Line 1;

(2) short-circuit fault (SCF) with L_{short} = 1 mH on Line 2.

More specifically, for the OCF, it is assumed that the fault happens at 4 s, during the fault there is an equilibrium point, and the fault will be cleared by restoring Line 1 at 8 s. For the SCF, it is assumed that the fault happens at 2 s, during fault there is no equilibrium point, and the fault will be cleared by disconnecting Line 2 after 250 ms.

To achieve a fair comparison, the control parameters of the three methods are designed to be equivalent. Also, two groups of control parameters considering different voltage oscillator convergence speeds are investigated, including a fast- and a slow- oscillator convergence speed. A larger value of β, α or ξ_1 means a faster voltage convergence speed [196]. The detailed electrical and control parameters of the test system are given in Table 7-1. The dynamic equations for the three VOC approaches can be obtained for the system transient stability analysis. The frequency and voltage dynamic equations for dVOC1 can be obtained as (7. 31) and the equations for dVOC2 are given in (7. 32), where γ and η are the power control gains, β and α are oscillator convergence speed. For the proposed method, the current loop has almost no impact on system transient stability due to its small control gain and thus can be neglected. The frequency and voltage dynamic equations for PVOC can then be obtained as (7. 33), where ξ_1 is the oscillator convergence speed, ξ_2 and ξ_3 are the power loop control parameters. Note that u in these equations

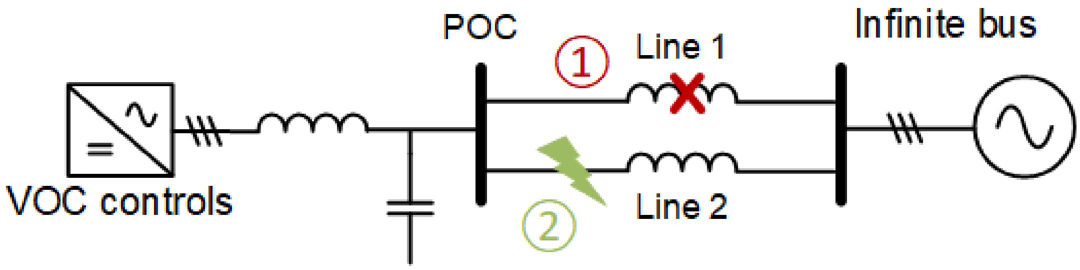

Figure 7-5. Test scenarios of the transient stability analysis.

Table 7-1. Electrical and control parameters of the test system.

<table>
<tr><th colspan="2">Variables</th><th>Value</th><th>Variables</th><th>Value</th></tr>
<tr><td colspan="2">Output power</td><td>600 W/ 1 pu</td><td>Peak phase voltage</td><td>40.8 V/ 1 pu</td></tr>
<tr><td colspan="2">System frequency</td><td>60 Hz</td><td>Line 1</td><td>6 mH/ 0.54 pu</td></tr>
<tr><td colspan="2">Output inductance</td><td>2.4mH/ 0.22 pu</td><td>Line 2</td><td>6 mH/ 0.54 pu</td></tr>
<tr><td colspan="2">Power droop gain</td><td colspan="3">$\gamma = \eta = |\xi_2| = \xi_3 = 15$</td></tr>
<tr><td rowspan="2">Oscillator convergence speed</td><td>Fast</td><td colspan="3">$\beta = \xi_1 = \frac{\eta\alpha}{u_{ref}^2} = 0.02$</td></tr>
<tr><td>Slow</td><td colspan="3">$\beta = \xi_1 = \frac{\eta\alpha}{u_{ref}^2} = 0.001$</td></tr>
</table>

is the control voltage, not the output voltage of the inverter. Also, assume that the cut-off frequency of the LPFs in the measured power signals is large enough, so their impacts can be neglected for the transient stability analysis here.

$$\begin{cases} \dot{\delta} = \frac{\gamma}{u^2}\left\{P_{ref} - P(u)\sin\delta\right\} \\ \dot{u} = \beta\left(u_{ref}^2 - u^2\right)u + \frac{\gamma}{u}\left\{Q_{ref} - Q(u,\delta)\right\} \end{cases} \tag{7. 31}$$

$$\begin{cases} \dot{\delta} = \eta\left(\frac{P_{ref}}{u_{ref}^2} - \frac{P(u)\sin\delta}{u^2}\right) \\ \dot{u} = \frac{\eta\alpha}{u_{ref}^2}\left(u_{ref}^2 - u^2\right)u + \eta\left(\frac{Q_{ref}}{u_{ref}^2} - \frac{Q(u,\delta)}{u^2}\right)u \end{cases} \tag{7. 32}$$

$$\begin{cases} \dot{\delta} = \xi_3\left(\frac{P_{ref}}{u_{ref}^2} - \frac{P(u)\sin\delta}{u^2}\right) \\ \dot{u} = \xi_1\left(u_{ref}^2 - u^2\right)u + \xi_2\left(\frac{Q_{ref}}{u_{ref}^2} - \frac{Q(u,\delta)}{u^2}\right)u \end{cases} \tag{7. 33}$$

To analyze the system transient stability, these two coupled dynamic equations in (7. 31)-(7. 33) will be numerically solved using the MATLAB command 'ode45' with which the phase portrait $\dot{\delta} - \delta$ and $u - \delta$ curve can be plotted, then the time-domain simulation results will be obtained to further verify the analysis results.

A. Transient stability under different fault conditions

Case 1. Fast convergence speed under OCF

In Case I with the OCF on Line 1 and with the fast convergence speed of the oscillator control, it can be seen from Figure 7-6 that the system with all three control methods can reach a steady-state operating point before the fault occurs (i.e., $\dot{\delta} = 0$ in phase portrait) from a random initial point, during the fault, and after the fault is cleared, separately.

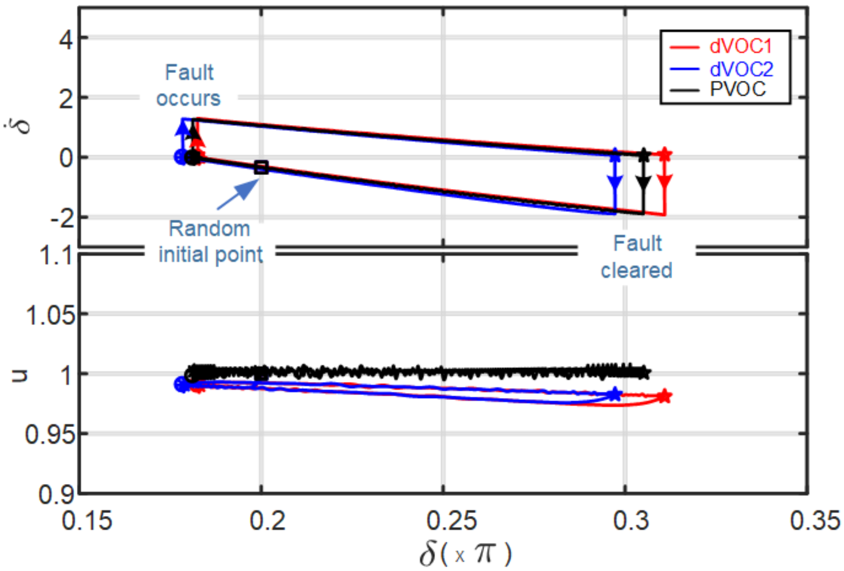

(a)

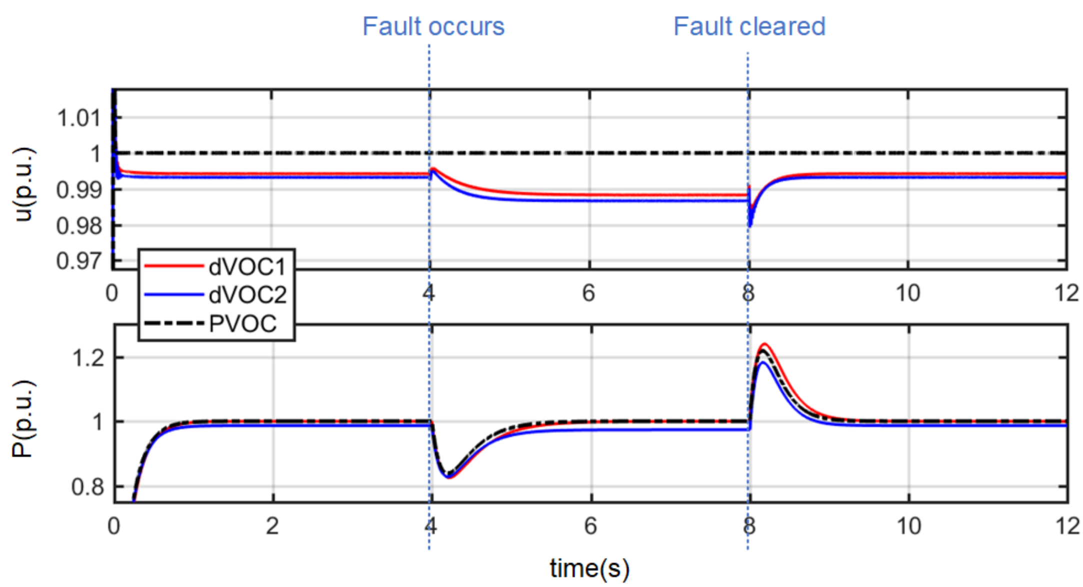

(b)

Figure 7-6. Transient stability under OCF with fast convergence speed: (a) analytical result and (b) simulation result.

Also, since the fault is cleared by restoring Line 1, the system will return to the same operating point as the pre-fault condition after the fault is cleared. Additionally, the PVOC has better control voltage regulation capability (i.e., u = 1 p.u.) than the other two approaches.

Case 2. Slow convergence speed under OCF

In Case 2 with the OCF on Line 1 and with a slow convergence speed of the oscillator control, it can be seen from Figure 7-7 that the system with dVOC2 and PVOC can reach a steady-state operating point before the fault occurs, during the fault, and after the fault is cleared, separately. However, the system with dVOC1 loses synchronism during the fault and cannot return to steady-state conditions after the fault is cleared because of the sharp voltage drop. Additionally, the proposed PVOC has better voltage and power regulation capability than dVOC2.

Case 3. Fast convergence speed under SCF

In Case 3 with the SCF on Line 2 and with the fast convergence speed of the oscillator control, it can be seen from Figure 7-8 that the system with all the three control methods can reach a steady-state operating point before the fault occurs and after the fault is cleared, separately. And during the fault, since no equilibrium point exists, none of the three methods can reach a steady state. In addition, the fault is cleared by disconnecting Line 2, so the system will return to another operating point after the fault is cleared. Additionally, it can also be noticed that the PVOC approach has better voltage regulation capability than the other two approaches.

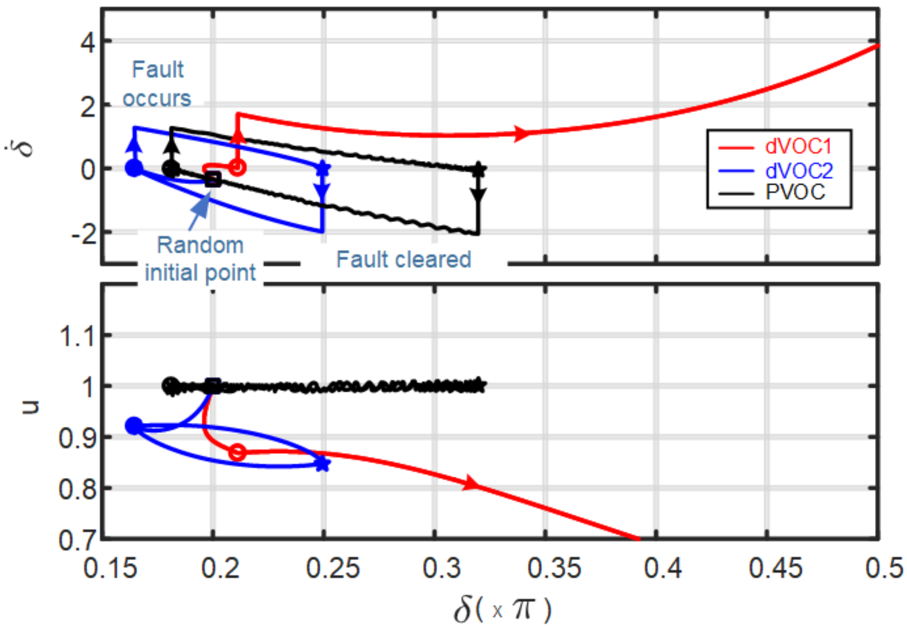

(a)

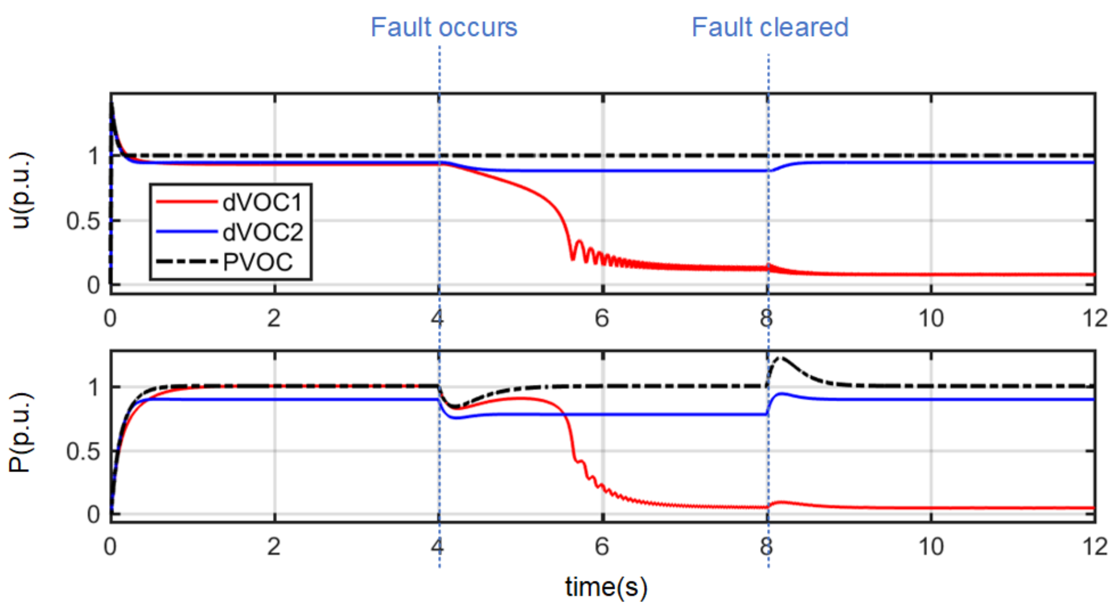

(b)

Figure 7-7. Transient stability under OCF with slow convergence speed: (a) analytical result and (b) simulation result.

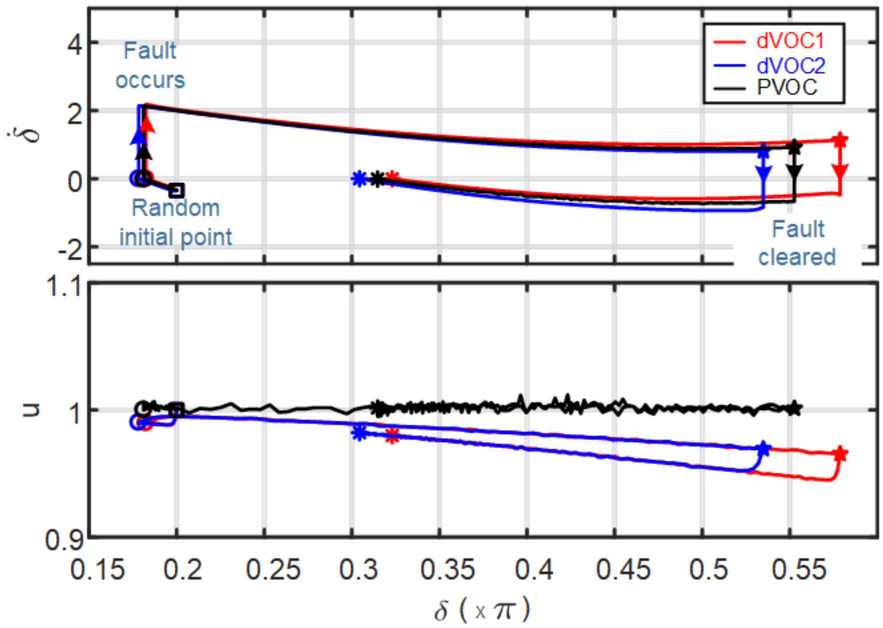

(a)

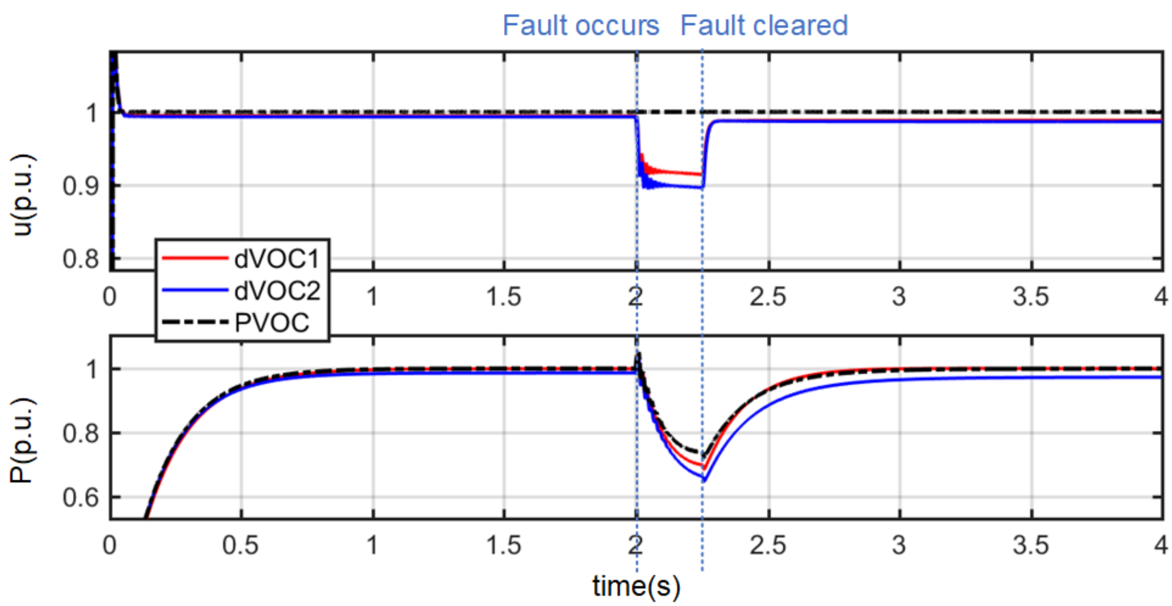

(b)

Figure 7-8. Transient stability under SCF with fast convergence speed: (a) analytical result and (b) simulation result.

Case 4. Slow convergence speed under SCF

In Case 4 with the SCF on Line 2 and with a slow convergence speed of the oscillator control, it can be seen from Figure 7-9 that the system with both dVOC2 and PVOC can reach a steady-state operating point before the fault occurs and after the fault is cleared, separately.

And during the fault, since no equilibrium point exists, neither of the two methods can reach a steady state. In addition, the fault is cleared by disconnecting Line 2, so the system will return to another operating point after the fault is cleared.

Moreover, the proposed PVOC has better voltage regulation and power regulation capability than dVOC2. While the system with dVOC1 will lose synchronism during the fault and cannot return to a steady state after the fault is cleared due to the sharp voltage drop.

B. Impacts of LPFs in Power Loops on System Stability

From the results of the comparisons above, it can be concluded that dVOC1 has worse stability performance than dVOC2 and PVOC. In addition, dVOC2 has poorer voltage and power regulation capability than PVOC.

And in this subsection, stability comparisons will be continued between dVOC2 and PVOC with considering the LPFs in the power measurement loops when the cut-off frequency is low.

Normally, LPFs are added to filter out the noises in the measured power. So, the phase and voltage dynamics of dVOC2 and PVOC can be modified as (7. 34) and (7. 35), separately, where ω_{LPF} is the cut-off frequency of the LPF and s is the Laplace operator.

The system transient stability will be analyzed under Scenario 4 where there is a short-circuit fault on Line 2 with slow oscillator voltage convergence speed. The cut-off frequency of the LPFs that are added in both active power and reactive power loops is 1 Hz.

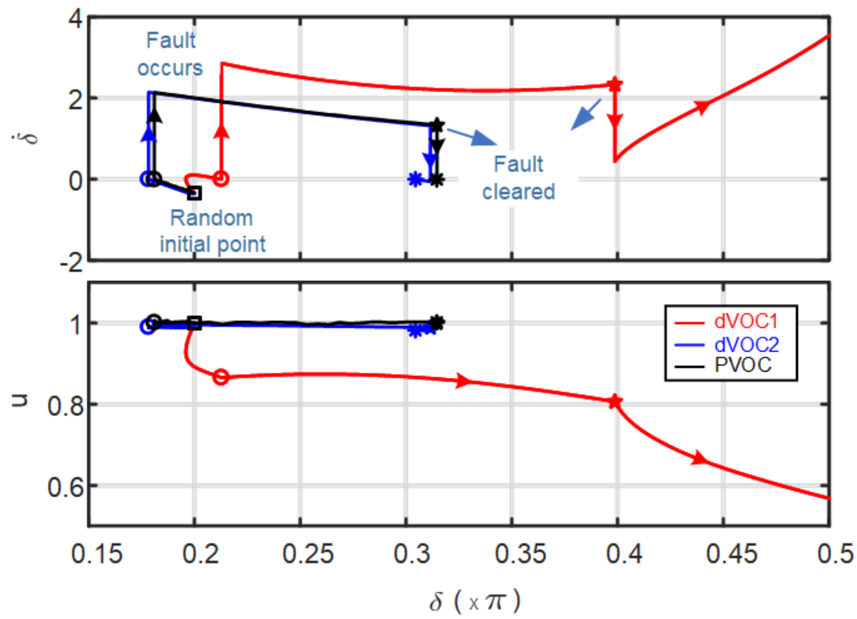

(a)

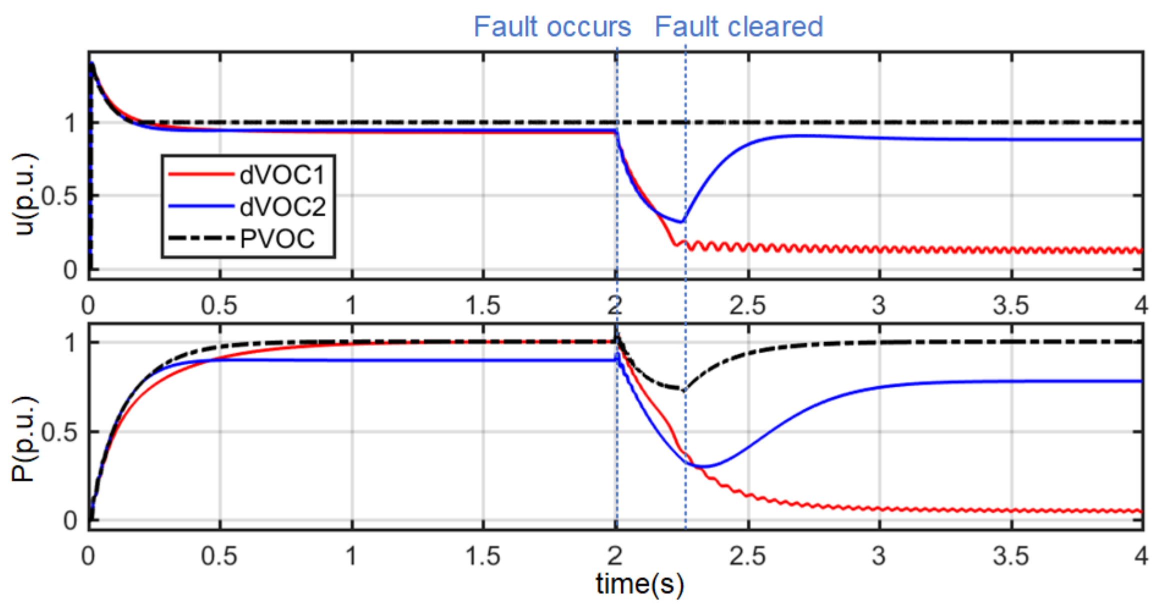

(b)

Figure 7-9. Transient stability under SCF with slow convergence speed: (a) analytical result and (b) simulation result.

$$\begin{cases} \dot{\delta} = \eta\left(\frac{P_{ref}}{u_{ref}^2} - \frac{\omega_{LPF}}{s+\omega_{LPF}}\frac{P(u)\sin\delta}{u^2}\right) \\ \dot{u} = \frac{\eta\alpha}{u_{ref}^2}\left(u_{ref}^2 - u^2\right)u + \eta\left(\frac{Q_{ref}}{u_{ref}^2} - \frac{\omega_{LPF}}{s+\omega_{LPF}}\frac{Q(u,\delta)}{u^2}\right)u \end{cases} \tag{7. 34}$$

$$\begin{cases} \dot{\delta} = \xi_3\left(\frac{P_{ref}}{u_{ref}^2} - \frac{\omega_{LPF}}{s+\omega_{LPF}}\frac{P(u)\sin\delta}{u^2}\right) \\ \dot{u} = \xi_1\left(u_{ref}^2 - u^2\right)u + \xi_2\left(\frac{Q_{ref}}{u_{ref}^2} - \frac{\omega_{LPF}}{s+\omega_{LPF}}\frac{Q(u,\delta)}{u^2}\right)u \end{cases} \tag{7. 35}$$

Figure 7-10 and Figure 7-11 show the simulation results of the transient stability with dVOC2 and PVOC. Since it is difficult to solve the dynamic equations in (7. 34) and (7. 35) directly, the $\dot{\delta} - u - \delta$ will be drawn based on the simulation results instead as in Figure 7-10. From the time-domain simulation results in Figure 7-11, it can be seen that dVOC2 will lose synchronism when the fault occurs and cannot return to steady-state operating conditions after the fault is cleared due to the sharp voltage drop when LPFs are added to the power measurement loops. The proposed PVOC approach can maintain system stability even though the slow dynamics of LPFs are considered.

Also, the impacts of the two LPFs in the active power and reactive power loop of dVOC2 are unlike those in the conventional active power-frequency (*p*-*f*) and reactive power-voltage (*Q*-*v*) droop control. Ref. [158] concludes that the slow LPF in the *p*-*f* droop control loop will degrade the system stability, while the slow LPF in *Q*-*v* droop control loop can improve the system stability. However, for the dVOC2 approaches, the LPF in the active power loop does not affect system stability, while the LPF in the reactive power loop will affect system transient stability. That is, a slow LPF with a low cut-off frequency of reactive power loop can exacerbate the system transient stability. As shown in Figure 7-12, it is assumed that $\omega_{LPF} = 1$ Hz in the active power loop, and

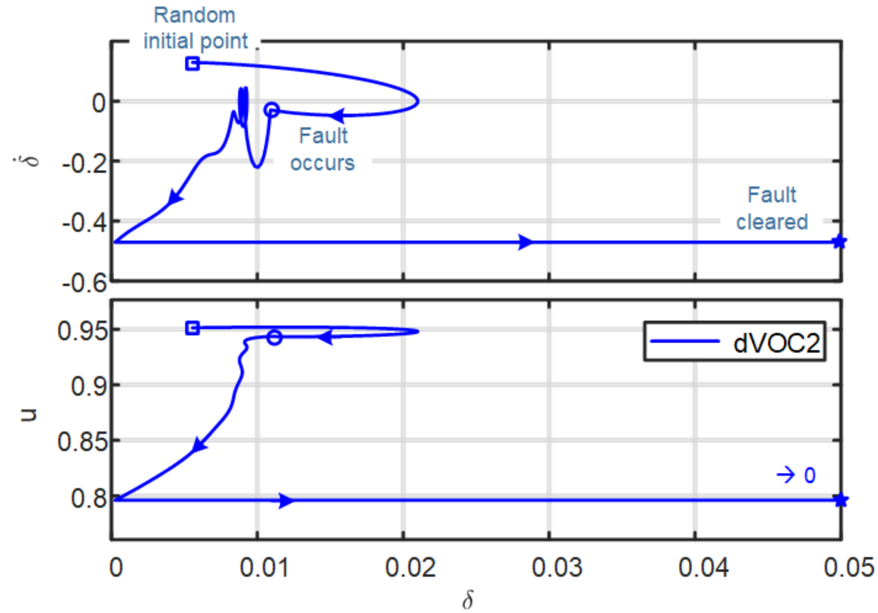

(a)

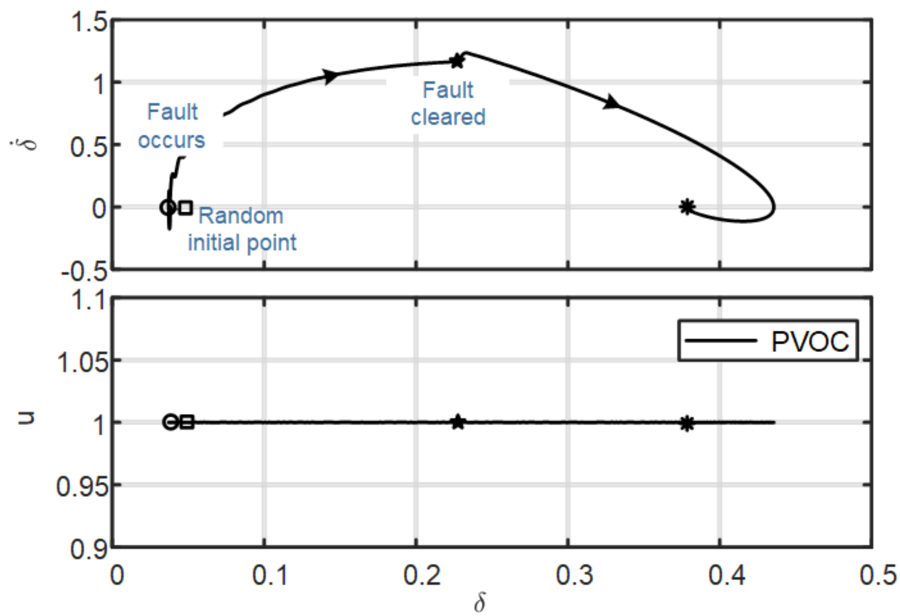

(b)

Figure 7-10. Simulation results of transient stability under SCF with fast convergence speed and LPFs in power measurement loop: (a) $\dot{\delta} - u - \delta$ curve of dVOC2 and (b) $\dot{\delta} - u - \delta$ curve of PVOC.

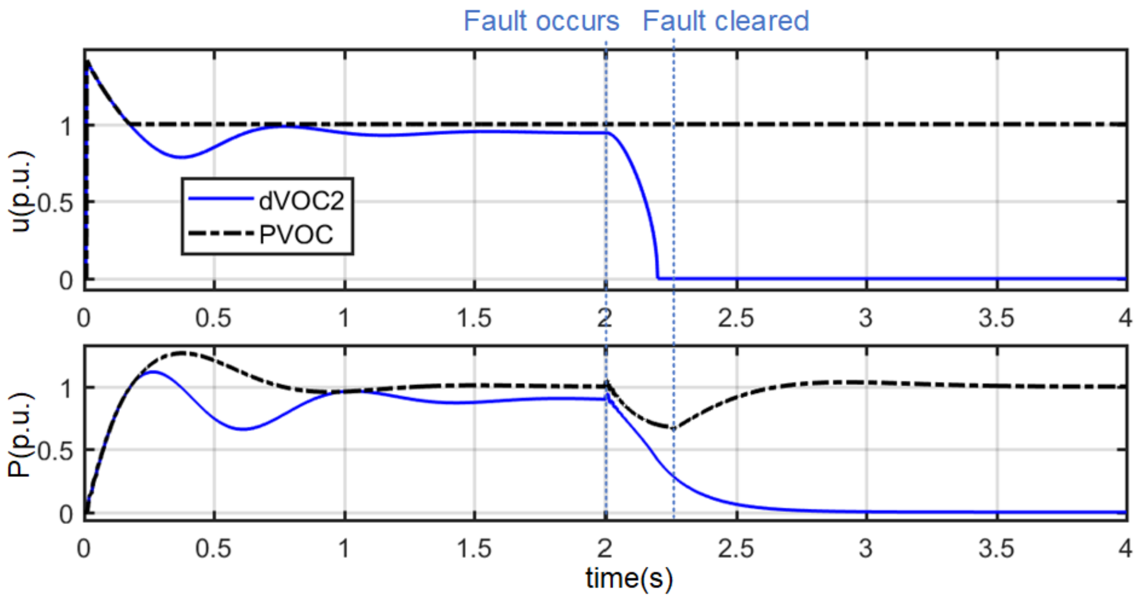

Figure 7-11. Time-domain simulation results of transient stability under SCF with fast convergence speed and LPFs in the power measurement loop.

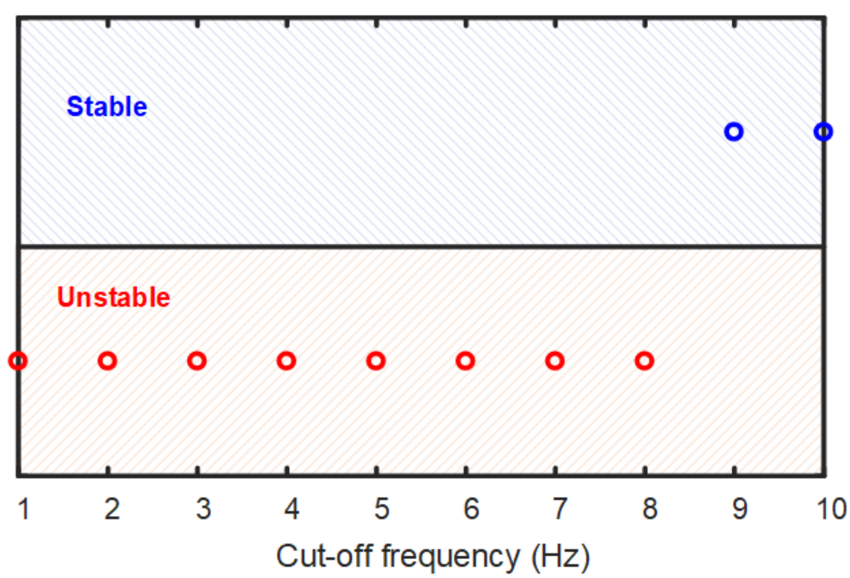

Figure 7-12. Transient stability of dVOC2 in Scenario 4 with different ω_{LPF} of reactive power loop (ω_{LPF} = 1 Hz of active power loop).

with the increase of ω_{LPF} in the reactive power loop, the system can be stabilized. Also, if the ω_{LPF} is infinite (i.e., no LPFs), the system with dVOC2 is stable as shown in Figure 7-9.

The LPFs in the power loops of the proposed PVOC will not affect system transient stability because of the good voltage regulation capability provided by the pumping-and-damping motion in the reactive power loop.

C. Discussions

The comparative transient stability studies above are under the system natural responses without considering any control limits or hardware limits. In this subsection, the impacts of these limits on system stability performance will be discussed.

1) Control limits

In the above analysis, it is assumed that the fault conditions will not trigger the overcurrent protection of the inverter. The current limitation control scheme for VOC approaches is still an open issue, and it is out of the scope of this research.

The control limits that are going to be considered are the frequency saturation in the active power loop and voltage saturation in the reactive power loop of the dVOC2 and PVOC approaches as shown in Figure 7-13. The frequency limitations are designed as ±5% of ω_{nom}, and the voltage limitations are designed as ±10% of nominal voltage. Also, the two LPFs with 1 Hz cut-off frequency in the active power and reactive power loops are considered. In dVOC1, there is no such saturation block so it will not be considered here.

To investigate the impacts of the control limits on system transient stability, simulations for both dVOC2 and PVOC are conducted under Scenario 4.

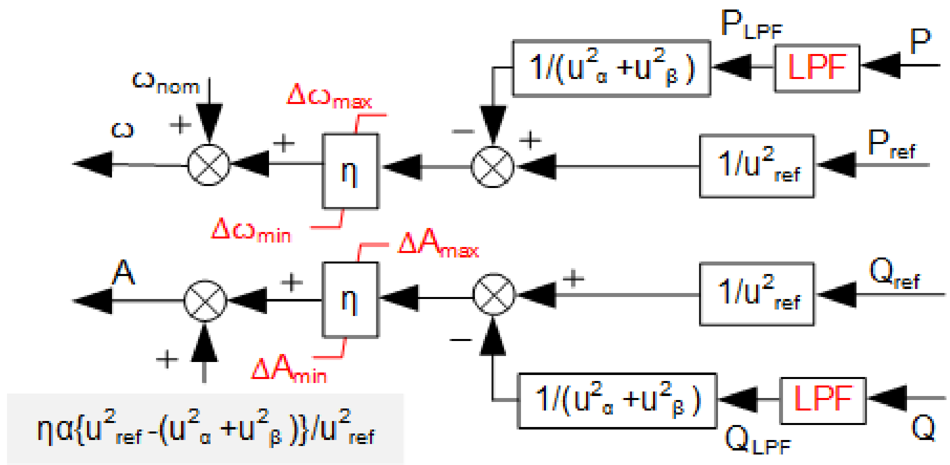

(a)

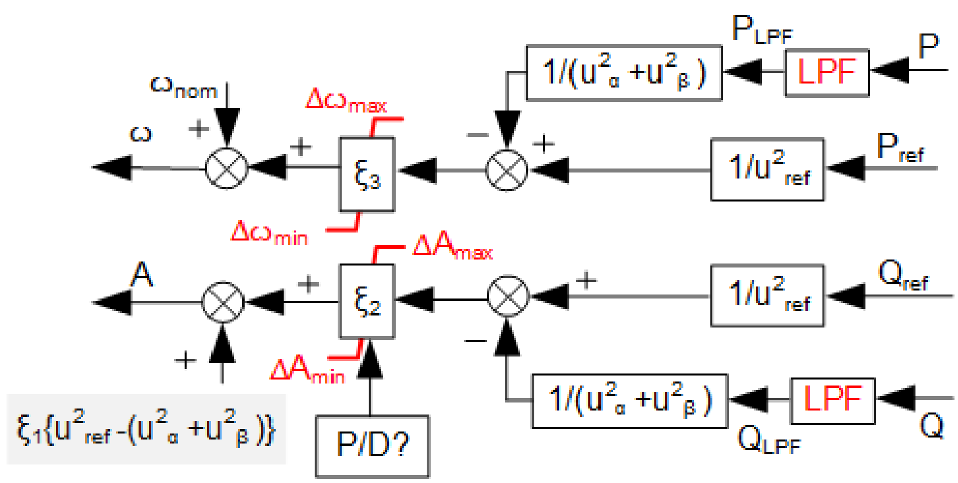

(b)

Figure 7-13. Control diagrams with frequency and voltage saturation blocks: (a) dVOC2 and (b) PVOC.

Figure 7-14 shows the simulation results of dVOC2. It can be observed that during the SCF if there is no saturation block in either loop, the system will lose synchronism during a fault and after the fault is cleared; but if there are saturation blocks in both loops, the frequency loop is not saturated, while the voltage is saturated. And by limiting the voltage during the fault, the system stability is improved and can return to stable operations after the fault is cleared.

Figure 7-15 shows the simulation results of PVOC under Scenario 4. It can be seen that the saturation blocks in the two loops will not affect system transient stability.

2) Requirements for Inverter Capability

Though the current limitation of GFMs is neglected in this chapter, it is still important to examine the requirements on the inverter capability when applying the proposed PVOC approach.

Also, the requirements for the inverter capability of dVOC1 and dVOC2 are compared while still considering system transient stability under Scenario 4.

The simulation results (inductor phase *a* current i_{La}, control voltage u, and reactive power Q) under dVOC1, dVOC2 with or without the saturation blocks, and PVOC with and without the saturation blocks are given in Figure 7-16. The peak currents of phase *a* during fault under all these VOC controls are practically the same, which is about 4 p.u.. The overcurrent duration of PVOC is longer than the other two approaches, and the reactive power of PVOC during fault is larger than dVOC approaches. This means that in order to have better system transient stability performance, it is necessary to have higher inverter reactive capacity. Specifically, the PVOC approach can provide more reactive power to maintain the control voltage during the fault, therefore, the system stability is guaranteed; while for dVOC1 and dVOC2 (no saturation block), due to the sharp voltage drop during the fault, the system loses synchronism and cannot return to steady state after the fault is cleared. It can also be inferred that if there are extra reactive power

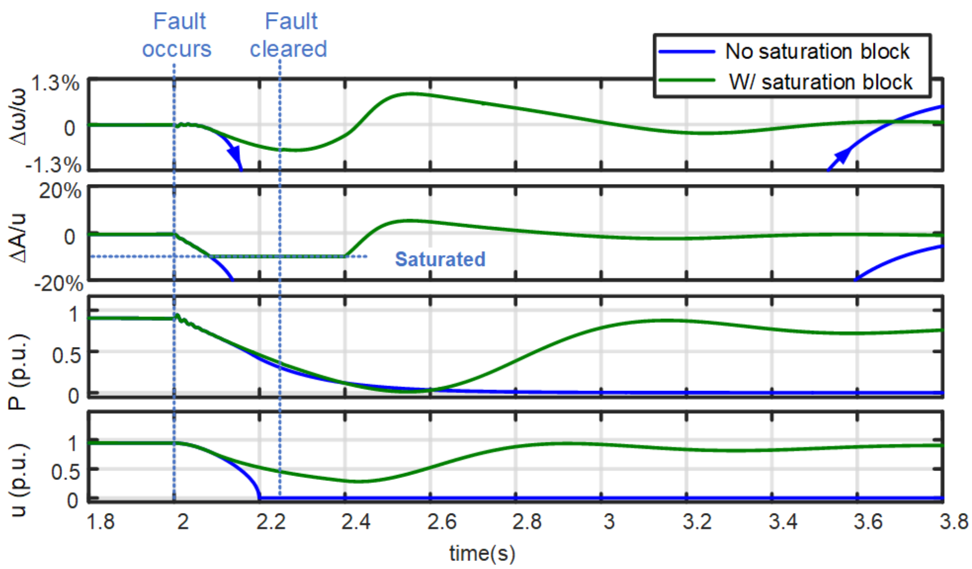

Figure 7-14. Transient stability of dVOC2 under Scenario 4 w/ and w/o power loop saturation blocks.

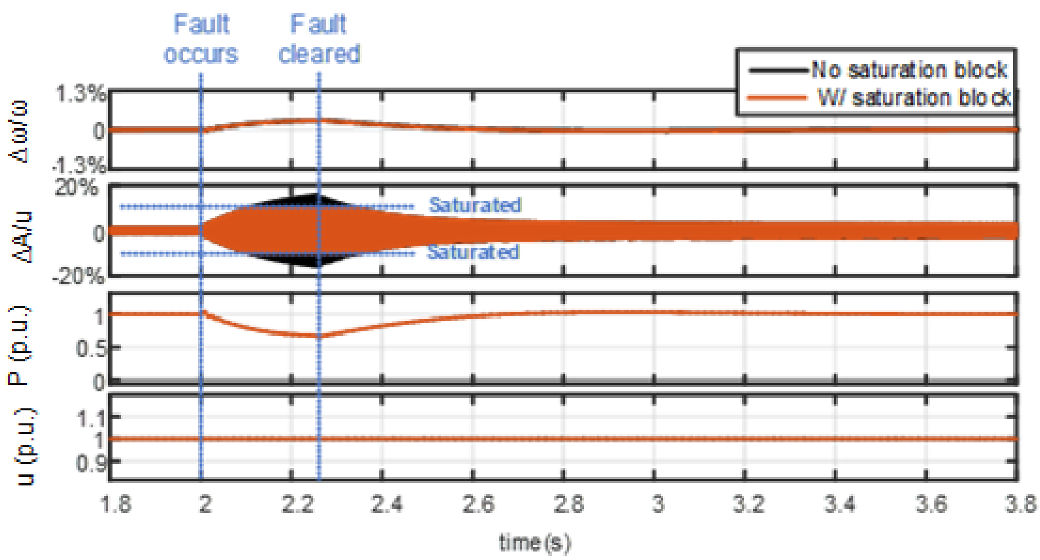

Figure 7-15. Transient stability of PVOC under Scenario 4 w/ and w/o power loop saturation blocks.

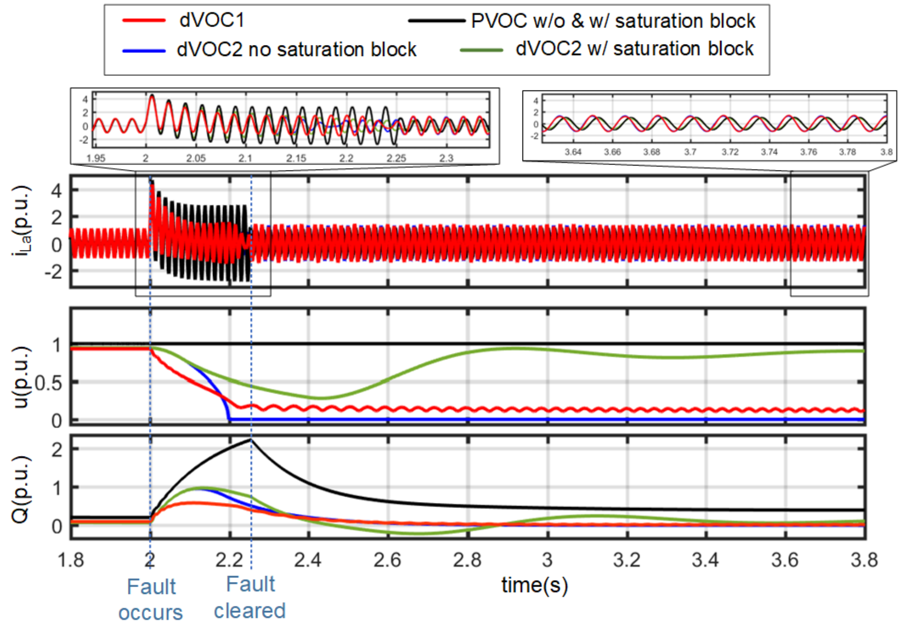

Figure 7-16. Requirements on inverter capability of dVOC1, dVOC2, and PVOC.

injections in dVOC1 and dVOC2 to keep the control voltage during a fault (e.g., dVOC2 w/ saturation block), and the system stability could be improved. On the other hand, the inverter rating is largely determined by the peak current due to the small thermal capacity of the inverter. Even though the PVOC requires a longer overcurrent duration than the dVOC approaches, it has similar peak currents to them, indicating that the PVOC approach can achieve the inverter passivity for better system stability with only a slight increase in inverter rating. Note that the active power is selected as the base power for the analysis here.

In addition, the control voltage-regulation capability of PVOC does not necessarily come from the reactive power capability that the hardware can withstand. Instead, the pumping-and-damping motion is the key to maintaining the voltage. In other words, if the inverter can provide the reactive power as much as the system needs during transient, the voltage can be maintained to be 1 p.u. as shown in Figure 7-16; while if the reactive power capability is limited during a transient, the pumping-and-damping motion of PVOC can still help to maintain the control voltage to the pre-specified value and help improve system stability. For example, as shown in Figure 7-17 under Scenario 4, if there is no pumping-and-damping block, the system loses synchronism; if the pumping-and-damping block is enabled when control voltage drops to 0.5 p.u., the voltage will be clamped during the fault, and the system can also return to stable operations after the fault is cleared.

According to the transient stability analysis results above, it can be concluded that the proposed PVOC approach has similar control dynamic equations as existing dVOC approaches. But due to the passivity-based design achieved by the pumping and damping control action in the reactive power loop, the PVOC approach will show enhanced transient stability compared to existing dVOC approaches.

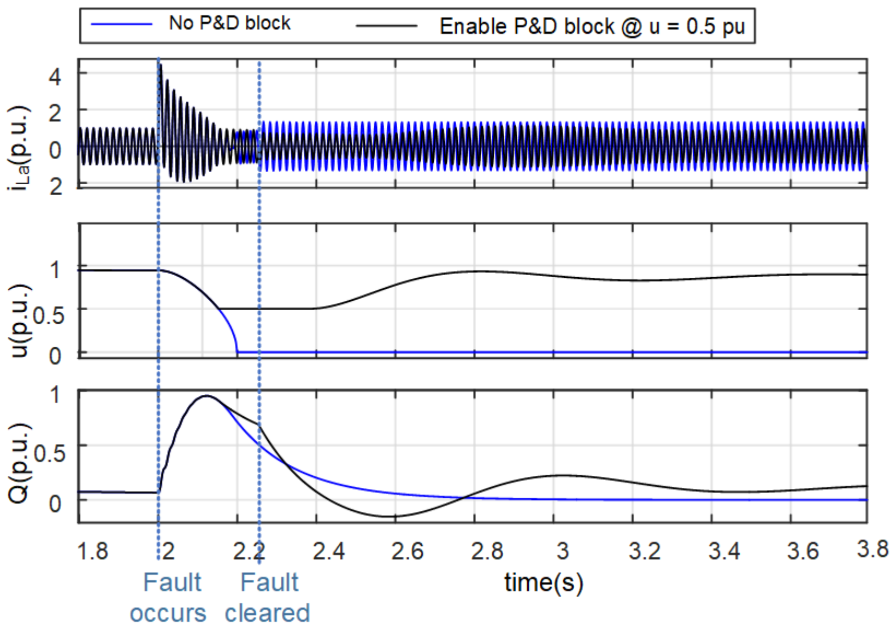

Figure 7-17. Enabling pumping-and-damping block when *u* drops 0.5 p.u. in PVOC.

7.4 Parameter Design of Proposed Control Considering Dynamic Requirements

In addition to the limitation of stability design criteria on the selection of control parameters, the dynamic response of the converter should also be considered. Therefore, in this section, several tips on the control parameter design are discussed.

A. Voltage Dynamics

By ignoring the slower power dynamics, the voltage dynamics equation can be derived as (7. 36). Then the time of voltage rising from k_1V_{ref} to k_2V_{ref} can be calculated based on this first-order differential equation as shown in (7. 37).

$$\dot{v} = \xi_1\left(v_{ref}^2 - |v|^2\right)v \tag{7. 36}$$

$$t = \frac{1}{2\xi_1 v_{ref}^2} ln\left(\frac{k_2^2(k_1^2-1)}{k_1^2(k_2^2-1)}\right) \tag{7. 37}$$

For example, if the time of voltage rising from $0.1V_{ref}$ to $0.9V_{ref}$ is 20 ms, then, ξ_1 is calculated to be 0.0605 with V_{ref} = 50 V. The simulation waveform of the voltage dynamics is shown in Figure 7-18.

B. Power Dynamics

Taking power dynamics into consideration, the system is then expressed as (7. 38). For simplicity, the dynamics of a faster inner voltage loop are ignored, therefore, the system dynamics can be simplified as (7. 39)

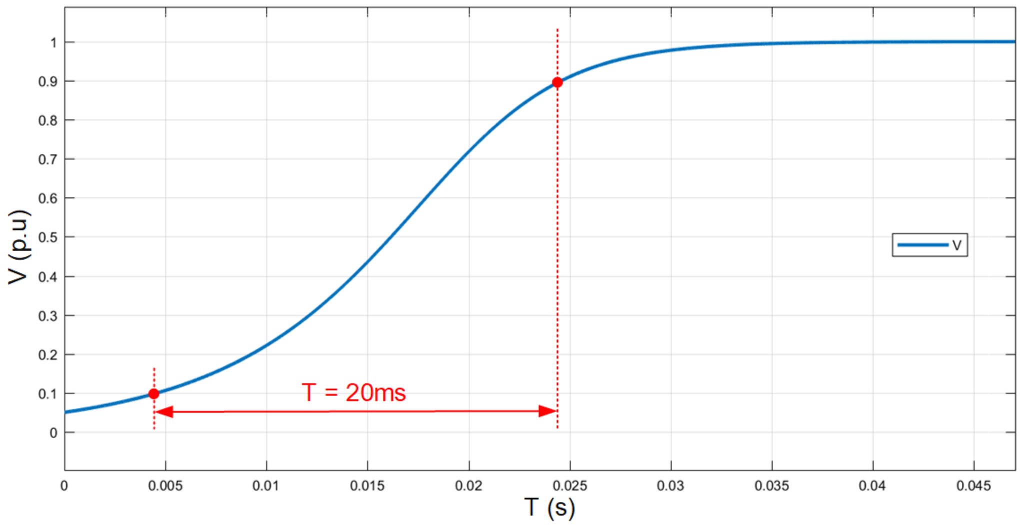

Figure 7-18. Voltage dynamics with designed ξ_{1}.

$$\begin{cases} \dot{V} = \boldsymbol{\xi_1}\left(V_{ref}^2 - |V|^2\right)V + \boldsymbol{\xi_2}\left(\frac{Q_{ref}}{V_{ref}^2} - \frac{Q_m}{V^2}\right)v \\ \dot{\theta} = \omega_R + \boldsymbol{\xi_3}\left(\frac{P_{ref}}{V_{ref}^2} - \frac{P_m}{V^2}\right) \end{cases} \tag{7. 38}$$

$$\begin{cases} \dot{V} = V_{ref} + \frac{\boldsymbol{\xi_2}}{V_{ref}}\left(Q_{ref} - Q_m\right) \\ \dot{\theta} = \omega_R + \frac{\boldsymbol{\xi_3}}{V_{ref}^2}\left(P_{ref} - P_m\right) \end{cases} \tag{7. 39}$$

It can be observed from (7. 39) that the dynamics of VOC control are quite similar to conventional droop control as shown in (7. 40).

In the real application, the selection of the *P-f* droop gain *m* and *Q-v* droop gain *n* are usually designed to be several percentages of the nominal value as shown in (7. 41) Therefore, mapping from VOC to droop control, the parameter design can simply follow the suggestions in (7. 42). For example, $k_p = 2\%$, $k_q = 10\%$, so $\xi_3 = 31.4$, $|\xi_2| = 0.42$.

Note that ξ_3 should not be designed to be too large because it needs to meet the presumption that the converter and the grid have the same oscillation frequency for the power flow calculation.

$$\begin{cases} \dot{V} = V_{ref} + n\left(Q_{ref} - Q_m\right) \\ \dot{\theta} = \omega_R + m\left(P_{ref} - P_m\right) \end{cases} \tag{7. 40}$$

$$\begin{cases} n = k_q \frac{V_{ref}}{P_{ref}} \\ m = k_p \frac{\omega_R}{P_{ref}} \end{cases} \tag{7. 41}$$

$$\begin{cases} |\xi_2| = k_q \dfrac{V_{ref}^2}{P_{ref}} \\ \xi_3 = k_p \dfrac{\omega_R V_{ref}^2}{P_{ref}} \end{cases} \tag{7. 42}$$

C. Inner Current Loop Control Dynamics

The inner current dynamics have the least impact on system stability, and they may have some impact on system load transient performance. To have a suggested control parameter design of the inner current loop, the equivalent circuit is obtained as shown in Figure 7-19.

Then, the model of the inner current loop can be derived as (7. 43), where $G_{ui} = \frac{sC_f}{(sL_f+R_f)sC_f+1}$. To have faster voltage transient, ξ_4 should be designed to cause small Δv following equations in (7. 44).

$$T_i = -G_{ui}(L_f\xi_4 + R_f) \tag{7. 43}$$

$$\Delta v = \frac{-L_f\xi_4 i_{Lref}}{1 + T_i} \tag{7. 44}$$

For example, with different ξ_4 values, the system exhibits different voltage dynamics, though the differences are small. As shown in Figure 7-20, ξ_4 is preferred to be selected as -20 to reduce the voltage variation during load change transients.

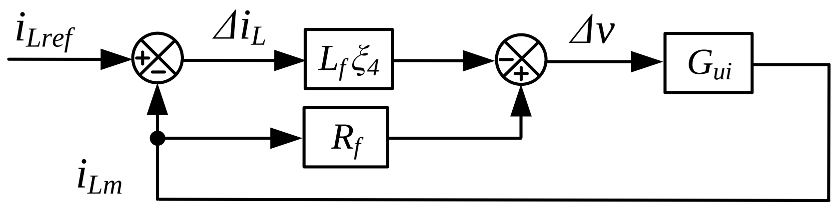

Figure 7-19. Equivalent circuit of the inner current loop.

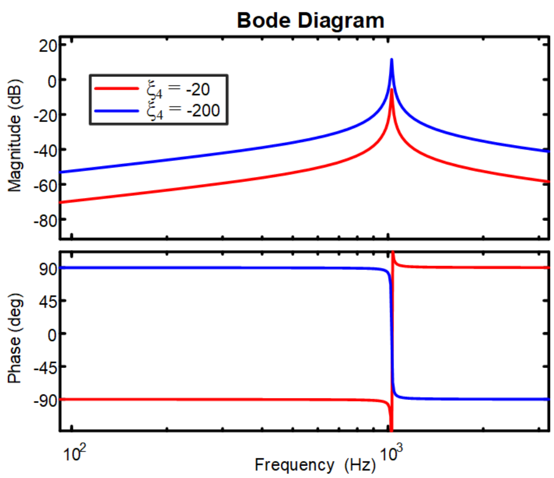

(a)

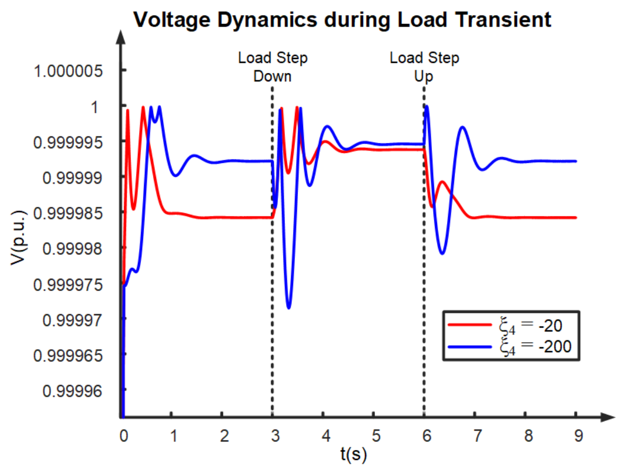

(b)

Figure 7-20. Impacts of ξ_4 on system transient dynamics: (a) Bode diagram and (b) voltage dynamics during load transient.

The proposed PVOC also shows some advantages over dVOC1 as discussed below in terms of the degree of freedom in the selection of control parameters. If ignoring the internal current dynamics, both control methods can be modeled by the dynamic equations as shown in (7. 45) for dVOC1 in [196] and (7. 46) for the proposed control. Accordingly, the design comparisons of dVOC1 and the proposed method can be summarized as shown in Table 7-2, including the voltage rising time, maximum frequency deviation, and the minimal terminal voltage. It can be observed that there are two degrees of freedom (DOF) in the selection of the control parameters for dVOC1, while there are three DOFs for the design of the proposed control, which means that the proposed method will have a larger feasible design range than dVOC1. For example, as shown in Figure 7-21, if the maximum voltage rising time is 120 ms, and the maximum frequency deviation is 2π rad/s, under different requirements for minimum terminal voltage, the feasible regions for the control parameters are different. When $V_{min,pu} = 0.95$, there are some feasible designs for dVOC1; but when $V_{min,pu} = 0.75$, there is no feasible design existing. While for $V_{min,pu}$ = 0.95 or 0.75, there are always feasible designs for the proposed control method because of the more DOFs in parameter selections.

$$\begin{cases} \dot{\delta} = \dfrac{\kappa_v \kappa_i}{3C} \dfrac{1}{v^2} \left(P_{ref} - P(v) \sin\delta\right) \\ \dot{v} = \dfrac{\xi}{\kappa_v^2} v\left(2v_{ref}^2 - 2v^2\right) + \dfrac{\kappa_v \kappa_i}{3C} \dfrac{1}{v} \left(Q_{ref} - Q(v,\delta)\right) \end{cases} \tag{7. 45}$$

$$\begin{cases} \dot{\delta} = \xi_3 \left(\dfrac{P_{ref}}{v_{ref}^2} - \dfrac{P(v)\sin\delta}{v^2}\right) \\ \dot{v} = \xi_1 (v_{ref}^2 - v^2) v + \xi_2 v \left(\dfrac{Q_{ref}}{v_{ref}^2} - \dfrac{Q(v,\delta)}{v^2}\right) \end{cases} \tag{7. 46}$$

Table 7-2. Design comparisons between dVOC1 and PVOC under various system performances.

System performance	**dVOC1**	**PVOC**
Voltage rising time from $0.1V_{ref}$ to $0.9V_{ref}$ t_{rise}	$\frac{3\kappa_v^2}{2\xi v_{phase,ref}^2}$	$\frac{3}{\xi_1 v_{ref}^2}$
Maximum frequency deviation $\Delta\omega$ (P = 1pu, P_{ref} = 0)	$\frac{1}{\sqrt{2}Cv_{min,pu}^2}$	$\frac{\xi_3 S_{rated}}{\sqrt{2}v_{ref}^2 v_{min,pu}^2}$
Minimum terminal voltage $V_{min,pu}$ (Q = 1pu, Q_{ref} = 0)	$\sqrt{\frac{1+\sqrt{1-\frac{\sqrt{2}}{C\xi}}}{2}}$	$\sqrt{\frac{1+\sqrt{1-2\sqrt{2}\frac{\xi_2 S_{rated}}{\xi_1 v_{ref}^4}}}{2}}$

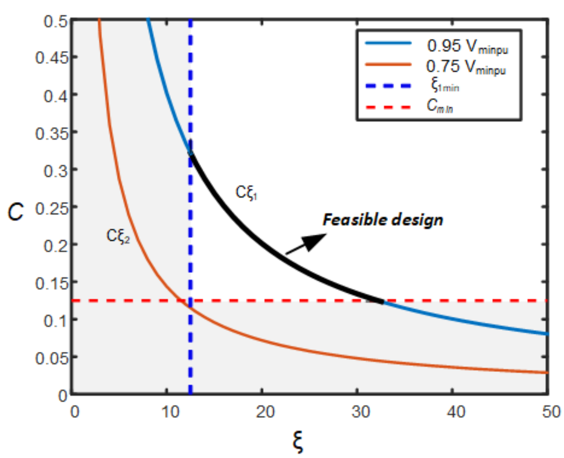

(a)

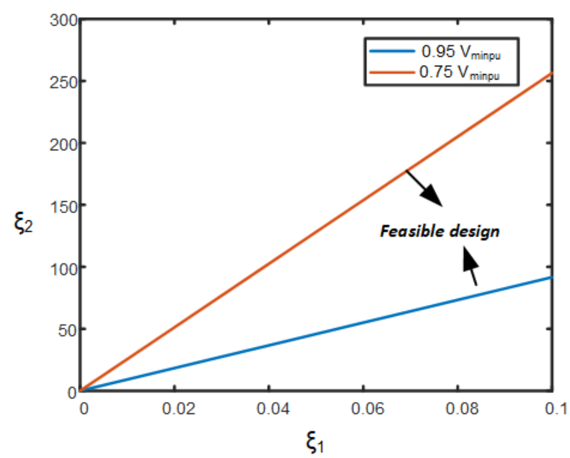

(b)

Figure 7-21. Feasible design region: (a) dVOC1 and (b) proposed PVOC.

7.5 Validations of Proposed Control Approaches

To validate the effectiveness of the proposed control method, several scenarios are simulated and examined in MATLAB/Simulink, including a single converter in grid-connected mode and an IEEE 9-bus system.

7.5.1 Operation of a single inverter in grid-connected mode

A. Simulation Testing

In the grid-connected single converter test, a GFM with the proposed PVOC is built in MATLAB/Simulink. The control parameters and working conditions are listed in Table 7-3. Note that the control parameters are selected based on the recommended parameter design method in Section 7.4. The simulation results are given in Figure 7-22. The GFM can be connected to the grid smoothly at t = 0.5 s.

B. Experimental Testing

For further validation, an experimental setup of the grid-connected converter is built to verify the effectiveness of the proposed passive control strategy with the same parameters as listed in Table 7-3. The experimental results are given in Figure 7-23, which shows that the system is stable in grid-connected mode. Note that this simple single-inverter test is to validate the functionality and feasibility of the proposed control approach in a real converter.

7.5.2 Proposed PVOC in IEEE-9 Bus System

To validate the effectiveness of the proposed control in a more general power system, an IEEE 9-bus system [207] as shown in Figure 7-24 is adopted as a test case, where Bus 3 is connected to a synchronous generator, Bus 2 is connected to a GFM with droop control as shown in Figure 7-25,

Table 7-3. Working conditions and control parameters of the one-converter test system.

Variables	**Value**	**Variables**	**Value**
Dc voltage (V)	130	Grid impedance L_g (mH)	3.6 (0.54 pu)
Ac voltage (V)	50	Voltage rising time T_{rise} (ms)	20
Power references P_{ref}, Q_{ref} (kW, kvar)	0.6, 0	Control variable ξ_1	0.0605
Rated power S_{rated} (kVA)	1	Control variable $\lvert\xi_2\rvert$	0.42
Output inductor L_f (mH)	2.4 (0.36 pu)	Control variable ξ_3	31.4
Output capacitor C_f (μF)	10	Control variable ξ_4	-20

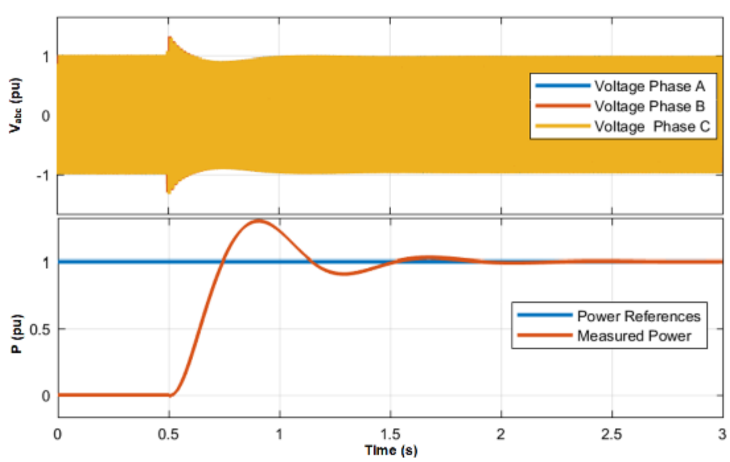

Figure 7-22. Simulation results of stable connection of the inverter with the proposed control into the grid.

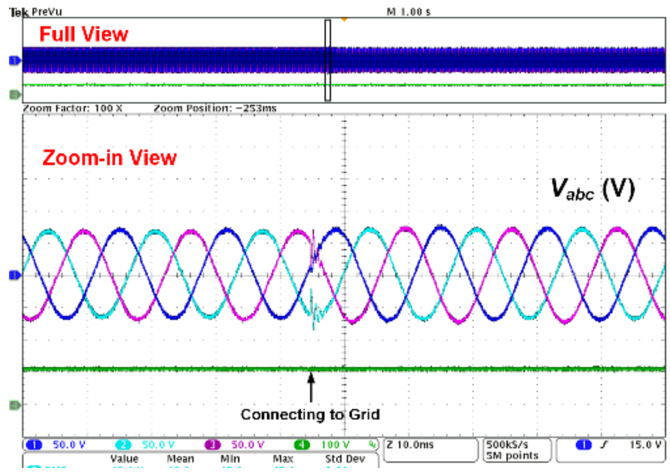

Figure 7-23. Experimental results of stable connection of the inverter with the proposed control into the grid.

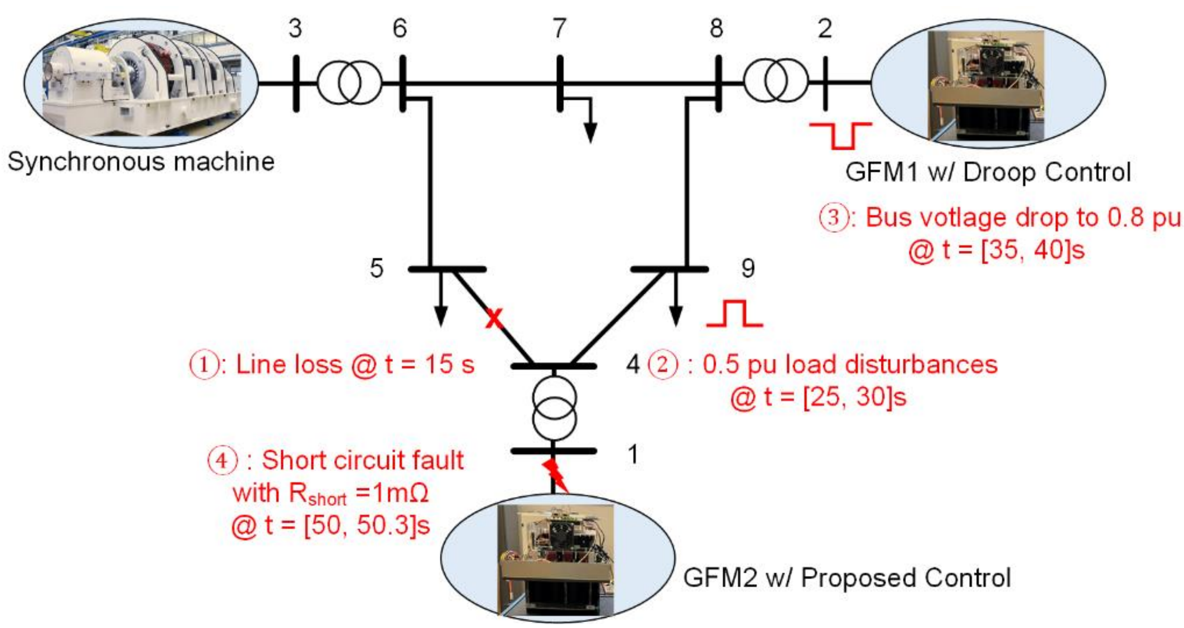

Figure 7-24. Circuit diagrams of IEEE 9-Bus System.

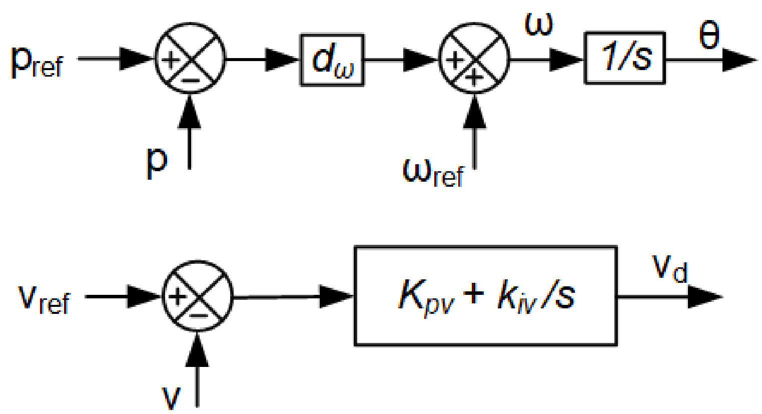

Figure 7-25. The control block of droop control in the test system.

and Bus 1 is connected to the GFM with the proposed control. As a comparison, Bus 1 is also connected to the GFM with the dVOC2 separately. The dynamic model of the synchronous generator can be modeled as (7. 47), where θ is the rotor angle, ω is the rotor angular speed, J is the inertia constant, T_m is mechanical torque, T_e is the electrical torque, and T_f id the friction windage torque. Additionally, $\psi_{s,dq}$ $v_{s,dq}$ and $i_{s,dq}$ denote the stator winding flux, voltage, and current in the dq axis, separately. $\psi_{f,d}$ $v_{f,d}$ and $i_{f,d}$ denote the field winding flux, voltage, and current in the d axis, respectively. Moreover, r_s and $r_{f,d}$ are stator and fielding winding resistances. In addition, ψ_D, v_D, i_D and R_D are the linkage flux, voltage, current, and damping winding resistance, separately. Finally, the governor and turbine dynamics are modeled by a droop control and a first-order dynamic equation, where p denotes the governor output power, d_p denotes governor speed droop gain of the governor, τ_g denotes the turbine time constant, and p_τ denotes the turbine output power. The dynamic model of the droop control used in the system at Bus 2 can be modeled as (7. 48), where d_ω is the frequency droop gain, K_{pv} and K_{iv} are the voltage proportional-integral controller.

$$\begin{cases} \dot{\theta} = \omega \\ J\dot{\omega} = T_m - T_e - T_f \\ \dot{\psi}_{s,dq} = v_{s,dq} - r_s i_{s,dq} - \mathcal{J}_2 \psi_{s,dq} \\ \dot{\psi}_{f,d} = v_{f,d} - r_{f,d} i_{f,d} \\ \dot{\psi}_D = v_D - R_D i_D \\ p = p^* + d_p(\omega^* - \omega) \\ \tau_g \dot{p}_\tau = p - p_\tau \end{cases} \tag{7. 47}$$

$$\begin{cases} \dot{\theta} = \omega \\ \omega = \omega_{ref} + d_\omega (p_{ref} - p) \\ v_d = K_{pv}\left(v_{ref} - v\right) + K_{iv} \int_0^T \left(v_{ref} - v(t)\right) dt \end{cases} \tag{7. 48}$$

The detailed parameters of the system can be seen in Table 7-4. Note that the control parameters of the proposed PVOC and dVOC2 are designed equal, and the parameters η and α are defined as shown in (7. 32) which can be equivalent to $\xi_{1,2,3}$ in (7. 33). The only difference between PVOC and dVOC2 is that PVOC has a pumping-and-damping block to maintain the voltage magnitude, while dVOC2 does not have such a control block. Also, for both dVOC2 and PVOC, the frequency is limited to 60 ±5 Hz and the voltage amplitude is limited within [0.2 pu, 2 pu] in the controller.

Four transient scenarios are considered in the test system, including

(1) loss of line 4-5 at t = 15 s;

(2) 0.5 pu load disturbances at Bus 9 during t = [25, 30] s;

(3) voltage dropping to 0.8 pu at Bus 2 during t = [35, 40] s;

(4) SCF with 1 mΩ fault resistance at Bus 1 at t = 50 s with 300 ms fault clearing time.

Before considering the impact of the proposed control on the system stability, the system is first verified to be stable with Bus 1 connecting with an ideal voltage source. In this study, simulations are conducted under these four scenarios to check the system stability. That means, the original system is stable, and the synchronous generator on Bus 3 and droop controlled GFM on Bus 2 (denoted as GFM1) are well designed for system stability. Therefore, once Bus 1 is connected with a real GFM (denoted as GFM2) instead of an ideal voltage source, the system stability will be mainly determined by the performance of this inverter. Specifically, if the GFM2 is a ‘good grid citizen’, the system will remain stable; however, if the GFM2 is not well designed, it might induce some instability issues in the system.

Table 7-4. Working conditions and control parameters of the 9-bus test system [207].

Base Value of IEEE 9-Bus Test System					
S_b	100 MVA	v_b	230 kV	ω_b	2π 60 rad/s
Per Unit Value of *R-L* Transmission Lines					
Line 4-5	0.039, 0.17	Line 5-6	0.017 0.092	Line 6-7	0.01, 0.085
Line 7-8	0.032, 0.161	Line 8-9	0.0085, 0.072	Line 9-4	0.0119, 0.1008
MV/HV Transformer					
S_r	201 MVA	v_1	13.8 kV	v_2	230 kV
$R_1 = R_2$	0.0027 pu	$L_1 = L_2$	0.08 pu	$R_m = L_m$	500 pu
LV/MV transformer					
S_r	1.6 MVA	v_1	1 kV	v_2	13.8 kV
$R_1 = R_2$	0.0073 pu	$L_1 = L_2$	0.018 pu	$R_m = L_m$	347156 pu
Synchronous Generator					
S_r	100 MVA	v_r	13.8 kV	ω_b	2π 60 rad/s
H	3.7 s	d_P	1%	τ_g	5 s
Equivalent Circuit Parameters of GFMs					
S_r	100 MVA	V_{dc}	2.4495 kV	V_{LLrms}	1kV
R	5 μΩ	L	1 μH	C	0.06 F
GFM1 with droop control					
d_ω	2π 0.06 rad/s	ω_{ref}	2π 60 rad/s	k_{pv}, k_{iv}	0.001, 0.5
GFM2 with PVOC control and dVOC2					
η	0.021	α	666	ω_f	0.1 ω_b

Then, Bus 1 is connected to GFM2 with dVOC2. The simulation results under these four transient scenarios are given in Figure 7-26. The entire system is stable after the fault is cleared.

Replacing dVOC2 with PVOC and repeating the same transient scenarios, with the proposed PVOC, the system also remains stable as shown in Figure 7-27.

However, under Scenario 4 as shown in Figure 7-28, if the fault clearing time is longer, for example, 2 s in the simulation, the system with dVOC2 may lose synchronism after the fault is cleared, while the system with proposed PVOC can remain stable after the fault is cleared. This is mainly due to the fact that dVOC2 may run into transient instability issues due to the sharp voltage drop under some large disturbances, while PVOC has the pumping-and-damping motion that can help maintain control voltage magnitude under system disturbances and enhance system stability.

For dVOC2, a shorter fault clearing time does not necessarily mean a more stable system. For example, as shown by the simulation results in Figure 7-29, when fault clearing time is 210 ms or 490 ms, the system loses synchronism after the fault is cleared; while when fault clearing time is 300 ms or 450 ms, the system returns to synchronism after the fault is cleared. It can be observed that a proper time to clear the fault for dVOC2, so that instability issues can be avoided, is highly dependent on the system working conditions and transient behaviors. If the fault is cleared at the instant when the bus voltage drops to a low value, the system will not be able to return to desired steady-state operating conditions. While for the proposed PVOC, there is no need for such concerns since the control voltage can always be maintained so that no matter when to clear the fault, the system can be able to reach stable operations.

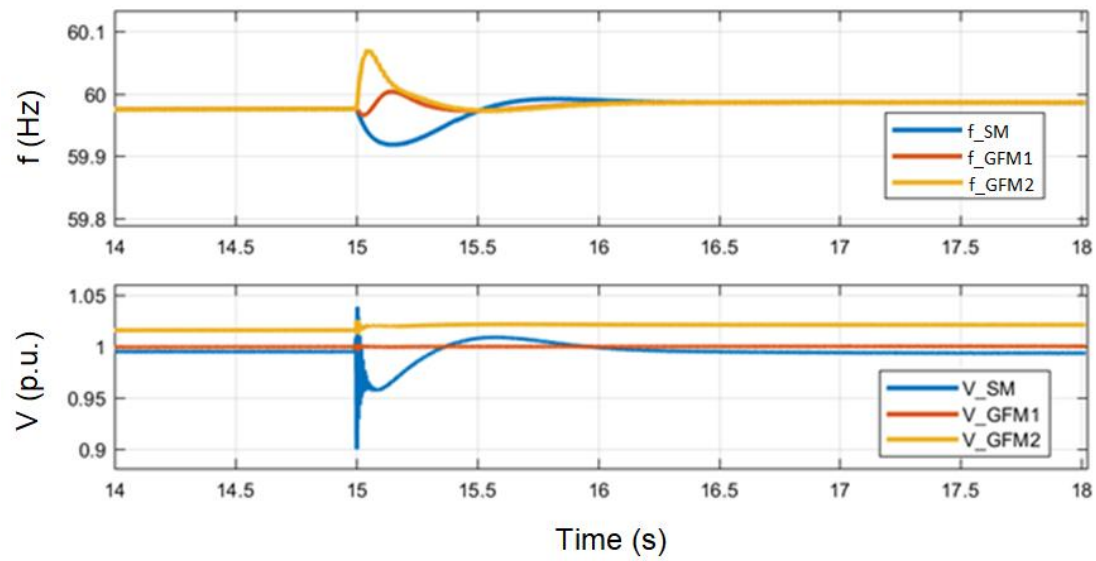

(a)

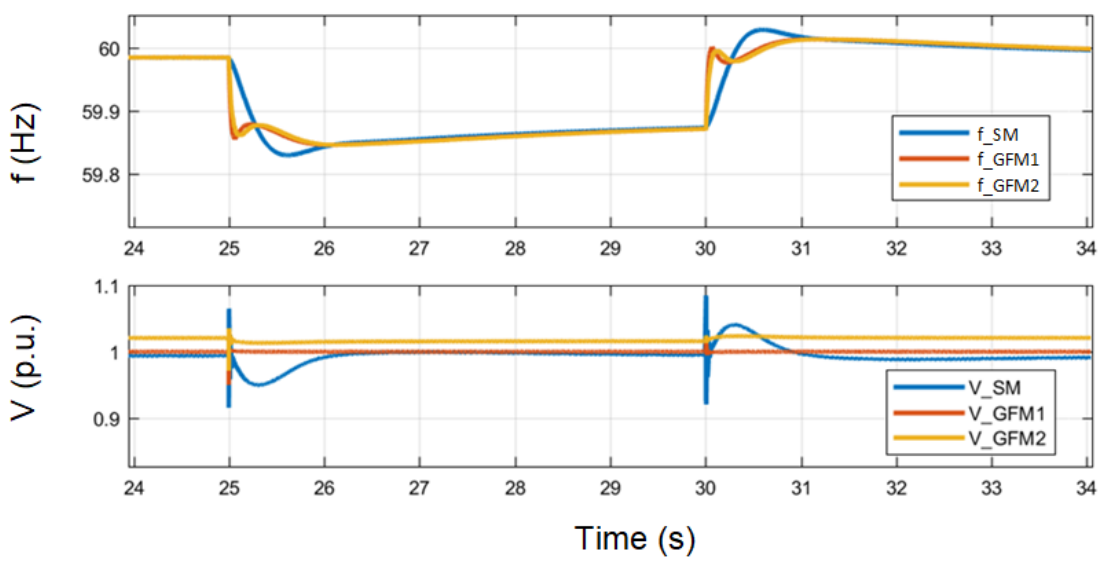

(b)

Figure 7-26. Simulation results of IEEE 9-bus system with Bus 1 connecting to dVOC2: (a) Scenario 1, (b) Scenario 2, (c) Scenario 3, and (d) Scenario 4.

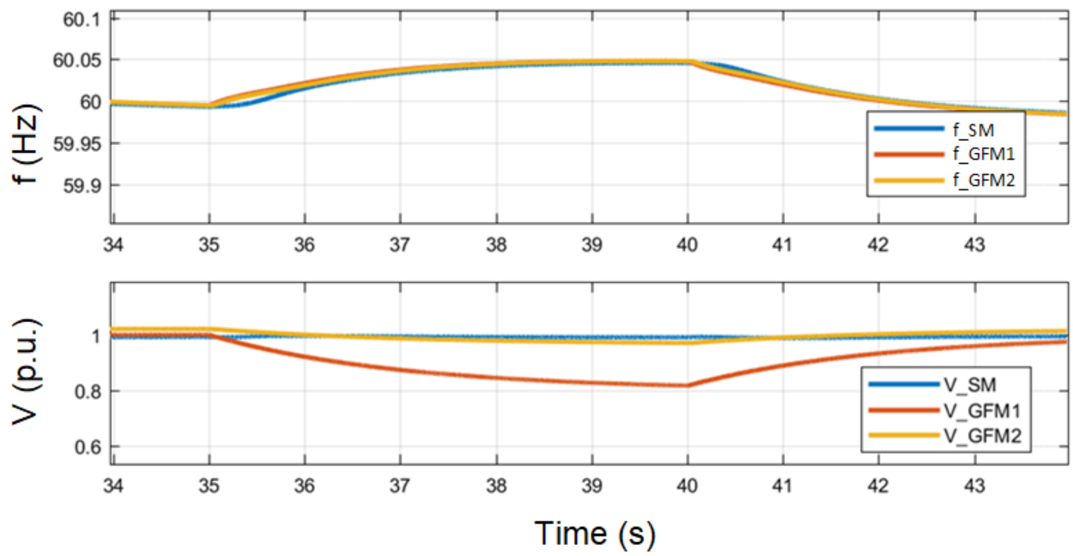

(c)

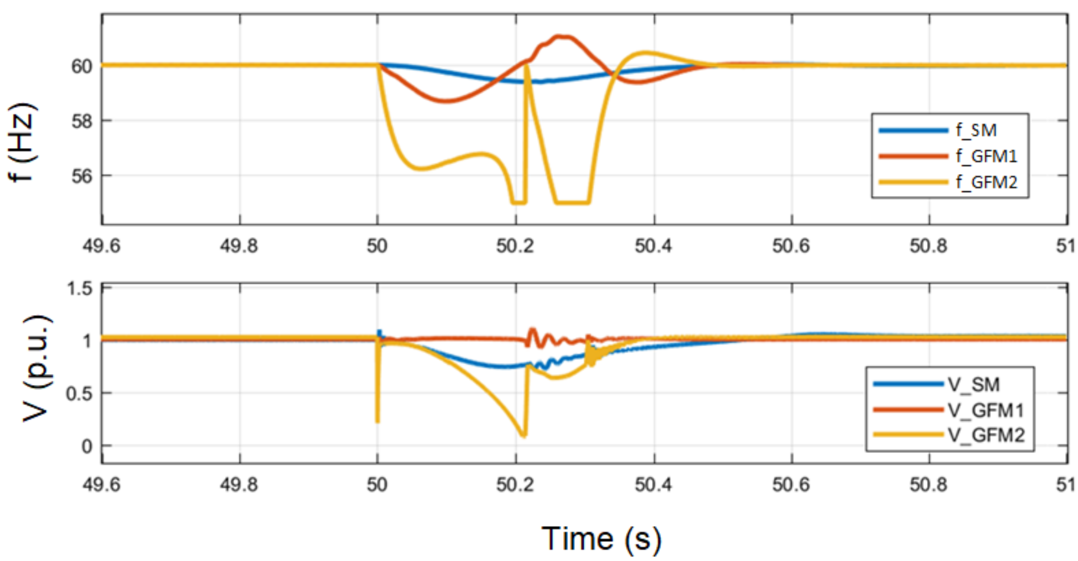

(d)

Figure 7-26. (continued).

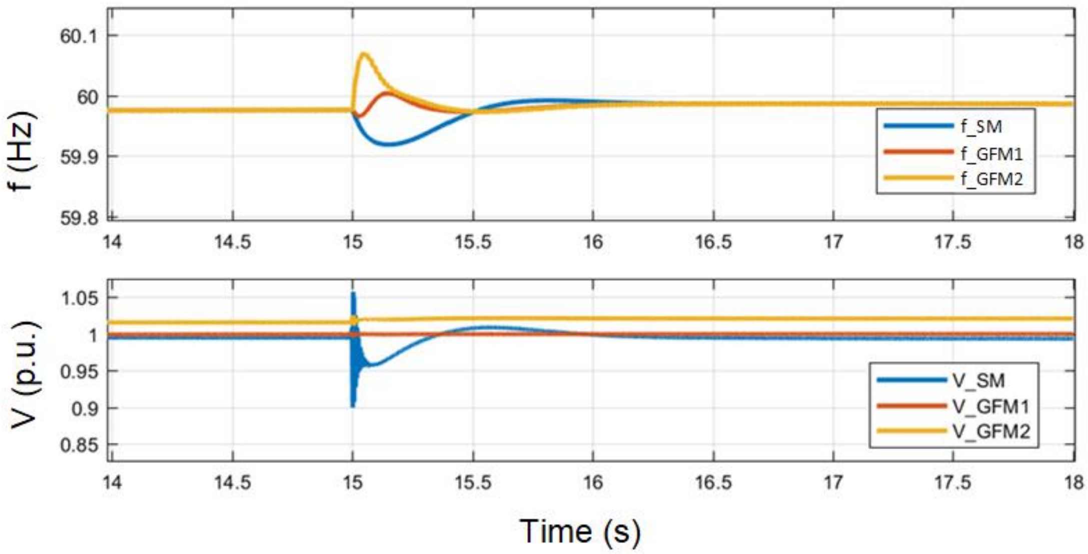

(a)

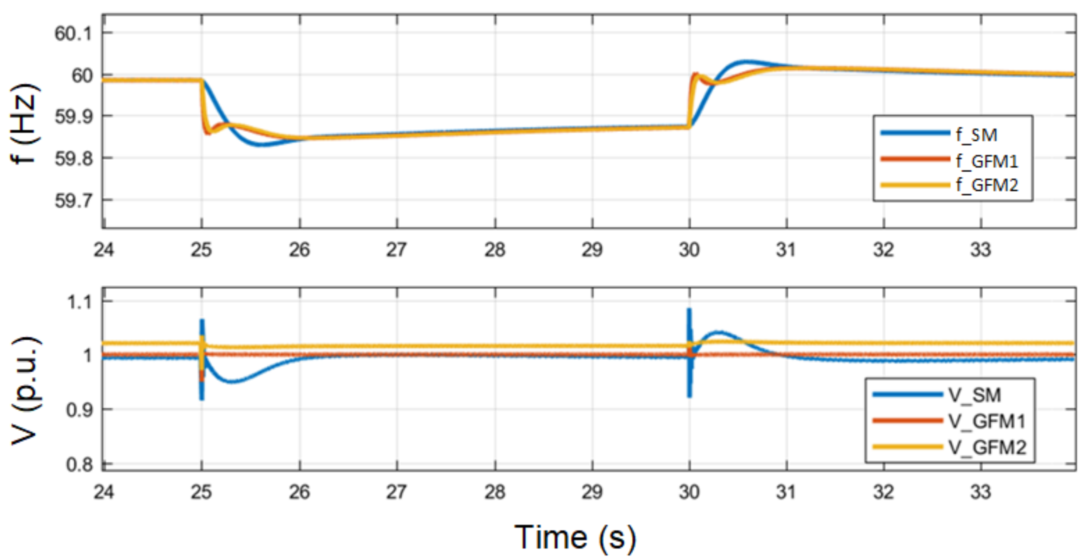

(b)

Figure 7-27. Simulation results of IEEE 9-bus system with Bus 1 connecting to PVOC: (a) Scenario 1, (b) Scenario 2, (c) Scenario 3, and (d) Scenario 4.

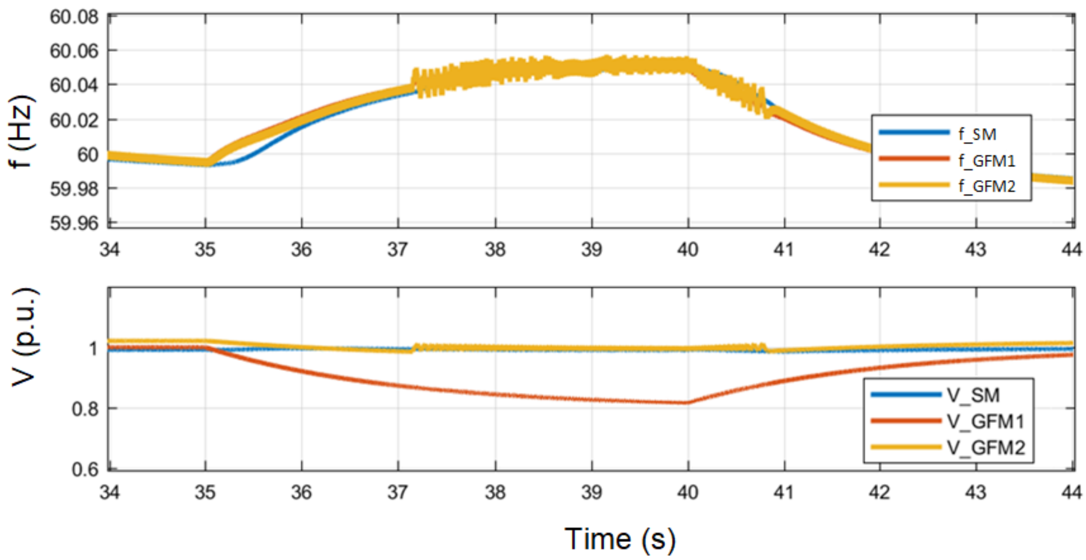

(c)

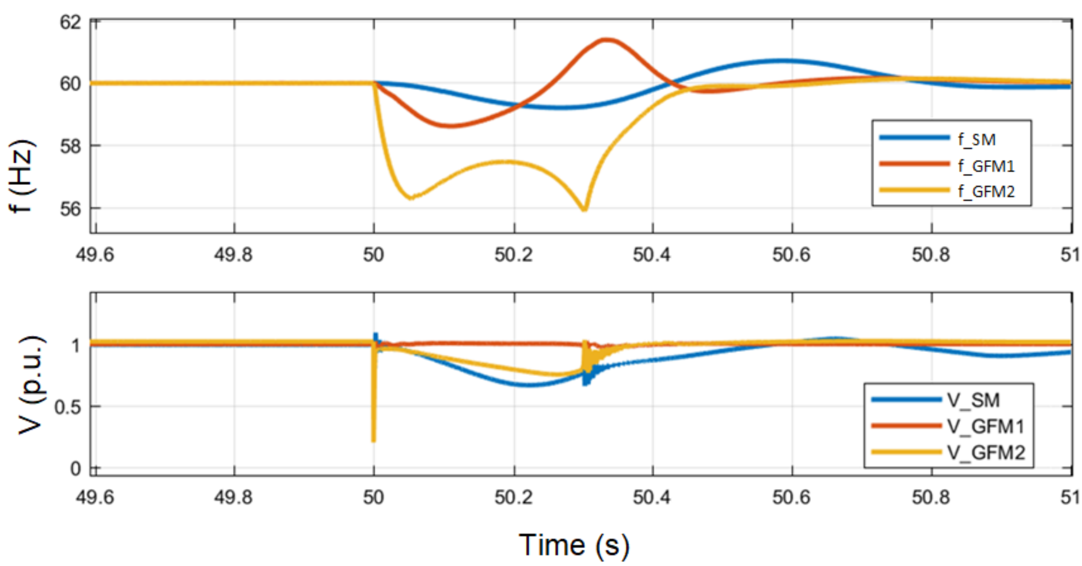

(d)

Figure 7-27. (continued).

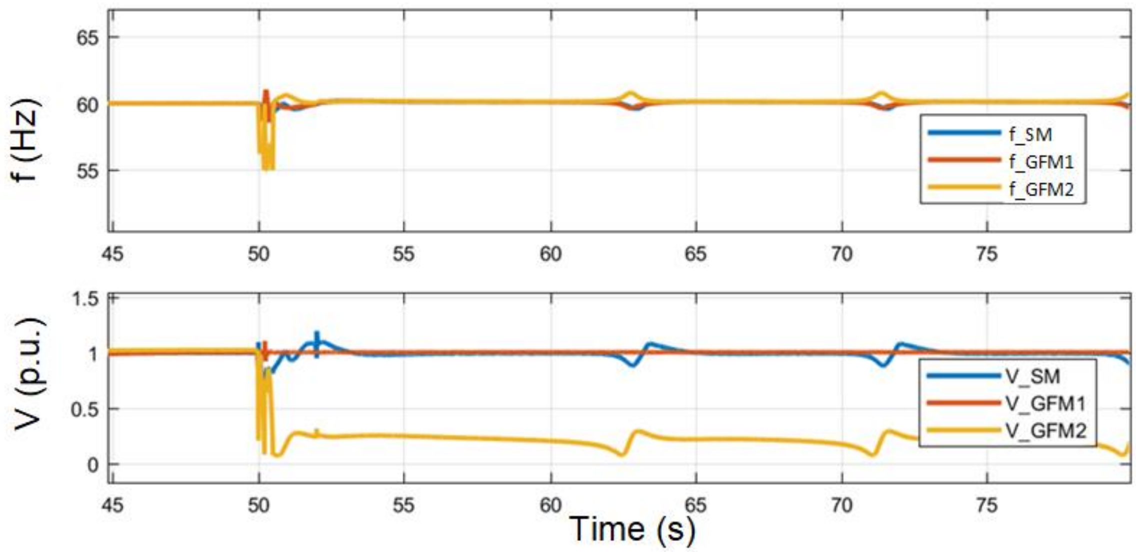

(a)

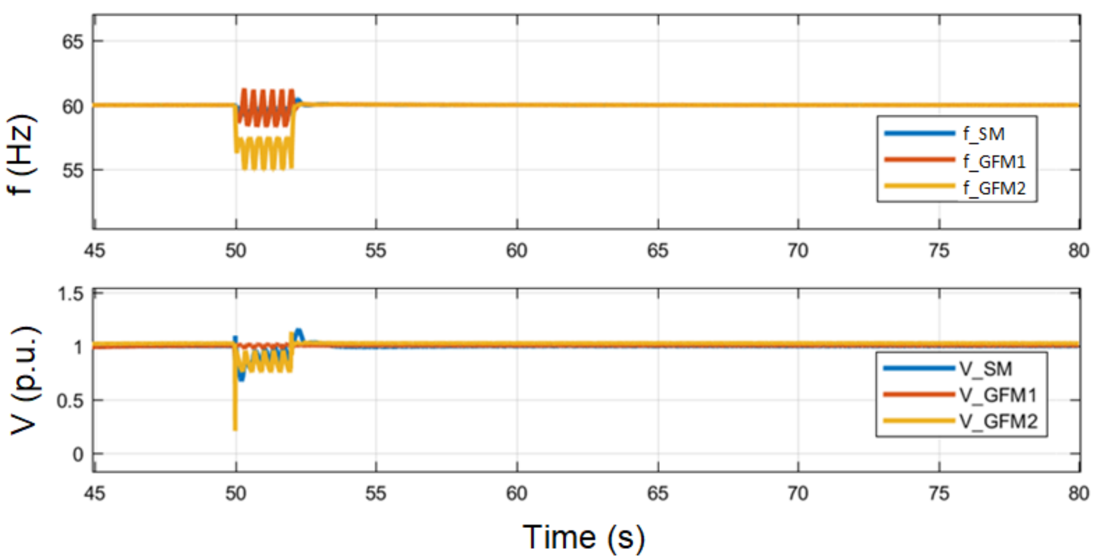

(b)

Figure 7-28. Comparison of simulation results of IEEE 9-bus system under Scenario 4 with 2 s fault clearing time with Bus 1 connecting to (a) dVOC2 and (b) PVOC.

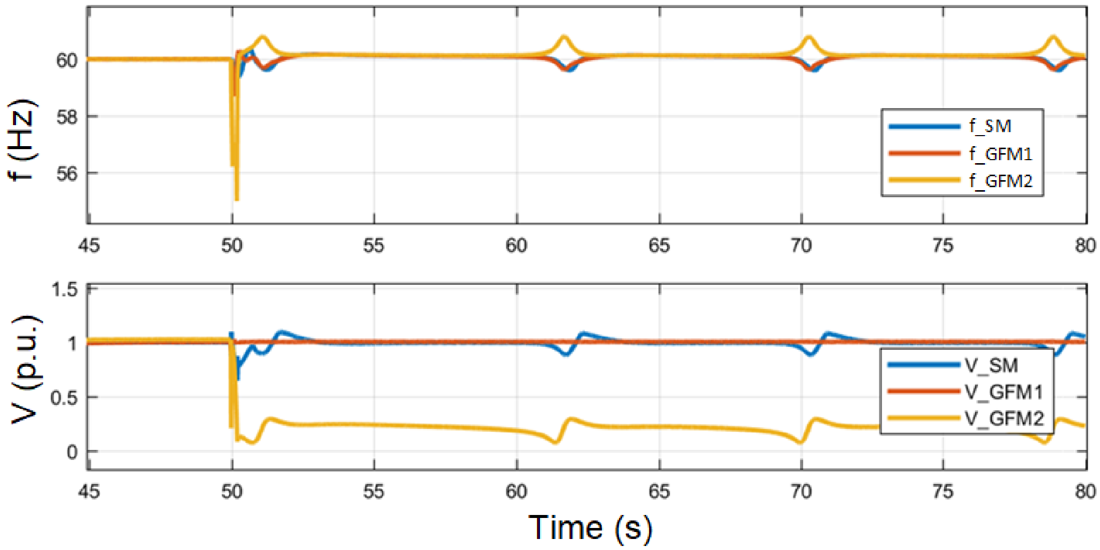

(a)

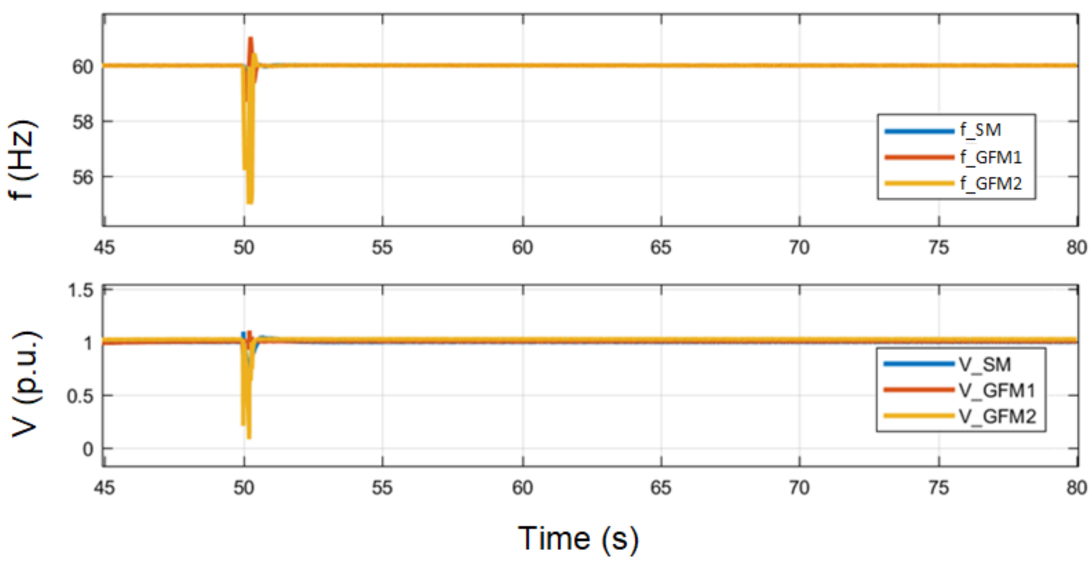

(b)

Figure 7-29. Simulation results of IEEE 9-bus system with Bus 1 connecting to dVOC2 under Scenario 4 with different fault-clearing time: (a) 0.21s, (b) 0.3 s, (c) 0.45 s, and (d) 0.49 s.

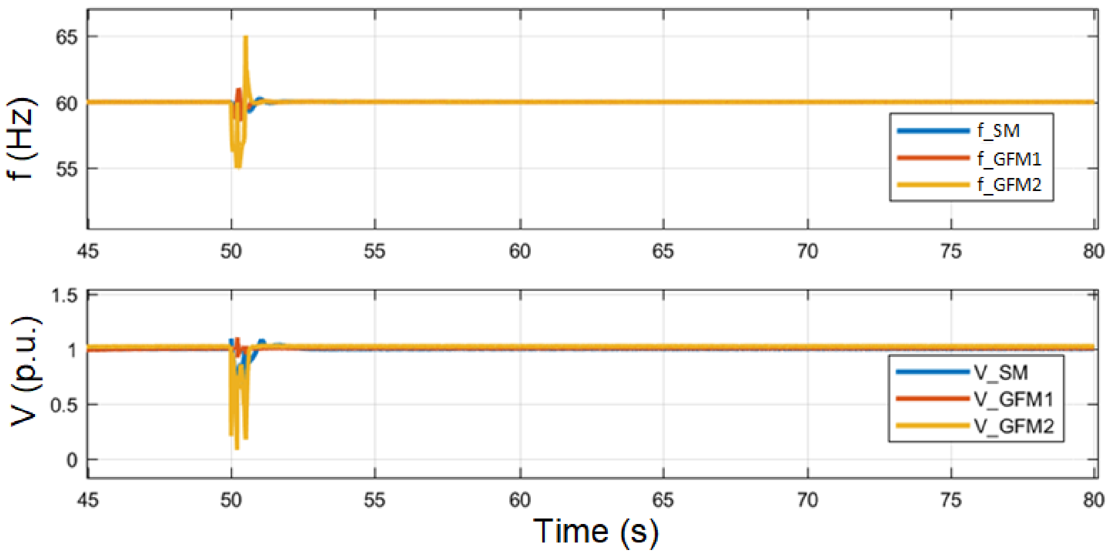

(c)

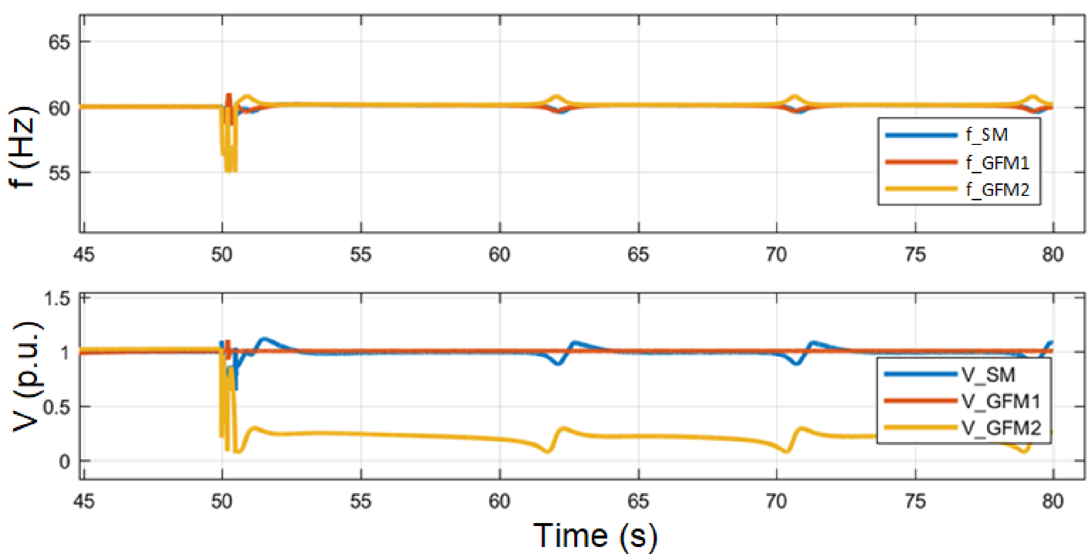

(d)

Figure 7-29. (continued).

7.6 Conclusions

In this chapter, the proposed PVOC control is extended for a more general power system that is not necessarily passive. A Lyapunov function is constructed from the Hamiltonian function, and the global asymptotic stability is then analyzed. In addition, the proposed control shows enhanced synchronization stability and exhibits more flexibility in the control parameter design, compared with existing dispatchable virtual oscillator control approaches. To further verify the proposed approach, it is implemented in the IEEE 9-bus system with different fault scenarios being considered. It can be concluded that the proposed control approach is a ‘good grid citizen’ and can be stably connected to any existing system as long as a desired equilibrium operating point exists.

Chapter 8. Impacts of Stability Requirements on the Design of PEC-Rich Power Systems

In conventional electric power systems, ac is the dominant power type. But with the development of PECs, more and more applications tend to adopt dc power due to the improved efficiency, controllability, cost, and size. Examples include data centers, dc residential power systems, medium voltage dc (MVDC) shipboard systems, high-voltage transmission lines, etc. [2, 208-210]. Among these trending dc applications, aircraft electric power system (EPS) is one of the most popular topics as reported in [211-214] because of the reduced weight compared with conventional ac distribution. However, the assessment of weight reduction is usually obtained under the static performance requirements of the system. Dynamic requirements, including small-signal stability, normal load transient, and abnormal transient have not been fully considered. Therefore, in this chapter, a design example under comprehensive system requirements is provided to study the impacts of dynamic requirements on dc and ac, separately.

8.1 Introduction and Background

A chart regarding the historical evolution of electric power and voltage of onboard EPSs is shown in Figure 8-1 [212]. In the first days of powered flight, the aircraft EPSs (6 V /12 V dc voltage and less than 500 W) were mainly designed for communication and ignition systems. Then, with the installation of lighting, signaling, and heating systems, the dc voltage level was increased to 28 V, and the generator capacity was increased up to 1 kW.

In the 1960s and thereafter, with the increased electric power demand due to the increasing speed and size of aircraft, integration of ac generation was observed, due to its several advantages

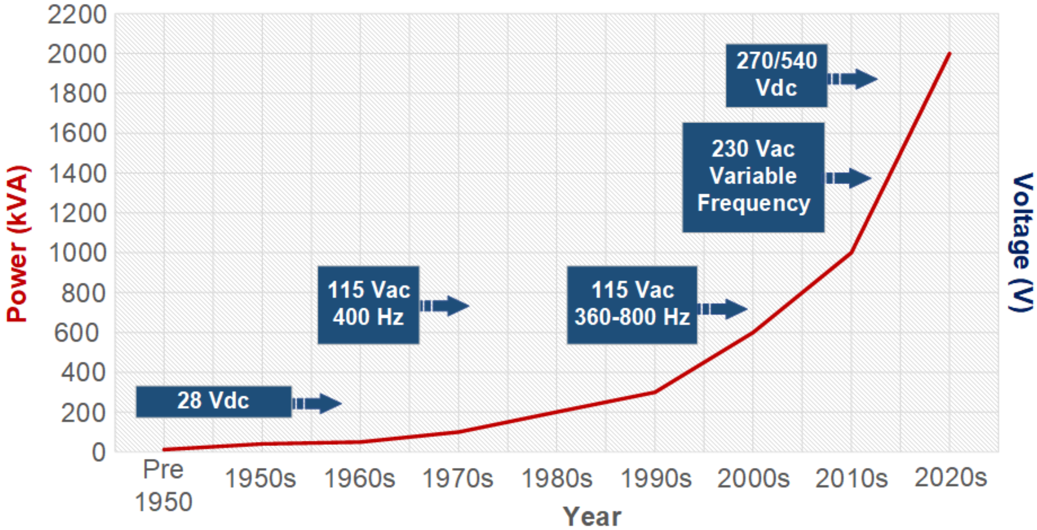

Figure 8-1. Electric power and voltage evolutions of aircraft EPSs.

compared with dc generations [212, 215]. First, the power density of ac generations (0.66 - 1.33 kVA/kg) was higher than the dc topology (less than 0.5 kW/kg) in the 1950s. Second, a potentially much higher voltage, i.e., 115 Vac compared with 28 Vdc, could be adopted which would bring a cabling weight reduction. Third, there was no need for commutators in ac generators, therefore, the system reliability was improved. In addition, 400 Hz was selected among many candidates (60, 180, 240, 360, 400, and 800 Hz) as the standard frequency by the Army Air Corps in 1943, and then made mandatory for use by the US Air Force in 1959, since it was more feasible for the generator speed with practically minimal motor and transformer weight. However, to obtain the constant frequency, constant speed drives (CSD) were needed which required regular maintenance and increased weight and size of the system. In addition, the onboard energy-consuming loads, i.e., resistive loads, are frequency insensitive. While for the frequency-sensitive loads, by connecting transformers and/or more mature power electronics converters with variable frequency generators, certain voltage types can be achieved easily.

For these reasons, from the 1980s and onwards, the main bus voltage of aircraft EPSs uses a hybrid system with 115 Vac and a variable frequency of 360 - 800 Hz. Starting from the 1990s, the major thrust for the evolution of aircraft EPSs is the reduction of fuel consumption for an eco-friendly system and a possible weight reduction, which promotes the more electric aircraft (MEA) concept, e.g., Boeing B787 and Airbus A380. That is, all the aircraft secondary systems which are currently operated by mechanical, hydraulic, and pneumatic systems will be replaced by electric systems. Due to the increasing power demand, the main bus voltage is also increased in some newer developments using 230 Vac with variable frequency or 270/540 Vdc. But the optimal solution to using ac or dc for the main bus voltage is still under investigation for future MEA and electrified propulsion.

To fully capture the pros and cons of using ac power and dc power, comparative studies are usually conducted. This comparative study of ac and dc aircraft EPSs are similar to other trending dc applications in the literature [216-221], e.g., microgrids or high voltage transmission lines, with a different design goal, i.e., the minimum system weight. However, the existing comparisons have been mainly conducted under the system static requirements (e.g., power balance, total harmonic distortions, thermal limits, etc.), while the impacts of dynamic requirements on system design have not been considered.

Therefore, this chapter aims to develop a design process to study the impacts of dynamic requirements on system design. Notional dc and ac EPSs are designed under both static requirements and dynamic requirements. Besides, system weight as the design target is used to quantify the dynamic impacts.

8.2 Case Study with a Notional Structure of Aircraft Electrical Power Systems

An example architecture of MEA EPS is shown in Figure 8-2 based on the EPS of the B787. There are four variable frequency starter/generators, four 540 Vdc 18-pulse autotransformer rectifier units (ATRU), four 28 Vdc 18-pulse transformer rectifier units (TRU), two 6-phase inverters, and many protection devices [222].

From this example, it can be seen that the main components of an aircraft EPS include generators, rectifiers, motor loads, and resistive loads. Another example of a 20 MW electrified aircraft in [214] also has a similar structure and components. Therefore, to simplify the design process, and meanwhile, to keep the intrinsic characteristics of aircraft EPSs, the system is simplified as two notional structures as shown in Figure 8-3.

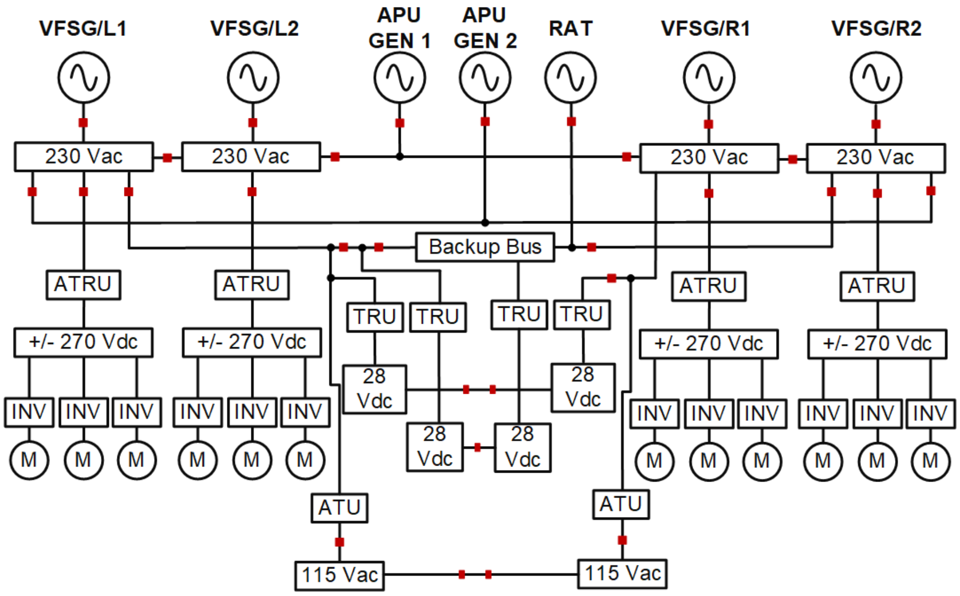

Figure 8-2. Example architecture of an MEA EPS.

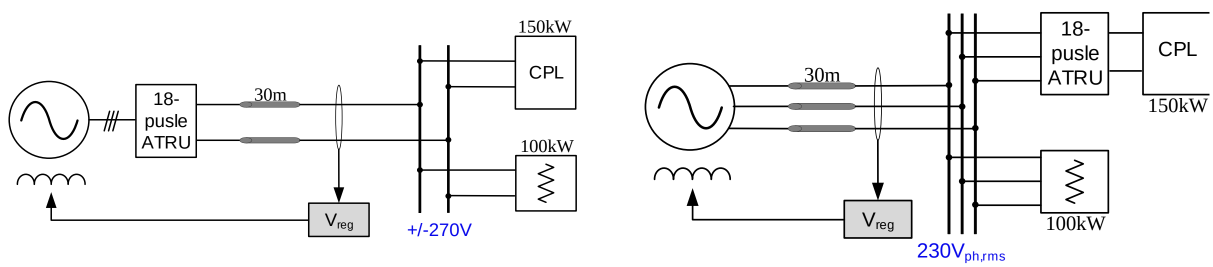

(a) (b)

Figure 8-3. Notional aircraft EPSs.

The main bus voltages of the two notional systems are +/-270 Vdc and 230 Vac, respectively. Also, in each system, it is assumed that there are one 150 kW inverter-driven motor load which is modeled as a constant power load (CPL), and one 100 kW resistive load. The feeder length in both systems is assumed to be 30 m. The source side is a synchronous generator (SG). And an 18-pulse ATRU is used to convert ac voltage to dc voltage in both systems. Additionally, no redundancy for system safety is considered in this study.

In addition to the given notional structure and working conditions, the desired system performance and a design goal should also be clarified to start the design procedure. In this study, the performance requirements for both ac and dc notional systems are from the following aircraft EPS standards: SAE-AS-50881F, MIL-STD-704E, and RTCA/DO-160G. And the design goal for the aircraft EPS is to minimize the weight of the aircraft's electric system. Therefore, with the given system framework, loading conditions, performance requirements, and certain objectives, a conceptual design of these two notional aircraft EPSs can then be conducted.

8.2.1 Conceptual Design of Aircraft EPSs Considering Static Requirements

The conventional sizing methods of aircraft EPS include the following four aspects [223, 224]:

(1) Framework and component models to determine power demands.

(2) Power distribution for insulated conductors (insulation thickness and insulation materials).

(3) Wiring.

(4) Heat exchanger design.

This chapter is mainly focused on the electric component design, including the sizing of cables, ATRUs, and generations.

To design the system under static requirements, several assumptions are made first:

(1) Feeders are single-insulated aluminum conductors (600V, 175^{o}C) with a 50mm spacing in-plane arrangement as shown in Figure 8-4.

(2) The ambient temperature is assumed as -20 ^{o}C when the aircraft's flying altitude is 40,000 feet and +40 ^{o}C when the aircraft is on the ground;

(3) The power factor and efficiency of 18-pulse ATRU in this study are assumed to be 0.98 and 98% based on the current technology [225].

With all the assumptions, the design procedure can then follow the weight determination algorithm as shown in Figure 8-5. With the given load power and system losses, line currents can be obtained. Considering permissible temperature ratings, the cable diameter is chosen based on SAE-AS-50881F. Then, the result is checked with the bundle and altitude derating factors. If the current capability of the selected wire does not meet the line current requirements, then a larger cable diameter should be selected and examined. If it meets the requirements, then the generator power ratings can be calculated. The system weight can then be estimated according to the power density data.

Therefore, the feeders in ac EPS are selected to be 4×AWG 4/0 (47.85 kg) and in dc EPS are 2×AWG 2/0 (23.93 kg). Correspondingly, the required SG power ratings are obtained: the generator in ac system is 297 kVA and in the dc system is 291 kVA. Assuming the power density of the SG is 0.34 kg/kVA and of the ATRU is 0.24 kg/kVA, the weight of the SG and ATRU for both systems can then be calculated.

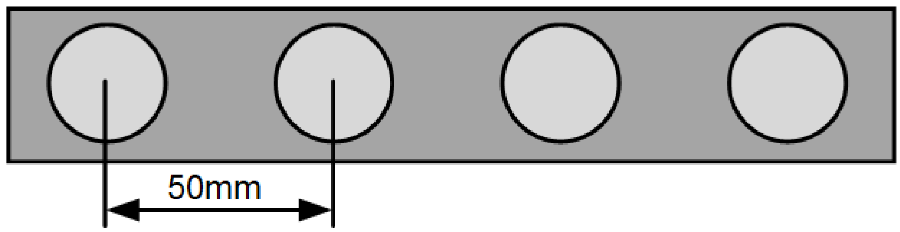

Figure 8-4. In-plane arrangement of conductors.

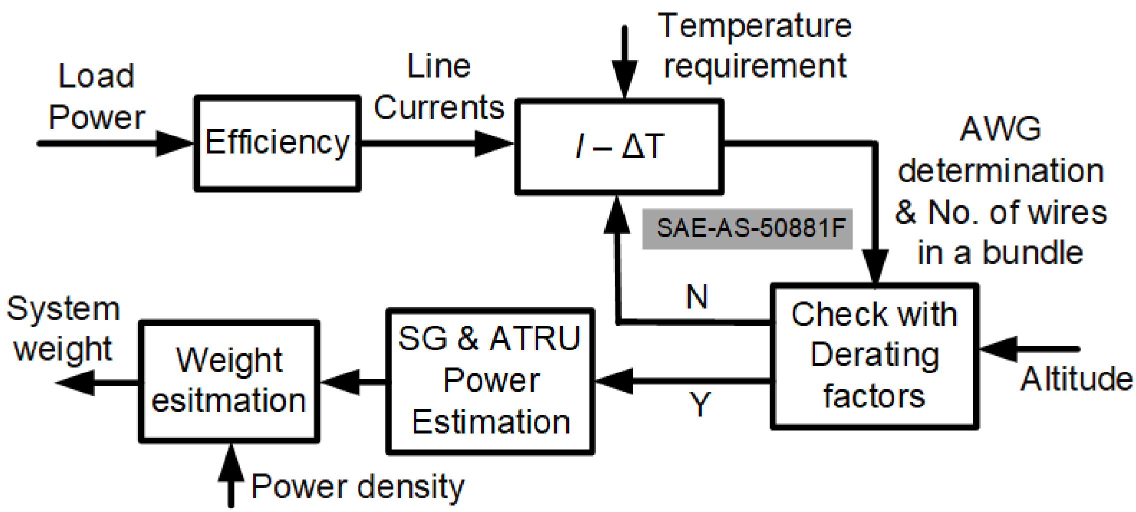

Figure 8-5. System weight determination algorithm.

8.2.2 Conceptual Design of Aircraft EPSs Considering Dynamic Requirements

The dynamic performance of aircraft EPS is also important for system design. Hence, the impacts of dynamic requirements on system design are studied in this section, including small-signal stability, normal load transient, and abnormal transient.

A. Small-Signal Stability Design

Small-signal stability performance is examined with the static design results obtained in Section 8.2.1.

1) Ac Notional System

The PBSC is used for ac system analysis, i.e., if the bus impedance of the ac system is passive, then it is a stable system. In the ac system, the bus impedance can be modeled as the parallel connection of the input impedance seen from the ATRU side, the resistive load R_L, and the output impedance of the source side Z_{ov} as shown in Figure 8-6. The SG is assumed as an ideal voltage source, so the passivity of the bus impedance is mainly determined by $Z_{ATRU+CPL}$. Modeling of the sequence impedance of the 18-pulses ATRU can be found in [226]. The small-signal stability criterion for the ac notional system is then simplified as (8 1).

$$Re(Z_{ATRU}(j\omega)) > 0, \forall\omega \in (-\infty, +\infty) \quad (8\ 1)$$

Therefore, the stability analysis can be conducted as shown in Figure 8-7 and the ac notional system is small-signal stable with the static design results. Note that the PBSC is a conservative approach. In this study, the static design happens to result in a passive design, therefore, the PBSC can be used for simplicity. But in other cases, if the bus impedance is non-passive, it does not necessarily mean the system is unstable, and the NSC should be adopted for further verification.

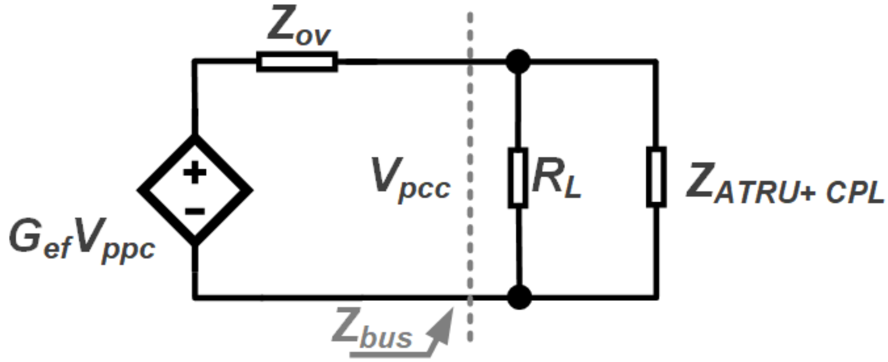

Figure 8-6. Bus impedance of the ac notional EPS.

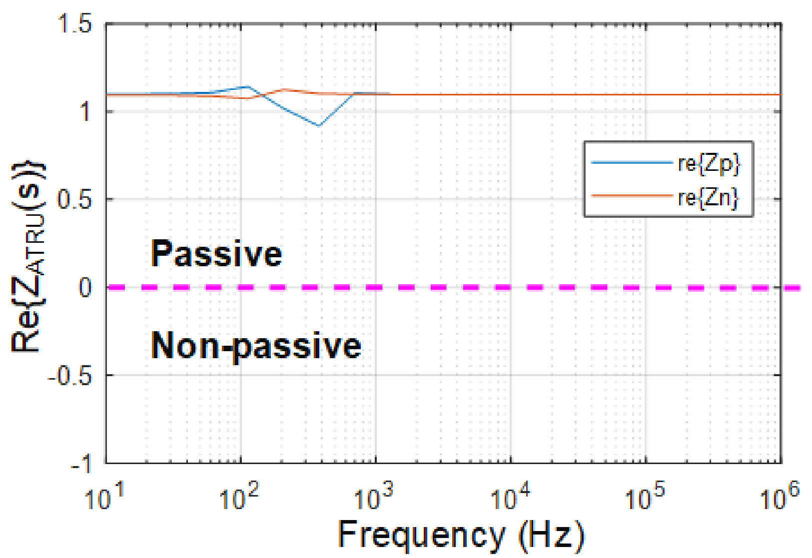

Figure 8-7. Passivity-based stability analysis of the notional ac EPS.

2) Dc Notional System

The Middlebrook criterion is used for the dc notional EPS to check the interaction of the impedances between the source side and load side as shown in Figure 8-8. The generator and the 18-pulse ATRU are regarded as the source side and the output impedance is modeled as Z_S. The overall load side impedance is modeled as Z_L. Besides, the dc voltage control loop is denoted by T_v as shown in Figure 8-8 (b) with f_{BW} as its control bandwidth.

The stability criterion for the dc notional system is given in (8. 2), where, $Z_L = \frac{-R_L V_{dc}^2}{P_{CPL} R_L - V_{dc}^2}$ and $|Z_s|_{peak} = \frac{1}{2\pi f_{BW} C_{cable}}$, which shows that the stability margin Z_m of the system should be larger than 0 dB. It is then calculated that the dc EPS is stable with a 32 dB impedance stability margin. Therefore, there is no need to modify the static design results. The Middlebrook criterion is also a conservative approach, so if the impedance ratio does not meet the stability requirement in (8. 2), the Nyquist stability criterion is needed for further checking.

$$Re(Z_{ATRU}(j\omega)) > 0, \forall \omega \in (-\infty, +\infty) \tag{8. 2}$$

B. Normal Load Transient Design

For normal load transient performance estimation, simulations with load step-down and step-up (100% to 5% to 100%) transients are conducted for both systems.

1) Ac Notional System

The simulation results of load step-down transients are given in Figure 8-9. As the load reference steps down from 100% to 5% of the overall power value, ac currents will follow a quasi-sinusoidal trajectory and drop to 0, and the ac contactor will switch at this zero-crossing point, so there is no large voltage spike. During the load step-up transient, the response of ac bus voltage

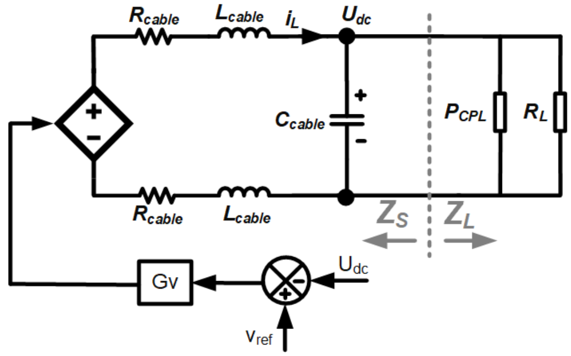

(a)

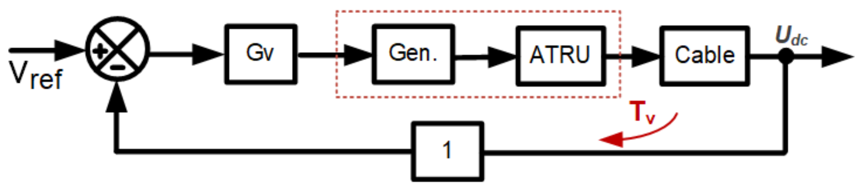

(b)

Figure 8-8. Impedance models of the dc notional EPS.

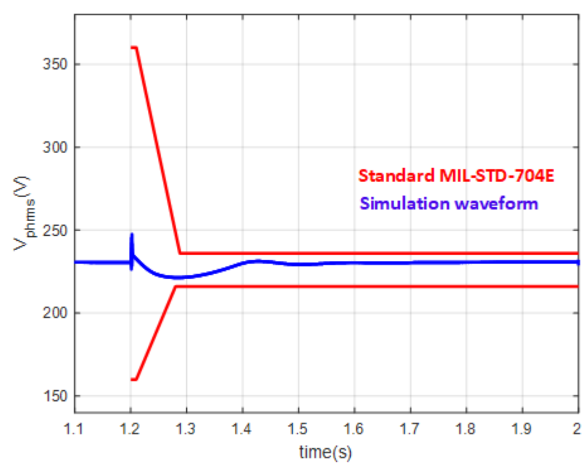

Figure 8-9. Load step down in ac EPS from 100% to 5% at t = 1.2 s.

can also meet the standard as shown in Figure 8-10. Therefore, there is no need to modify the original design for the ac system that is obtained under static requirements.

2) Dc Notional System

Similarly, the load transient simulations are conducted on the dc notional EPS as shown in Figure 8-11 and Figure 8-12. It is seen that the dc bus voltage during load step-down can meet the transient standard, but the load step-up transient cannot meet the requirement. Therefore, there is a need to modify the previous static design for the normal transient performance.

The reason for this sharp voltage spike during load step-up transient in the dc system is due to the lack of energy storage capability. Therefore, a dc-link capacitor is needed. The scheme of the modified dc system is shown in Figure 8-13. And the transient bus current and voltage can be estimated by (8. 3) and (8. 4) so that the required dc-link capacitance can be calculated.

$$\frac{di_L}{dt} = -\frac{R_{cable}}{L_{cable}} i_L + \frac{V_{dc} - U_{dc}}{2L_{cable}} \tag{8. 3}$$

$$\frac{dU_{dc}}{dt} = \frac{i_L}{(C_{cable} + C_{dcbus})} - \frac{P_{CPL}}{(C_{cable} + C_{dcbus})U_{dc}} - \frac{U_{dc}}{(C_{cable} + C_{dcbus})R_L} \tag{8. 4}$$

In this study, a 5 mF (9 kg) bus capacitor is required to meet the load transient requirements. The simulation results of the load transient with adding a bus capacitor are shown in Figure 8-14 and Figure 8-15. With the modified design, the normal load transient performance can meet the standard. In addition, the small-signal stability margin needs to be recalculated. In this case, the modified system was verified to be stable with a reduced stability margin, i.e., 6.3 dB.

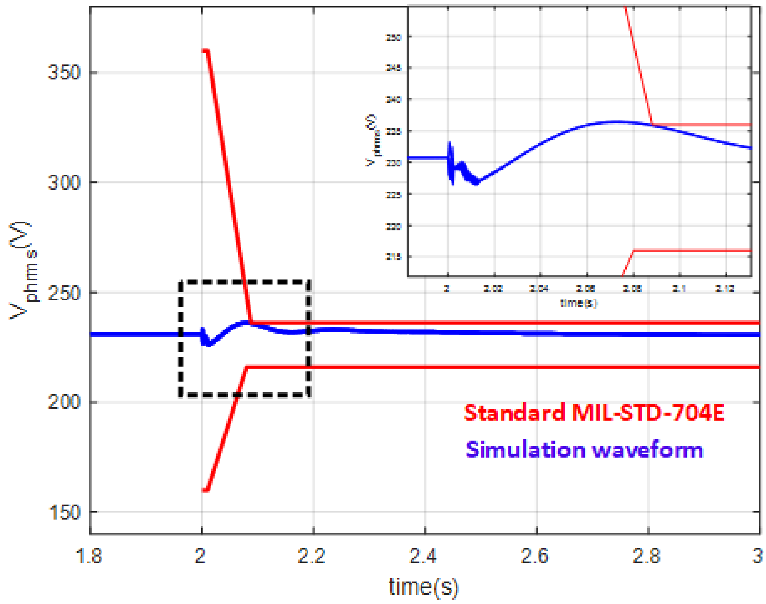

Figure 8-10. Load step-up in ac EPS from 5% to 100% at t = 2 s.

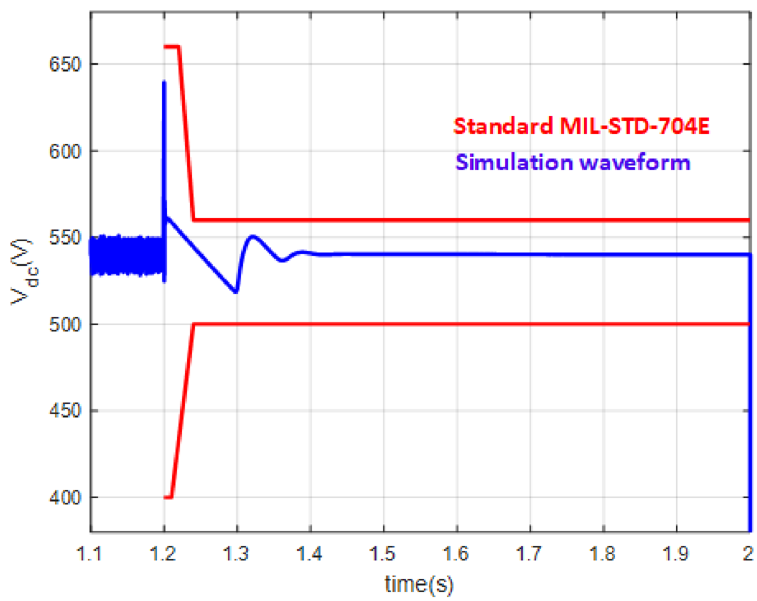

Figure 8-11. Load step down in dc EPS from 100% to 5% at t = 1.2 s.

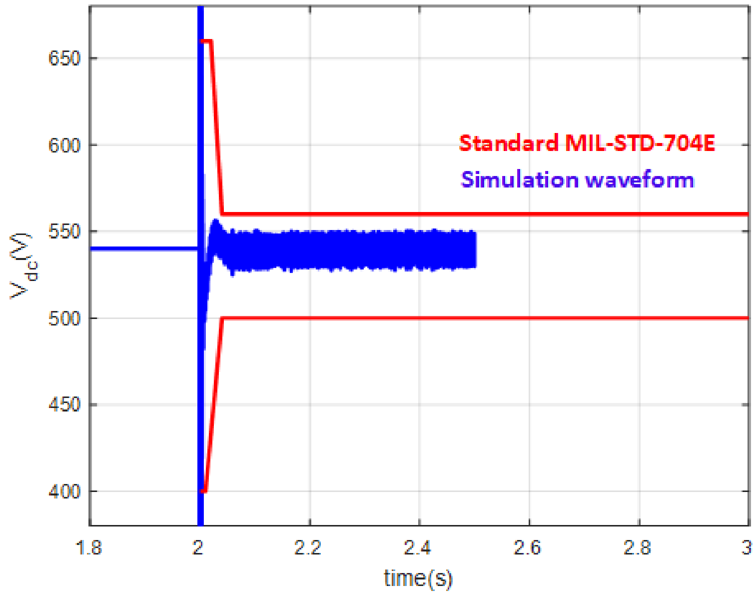

Figure 8-12. Load step-up in dc EPS from 5% to 100% at t = 2 s.

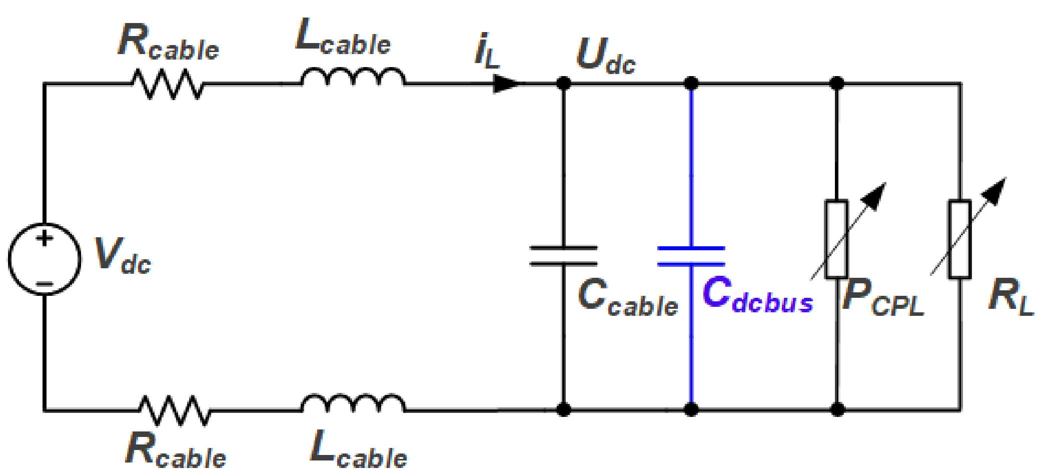

Figure 8-13. Modified dc system considering load step-up transient.

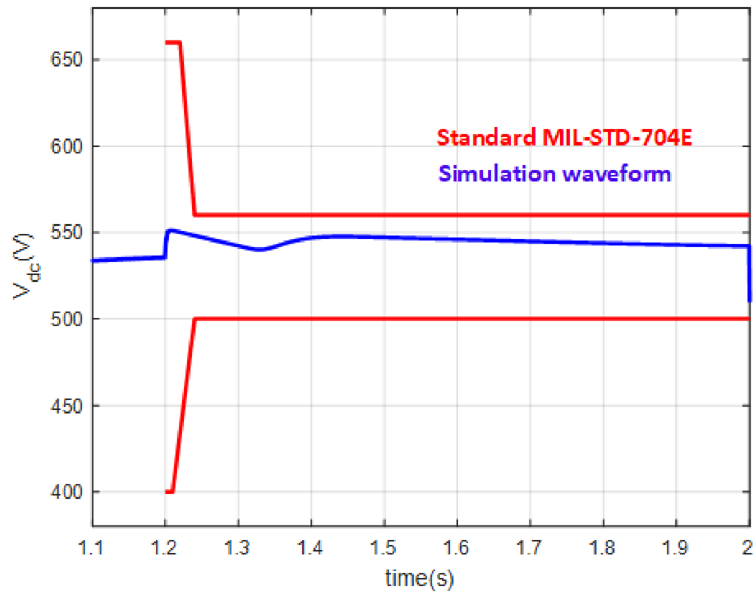

Figure 8-14. Load step-down in dc EPS from 100% to 5% at t = 1.2 s.

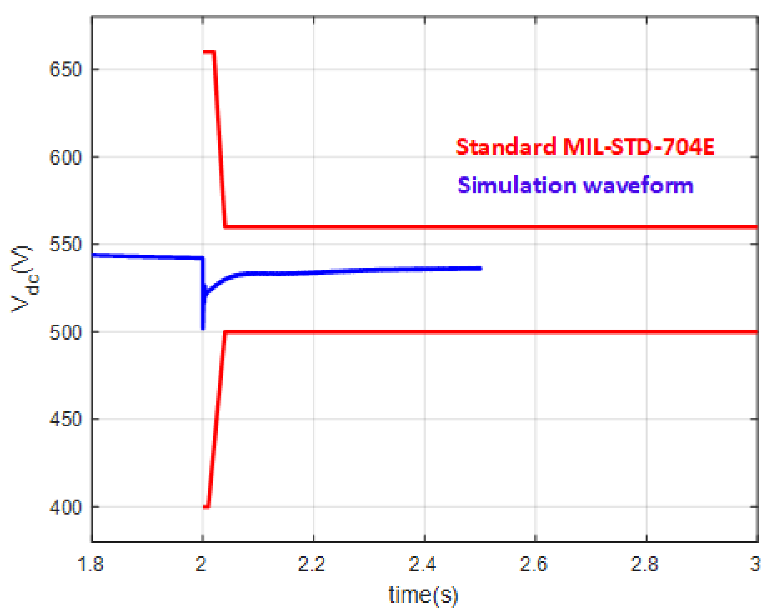

Figure 8-15. Load step-up in dc EPS from 5% to 100% at t = 2 s.

C. Abnormal Transient Design

In addition to the normal load transient, the abnormal transient performance should also be considered. Therefore, for such a study, a phase-to-phase short-circuit fault and a pole-to-pole short-circuit fault is assumed separately in the ac and dc EPSs at the input side of the CPL with the short-circuit resistance R_{short} = 0.01 Ω at t = 1 s. The natural responses of the relative bus currents (= real current / nominal current) of both systems are given in Figure 8-16 and Figure 8-17. It can be seen that the natural response of the fault currents in the dc EPS (×120 i_{nom}) is much larger than that in the ac EPS (× 23 i_{nom}). This is because the voltage holding capability of the dc bus capacitors is much larger than that in ac system as shown by the equivalent circuits of the immediate transient during fault of both systems in Figure 8-18.

To limit the fault current to be less than 9 times of the nominal current based on the requirements, the combined use of a superconducting fault current limiter (SFCL)[227], which is to suppress the fault current, and a solid-state circuit breaker (SSCB) [228], which is to quickly isolate faults, is assumed in this study. In addition, the response time of SSCBs used in this study is assumed as 50 μs. The bus performance during faults with proper protection devices is shown in Figure 8-19 and Figure 8-20. Based on the simulations, the required equivalent resistance of SFCLs in the dc EPS is about two times of that in ac EPS. Therefore, the power ratings for the protection devices can be calculated. For faults at other locations or of other types, similar simulations are conducted and the corresponding protection devices can be selected. Note that the design of the protection devices is conducted under complete selectivity conditions. In the end, assuming the power density of the SSCBs (ac: 2.9 g/kW, dc: 5 g/kW) and the SFCLs (ac: 1.58 g/kW, dc: 0.524 g/kW), the total weight of all the protection devices can then be estimated (ac: 16.9 kg, dc: 20.4 kg).

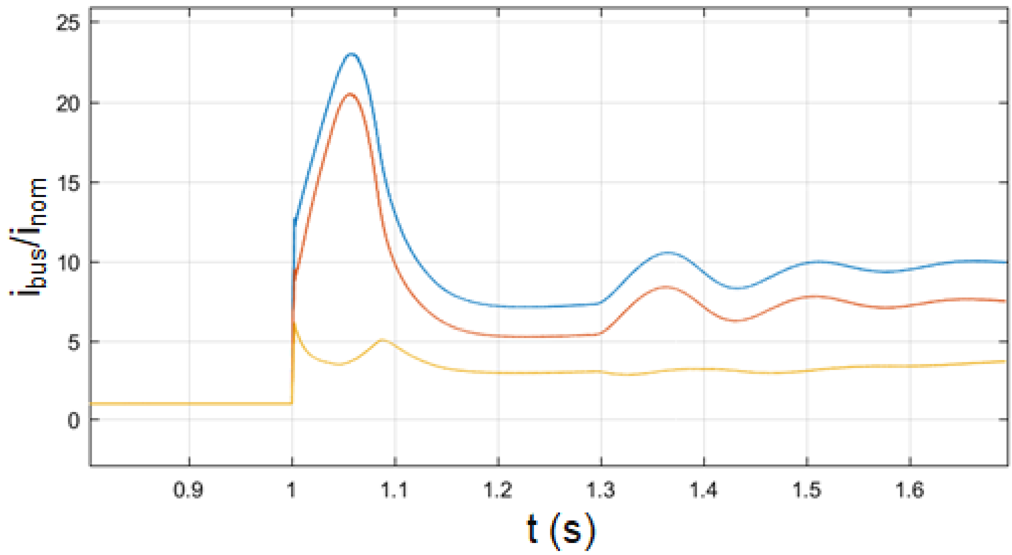

Figure 8-16. Relative bus currents during a fault at t = 1 s in ac EPS.

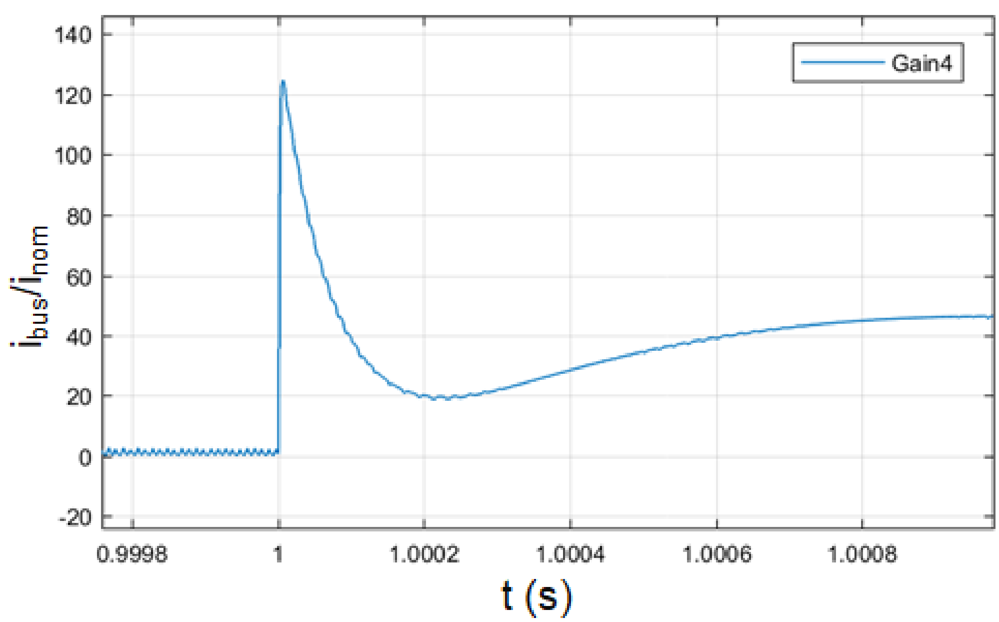

Figure 8-17. Relative bus currents during a fault at t = 1 s in dc EPS.

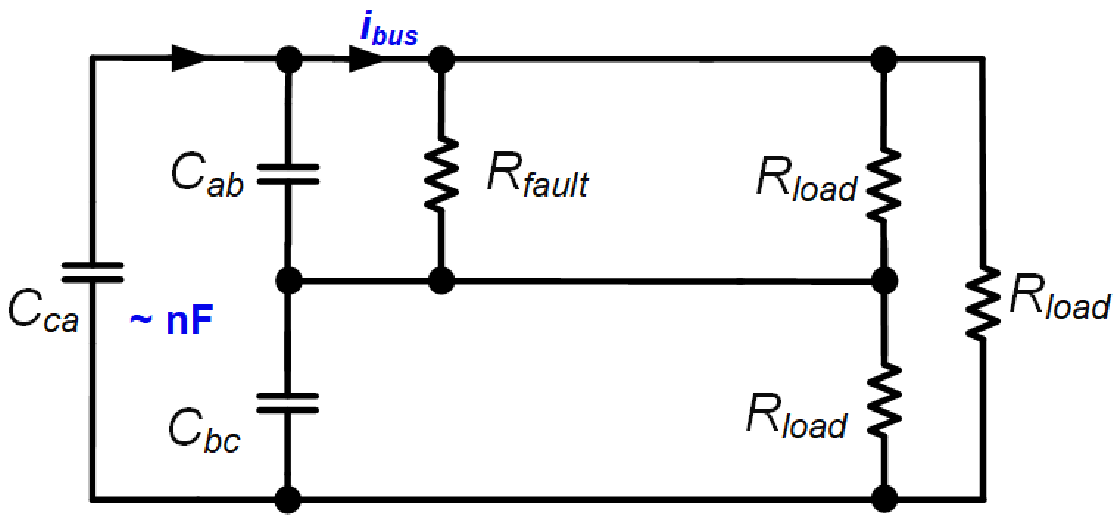

(a)

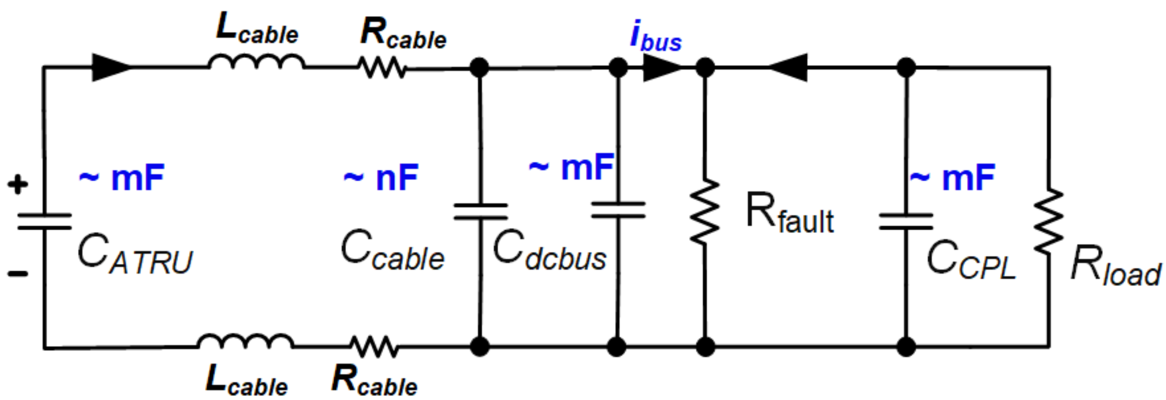

(b)

Figure 8-18. Equivalent circuit of immediate transient: (a) ac EPS and (b) dc EPS.

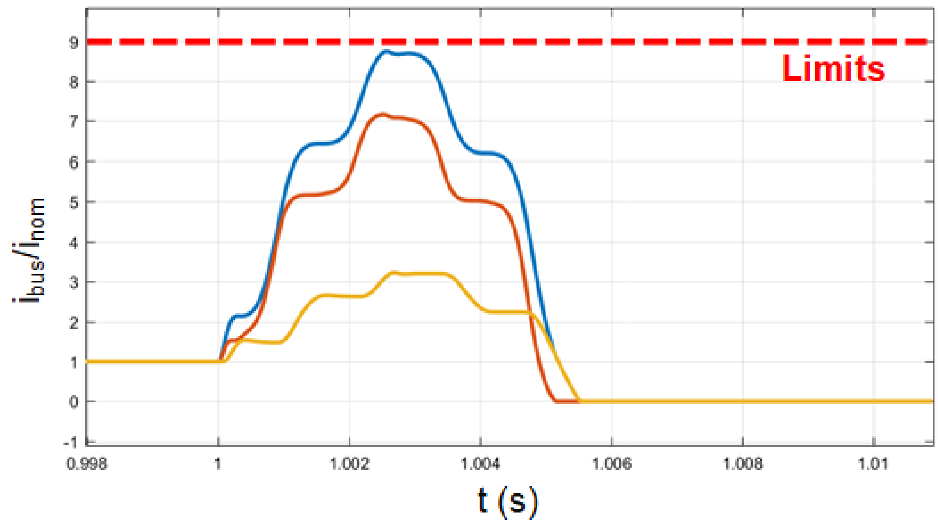

(a)

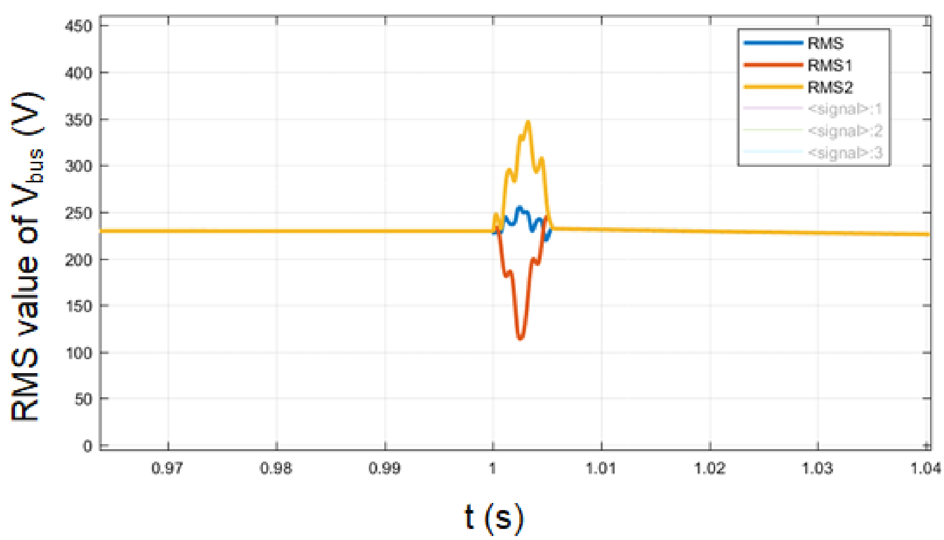

(b)

Figure 8-19. Bus currents and voltage during a fault in ac EPS with protection devices: (a) relative bus currents and (b) bus voltage.

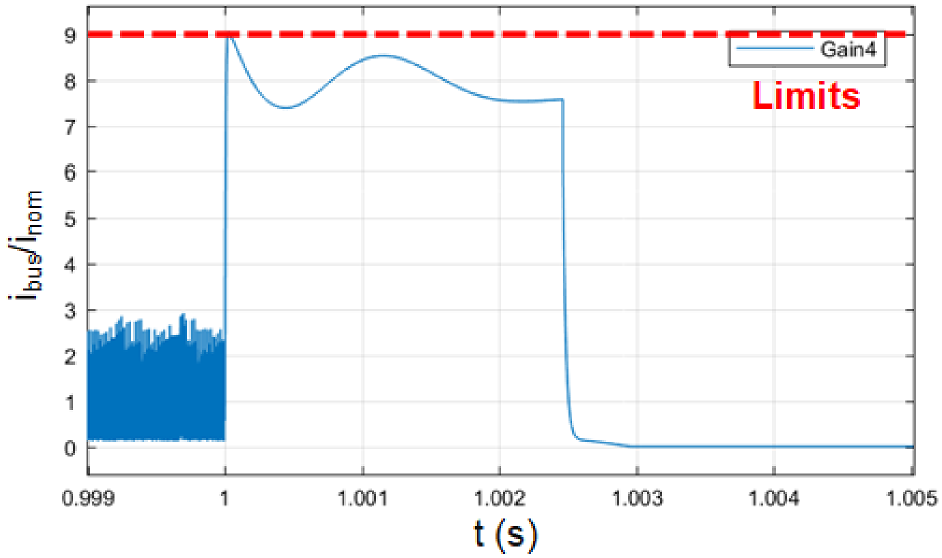

(a)

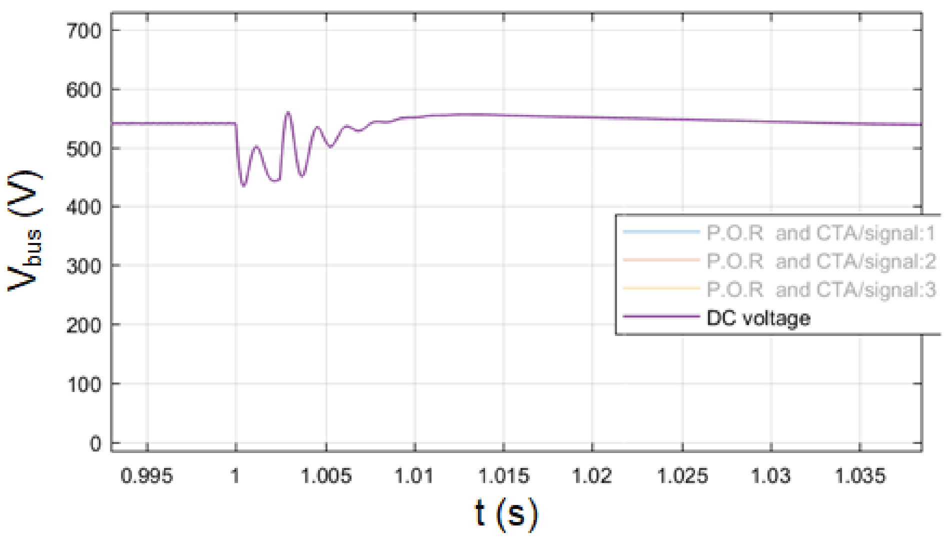

(b)

Figure 8-20. Bus currents and voltage during a fault in dc EPS with protection devices: (a) relative bus currents and (b) bus voltage.

8.2.3 Results and Discussions

The overall system weight considering both static requirements and dynamic requirements can then be summarized as shown in Figure 8-21, with the breakdown comparisons of each part in Figure 8-21(a) and system weight comparisons with and without considering dynamic requirements in Figure 8-21(b). From the results, it can be seen that compared with ac EPS, dc EPS saves some weight due to lighter feeders under static requirements only. But if the stability requirements are included, dc EPS will need an additional dc bus capacitor to provide energy storage capacity during the load transient. It also requires a larger SFCL to limit the much faster fault current dynamics. Therefore, when considering these dynamic design requirements, dc systems will have significant additional weight added compared to ac systems. Note that the power density values used in this study are from the literature or commercial products which might change with different technologies, but the methods to consider the impacts of dynamic requirements on system design are general.

8.3 Conclusions

This chapter examined the impacts of dynamic requirements on the system design of dc and ac EPSs. If only static requirements are considered, the dc EPS will be lighter than ac EPS mainly because of the lighter feeders in the dc system. However, if stability requirements are considered as well, the dc EPS might be heavier than the ac EPS due to the need for extra ESS to provide enough short-term energy during load transient and larger SFCL to limit the faster fault currents. Therefore, stability requirements have more impact on dc system design than ac. The same methodology in the design process can also be extended to other applications with certain design goals, e.g., dc and ac microgrids design for minimized system cost.

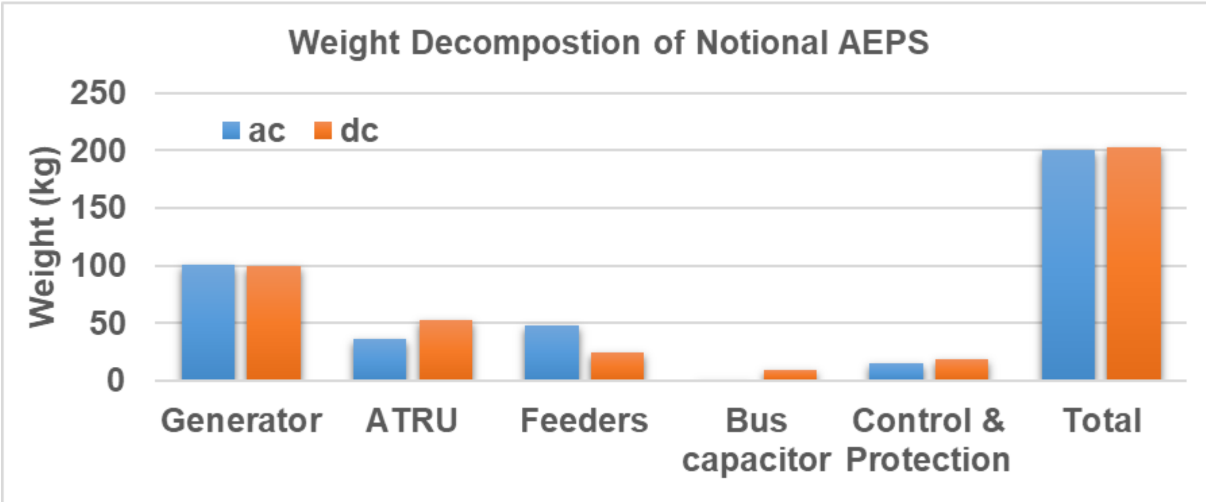

(a)

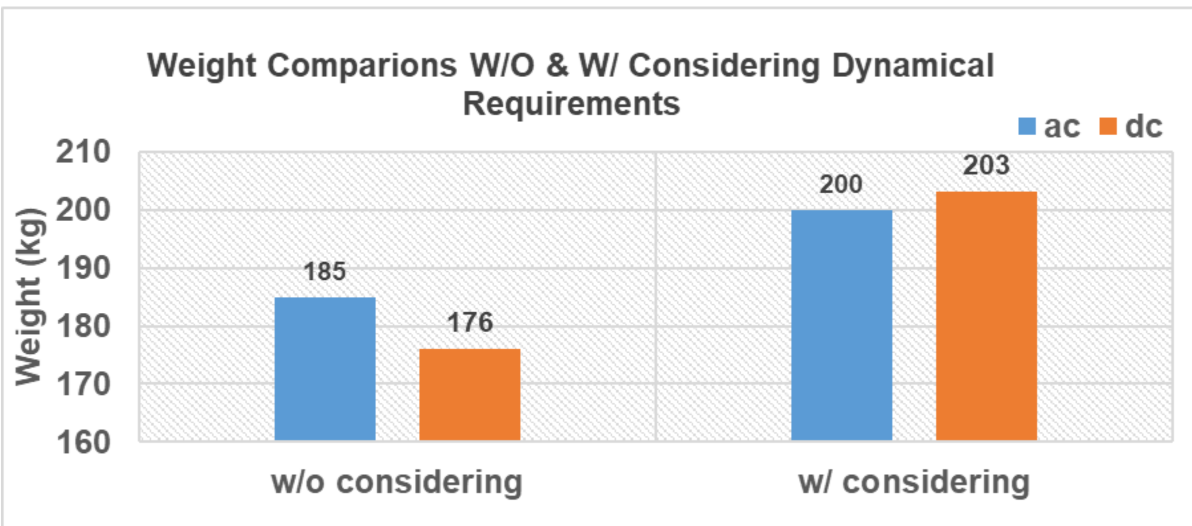

(b)

Figure 8-21. Estimated system weight: (a) weight decomposition of notional Aircraft EPS and (b) weight comparisons.

Chapter 9. Conclusions and Future Work

This chapter summarizes the work in this dissertation and recommends future work.

9.1 Conclusions

System stability analysis and design for power electronic converter-rich power systems under both small and large disturbances have been investigated in this dissertation. The conclusions can be drawn as follows:

- An improved small-signal dc impedance model of MMCs is proposed by considering the dynamics of both submodule capacitor voltages and circulating currents. The refined impedance model can be used for system stability analysis at the dc side in PEC-rich power systems with MMCs.
- A simple-to-use method for dc impedance measurement in medium- or high-voltage, high-power applications is proposed, which is easy to set up without any dedicated equipment by using existing converters in the system. The measured dc impedance model can be used to validate the derived analytical model or to be directly used for system stability analysis.
- Two linear control methods for GFMs to enhance system small-signal stability are proposed. It is found that the existing virtual impedance block Z_v - based control approach, though can help with system HF stability, might cause LF stability issues as a side effect. Therefore, the first approach is to use an online harmonic detection-based control method to eliminate HF stability without using the Z_v block. The second approach is to introduce an angle-droop control block into the outer power control loop to directly compensate for the possible negative impact of the Z_v block on system LF stability.

- A port-Hamiltonian-based control approach is proposed to render GFMs passive. The passivity property is achieved through energy damping and pumping motion by defining a proper Hamiltonian function. The basic concept of the proposed method is to design the GFMs to emulate the behavior of a passive coupled harmonic oscillator so that when it is connected to another passive grid or connected with other passive GFMs, the system will be synchronized and stabilized autonomously. This pH-based control approach is also extended for a non-passive but stable system. A Lyapunov function is constructed based on the Hamiltonian function, and the Lyapunov stability of the system can then be guaranteed.
- A notional aircraft electric power system is adopted as a test case to study the impacts of stability requirements on system design with the consideration of ac bus and dc bus. The system weight is defined as the system design target so that the impacts of both the small-signal stability requirements and large-signal stability requirements on system design are quantified and compared. Also, the fundamental mechanisms of the stability requirements in the selection of hardware components are discussed.

9.2 Recommended Future Work

Some recommended future work is listed as follows.

(1) Stability analysis and control design for GFMs considering dc bus dynamics

The research works in this dissertation about the control design for GFMs are conducted based on the assumption of ideal dc bus voltage. However, the assumption of an ideal dc bus is not always true since the dc bus dynamics might be coupled to the ac side and affect system stability, especially in the low-frequency region. For example, in a study for grid-following inverters, this non-ideal dc bus dynamics would reduce the inverter impedance at low-frequency and cause instability issues [229]. However, the impacts of dc bus dynamics on the design of GFMs have not been fully investigated yet. Therefore, it is important to incorporate dc bus dynamics into the stability analysis and control design of GFMs in the future.

(2) Stability analysis and controller design for PECs under unbalanced grid conditions

The research work in this dissertation has only considered the balanced three-phase power system. However, it is common that the grid is operated under unbalanced conditions, such as unbalanced loads or unbalanced faults. There is still a limited number of studies on system stability under unbalanced conditions. Therefore, it is of significance to develop some stability analysis and control approaches for unbalanced power-electronics-based power grids.

(3) Stability analysis and improvement for large-scale power-electronics-based power grids

With the increasing penetration of PECs, the power-electronics-based power grids (PEGs) become larger and larger, which brings more challenges to maintaining stable operations of the system. First, to analyze such a large-scale PEG, a high-order state-space matrix or a large impedance matrix might be needed, which might be non-solvable due to the huge computation burden of the excess matrix dimensions. Therefore, an improved stability analysis approach with less computation burden is expected to analyze the stability of a large-scale PEG. In addition, a distributed smart control approach to enhance system stability would be beneficial for the design of large-scale power systems, like the proposed PVOC approach in Chapter 7. But this approach needs to be further examined in a large-scale system in the future since even though the stability maintenance capability of this approach can be proved theoretically, there could be some implementation and computation issues in the real application.

(4) Comparative study of aircraft EPSs under more realistic conditions with more analysis

The comparative study of notional ac and dc aircraft EPSs in Chapter 8 presents some preliminary results under certain assumptions. For future work, it is suggested to consider more realistic conditions. Also, for the large-signal stability analysis of the aircraft EPS, more theoretical analysis should be conducted to have closed-form solutions in the future.

References

[1] "Green Technology and Sustainability Market Research Report." https://www.psmarketresearch.com/market-analysis/green-technology-and-sustainability-market (accessed 06/07, 2022).

[2] D. Boroyevich, I. Cvetković, D. Dong, R. Burgos, F. Wang, and F. Lee, "Future Electronic Power Distribution Systems A Contemplative View," in *International Conference on Optimization of Electrical and Electronic Equipment*, 2010, pp. 1369-1380.

[3] "Challenges and Solutions for Power Electronics Testing Applications." https://www.keysight.com/us/en/assets/7018-04941/technical-overviews/5992-1038.pdf (accessed Jul. 22, 2021).

[4] P. K. Steimer, "Enabled by High Power Electronics - Energy Efficiency, Renewables and Smart Grids," in *International Power Electronics Conference - ECCE ASIA*, 2010, pp. 11-15.

[5] J. M. Carrasco, L. G. Franquelo, J. T. Bialasiewicz, E. Galvan, R. C. PortilloGuisado, M. A. M. Prats *et al.*, "Power-Electronic Systems for the Grid Integration of Renewable Energy Sources: A Survey," *IEEE Transactions on Industrial Electronics,* vol. 53, no. 4, pp. 1002-1016, 2006.

[6] N. Hatziargyriou, J. V. Milanovic, C. Rahmann, V. Ajjarapu, C. Canizares, I. Erlich *et al.*, "Definition and Classification of Power System Stability -Revisited & Extended," *IEEE Transactions on Power Systems,* vol. 36, no. 4, pp. 3271-3281, 2021.

[7] S. Peyghami, P. Palensky, and F. Blaabjerg, "An Overview on the Reliability of Modern Power Electronic Based Power Systems," *IEEE Open Journal of Power Electronics,* vol. 1, pp. 34-50, 2020.

[8] B. Shakerighadi, S. Peyghami, E. Ebrahimzadeh, F. Blaabjerg, and C. L. Bak, "Security Analysis of Power Electronic-based Power Systems," in *Annual Conference of the IEEE Industrial Electronics Society (IECON)*, 2019, vol. 1, pp. 4933-4937.

[9] P. Kundur, J. Paserba, V. Ajjarapu, G. Andersson, A. Bose, C. Canizares *et al.*, "Definition and Classification of Power System Stability IEEE/CIGRE Joint Task Force on Stability Terms and Definitions," *IEEE Transactions on Power Systems,* vol. 19, no. 3, pp. 1387-1401, 2004.

[10] X. Yue, X. Wang, and F. Blaabjerg, "Review of Small-Signal Modeling Methods Including Frequency-Coupling Dynamics of Power Converters," *IEEE Transactions on Power Electronics,* vol. 34, no. 4, pp. 3313-3328, 2019.

[11] X. Wang and F. Blaabjerg, "Harmonic Stability in Power Electronic-Based Power Systems: Concept, Modeling, and Analysis," *IEEE Transactions on Smart Grid,* vol. 10, no. 3, pp. 2858-2870, 2019.

[12] Q. Xu, "Overview of Stability Analysis Methods in Power Electronics," in *Control of Power Electronic Converters and Systems*: Elsevier, 2021, pp. 169-197.

[13] J. C. Mayo-Maldonado and P. Rapisarda, "A Systematic Approach to Constant Power Load Stabilization by Passive Damping," in *2015 54th IEEE Conference on Decision and Control (CDC)*, 2015, pp. 1346-1351.

[14] Y. Huangfu, S. Pang, B. Nahid-Mobarakeh, L. Guo, A. K. Rathore, and F. Gao, "Stability Analysis and Active Stabilization of On-board DC Power Converter System with Input Filter," *IEEE Transactions on Industrial Electronics*, vol. 65, no. 1, pp. 790-799, 2018.

[15] L. Zhou, W. Wu, Y. Chen, Z. He, X. Zhou, X. Huang *et al.*, "Virtual Positive-Damping Reshaped Impedance Stability Control Method for the Offshore MVDC System," *IEEE Transactions on Power Electronics*, pp. 1-1, 2018.

[16] J. Serrano, S. Cobreces, E. J. Bueno, and M. Rizo, "Passivity-Based Robust Current Control of Grid-Connected VSCs," in *IEEE Applied Power Electronics Conference and Exposition (APEC)*, 2020, pp. 745-752.

[17] L. Yang, X. Zhang, Y. Ma, J. Wang, L. Hang, K. Lin *et al.*, "Hardware Implementation and Control Design of Generator Emulator in Multi-Converter System," in *IEEE Applied Power Electronics Conference and Exposition (APEC)*, 2013, pp. 2316-2323.

[18] J. Wang, L. Yang, Y. Ma, J. Wang, L. M. Tolbert, F. Wang *et al.*, "Static and Dynamic Power System Load Emulation in a Converter-based Reconfigurable Power Grid Emulator," *IEEE Transactions on Power Electronics*, vol. 31, no. 4, pp. 3239-3251, 2016.

[19] R. Ahmadi, D. Paschedag, and M. Ferdowsi, "Closed-Loop Input and Output Impedances of DC-DC Switching Converters Operating in Voltage and Current Mode Control," in *Annual Conference on IEEE Industrial Electronics Society (IECON)*, 2010, pp. 2311-2316.

[20] M. Amin and M. Molinas, "Impedance based Stability Analysis of VSC-based HVDC System," in *IEEE Eindhoven PowerTech*, 2015, pp. 1-6.

[21] L. Xu, L. Fan, and Z. Miao, "DC Impedance-Model-Based Resonance Analysis of a VSC–HVDC System," *IEEE Transactions on Power Delivery*, vol. 30, no. 3, pp. 1221-1230, 2015.

[22] X. Yue, S. Yang, Y. Chen, F. Zhuo, and Y. Pei, "Modeling and Analysis for Output Impedance of Buck Converters," in *International Conference on Power Electronics and ECCE Asia (ICPE-ECCE Asia)*, 2015, pp. 2513-2519.

[23] M. Sanz, M. Bermejo, A. Lazaro, D. Lopez-del-Moral, P. Zumel, C. Fernandez *et al.*, "Simple Input Impedance Converter Model to Design Regulators for DC-Distributed System," in *IEEE Workshop on Control and Modeling for Power Electronics (COMPEL)*, 2016, pp. 1-6.

[24] B. Wen, D. Boroyevich, R. Burgos, P. Mattavelli, and Z. Shen, "Analysis of D-Q Small-Signal Impedance of Grid-Tied Inverters," *IEEE Transactions on Power Electronics*, vol. 31, no. 1, pp. 675-687, 2016.

[25] W. Cao, Y. Ma, and F. Wang, "Sequence-Impedance-Based Harmonic Stability Analysis and Controller Parameter Design of Three-Phase Inverter-Based Multibus AC Power Systems," *IEEE Transactions on Power Electronics*, vol. 32, no. 10, pp. 7674-7693, 2017.

[26] W. Cao, Y. Ma, L. Yang, F. Wang, and L. M. Tolbert, "D–Q Impedance Based Stability Analysis and Parameter Design of Three-Phase Inverter-Based AC Power Systems," *IEEE Transactions on Industrial Electronics*, vol. 64, no. 7, pp. 6017-6028, 2017.

[27] S. Shah and L. Parsa, "Impedance Modeling of Three-Phase Voltage Source Converters in DQ, Sequence, and Phasor Domains," *IEEE Transactions on Energy Conversion*, vol. 32, no. 3, pp. 1139-1150, 2017.

[28] X. Wang, L. Harnefors, and F. Blaabjerg, "Unified Impedance Model of Grid-Connected Voltage-Source Converters," *IEEE Transactions on Power Electronics*, vol. 33, no. 2, pp. 1775-1787, 2018.

[29] J. S. Lee, G. Y. Lee, S. S. Park, and R. Y. Kim, "Impedance-Based Modeling and Common Bus Stability Enhancement Control Algorithm in DC Microgrid," *IEEE Access*, vol. 8, pp. 211224-211234, 2020.

[30] Y. Li, Y. Gu, Y. Zhu, A. J. Ferre, X. Xiang, and T. C. Green, "Impedance Circuit Model of Grid-Forming Inverter: Visualizing Control Algorithms as Circuit Elements," *IEEE Transactions on Power Electronics*, vol. 36, no. 3, pp. 3377-3395, 2020.

[31] Y. Liao and X. Wang, "Impedance Decomposition for Design-Oriented Analysis of Grid-Forming Voltage-Source Converters," *TechRixv*, 2020.

[32] H. Mu, Y. Zhang, X. Tong, W. Chen, B. He, L. Shu *et al.*, "Impedance-Based Stability Analysis Methods for DC Distribution Power System With Multivoltage Levels," *IEEE Transactions on Power Electronics*, vol. 36, no. 8, pp. 9193-9208, 2021.

[33] W. Cao, Y. Ma, X. Zhang, and F. Wang, "Sequence Impedance Measurement of Three-Phase Inverters using a Parallel Structure," in *IEEE Applied Power Electronics Conference and Exposition (APEC)*, 2015, pp. 3031-3038.

[34] S. P. Rosado, "Voltage Stability and Control in Autonomous Electric Power Systems with Variable Frequency," Ph.D. dissertation, Dept. Elect. Comput. Eng., Virginia Tech, Blacksburg, VA, USA, 2007. [Online].

[35] W. Cao, "Impedance-Based Stability Analysis and Controller Design of Three-Phase Inverter-Based ac Systems," Ph.D. dissertation Dept. Elect. Comput. Eng., University of Tennessee, Knoxville, Knoxville, TN, USA, 2017. [Online].

[36] J. Adams, V. A. Pappu, and A. Dixit, "ERCOT Experience Screening for Sub-Synchronous Control Interaction in the Vicinity of Series Capacitor Banks," in *IEEE Power and Energy Society General Meeting*, 2012, pp. 1-5.

[37] C. Li, "Unstable Operation of Photovoltaic Inverter From Field Experiences," *IEEE Transactions on Power Delivery*, vol. 33, no. 2, pp. 1013-1015, 2018.

[38] J. H. R. Enslin and P. J. M. Heskes, "Harmonic Interaction Between A Large Number of Distributed Power Inverters and the Distribution Network," *IEEE Transactions on Power Electronics*, vol. 19, no. 6, pp. 1586-1593, 2004.

[39] I. Erlich, F. Shewarega, S. Engelhardt, J. Kretschmann, J. Fortmann, and F. Koch, "Effect of Wind Turbine Output Current during Faults on Grid Voltage and the Transient Stability of Wind Parks," in *IEEE Power & Energy Society General Meeting*, 2009, pp. 1-8.

[40] T. Souxes and C. Vournas, "System Stability Issues Involving Distributed Sources Under Adverse Network Conditions," in *Proc. IREP Symp. Bulk Power System Dyn. Control-X (IREP)*, 2017, pp. 1-9.

[41] J. Shair, H. Li, J. Hu, and X. Xie, "Power System Stability Issues, Classifications and Research Prospects in the Context of High-Penetration of Renewables and Power Electronics," *Renewable and Sustainable Energy Reviews*, vol. 145, 2021.

[42] J. Ainsworth, "Harmonic Instability Between Controlled Static Convertors and AC Networks," in *Proceedings of the Institution of Electrical Engineers*, 1967, vol. 114, no. 7: IET, pp. 949-957.

[43] X. Wang, M. G. Taul, H. Wu, Y. Liao, F. Blaabjerg, and L. Harnefors, "Grid-Synchronization Stability of Converter-Based Resources—An Overview," *IEEE Open Journal of Industry Applications*, vol. 1, pp. 115-134, 2020.

[44] P. Kundur, "Power System Stability," *Power system stability and control*, pp. 7-1, 2007.

[45] C. M. Wildrick, F. C. Lee, B. H. Cho, and B. Choi, "A Method of Defining the Load Impedance Specification for a Stable Distributed Power System," *IEEE Transactions on Power Electronics*, vol. 10, no. 3, pp. 280-285, 1995.

[46] Q. Zhong and X. Zhang, "Impedance-Sum Stability Criterion for Power Electronic Systems with Two Converters/Sources," *IEEE Access*, vol. 7, pp. 21254-21265, 2019.

[47] J. Siegers, S. Arrua, and E. Santi, "Allowable Bus Impedance Region for MVDC Distribution Systems and Stabilizing Controller Design using Positive Feed-Forward Control," in *IEEE Energy Conversion Congress and Exposition (ECCE)*, Milwaukee, WI, USA, 2016, pp. 1-8.

[48] R. Middlebrook, "Input Filter Considerations in Design and Application of Switching Regulators," in *IEEE Industry Applications Society Annual Metting*, pp. 366-382.

[49] X. Feng, J. Liu, and F. C. Lee, "Impedance Specifications for Stable DC Distributed Power Systems," *IEEE Transactions on Power Electronics*, vol. 17, no. 2, pp. 157-162, 2002.

[50] S. D. Sudhoff, S. F. Glover, P. T. Lamm, D. H. Schmucker, and D. E. Delisle, "Admittance Space Stability Analysis of Power Electronic Systems," *IEEE Transactions on Aerospace and Electronic Systems,* vol. 36, no. 3, pp. 965-973, 2000.

[51] S. D. Sudhoff and J. M. Crider, "Advancements in Generalized Immittance based Stability Analysis of DC Power Electronics Based Distribution Systems," in *IEEE Electric Ship Technologies Symposium*, Alexandria, VA, USA, 2011, pp. 207-212.

[52] A. Riccobono and E. Santi, "Comprehensive Review of Stability Criteria for DC Power Distribution Systems," *IEEE Transactions on Industry Applications,* vol. 50, no. 5, pp. 3525-3535, 2014.

[53] A. Riccobono and E. Santi, "Stability Analysis of an All-Electric Ship MVDC Power Distribution System using a Novel Passivity-based Stability Criterion," in *IEEE Electric Ship Technologies Symposium (ESTS)*, Arlington, VA, USA, 2013, pp. 411-419.

[54] Y. Liao, X. Wang, and F. Blaabjerg, "Passivity-Based Analysis and Design of Linear Voltage Controllers for Voltage- Source Converters," *IEEE Open Journal of the Industrial Electronics Society,* vol. 1, pp. 114-126, 2020.

[55] A. Akhavan, H. R. Mohammadi, J. C. Vasquez, and J. M. Guerrero, "Passivity-Based Design of Plug-and-Play Current-Controlled Grid-Connected Inverters," *IEEE Transactions on Power Electronics,* vol. 35, no. 2, pp. 2135-2150, 2020.

[56] H. Liu, L. Li, Y. Liu, D. Xu, and Q. Gao, "Passivity Based Damping Design for Grid-Connected Converter with Improved Stability," *IEEE Access,* vol. 7, pp. 185168-185178, 2019.

[57] Y. Liao and X. Wang, "Passivity Analysis and Enhancement of Voltage Control for Voltage-Source Converters," in *IEEE Energy Conversion Congress and Exposition (ECCE)*, 2019, pp. 5424-5429.

[58] H. Yu, H. Tu, and S. Lukic, "A Passivity-based Decentralized Control Strategy for Current-Controlled Inverters in AC Microgrids," in *IEEE Applied Power Electronics Conference and Exposition (APEC)*, 2018, pp. 1399-1406.

[59] J. U. Liceaga-Castro, I. I. Siller-Alcalá, E. Liceaga-Castro, and L. A. Amézquita-Brooks, "MIMO Passive Control Systems Are Not Necessarily Robust," *Journal of Control Science and Engineering,* p. 508102, 2015.

[60] J. Sun, "Impedance-based Stability Criterion for Grid-Connected Inverters," *IEEE Transactions on Power Electronics,* vol. 26, no. 11, pp. 3075-3078, 2011.

[61] Y. Liao and X. Wang, "Impedance-Based Stability Analysis for Interconnected Converter Systems with Open-Loop RHP Poles," *IEEE Transactions on Power Electronics,* vol. 35, no. 4, pp. 4388-4397, 2020.

[62] U. Javaid, F. D. Freijedo, W. v. d. Merwe, and D. Dujic, "Stability Analysis of Multi-Port MVDC Distribution Networks for All-Electric Ships," *IEEE Journal of Emerging and Selected Topics in Power Electronics,* vol. 8, no. 2, pp. 1164-1177, 2020.

[63] W. Cao, Y. Ma, F. Wang, L. M. Tolbert, and Y. Xue, "Low-Frequency Stability Analysis of Inverter-based Islanded Multiple-Bus AC Microgrids based on Terminal Characteristics," *IEEE Transactions on Smart Grid*, vol. 11, no. 5, pp. 3662-3676, 2020.

[64] D. Lumbreras, E. L. Barrios, A. Urtasun, A. Ursúa, L. Marroyo, and P. Sanchis, "On the Stability of Advanced Power Electronic Converters: the Generalized Bode Criterion," *IEEE Transactions on Power Electronics*, vol. 34, no. 9, pp. 9247-9262, 2019.

[65] Y. Liao and X. Wang, "General Rules of Using Bode Plots for Impedance based Stability Analysis," presented at the IEEE Workshop on Control and Modeling for Power Electronics (*COMPEL)*, Padova, Italy, 2018.

[66] J. R. Forbes, "Extensions of Input-Output Stability Theory and the Control of Aerospace Systems," University of Toronto, 2011. [Online].

[67] W. Xie, M. Han, W. Cao, J. M. Guerrero, and J. C. Vasquez, "System-Level Large-Signal Stability Analysis of Droop-Controlled DC Microgrids," *IEEE Transactions on Power Electronics*, vol. 36, no. 4, pp. 4224-4236, 2021.

[68] H. Kim, S. Kang, G. Seo, P. Jang, and B. Cho, "Large-signal Stability Analysis of DC Power System with Shunt Active Damper," *IEEE Transactions on Industrial Electronics*, vol. 63, no. 10, pp. 6270-6280, 2016.

[69] M. Kabalan, P. Singh, and D. Niebur, "Large Signal Lyapunov-Based Stability Studies in Microgrids: A Review," *IEEE Transactions on Smart Grid*, vol. 8, no. 5, pp. 2287-2295, 2017.

[70] I. W. Sandberg, "On the Properties of Some Systems that Distort Signals — I," *The Bell System Technical Journal*, vol. 42, no. 5, pp. 2033-2046, 1963.

[71] I. W. Sandberg, "On the Properties of Some Systems that Distort Signals — II," *The Bell System Technical Journal*, vol. 43, no. 1, pp. 91-112, 1964.

[72] I. W. Sandberg, "On the L2-Boundedness of Solutions of Nonlinear Functional Equations," *Bell System Technical Journal*, vol. 43, no. 4, pp. 1581-1599, 1964.

[73] G. Zames, "On the Input-Output Stability of Time-Varying Nonlinear Feedback Systems Part one: Conditions Derived Using Concepts of Loop Gain, Conicity, and Positivity," *IEEE Transactions on Automatic Control*, vol. 11, no. 2, pp. 228-238, 1966.

[74] G. Zames, "On the Input-Output Stability of Time-Varying Nonlinear Feedback Systems--Part II: Conditions Involving Circles in the Frequency Plane and Sector Nonlinearities," *IEEE Transactions on Automatic Control*, vol. 11, no. 3, pp. 465-476, 1966.

[75] A. J. Van der Schaft and A. Van Der Schaft, *L2-gain and Passivity Techniques in Nonlinear Control*. Springer, 2000.

[76] R. Ortega, D. Jeltsema, and J. M. A. Scherpen, "Stabilization of Nonlinear RLC Circuits: Power Shaping and Passivation," in *42nd IEEE International Conference on Decision and Control (IEEE Cat. No.03CH37475)*, 2003, vol. 6, pp. 5597-5602 Vol.6.

[77] D. Jeltsema and J. M. A. Scherpen, "Multidomain Modeling of Nonlinear Networks and Systems," *IEEE Control Systems Magazine*, vol. 29, no. 4, pp. 28-59, 2009.

[78] R. Ortega, J. A. L. Perez, P. J. Nicklasson, and H. J. Sira-Ramirez, *Passivity-based Control of Euler-Lagrange systems: Mechanical, Electrical and Electromechanical Applications*. Springer Science & Business Media, 2013.

[79] S. Arjan van der and J. Dimitri, *Port-Hamiltonian Systems Theory: An Introductory Overview*. Now Foundations and Trends, 2014, p. 1.

[80] R. K. Brayton and J. K. Moser, "A Theory of Nonlinear Networks - I," *Quarterly of Applied Mathematics*, vol. 22, no. 1, pp. 1-33, 1964.

[81] R. K. Brayton and J. K. Moser, "A Theory of Nonlinear Networks,II," *Quarterly of Applied Mathematics*, vol. 22, no. 2, pp. 81-104, 1964.

[82] K. C. Kosaraju, M. Cucuzzella, J. M. A. Scherpen, and R. Pasumarthy, "Differentiation and Passivity for Control of Brayton–Moser Systems," *IEEE Transactions on Automatic Control*, vol. 66, no. 3, pp. 1087-1101, 2021.

[83] J. Jiang, F. Liu, S. Pan, X. Zha, W. Liu, C. Chen *et al.*, "A Conservatism-Free Large Signal Stability Analysis Method for DC Microgrid based on Mixed Potential Theory," *IEEE Transactions on Power Electronics*, vol. 34, no. 11, pp. 11342-11351, 2019.

[84] F. Chang, X. Cui, M. Wang, W. Su, and A. Q. Huang, "Large-Signal Stability Criteria in DC Power Grids with Distributed-Controlled Converters and Constant Power Loads," *IEEE Transactions on Smart Grid*, vol. 11, no. 6, pp. 5273-5287, 2020.

[85] M. Zhu, H. Nian, Y. Xu, and L. Chen, "Impedance-Based Stability Analysis of MMC-HVDC for Offshore DFIG-Based Wind Farms," in *2018 21st International Conference on Electrical Machines and Systems (ICEMS)*, 2018, pp. 1139-1144.

[86] J. Sun and H. Liu, "Sequence Impedance Modeling of Modular Multilevel Converters," *IEEE Journal of Emerging and Selected Topics in Power Electronics*, vol. 5, no. 4, pp. 1427-1443, 2017.

[87] J. Lyu, X. Cai, and M. Molinas, "Impedance Modeling of Modular Multilevel Converters," in *Annual Conference of the IEEE Industrial Electronics Society (IECON)*, 2015, pp. 000180-000185.

[88] X. Shi, Z. Wang, B. Liu, Y. Li, L. M. Tolbert, and F. Wang, "DC Impedance Modelling of a MMC-HVDC system for DC Voltage Ripple Prediction under a Single-Line-to-

Ground Fault," in *IEEE Energy Conversion Congress and Exposition (ECCE)*, Pittsburgh, PA, USA, 2014, pp. 5339-5346.

[89] R. Mo, Q. Ye, and H. Li, "DC Impedance Modeling and Stability Analysis of Modular Multilevel Converter for MVDC Application," in *IEEE Energy Conversion Congress and Exposition (ECCE)*, 2016: IEEE, pp. 1-5.

[90] H. Yang, Y. Dong, W. Li, and X. He, "Average-Value Model of Modular Multilevel Converters Considering Capacitor Voltage Ripple," *IEEE Transactions on Power Delivery,* vol. 32, no. 2, pp. 723-732, 2017.

[91] M. Hiermeier, J. Pforr, M. Mürken, and T. Hackner, "Measurement Technique to Determine the Impedance of Automotive Energy Nets for Stability Analysis Purpose based on a Floating Capacitor H-Bridge Converter," in *IEEE Energy Conversion Congress and Exposition (ECCE)*, Milwaukee, WI, USA, 2016, pp. 1-8.

[92] Z. Shen, M. Jaksic, I. Cvetkovic, R. Burgos, and D. Boroyevich, "Small-Signal Impedance Measurement in Medium-Voltage DC Power Systems," in *International Conference on Electrical Systems for Aircraft, Railway, Ship Propulsion and Road Vehicles (ESARS)*, Aachen, Germany, 2015, pp. 1-5.

[93] J. Vega-Herrera, C. A. Rahmann, F. Valencia, and K. Strunz, "Analysis and Application of Quasi-static and Dynamic Phasor Calculus for Stability Assessment of Integrated Power Electric and Electronic Systems," *IEEE Transactions on Power Systems*, vol. 36, no. 3, pp. 1750-1760, 2021.

[94] Y. Ji, W. He, S. Cheng, J. Kurths, and M. Zhan, "Dynamic Network Characteristics of Power-electronics-based Power Systems," *Scientific Reports*, vol. 10, no. 1, p. 9946, 2020.

[95] K. M. Alawasa, Y. A. I. Mohamed, and W. Xu, "Active Mitigation of Subsynchronous Interactions Between PWM Voltage-Source Converters and Power Networks," *IEEE Transactions on Power Electronics*, vol. 29, no. 1, pp. 121-134, 2014.

[96] L. Harnefors, A. G. Yepes, A. Vidal, and J. Doval-Gandoy, "Passivity-Based Controller Design of Grid-Connected VSCs for Prevention of Electrical Resonance Instability," *IEEE Transactions on Industrial Electronics*, vol. 62, no. 2, pp. 702-710, 2015.

[97] G. Denis, T. Prevost, M. Debry, F. Xavier, X. Guillaud, and A. Menze, "The Migrate Project: the Challenges of Operating a Transmission Grid with only Inverter-based Generation. A grid-Forming Control Improvement with Transient Current-Limiting Control," *IET Renewable Power Generation*, vol. 12, no. 5, pp. 523-529, 2018.

[98] J. Z. Zhou, H. Ding, S. Fan, Y. Zhang, and A. M. Gole, "Impact of Short-Circuit Ratio and Phase-Locked-Loop Parameters on the Small-Signal Behavior of a VSC-HVDC Converter," *IEEE Transactions on Power Delivery*, vol. 29, no. 5, pp. 2287-2296, 2014.

[99] A. Zheng, C. Guo, P. Cui, W. Jiang, and C. Zhao, "Comparative Study on Small-Signal Stability of LCC-HVDC System With Different Control Strategies at the Inverter Station," *IEEE Access*, vol. 7, pp. 34946-34953, 2019.

[100] H. Liu and J. Sun, "Voltage Stability and Control of Offshore Wind Farms With AC Collection and HVDC Transmission," *IEEE Journal of Emerging and Selected Topics in Power Electronics*, vol. 2, no. 4, pp. 1181-1189, 2014.

[101] E. Ebrahimzadeh, F. Blaabjerg, X. Wang, and C. L. Bak, "Bus Participation Factor Analysis for Harmonic Instability in Power Electronics Based Power Systems," *IEEE Transactions on Power Electronics*, vol. 33, no. 12, pp. 10341-10351, 2018.

[102] C. Xie, K. Li, J. Zou, D. Liu, and J. M. Guerrero, "Passivity-Based Design of Grid-Side Current-Controlled LCL-Type Grid-Connected Inverters," *IEEE Transactions on Power Electronics*, vol. 35, no. 9, pp. 9813-9823, 2020.

[103] L. Harnefors, X. Wang, A. G. Yepes, and F. Blaabjerg, "Passivity-Based Stability Assessment of Grid-Connected VSCs—An Overview," *IEEE Journal of Emerging and Selected Topics in Power Electronics*, vol. 4, no. 1, pp. 116-125, 2016.

[104] F. Hans, W. Schumacher, S. Chou, and X. Wang, "Passivation of Current-Controlled Grid-Connected VSCs Using Passivity Indices," *IEEE Transactions on Industrial Electronics*, pp. 1-1, 2018.

[105] H. Yu, M. A. Awal, H. Tu, Y. Du, S. Lukic, and I. Husain, "Passivity-Oriented Discrete-Time Voltage Controller Design for Grid-Forming Inverters," in *IEEE Energy Conversion Congress and Exposition (ECCE)*, 2019, pp. 469-475.

[106] W. Cao, Y. Ma, and F. Wang, "Adaptive Impedance Compensation of Inverters for Stable Grid Integration Based on Online Resonance Detection," in *IEEE Applied Power Electronics Conference and Exposition (APEC)*, 2019, pp. 3151-3158.

[107] X. Wang, F. Blaabjerg, and P. C. Loh, "Passivity-Based Stability Analysis and Damping Injection for Multiparalleled VSCs with LCL Filters," *IEEE Transactions on Power Electronics*, vol. 32, no. 11, pp. 8922-8935, 2017.

[108] M. Lu, X. Wang, P. C. Loh, and F. Blaabjerg, "Resonance Interaction of Multiparallel Grid-Connected Inverters With LCL Filter," *IEEE Transactions on Power Electronics*, vol. 32, no. 2, pp. 894-899, 2017.

[109] S. He, Y. Pan, D. Zhou, X. Wang, and F. Blaabjerg, "Current Harmonic Analysis of Multisampled LCLType Grid-connected Inverter," in *IEEE Energy Conversion Congress and Exposition (ECCE)*, 2020, pp. 4329-4335.

[110] D. Yang, X. Wang, and F. Blaabjerg, "Sideband Harmonic Instability of Paralleled Inverters With Asynchronous Carriers," *IEEE Transactions on Power Electronics,* vol. 33, no. 6, pp. 4571-4577, 2018.

[111] C. Yu, X. Zhang, F. Liu, F. Li, H. Xu, R. Cao *et al.*, "Modeling and Resonance Analysis of Multiparallel Inverters System Under Asynchronous Carriers Conditions," *IEEE Transactions on Power Electronics,* vol. 32, no. 4, pp. 3192-3205, 2017.

[112] L. Harnefors, R. Finger, X. Wang, H. Bai, and F. Blaabjerg, "VSC Input-Admittance Modeling and Analysis Above the Nyquist Frequency for Passivity-Based Stability Assessment," *IEEE Transactions on Industrial Electronics,* vol. 64, no. 8, pp. 6362-6370, 2017.

[113] D. Yang, X. Wang, F. Liu, K. Xin, Y. Liu, and F. Blaabjerg, "Symmetrical PLL for SISO Impedance Modeling and Enhanced Stability in Weak Grids," *IEEE Transactions on Power Electronics,* vol. 35, no. 2, pp. 1473-1483, 2020.

[114] Y. Liao, X. Wang, F. Liu, K. Xin, and Y. Liu, "Sub-Synchronous Control Interaction in Grid-Forming VSCs with Droop Control," in *IEEE Workshop on the Electronic Grid (eGRID)*, 2019, pp. 1-6.

[115] X. Wu, Z. Du, X. Yuan, G. Wu, and F. Zeng, "Subsynchronous Oscillation Analysis of Grid-Connected Converter Based on MIMO Transfer Functions," *IEEE Access,* vol. 8, pp. 92089-92097, 2020.

[116] H. Zhang, L. Harnefors, X. Wang, H. Gong, and J. Hasler, "Stability Analysis of Grid-Connected Voltage-Source Converters Using SISO Modeling," *IEEE Transactions on Power Electronics*, vol. 34, no. 8, pp. 8104-8117, 2019.

[117] Q. Hu, L. Fu, F. Ma, F. Ji, and Y. Zhang, "Analogized Synchronous-Generator Model of PLL-Based VSC and Transient Synchronizing Stability of Converter Dominated Power System," *IEEE Transactions on Sustainable Energy*, vol. 12, no. 2, pp. 1174-1185, 2021.

[118] J. Fang, X. Li, H. Li, and Y. Tang, "Stability Improvement for Three-Phase Grid-Connected Converters Through Impedance Reshaping in Quadrature-Axis," *IEEE Transactions on Power Electronics*, vol. 33, no. 10, pp. 8365-8375, 2018.

[119] X. Zhang, D. Xia, Z. Fu, G. Wang, and D. Xu, "An Improved Feedforward Control Method Considering PLL Dynamics to Improve Weak Grid Stability of Grid-Connected Inverters," *IEEE Transactions on Industry Applications*, vol. 54, no. 5, pp. 5143-5151, 2018.

[120] W. Du, Z. Chen, K. P. Schneider, R. H. Lasseter, S. P. Nandanoori, F. K. Tuffner *et al.*, "A Comparative Study of Two Widely Used Grid-Forming Droop Controls on Microgrid Small-Signal Stability," *IEEE Journal of Emerging and Selected Topics in Power Electronics*, vol. 8, no. 2, pp. 963-975, 2020.

[121] "IEEE Guide for Planning DC Links Terminating at AC Locations Having Low Short-Circuit Capacities," *IEEE Std 1204-1997*, pp. 1-216, 1997.

[122] A. Emadi, A. Khaligh, C. H. Rivetta, and G. A. Williamson, "Constant power loads and negative impedance instability in automotive systems: definition, modeling, stability, and control of power electronic converters and motor drives," *IEEE Transactions on Vehicular Technology*, vol. 55, no. 4, pp. 1112-1125, 2006.

[123] C. Rivetta, G. A. Williamson, and A. Emadi, "Constant Power Loads and Negative Impedance Instability in Sea and Undersea Vehicles: Statement of the Problem and Comprehensive Large-Signal Solution," in *IEEE Electric Ship Technologies Symposium*, 2005, pp. 313-320.

[124] A. M. Rahimi, A. Khaligh, and A. Emadi, "Design and Implementation of an Analog Constant Power Load for Studying Cascaded Converters," in *Annual Conference on IEEE Industrial Electronics*, 2006, pp. 1709-1714.

[125] M. K. AL-Nussari, "Constant Power Loads with Microgirds: Problem Definition, Stability Analysis and Compensation Techniques," *Energies*, vol. 10, no. 1656, 2017.

[126] M. Cupelli, L. Zhu, and A. Monti, "Why Ideal Constant Power Loads Are Not the Worst Case Condition From a Control Standpoint," *IEEE Transactions on Smart Grid*, vol. 6, no. 6, pp. 2596-2606, 2015.

[127] J. Sun, G. Wang, X. Du, and H. Wang, "A Theory for Harmonics Created by Resonance in Converter-Grid Systems," *IEEE Transactions on Power Electronics*, vol. 34, no. 4, pp. 3025-3029, 2019.

[128] L. Kong, Y. Xue, L. Qiao, and F. Wang, "Review of Small-Signal Converter-Driven Stability Issues in Power Systems," *IEEE Open Access Journal of Power and Energy,* vol. 9, pp. 29-41, 2022.

[129] Y. Gu, W. Li, and X. He, "Passivity-based control of DC microgrid for self-disciplined stabilization," *IEEE Transactions on Power Systems*, vol. 30, no. 5, pp. 2623-2632, 2014.

[130] L. Harnefors, A. G. Yepes, A. Vidal, and J. Doval-Gandoy, "Passivity-Based Stabilization of Resonant Current Controllers with Consideration of Time Delay," *IEEE Transactions on Power Electronics*, vol. 29, no. 12, pp. 6260-6263, 2014.

[131] C. Hirsching, S. Wenig, S. Beckler, M. Goertz, P. Praeger, M. Suriyah *et al.*, "Passivity-Based Sensitivity Analysis of the Inner Current Controller in Grid-Following MMC-HVDC Applications - An Overview," in *Annual Conference of the IEEE Industrial Electronics Society*, 18-21 Oct. 2020 2020, pp. 1412-1417.

[132] M. Zhao, X. Yuan, J. Hu, and Y. Yan, "Voltage Dynamics of Current Control Time-Scale in a VSC-Connected Weak Grid," *IEEE Transactions on Power Systems*, vol. 31, no. 4, pp. 2925-2937, 2016.

[133] L. Meegahapola, A. Sguarezi, J. S. Bryant, M. Gu, E. R. Conde D., and R. B. A. Cunha, "Power System Stability with Power-Electronic Converter Interfaced Renewable Power Generation: Present Issues and Future Trends," *Energies*, vol. 13, no. 13, p. 3441, 2020.

[134] Q. Peng, Q. Jiang, Y. Yang, T. Liu, H. Wang, and F. Blaabjerg, "On the Stability of Power Electronics-Dominated Systems: Challenges and Potential Solutions," *IEEE Transactions on Industry Applications*, vol. 55, no. 6, pp. 7657-7670, 2019.

[135] E. G. Cate, K. Hemmaplardh, J. W. Manke, and D. P. Gelopulos, "Time Frame Notion and Time Response of the Models in Transient, Mid-Term and Long-Term Stability Programs," *IEEE Transactions on Power Apparatus and Systems*, vol. PAS-103, no. 1, pp. 143-151, 1984.

[136] X. Liu, H. Sun, R. Wang, Q. Sun, L. Zhang, and P. Wang, "Stability Enhancement Method for Grid-Connected Inverters Under Weak Grid: An Improved Feedforward Control Considering Phase-Locked Loop," *IET Electric Power Applications,* vol. n/a, no. n/a, 2022.

[137] Y. Han, M. Yang, P. Yang, L. Xu, and F. Blaabjerg, "Passivity-Based Stability Analysis of Parallel Single-Phase Inverters with Hybrid Reference Frame Control Considering PLL Effect," *International Journal of Electrical Power & Energy Systems*, vol. 135, p. 107473, 2022.

[138] X. Lin, Y. Wen, R. Yu, J. Yu, and H. Wen, "Improved Weak Grids Synchronization Unit for Passivity Enhancement of Grid-Connected Inverter," *IEEE Journal of Emerging and Selected Topics in Power Electronics (Early Access)* pp. 1-1, 2022.

[139] C. Spanias, P. Aristidou, and M. Michaelides, "A Passivity-Based Framework for Stability Analysis and Control Including Power Network Dynamics," *IEEE Systems Journal,* vol. 15, no. 4, pp. 5000-5010, 2021.

[140] Y. Qi, H. Deng, J. Wang, and Y. Tang, "Passivity-Based Synchronization Stability Analysis for Power-Electronic-Interfaced Distributed Generations," *IEEE Transactions on Sustainable Energy*, vol. 12, no. 2, pp. 1141-1150, 2021.

[141] M. Kabalan, *Large-Signal Lyapunov-Based Stability Analysis of DC/AC Inverters and Inverter-Based Microgrids*. Villanova University, 2016.

[142] W. Du, J. Zhang, Y. Zhang, and Z. Qian, "Stability Criterion for Cascaded System With Constant Power Load," *IEEE Transactions on Power Electronics*, vol. 28, no. 4, pp. 1843-1851, 2013.

[143] F. Umbría, J. Aracil, and F. Gordillo, "Singular Perturbation Stability Analysis of Three Phase Two-Level Power Converters," in *18th Mediterranean Conference on Control and Automation, MED'10*, 23-25 June 2010 2010, pp. 123-128.

[144] Y. Liu, M. Huang, L. Qu, and X. Zha, "Interaction of voltage and current control loop in three-phase voltage source converter," in *Annual Conference of the IEEE Industrial Electronics Society (IECON)*, 2017, pp. 6847-6852.

[145] F. A. Rengifo, L. Romeral, J. Cusidó, and J. J. Cárdenas, "New Model of a Converter-Based Generator Using Electrostatic Synchronous Machine Concept," *IEEE Transactions on Energy Conversion*, vol. 29, no. 2, pp. 344-353, 2014.

[146] P. Hart and B. Lesieutre, "Energy function for a grid-tied, droop-controlled inverter," in *2014 North American Power Symposium (NAPS)*, 7-9 Sept. 2014 2014, pp. 1-6.

[147] M. Kabalan, P. Singh, and D. Niebur, "Nonlinear Lyapunov Stability Analysis of Seven Models of a DC/AC Droop Controlled Inverter Connected to an Infinite Bus," *IEEE Transactions on Smart Grid*, vol. 10, no. 1, pp. 772-781, 2019.

[148] B. Fan and X. Wang, "A Lyapunov-Based Nonlinear Power Control Algorithm for Grid-Connected VSCs," *IEEE Transactions on Industrial Electronics*, vol. 69, no. 3, pp. 2916-2926, 2022.

[149] H. Yu, M. A. Awal, H. Tu, I. Husain, and S. Lukic, "Comparative Transient Stability Assessment of Droop and Dispatchable Virtual Oscillator Controlled Grid-Connected Inverters," *IEEE Transactions on Power Electronics*, vol. 36, no. 2, pp. 2119-2130, 2021.

[150] X. Fu, J. Sun, M. Huang, Z. Tian, H. Yan, H. H. C. Iu *et al.*, "Large-Signal Stability of Grid-Forming and Grid-Following Controls in Voltage Source Converter: A Comparative Study," *IEEE Transactions on Power Electronics,* vol. 36, no. 7, pp. 7832-7840, 2021.

[151] X. Liu and Y. Bian, "Large Signal Stability Analysis of the DC Microgrid with the Storage System," in *IEEE International Conference on Electrical Machines and Systems (ICEMS)*, Sydney, NSW, Australia, 2017, pp. 1-5.

[152] M. Cupelli, F. Ponci, G. Sulligoi, A. Vicenzutti, C. S. Edrington, T. El-Mezyani *et al.*, "Power Flow Control and Network Stability in an All-Electric Ship," *Proceedings of the IEEE,* vol. 103, no. 12, pp. 2355-2380, 2015.

[153] E. Hossain, R. Perez, A. Nasiri, and S. Padmanaban, "A Comprehensive Review on Constant Power Loads Compensation Techniques," *IEEE Access,* vol. 6, pp. 33285-33305, 2018.

[154] Y. Zhao, W. Qiao, and D. Ha, "A Sliding-Mode Duty-Ratio Controller for DC/DC Buck Converters With Constant Power Loads," *IEEE Transactions on Industry Applications,* vol. 50, no. 2, pp. 1448-1458, 2014.

[155] R. Leyva, L. Martinez-Salamero, H. Valderrama-Blavi, J. Maixe, R. Giral, and F. Guinjoan, "Linear State-Feedback Control of a Boost Converter for Large-Signal Stability," *IEEE Transactions on Circuits and Systems I: Fundamental Theory and Applications,* vol. 48, no. 4, pp. 418-424, 2001.

[156] C. N. Onwuchekwa and A. Kwasinski, "Analysis of Boundary Control for Buck Converters with Instantaneous Constant-Power Loads," *IEEE Transactions on Power Electronics,* vol. 25, no. 8, pp. 2018-2032, 2010.

[157] Z. Tian, Y. Tang, X. Zha, J. Sun, M. Huang, X. Fu *et al.*, "Hamilton-Based Stability Criterion and Attraction Region Estimation for Grid-tied Inverters Under Large-Signal Disturbances," *IEEE Journal of Emerging and Selected Topics in Power Electronics*, pp. 1-1, 2021.

[158] D. Pan, X. Wang, F. Liu, and R. Shi, "Transient Stability of Voltage-Source Converters with Grid-Forming Control: A Design-Oriented Study," *IEEE Journal of Emerging and Selected Topics in Power Electronics*, vol. 8, no. 2, pp. 1019-1033, 2020.

[159] C. A. Soriano-Rangel, W. He, F. Mancilla-David, and R. Ortega, "Voltage Regulation in Buck–Boost Converters Feeding an Unknown Constant Power Load: An Adaptive Passivity-Based Control," *IEEE Transactions on Control Systems Technology*, vol. 29, no. 1, pp. 395-402, 2021.

[160] S. Barman, S. Samanta, J. P. Mishra, P. Roy, and B. K. Roy, "Design and Implementation of an IDA-PBC for a Grid Connected Inverter used in a Photovoltaic System," *IFAC-PapersOnLine*, vol. 51, no. 1, pp. 680-685, 2018.

[161] N. Khefifi, A. Houari, M. Machmoum, M. Ghanes, and M. Ait-Ahmed, "Control of Grid Forming Inverter based on Robust IDA-PBC for Power Quality Enhancement," *Sustainable Energy, Grids and Networks*, vol. 20, p. 100276, 2019.

[162] F. Strehle, A. J. Malan, S. Krebs, and S. Hohmann, "A Port-Hamiltonian Approach to Plug-and-Play Voltage and Frequency Control in Islanded Inverter-Based AC Microgrids," in *IEEE Conference on Decision and Control (CDC)*, 2019, pp. 4648-4655.

[163] P. Yang, F. Liu, Z. Wang, and C. Shen, "Distributed Stability Conditions for Power Systems With Heterogeneous Nonlinear Bus Dynamics," *IEEE Transactions on Power Systems*, vol. 35, no. 3, pp. 2313-2324, 2020.

[164] Q. C. Zhong and M. Stefanello, "A Port-Hamiltonian Control Framework to Render a Power Electronic System Passive," *IEEE Transactions on Automatic Control,* vol. 67, no. 4, pp. 1960 - 1965, 2021.

[165] Q. C. Zhong and M. Stefanello, "Port-Hamiltonian Control of Power Electronic Converters to Achieve Passivity," in *2017 IEEE 56th Annual Conference on Decision and Control (CDC)*, 12-15 Dec. 2017 2017, pp. 5092-5097.

[166] Y. Wang, C. Hu, R. Ding, L. Xu, C. Fu, and E. Yang, "A Nearest Level PWM Method for the MMC in DC Distribution Grids," *IEEE Transactions on Power Electronics,* vol. 33, no. 11, pp. 9209-9218, 2018.

[167] M. M. Steurer, K. Schoder, O. Faruque, D. Soto, M. Bosworth, M. Sloderbeck *et al.*, "Multifunctional Megawatt-Scale Medium Voltage DC Test Bed Based on Modular Multilevel Converter Technology," *IEEE Transactions on Transportation Electrification*, vol. 2, no. 4, pp. 597-606, 2016.

[168] J. Wang, R. Burgos, and D. Boroyevich, "Switching-Cycle State-Space Modeling and Control of the Modular Multilevel Converter," *IEEE Journal of Emerging and Selected Topics in Power Electronics*, vol. 2, no. 4, pp. 1159-1170, 2014.

[169] R. Marquardt, "Modular Multilevel Converter: An Universal Concept for HVDC-Networks and Extended DC-Bus-pplications," in *The 2010 International Power Electronics Conference - ECCE ASIA* 2010, pp. 502-507.

[170] A. Lesnicar and R. Marquardt, "An Innovative Modular Multilevel Converter Topology Suitable for a Wide Power Range," in *IEEE Bologna Power Tech Conference Proceedings*, 2003, vol. 3, p. 6.

[171] S. Zhang, S. Wang, N. Praisuwanna, L. Kong, Y. Li, R. B. Martin *et al.*, "Development of a Flexible Modular Multilevel Converter Test-Bed," in *IEEE Energy Conversion Congress and Exposition (ECCE)*, 2018, pp. 5250-5257.

[172] Y. Zhang, X. Chen, and J. Sun, "Impedance Modeling and Analysis of MMC in Single-Star Configuration," in *IEEE Workshop on Control and Modeling for Power Electronics (COMPEL)*, 2017, pp. 1-8.

[173] W. Li, L. Grégoire, and J. Bélanger, "Modeling and Control of a Full-Bridge Modular Multilevel STATCOM," in *IEEE Power and Energy Society General Meeting*, 2012, pp. 1-7.

[174] Z. Yan, H. Xue-hao, T. Guang-fu, and H. Zhi-yuan, "A Study on MMC Model and its Current Control Strategies," in *International Symposium on Power Electronics for Distributed Generation Systems*, 2010, pp. 259-264.

[175] Y. Li, E. A. Jones, and F. Wang, "Circulating Current Suppressing Control's Impact on Arm Inductance Selection for Modular Multilevel Converter," *IEEE Journal of Emerging and Selected Topics in Power Electronics*, vol. 5, no. 1, pp. 182-188, 2017.

[176] S. Geng, Y. Gan, Y. Li, L. Hang, and G. Li, "Novel Circulating Current Suppression Strategy for MMC based on Quasi-PR Controller," in *IEEE Applied Power Electronics Conference and Exposition (APEC)*, 2016, pp. 3560-3565.

[177] W. Lin, W. Ping, L. Zixin, and L. Yaohua, "A Novel Capacitor Voltage Balancing Control Strategy for Modular Multilevel Converters (MMC)," in *International Conference on Electrical Machines and Systems (ICEMS)*, 2013, pp. 1804-1807.

[178] M. Wan, J. Hu, Z. He, and Z. He, "Modeling and Analysis of DC Voltage Dynamics in Modular Multilevel Converter," in *Annual Conference of the IEEE Industrial Electronics Society (IECON)*, 2017, pp. 4531-4537.

[179] T. Li, A. M. Gole, and C. Zhao, "Harmonic Instability in MMC-HVDC Converters Resulting From Internal Dynamics," *IEEE Transactions on Power Delivery*, vol. 31, no. 4, pp. 1738-1747, 2016.

[180] L. Kong, S. Wang, N. Praisuwanna, F. Wang, and L. M. Tolbert, "Stability Analysis and Controller Design of MMC Considering Control Delay," in *2020 IEEE Applied Power Electronics Conference and Exposition (APEC)*, 2020, pp. 1884-1890.

[181] B. Wei, J. M. Guerrero, J. C. Vásquez, and X. Guo, "A Circulating Current Suppression Method for Parallel Connected Voltage-Source-Inverters (VSI) with Common DC and AC Buses," in *IEEE Energy Conversion Congress and Exposition (ECCE)*, 2016, pp. 1-6.

[182] Y. Ma, L. Yang, J. Wang, X. Shi, F. Wang, and L. M. Tolbert, "Circulating Current Control and Reduction in a Paralleled Converter Test-bed System," in *IEEE Energy Conversion Congress and Exposition*, 2013, pp. 5426-5432.

[183] Y. Zhihong, D. Boroyevich, C. Jae-Young, and F. C. Lee, "Control of Circulating Current in Two Parallel Three-Phase Boost Rectifiers," *IEEE Transactions on Power Electronics*, vol. 17, no. 5, pp. 609-615, 2002.

[184] M. Lu, X. Wang, P. C. Loh, F. Blaabjerg, and T. Dragicevic, "Graphical Evaluation of Time-Delay Compensation Techniques for Digitally Controlled Converters," *IEEE Transactions on Power Electronics,* vol. 33, no. 3, pp. 2601-2614, 2018.

[185] Q.-C. Zhong, *Power Electronics-Enabled Autonomous Power Systems: Next Generation Smart Grids*. John Wiley & Sons, 2020.

[186] M. A. Awal, H. Yu, S. Lukic, and I. Husain, "Droop and Oscillator Based Grid-Forming Converter Controls: A Comparative Performance Analysis," *Frontiers in Energy Research,* Original Research vol. 8, no. 168, 2020.

[187] G. Seo, M. Colombino, I. Subotic, B. Johnson, D. Groß, and F. Dörfler, "Dispatchable Virtual Oscillator Control for Decentralized Inverter-dominated Power Systems: Analysis and Experiments," in *2019 IEEE Applied Power Electronics Conference and Exposition (APEC)*, 2019, pp. 561-566.

[188] M. C. Chandorkar, D. M. Divan, and R. Adapa, "Control of Parallel Connected Inverters in Standalone AC Supply Systems," *IEEE Transactions on Industry Applications,* vol. 29, no. 1, pp. 136-143, 1993.

[189] R. Rosso, X. Wang, M. Liserre, X. Lu, and S. Engelken, "Grid-Forming Converters: Control Approaches, Grid-Synchronization, and Future Trends - A Review," *IEEE Open Journal of Industry Applications,* vol. 2, pp. 93 - 109, 2021.

[190] G. Yajuan, W. Weiyang, G. Xiaoqiang, and G. Herong, "An Improved Droop Controller for Grid-Connected Voltage Source Inverter in Microgrid," in *International Symposium on Power Electronics for Distributed Generation Systems*, 2010, pp. 823-828.

[191] Y. Sun, X. Hou, J. Yang, H. Han, M. Su, and J. M. Guerrero, "New Perspectives on Droop Control in AC Microgrid," *IEEE Transactions on Industrial Electronics*, vol. 64, no. 7, pp. 5741-5745, 2017.

[192] R. Majumder, G. Ledwich, A. Ghosh, S. Chakrabarti, and F. Zare, "Droop Control of Converter-Interfaced Microsources in Rural Distributed Generation," *IEEE Transactions on Power Delivery*, vol. 25, no. 4, pp. 2768-2778, 2010.

[193] B. B. Johnson, M. Sinha, N. G. Ainsworth, F. Dörfler, and S. V. Dhople, "Synthesizing Virtual Oscillators to Control Islanded Inverters," *IEEE Transactions on Power Electronics*, vol. 31, no. 8, pp. 6002-6015, 2016.

[194] M. Sinha, F. Dörfler, B. B. Johnson, and S. V. Dhople, "Virtual Oscillator Control Subsumes Droop Control," in *2015 American Control Conference (ACC)*, 1-3 July 2015 2015, pp. 2353-2358.

[195] M. Colombino, D. Groß, J. Brouillon, and F. Dörfler, "Global Phase and Magnitude Synchronization of Coupled Oscillators With Application to the Control of Grid-Forming Power Inverters," *IEEE Transactions on Automatic Control*, vol. 64, no. 11, pp. 4496-4511, 2019.

[196] M. Lu, S. Dutta, V. Purba, S. Dhople, and B. Johnson, "A Grid-compatible Virtual Oscillator Controller: Analysis and Design," in *2019 IEEE Energy Conversion Congress and Exposition (ECCE)*, 2019, pp. 2643-2649.

[197] M. A. Awal and I. Husain, "Unified Virtual Oscillator Control for Grid-Forming and Grid-Following Converters," *IEEE Journal of Emerging and Selected Topics in Power Electronics*, vol. 9, no. 4, pp. 4573 - 4586, 2020.

[198] L. M. Tolbert, F. Wang, K. Tomsovic, K. Sun, J. Wang, Y. Ma *et al.*, "Reconfigurable Real-Time Power Grid Emulator for Systems with High Penetration of Renewables," *IEEE Open Access Journal of Power and Energy,* vol. 7, pp. 489-500, 2020.

[199] C. Zhou and K. H. Low, "Design and Locomotion Control of a Biomimetic Underwater Vehicle With Fin Propulsion," *IEEE/ASME Transactions on Mechatronics,* vol. 17, no. 1, pp. 25-35, 2012.

[200] E. Panteley, A. Loría, and A. El-Ati, "Practical Dynamic Consensus of Stuart–Landau Oscillators over Heterogeneous Networks," *International Journal of Control,* vol. 93, no. 2, pp. 261-273, 2020.

[201] Q. Qiu, B. Zhou, P. Wang, L. He, Y. Xiao, Z. Yang *et al.*, "Origin of Amplitude Synchronization in Coupled Nonidentical Oscillators," *Physical Review* vol. 101, no. 2, p. 022210, 2020.

[202] L. V. Gambuzza, J. Gómez-Gardeñes, and M. Frasca, "Amplitude Dynamics Favors Synchronization in Complex Networks," *Scientific Reports,* vol. 6, no. 1, p. 24915, 2016.

[203] M. C. Cross, J. L. Rogers, R. Lifshitz, and A. Zumdieck, "Synchronization by Reactive Coupling and Nonlinear Frequency Pulling," *Physical Review E,* vol. 73, no. 3, p. 036205, 03/06/ 2006.

[204] R. Ortega, A. van der Schaft, B. Maschke, and G. Escobar, "Interconnection and Damping Assignment Passivity-Based Control of Port-Controlled Hamiltonian Systems," *Automatica,* vol. 38, no. 4, pp. 585-596, 2002.

[205] B. Yi, R. Ortega, D. Wu, and W. Zhang, "Orbital Stabilization of Nonlinear Systems via Mexican Sombrero Energy Shaping and Pumping-and-Damping Injection," *Automatica*, vol. 112, p. 108661, 2020.

[206] H. K. Khalil, *Nonlinear Systems*, 3rd ed. Upper Saddle River,: Prentice Hall, 2002.

[207] A. Tayyebi, D. Groß, A. Anta, F. Kupzog, and F. Dörfler, "Interactions of Grid-Forming Power Converters and Synchronous Machines," *arXiv preprint arXiv:1902.10750*, 2019.

[208] V. A. K. Prabhala, B. P. Baddipadiga, and M. Ferdowsi, "DC Distribution Systems-An Overview," in *International Conference on Renewable Energy Research and Application (ICRERA)*, 2014, pp. 307-312.

[209] W. Yang, Z. Yibin, Z. Donglai, and H. Han, "The Technical Trends and Suggestions on the Development of DC Power Grid," in *International Conference on Power System Technology*, 2014, pp. 1975-1979.

[210] E. Rodriguez-Diaz, M. Savaghebi, J. C. Vasquez, and J. M. Guerrero, "An Overview of Low Voltage DC Distribution Systems for Residential Applications," in *IEEE International Conference on Consumer Electronics - Berlin (ICCE-Berlin)*, 2015, pp. 318-322.

[211] J. Brombach, T. Schröter, A. Lücken, and D. Schulz, "Optimized Cabin Power Supply with a +/− 270 V DC Grid on a Modern Aircraft," in *International Conference-Workshop Compatibility and Power Electronics (CPE)*, 2011, pp. 425-428.

[212] V. Madonna, P. Giangrande, and M. Galea, "Electrical Power Generation in Aircraft: Review, Challenges, and Opportunities," *IEEE Transactions on Transportation Electrification*, vol. 4, no. 3, pp. 646-659, 2018.

[213] B. Rahrovi and M. Ehsani, "A Review of the More Electric Aircraft Power Electronics," in *IEEE Texas Power and Energy Conference (TPEC)*, 2019, pp. 1-6.

[214] P. Kshirsagar, J. Ewanchuk, B. v. Hassel, R. Taylor, S. Dwari, J. Rheaume *et al.*, "Anatomy of a 20 MW Electrified Aircraft: Metrics and Technology Drivers," in *AIAA/IEEE Electric Aircraft Technologies Symposium (EATS)*, 2020, pp. 1-9.

[215] A. K. Hyder, "A Century of Aerospace Electrical Power Technology," *Journal of Propulsion and Power,* vol. 19, no. 6, pp. 1155-1179, 2003.

[216] R. W. Johnson. "AC versus DC Power Distribution." Eaton. https://www.eaton.com/content/dam/eaton/markets/data-center/AC-Versus-DC-Power-Distribution.pdf (accessed 11/29/2020, 2020).

[217] T. Halder, "Comparative Study of HVDC and HVAC for a Bulk Power Transmission," in *International Conference on Power, Energy and Control (ICPEC)*, 2013, pp. 139-144.

[218] E. Planas, J. Andreu, J. I. Gárate, I. Martínez de Alegría, and E. Ibarra, "AC and DC Technology in Microgrids: A Review," *Renewable and Sustainable Energy Reviews,* vol. 43, pp. 726-749, 2015.

[219] A. Kalair, N. Abas, and N. Khan, "Comparative Study of HVAC and HVDC Transmission Systems," *Renewable and Sustainable Energy Reviews,* vol. 59, pp. 1653-1675, 2016.

[220] S. Qi, W. Sun, and Y. Wu, "Comparative Analysis on Different Architectures of Power Supply System for Data Center and Telecom Center," in *IEEE International Telecommunications Energy Conference (INTELEC)*, 2017, pp. 26-29.

[221] B. R. Shrestha, U. Tamrakar, T. M. Hansen, B. P. Bhattarai, S. James, and R. Tonkoski, "Efficiency and Reliability Analyses of AC and 380 V DC Distribution in Data Centers," *IEEE Access*, vol. 6, pp. 63305-63315, 2018.

[222] M. Rivard, C. Fallaha, and J. Paquin, "Real-Time Simulation of a More Electric Aircraft Power Generation and Distribution System," in *AIAA/IEEE Electric Aircraft Technologies Symposium (EATS)*, 2018, pp. 1-10.

[223] S. Byahut and A. Uranga, "Power Distribution and Thermal Management Modeling for Electrified Aircraft," in *AIAA/IEEE Electric Aircraft Technologies Symposium (EATS)*, 2020, pp. 1-15.

[224] D. F. Finger, C. Braun, and C. Bil, "Case Studies in Initial Sizing for Hybrid-Electric General Aviation Aircraft," in *AIAA/IEEE Electric Aircraft Technologies Symposium (EATS)*, 2018, pp. 1-22.

[225] J. Chen, J. Shen, J. Chen, P. Shen, Q. Song, and C. Gong, "Investigation on the Selection and Design of Step-Up/Down 18-Pulse ATRUs for More Electric Aircrafts," *IEEE Transactions on Transportation Electrification*, vol. 5, no. 3, pp. 795-811, 2019.

[226] J. Sun, Z. Bing, and K. J. Karimi, "Small-Signal Modeling of Multipulse Rectifiers for More-Electric Aircraft Applications," in *IEEE Power Electronics Specialists Conference*, 2008, pp. 302-308.

[227] S. M. Blair, C. D. Booth, I. M. Elders, N. K. Singh, G. M. Burt, and J. Mccarthy, "Superconducting Fault Current Limiter Application in A Power-Dense Marine Electrical System," *IET Electrical Systems in Transportation*, vol. 1, no. 3, pp. 93-102, 2011.

[228] S. Fletcher, P. Norman, S. Galloway, and G. Burt, "Solid State Circuit Breakers Enabling Optimised Protection of DC Aircraft Power Systems," in *Proceedings of the European Conference on Power Electronics and Applications*, 2011, pp. 1-10.

[229] I. Vieto and J. Sun, "Sequence Impedance Modeling and Converter-Grid Resonance Analysis Considering DC Bus Dynamics and Mirrored Harmonics," in *IEEE Workshop on Control and Modeling for Power Electronics (COMPEL)*, 2018, pp. 1-8.

Appendices

A. Coupling Strength Derivation in Chapter 7

Normally for coupled oscillators, the synchronization is achieved by adjusting the coupling strength γ and μ. However, in power systems, the coupling strength is fixed which is defined by the transmission line parameters, the system synchronization is then obtained by moving to the predefined steady-state working conditions, i.e., P_{ref} and Q_{ref}.

$$\begin{bmatrix} CP_\alpha \\ CP_\beta \end{bmatrix} = \begin{bmatrix} \gamma(v_{\alpha g} - v_\alpha) - \mu(v_{\beta g} - v_\beta) \\ \gamma(v_{\beta g} - v_\beta) + \mu(v_{\alpha g} - v_\alpha) \end{bmatrix} = \begin{bmatrix} -\gamma & \mu \\ -\mu & -\gamma \end{bmatrix} \begin{bmatrix} v_\alpha \\ v_\beta \end{bmatrix} + \begin{bmatrix} \gamma & -\mu \\ \mu & \gamma \end{bmatrix} \begin{bmatrix} v_{\alpha g} \\ v_{\beta g} \end{bmatrix} \tag{A. 1}$$

In steady-state, the instantaneous power flowing out of the converter to the grid can be calculated as (A. 2) and (A. 3), where, $\delta = \theta_g - \theta$.

$$\begin{aligned} P_{ref} &= \frac{v^2R - vv_g[R\cos(\delta) + \omega L_g sin(\delta)]}{R^2 + (\omega L_g)^2} \\ &= \mu v^2 - vv_g[\mu\cos(\delta) + \gamma sin(\delta)] \end{aligned} \tag{A. 2}$$

$$\begin{aligned} Q_{ref} &= \frac{v^2\omega L_g - vv_g[\omega L_g\cos(\delta) - R sin(\delta)]}{R^2 + (\omega L_g)^2} \\ &= \gamma v^2 - vv_g[\gamma\cos(\delta) - \mu sin(\delta)] \end{aligned} \tag{A. 3}$$

Therefore,

$$\mu\cos(\delta) + \gamma sin(\delta) = \frac{\mu v^2 - P_{ref}}{vv_g} \tag{A. 4}$$

$$\gamma\cos(\delta) - \mu sin(\delta) = \frac{\gamma v^2 - Q_{ref}}{v v_g} \tag{A. 5}$$

Assuming $v_g = v + \Delta v$, $v_{\alpha g} = v_g \cos\theta_g$, $v_{\beta g} = v_g \sin\theta_g$, and according to $\theta_g = \theta + \delta$,

$$\begin{bmatrix}\gamma & -\mu \\ \mu & \gamma\end{bmatrix}\begin{bmatrix}v_{\alpha g} \\ v_{\beta g}\end{bmatrix} = \begin{bmatrix}\gamma & -\mu \\ \mu & \gamma\end{bmatrix}\begin{bmatrix}v_g\cos\theta_g \\ v_g\sin\theta_g\end{bmatrix}$$

$$= \begin{bmatrix}\gamma & -\mu \\ \mu & \gamma\end{bmatrix}\begin{bmatrix}(v + \Delta v)(\cos\theta\cos\delta - \sin\theta\sin\delta) \\ (v + \Delta v)(\sin\theta\cos\delta + \sin\delta\cos\theta)\end{bmatrix}$$

$$= \begin{bmatrix}\gamma & -\mu \\ \mu & \gamma\end{bmatrix}$$

$$* \begin{bmatrix}v(\cos\theta\cos\delta - \sin\theta\sin\delta) + \Delta v(\cos\theta\cos\delta - \sin\theta\sin\delta) \\ v(\sin\theta\cos\delta + \sin\delta\cos\theta) + \Delta v(\sin\theta\cos\delta + \sin\delta\cos\theta)\end{bmatrix} \tag{A. 6}$$

$$= \begin{bmatrix}\gamma & -\mu \\ \mu & \gamma\end{bmatrix}\begin{bmatrix}v_\alpha\cos\delta - v_\beta\sin\delta + (\Delta_{v\alpha}\cos\delta - \Delta_{v\beta}\sin\delta) \\ v_\beta\cos\delta + v_\alpha\sin\delta + (\Delta_{v\beta}\cos\delta + \Delta_{v\alpha}\sin\delta)\end{bmatrix}$$

$$= \begin{bmatrix}\gamma & -\mu \\ \mu & \gamma\end{bmatrix}\begin{bmatrix}(v_\alpha + \Delta_{v\alpha})\cos\delta - (v_\beta + \Delta_{v\beta})\sin\delta \\ (v_\alpha + \Delta_{v\alpha})\sin\delta + (v_\beta + \Delta_{v\beta})\cos\delta\end{bmatrix}$$

$$= \begin{bmatrix}\gamma & -\mu \\ \mu & \gamma\end{bmatrix}\begin{bmatrix}\cos\delta & -\sin\delta \\ \sin\delta & \cos\delta\end{bmatrix}\begin{bmatrix}v_\alpha + \Delta_{v\alpha} \\ v_\beta + \Delta_{v\beta}\end{bmatrix}$$

$$= \begin{bmatrix}\gamma\cos\delta - \mu\sin\delta & -\gamma\sin\delta - \mu\cos\delta \\ \gamma\sin\delta + \mu\cos\delta & \gamma\cos\delta - \mu\sin\delta\end{bmatrix}\begin{bmatrix}v_\alpha \\ v_\beta\end{bmatrix}\frac{v_g}{v}$$

Then subsuming (A. 4), (A. 5) to (A. 6), (A. 7) can be obtained.

$$\begin{bmatrix} \gamma & -\mu \\ \mu & \gamma \end{bmatrix} \begin{bmatrix} v_{\alpha g} \\ v_{\beta g} \end{bmatrix} = \begin{bmatrix} \frac{\gamma v^2 - Q_{ref}}{v v_g} & -\frac{\mu v^2 - P_{ref}}{v v_g} \\ \frac{\mu v^2 - P_{ref}}{v v_g} & \frac{\gamma v^2 - Q_{ref}}{v v_g} \end{bmatrix} \begin{bmatrix} v_\alpha \\ v_\beta \end{bmatrix} \frac{v_g}{v}$$

$$= \begin{bmatrix} \gamma - \frac{Q_{ref}}{v^2} & -\mu + \frac{P_{ref}}{v^2} \\ \mu - \frac{P_{ref}}{v^2} & \gamma - \frac{Q_{ref}}{v^2} \end{bmatrix} \begin{bmatrix} v_\alpha \\ v_\beta \end{bmatrix} \tag{A. 7}$$

Therefore, the coupling term under the steady state can be modeled as (A. 8)

$$\begin{bmatrix} CP_{\alpha,ref} \\ CP_{\beta,ref} \end{bmatrix} = \begin{bmatrix} -\gamma & \mu \\ -\mu & -\gamma \end{bmatrix} \begin{bmatrix} v_\alpha \\ v_\beta \end{bmatrix} + \begin{bmatrix} \gamma - \frac{Q_{ref}}{v^2} & -\mu + \frac{P_{ref}}{v^2} \\ \mu - \frac{P_{ref}}{v^2} & \gamma - \frac{Q_{ref}}{v^2} \end{bmatrix} \begin{bmatrix} v_\alpha \\ v_\beta \end{bmatrix}$$

$$= \begin{bmatrix} -\frac{Q_{ref}}{v^2} & \frac{P_{ref}}{v^2} \\ -\frac{P_{ref}}{v^2} & -\frac{Q_{ref}}{v^2} \end{bmatrix} \begin{bmatrix} v_\alpha \\ v_\beta \end{bmatrix} \tag{A. 8}$$

B. Solving Control Vectors through the Matching Equation in Chapter 7

By matching (7. 9) and (7. 15), (B. 1) can be obtained as

$$\dot{x} = \left(\begin{bmatrix} 0 & 0 & 0 & 0 \\ 0 & 0 & 0 & 0 \\ 0 & 0 & 0 & b_{34} \\ 0 & 0 & b_{43} & 0 \end{bmatrix} - \begin{bmatrix} a_{11} & 0 & 0 & 0 \\ 0 & a_{22} & 0 & 0 \\ 0 & 0 & a_{33} & 0 \\ 0 & 0 & 0 & a_{44} \end{bmatrix} \right) \begin{bmatrix} i_{L\alpha} - i_{L\alpha ref} \\ i_{L\beta} - i_{L\beta ref} \\ v_\alpha \\ v_\beta \end{bmatrix} \tag{B. 1}$$

Then, the control vectors can be calculated as (B. 2)

$$\begin{bmatrix} u_\alpha \\ u_\beta \end{bmatrix} = \begin{bmatrix} 1 & 0 & 0 & 0 \\ 0 & 1 & 0 & 0 \end{bmatrix} \left(\begin{bmatrix} -a_{11} & 0 & 0 & 0 \\ 0 & -a_{22} & 0 & 0 \\ 0 & 0 & -a_{33} & b_{34} \\ 0 & 0 & b_{43} & -a_{44} \end{bmatrix} \begin{bmatrix} i_{L\alpha} - i_{L\alpha ref} \\ i_{L\beta} - i_{L\beta ref} \\ v_\alpha \\ v_\beta \end{bmatrix} \right. \tag{B. 2}$$
$$\left. - \begin{bmatrix} -R_f & 0 & -1 & 0 \\ 0 & -R_f & 0 & -1 \\ 1 & 0 & 0 & 0 \\ 0 & 1 & 0 & 0 \end{bmatrix} \begin{bmatrix} i_{L\alpha} \\ i_{L\beta} \\ v_\alpha \\ v_\beta \end{bmatrix} + \begin{bmatrix} 0 & 0 \\ 0 & 0 \\ 1 & 0 \\ 0 & 1 \end{bmatrix} \begin{bmatrix} i_{g\alpha} \\ i_{g\beta} \end{bmatrix} \right)$$

Rearrange (B. 2), it can then be obtained that

$$\begin{bmatrix} u_\alpha \\ u_\beta \end{bmatrix} = \begin{bmatrix} 1 & 0 & 0 & 0 \\ 0 & 1 & 0 & 0 \end{bmatrix} \left(\begin{bmatrix} -a_{11} i_{L\alpha} + a_{11} i_{L\alpha ref} + R_f i_{L\alpha} + v_\alpha \\ -a_{22} i_{L\beta} + a_{22} i_{L\beta ref} + R_f i_{L\beta} + v_\beta \\ -a_{33} v_\alpha + b_{34} v_\beta - i_{L\alpha} + i_{g\alpha} \\ b_{43} v_\alpha - a_{44} v_\beta - i_{L\beta} + i_{g\beta} \end{bmatrix} \right) \tag{B. 3}$$
$$= \begin{bmatrix} -L_f \xi_4 (i_{L\alpha ref} - i_{L\alpha}) + R_f i_{L\alpha} + v_\alpha \\ -L_f \xi_4 (i_{L\beta ref} - i_{L\beta}) + R_f i_{L\beta} + v_\beta \end{bmatrix}$$

C. Lyapunov Stability Analysis

Equation (7. 29) can be calculated as (C. 1)

$$\begin{aligned} V(x) &= H_l + \frac{1}{2}\Phi^2 \\ &= \frac{1}{2}L_f\left(i_{L\alpha} - i_{L\alpha ref}\right)^2 + \frac{1}{2}L_f\left(i_{L\beta} - i_{L\beta ref}\right)^2 + \frac{1}{2}(H_p - H_p^*)^2 \end{aligned} \tag{C. 1}$$

Taking the time derivative of $V(x)$, it can then be obtained that

$$\dot{V}(x) = L_f \ddot{i}_{L\alpha}\left(i_{L\alpha} - i_{L\alpha ref}\right) + L_f \ddot{i}_{L\beta}\left(i_{L\beta} - i_{L\beta ref}\right) + C_f \dot{v}_\alpha \Phi v_\alpha + C_f \dot{v}_\beta \Phi v_\beta \tag{C. 2}$$

$$\dot{V}(x) = -a_{11}\left(i_{L\alpha} - i_{L\alpha ref}\right)^2 - a_{22}\left(i_{L\beta} - i_{L\beta ref}\right)^2 - \Phi a_{33} v_\alpha^2 - \Phi a_{44} v_\beta^2 \tag{C. 3}$$

According to the modified passivity-based criteria, it can be concluded that

$$\dot{V}(x) < 0 \tag{C. 4}$$

Vita

Ms. Le Kong was born in Taizhou, Jiangsu Province, China in March 1992. She received her Bachelor of Science degree from the Nanjing University of Aeronautics and Astronautics, Nanjing, China, in 2014, and her Master of Science degree from the National Taiwan University, Taipei, Taiwan, in 2016, both in electrical engineering. She started her Ph.D. study in 2017 at the Center for Ultra-wide-area Resilient Electric Energy Transmission Networks (CURENT), the University of Tennessee, Knoxville. During 2016 - 2017, she was an application engineer at Silergy Corp., Hangzhou, China. Her research interests include modeling and control of power electronics converters, analysis of power system stability, etc.